Networks of the Late Quaternary

Analysing paleoclimate data using complex network techniques

D I S S E R T A T I O N

zur Erlangung des akademischen Grades

d o c t o r   r e r u m   n a t u r a l i u m
(Dr. rer. nat)
im Fach Physik

eingereicht an der
Mathematisch-Naturwissenschaftlichen Fakultät:
der Humboldt-Universität zu Berlin

von
M. Sc. Jasper Gideon Franke

Präsidentin der Humboldt-Universität zu Berlin:
Prof. Dr.-Ing. Dr. Sabine Kunst

Dekan der Mathematisch-Naturwissenschaftlichen Fakultät
Prof. Dr. Elmar Kulke

Gutachter:

1. Prof. Jürgen Kurths

2. Assoc. Prof. Peter Ditlevsen

3. Dr. Thomas Laepple

Tag der mündlichen Prüfung: 01.03.2019

Networks of the Late Quaternary

Analysing paleoclimate data using complex network techniques

A doctoral thesis submitted by
Jasper Gideon Franke
in December 2018

Humboldt-Universität zu Berlin
Department of Physics

Potsdam Institute for Climate Impact Research
Research Domain: Transdisciplinary Concepts & Methods
Research Group: CoSy-CC^2, Complex Systems Approaches to Understanding Causes and
Consequences of Past, Present and Future Climate Change

Abstract

In recent years, complex networks have become an increasingly popular tool to analyse relationships and structures in high-dimensional data sets in a variety of research fields. They have, however, rarely been applied to paleoclimate data sets, even though the growing number of published records demands efficient tools of multivariate analysis. The few published results that combine network methods and paleoclimate proxies are often not robust or have high uncertainty levels, linked tothe low dimensionality, resolution and the large uncertainties of most particulate time series.

In this thesis, I propose several ways to overcome these issues in order to obtain reliable and quantitative results from network based tools by taking the particularities of paleoclimate data into account. For this purpose, I present four case studies, focusing on two time periods, the late Holocene (last two millennia) and the transition from the last ice age to the recent warm period—the last deglaciation. These studies are all related to the North Atlantic, a key region in multi-decadal to millennial scale climate variability. I primarily use two methods, one of network based time series analysis named *visibility graphs* and one of spatial analysis, so called *climate networks.*

The first case study analyses the degree of complexity in a set of terrestrial records from Northern Europe, using the method of visibility graphs. Here, I propose an approach of both single record and ensemble based significance testing to overcome the high rate of false positives that is typical for the method. In this way, I show that during the last two millennia there were multiple time periods at which the regional climate system exhibited anomalous dynamics, possibly related to perturbations by solar and volcanic forcing.

In a second study, I propose a novel method to reconstruct integrative climate indices, in particular the North Atlantic Oscillation (NAO) for the last two millennia. In contrast to classical methods, this approach is not adversely affected by the non-stationary relationship between atmospheric patterns and paleoclimate archives, but actually utilizes it, by using network linkages between distant regions to reconstruct past multi-decadal variability.

For times beyond the Holocene, the uncertainties in paleoclimate records increase drastically, in particular due to the limitations of physical dating procedures. To be able to construct climate networks for these records, I systematically study the influences of different interpolation methods and different levels of time uncertainty in a Bayesian framework of correlation estimation. This approach is then used to construct spatial networks out of marine sediment records. In contrast to previous studies, the links in this network are probabilistic estimates, incorporating many sources of uncertainty. In this way, I am able to construct more robust and reliable networks, which still show the ocean circulation changes that accompanied the last deglaciation.

In the last case study, I turn away from proxy data to study high-dimensional climate networks obtained from a transient model simulation of the last 21,000 years. Here, abrupt transitions are cleary visible in the topology of associated climate networks, demonstrating their ability to identify patterns of changes in a complex system.

I therefore both further develop existing methods, but also propose new ways to yield reliable results when dealing with highly uncertain paleoclimate data. The case studies demonstrate the usefulness of network based data analysis to study patterns of regional climate variability. Hence, this work is another step in bringing network based approaches to a larger audience and towards a wider application of these methods.

Zusammenfassung

In den letzten Jahren erfreuen sich komplexe Netzwerke einer zunehmenden Beliebtheit, um Zusammenhänge und Strukturen in hoch-dimensionalen Datensätzen zu analysieren. Im Unterschied zu vielen anderen Forschungsgebieten wurden sie jedoch selten auf Paläoklima-Daten angewandt, obwohl die steigende Anzahl an veröffentlichen Zeitreihen die Nutzung effizienter Methoden multivariater Analyse ermöglicht. Die Resultate der wenigen Studien, in denen Netzwerkmethoden und Paläoklima-Daten kombiniert wurden, sind außerdem geprägt von niedriger Robustheit und hohen Unsicherheiten. Dies steht im Zusammenhang zu der niedrigen Anzahl und Auflösung der Zeitreihen als auch den Unsicherheiten, die den meisten Paläoklima-Rekonstruktionen zu eigen sind.

In dieser Doktorarbeit schlage ich verschiedene Wege vor, um diese Probleme zu überwinden, indem verlässlichere, quantitative Resultate ermöglicht werden, unter anderem indem die Datenunsicherheiten explizit in die Analyse mit einbezogen werden. Zu diesem Zweck präsentiere ich vier Fallstudien mit einem Fokus auf zwei Zeiträume, das späte Holozän (die letzten zweitausend Jahre) und den Übergang von der letzten Kaltzeit zur aktuellen Warmzeit, die letzte glaziale Termination. Alle diese Studien legen einen räumlichen Fokus auf den Nordatlantik, eine Schlüsselregion globaler Klimavariabilität. Ich beschränke mich hierbei auf zwei Methoden, eine der netzwerkbasierten Zeitreihenanalyse, *Sichtbarkeitsgraphen* genannt, und eine der räumlichen Analyse, sogenannte *Klimanetzwerke*.

Die erste Studie beschäftigt sich mit dem Grad von Komplexität in Zeitreihen aus Nordeuropa mithilfe der Methode der Sichtbarkeitsgraphen. Um die geringe Verlässlichkeit der Methode zu überwinden, schlage ich verschiedene Signifikanztests vor, sowohl für einzelne Zeitreihen, als auch für Ensembles mehrerer Proxies. Somit kann ich zeigen, dass es in den letzten zwei Jahrtausenden verschieden Perioden gab, in denen das regionale Klimasystem ungewöhnliche Dynamiken durchlief, wahrscheinlich ausgelöst durch Veränderungen in der Sonnenaktivität and Vulkaneruptionen.

In einer zweiten Studie entwickele ich eine neuartige Methode, um integrierte Klimaindizes zu rekonstruieren, in diesem Fall die Nordatlantische Oszillation für die letzten zweitausend Jahre. Während der nichttstationäre Zusammenhang zwischen großskaligen atmosphärischen Bedingungen und den einzelnen Proxies ein großes Problem für klassische Rekonstruktionen darstellt, basiert diese neue Methode genau auf dieser Eigenschaft, indem die Phase der NAO in Bezug zu den statistischen Abhängigkeitsstrukturen zwischen verschiedenen Regionen gesetzt wird.

Die Unsicherheiten in Paläoklima-Daten nehmen dramatisch zu, wenn Zeiten vor dem Holozän untersucht werden, insbesondere durch die ungenaue Datierung vieler Zeitreihen. Um Klimanetzwerke für diese Zeiten definieren zu können untersuche ich zunächst systematisch den Einfluss verschiedener Interpolationsmethoden und Unsicherheiten auf die Bayesianische Schätzung von Korrelationen. Dieser Zugang wird im folgenden angewendet, um Zeitreihen aus marinen Sedimenten der letzten 30.000 Jahre zu studieren. Die Verbindungen in diesen Netzwerken sind gegeben als Verteilungen, und somit können robuste und verlässliche Analysen an ihnen durchgeführt werden. Die so entstehnden Netzwerke spiegeln die Veränderungen in der Atlantikzirkulation während der letzten glazialen Termination wieder.

In einer letzten Fallstudie widme ich mich den Ergebnissen einer transienten Klimamodellsimulation der letzten 21.000 Jahre und wie diese in Klimanetzwerken dargestellt wird. Die abrupten Übergänge in der Variabilität sind klar sichtbar in der sich verändernden Topologie des Netzwerkes, was das Potential dieser Methode demonstriert, solche Veränderungen zu detektieren.

Zusammenfassend erweitere ich also sowohl existierende Methoden, schlage aber auch neue Wege vor, um verlässliche Resultate auch für Zeitreihen mit hohen Unsicherheiten zu erhalten. Diese Fallstudien demonstrieren, dass Netzwerkmethoden auch für die Analyse von Paläoklima-Daten nützlich sein können. Sie sind daher ein weiterer Schritt hin zu einer künftigen Anwendung durch eine größere Anzahl an Forschenden.

Acknowledgements

This thesis could never have been finished without the help and support of many people. My special thanks, however, go to Prof. Jürgen Kurths and Dr. Reik Donner for accepting me as their PhD student and for their supervision. In this respect, I am particularly grateful to Dr. Reik Donner for selecting me as a member of his research group and for his day-to-day supervision. In addition to all the scientific support, I much appreciated the freedom and flexibility that he has offered me, both in scientific endeavours, but also in times of personal difficulties.

I also want to thank Assoc. Prof. Peter Ditlevsen and Dr. Thomas Laepple for their willingness to review the thesis and Prof. Claudia Draxl and Dr. Sten Rüdiger for joining the committee.

Furthermore, I want to thank my fellow colleagues at PIK and all other friends, for all the support that I have received in the last years. In particular I want to thank Catrin, Chiranjit, Frederik, Max, Paul and Robin for contributing valuable comments on this thesis. I also thank Johannes P. Werner and Dimitry Divine for the extensive and productive scientific exchange.

I also owe sincere thanks to my family, foremost my mother Cordula, but also my father Eckhard, my sister Gesa, my step-father Peter, and my brother-in-law Jannes, all of whom took part in my journey towards this thesis. Last but not least, I am incredibly thankful to Sabrina, for the support that she has been to me in the last months.

Contents

List of Publications

The following publications were published, submitted, or prepared by me while working on this thesis. This thesis is largely built upon these results.

JF1   J. G. Franke and R. V. Donner (2017). "Dynamical anomalies in terrestrial proxies of North Atlantic climate variability during the last 2 ka". In: *Climatic Change* 143.1, pp. 87–100. DOI: 10.1007/s10584-017-1979-z.

JF2   J. G. Franke, J. P. Werner, and R. V. Donner (2017). "Reconstructing Late Holocene North Atlantic atmospheric circulation changes using functional paleoclimate networks". In: *Climate of the Past* 13.11, pp. 1593–1608. DOI: 10.5194/cp-13-1593-2017.

JF3   J. G. Franke and R. V. Donner (2019a). "Correlating Paleoclimate Time Series: Sources of Uncertainty and Potential Pitfalls". Submitted to: *Quaternary Science Reviews.*

JF4   J. G. Franke and R. V. Donner (2019b). "Relative timing and spatial co-variability of stable isotopes in benthic foraminifera in the Atlantic ocean during the last glacial termination". In preparation for: *Paleoceanography and Paleoclimatology.*

JF5   J. G. Franke, F. Särdquist, and R. V. Donner (2019). "Spatial variability of the TraCE-21ka simulation: a network perspective". In preparation for: *Nature Scientific Reports.*

List of Figures

List of Tables

Comments on notation and frequently used mathematical symbols

All the analysis presented in this thesis have been developed and conducted by me. Still, I did not do this alone, but with help and input of co-authors and under the supervision of Dr. Reik V. Donner. In general, I use first person singular (*I*), when talking about the thesis itself, but use first person plural (*we*) during the chapters in which I present results. In this way, I intend to stress the important roles that my co-authors played in each study, but also to include the reader in the presented line of thought. The latter applies in particular, when pointing towards specific results.

I follow two naming conventions for time in this thesis, in line with the established ways in the respective communities. Part II deals with the late Holocene, in particular the last two millennia. Here, we use the notation of *Common Era* (CE) and *Before Common Era* (BCE), which correspond to AD/BC, but lack the religious connotation. As we deal with much longer time periods in Part III, we use the notation of years before present (a BP) or thousand years before present (ka BP).

Note that plots also differ for the two time periods, in accordance with the corresponding conventions. For the Common Era, the most recent times are on the right end of a graph, while they are on the left for all previous times.

In addition, I want to some summarize mathematical symbols that are used frequently in this thesis. The detailed definitions are mainly given in Ch. 2, 3 and in the Appendices Ch. A and B. Less often used symbols are defined at the place of usage.

symbol	meaning
G	a graph, in this thesis used synonymously with the term network
$\mathcal{N}$	set of nodes of a graph
$\mathcal{E}$	set of edges of a graph
N	the number of nodes in a graph, $N = |\mathcal{N}|$
n_i	a specific node of a graph
A	adjacency matrix of a network
k_i	degree of node n_i
C_i	local clustering coefficients of node n_i
T	Transitivity of a network
k_i^f and k_i^b	forward and backward degree of node n_i
C_i^f and C_i^b	forward and backward clustering coefficients of node n_i
$\mathbf{X}$	a time series $\{x_t\} = \left(x_{t_1}, x_{t_2} \dots x_{t_M}\right)$
$\rho(\mathbf{X}, \mathbf{Y})$	linear Pearson correlation between two time series $\mathbf{X}$ and $\mathbf{Y}$
$\rho(\mathbf{X}, \mathbf{Y})_{MCMC}$	set of MCMC posterior samples of the linear correlation coefficient
$\{\mathbf{X}^i\}$	Ensembles of time series, with $i = 1, \dots, M$, M is the size of the ensemble
$\mathcal{W}$	fixed time window length
$t^{\mathcal{W}}$	a specific time window of length w, ending at time t, comprising the times $\{t^{\mathcal{W}}\} = \{t' | 0 \le t - t' \le \mathcal{W}\}$.
$\mathbf{X}_{t^{\mathcal{W}}}$	the observations corresponding to a specific time window $t^{\mathcal{W}}$

1 | Introduction

"Study the past if you would define the future."

— Confucius, *unsourced*

This saying, attributed to the Chinese philosopher Confucius, is invoked in countless articles and quotation collections to emphasise the importance of knowing the past in order to understand the present and predict future developments[1]. In the same spirit, it can be applied to the field of paleoclimatology, the study of past climates, as well. The need to understand and contextualise recent global climate changes, due to anthropogenic influences like greenhouse gas emissions or land cover change is one of the key motivations behind this field of research (IPCC, 2013), as is the role of past climate changes in the flourishment and collapse of past civilizations (Diamond, 2005; deMenocal, 2001).

These are very important aspects that will be stressed again and again in more depth throughout this thesis. However, in my view, this quote does not only tell us something about the motivation to study the past, but also about the nature of such an endeavour itself. While it is used frequently, I could not find a source of origin and, hence, it is not even clear if it originates from Confucius himself. Instead, it seems to me like a post-humorous simplification of his much more complex philosophy of learning and the central role the past plays in his views on the good life (for a discussion of these aspects, see, e.g., Pocock, 1962).

The approach to condense a complex phenomenon into a much simpler structure is mirrored in paleoclimatology as well. Here, researchers study a multitude of data, coming from many different archives, locations and times, to find those large-scale dynamics and physical mechanisms that actually drive climate evolution. They break

---

[1]Examples of such use can be found in Vanschoren et al. (2008), Wang (2008), and Yeats and Prentice (1996) among many others.

down complex and often conflicting lines of evidence to distil the dynamics that matter to understand the behaviour of the Earth system, for example, by developing simple, conceptual models of atmospheric and oceanic circulation.

This undertaking of reconstructing the essential features of past climate dynamics therefore demands tools which are capable to structure the information from variable sources and to detect patterns not accessible by simple visual inspection. One specific tool that has gained great popularity in the last decades is the theory of complex networks, with applications in ecology (e.g., Pimm, 1982), sociology (e.g., Kadushin, 2012), economics (e.g., Maluck and Donner, 2015), and many other disciplines. In general, a network is the combination of a set of *nodes* and connections between these nodes, the so called *links* or *edges*. The aim of network theory is to analyse the structure of connections in a graph, its *topology*, to understand the functioning of the system that the network represents.

Naturally, there have also been attempts to utilize network theory to understand the vast amount of climatological data that has become available to the public in recent years. These include in particular instrumental measurements, satellite observations and, increasingly so, data from complex climate models. The ways in which network theory is applied typically falls into one of two categories:

1. Networks used as a tool for time series analysis. Time-ordered observations are transformed to a network structure to characterize the underlying dynamics or to detect points of change in the data. Examples for these methods are *recurrence networks* (Donner et al., 2010b) or *visibility graphs* (Lacasa et al., 2008).

2. *Climate networks*, in which nodes represent different geographical locations and links are drawn based on a functional relationship between the observational time series at these locations. In this way, the structure of climate dynamics is thought to be revealed (Tsonis et al., 2006).

While the time series approach has been repeatedly applied to paleoclimate data (e.g., in Donges et al., 2011a; Schleussner et al., 2015; Donges et al., 2015a), the method of climate networks is mainly being used to analyse data from the 20th century, both on a global (Donges et al., 2015b) as well as on regional scales (Boers et al., 2013). Therefore, the use of climate networks has focused on climate phenomena on inter-seasonal to inter-decadal time scales, for example the El Niño Southern Oscillation (Tsonis and Swanson, 2008; Yamasaki et al., 2008; Wiedermann et al., 2016b) or monsoon systems (Boers et al., 2013; Stolbova et al., 2016). Monsoon systems are the only type of regional climate phenomena for which climate networks have been used in connection with paleoclimate proxy data, focusing on speleothem records covering the late Holocene (Rehfeld et al., 2013; McRobie et al., 2015; Oster and Kelley, 2016).

Still, both methods are so far lacking wide ranging application in the field of paleoclimate research. One reason for this could be that most researchers are not familiar with these methods, but their high uncertainties and method specific drawbacks might have hindered a wider use as well. Both network based approaches often have a rather high demand on the nature of time series, in particular they often need a high number of observations and these have to be sampled equally in time (Donner et al., 2010a). In addition, climate networks demand a high number of observations to yield meaningful results. In first applications, paleoclimate networks were hence mainly used

as visualization techniques to show similarities between single time series, due to the low number of paleoclimate records. However, these single links are highly uncertain and non-robust, mainly due to the low sample sizes, unequal sampling of records and time uncertainties. These topics have been discussed before by Kira Rehfeld in her dissertation and the publications it is based on (Rehfeld, 2013). While the method of visibility graphs that I use in this thesis does not suffer from these problems, it shows a high error rate, which make the results rather unreliable.

The main objective of this thesis is to develop these methods further with the specifics of paleoclimate data in mind. My goal is to obtain methods which are more reliable than previous ones and allow a quantitative analysis of past climate dynamics. For this reason, I do not only focus on the method development itself, but also on applications that bring network based methods of data analysis to the attention of a wider audience of paleoclimate scientists.

The geographical area from which the underlying data originate gets larger throughout the thesis, but always focuses on the Atlantic sector. This region is chosen for a number of reasons. First, it is a key region of regional and global climate dynamics, in particular through internal modes of variability like the oceanic Atlantic Meridional Overturning Circulation (AMOC) or the North Atlantic Oscillation (NAO). Second, it is one of the best studied regions with an abundance of paleoclimate time series available and, hence, is a prime candidate for a quantitative analysis using novel methods. Despite these features, it has so far not received the attention one would expect for the application of non-classical data analysis methods, something I aim to change with this thesis.

On a temporal scale, I focus on two key time periods of the Quaternary, the late Holocene and the transition from glacial climate into the warmer Holocene, the last deglaciation. The choice of these time periods derives from different motivations.

The Holocene[2] is commonly discussed as a period of stable conditions and low variability, even though there is much evidence on changing behaviours of key parts of the climate system (Cronin, 2010). The motivation to study these time series with methods derived from the study of complex systems is to test whether the assumptions about stability are justified. Furthermore, I want to study how network structures encode past climate variability in proxies and how climate dynamics can be reconstructed.

In contrast, the last deglaciation marks a period of massive, global climate changes, including a warming of 5-10℃, melting ice sheets and a sea level rise of ~ 130m[3]. Clearly, large scale dynamics play a role here. The main objective for analysing this time period is to investigate how climate networks behave at times of massive changes, as the method has only been applied to Holocene data before.

In this way, the thesis consists of three parts. The first part introduces the general methodology, followed by two parts, each of which is dedicated to one of the two time periods.

---

[2]The Holocene describes the recent geological epoch that started about 11,000 years ago. It is introduced in more depth in Ch. 4.

[3]Glacial-interglacial cycles and the dynamics associated with them are introduced shortly in Ch. 7

Part I: Methods Ch. 2 is restricted to reviewing methods that have previously been developed. Additional methods, that are not as central to this thesis, are discussed shortly in the Appendix Ch. A. These two chapters only discuss those aspects of the methods that were introduced in previous research. Any additional methodological development from my side is discussed in the respective chapters of applications.

As the estimation of correlations is an essential ingredient in the construction of climate networks, it deserves detailed attention. In Ch. 3, I discuss a Bayesian framework to estimate linear correlations and systematically test the influences of different proxy characteristics and levels of time uncertainty on the estimation, using synthetic proxy time series.

Part II: The late Holocene A short introduction into climate variability during the late Holocene is presented in Ch. 4.

In Ch. 5, the method of visibility graphs is applied to an ensemble of terrestrial paleoclimate records. Visibility graphs are capable to detect periods at which a time series cannot be described by a simple, stationary, and linear stochastic model. In this chapter, I try to answer the question if periods of complex dynamics exist during the Holocene, even if no obvious transitions are visible by eye.

In Ch. 6, I introduce a new method to reconstruct index values of climate variability for the past, which is based upon climate networks. The goal is to obtain an extended reconstruction of the leading mode of atmospheric circulation in the North Atlantic region, the NAO. In contrast to most classical reconstruction methods, this method does not rely on a stationary relationship between proxies and the target variable and is thus well suited for integrated climate variables like the NAO index.

Part III: The last deglaciation In the last part, only climate networks are used, but in two very different settings. Following a short introduction into the last deglaciation in Ch. 7, the probabilistic approach, introduced in Ch. 3, is used in Ch. 8 to analyse spatial patterns of marine records of benthic foraminifera during the last deglaciation. This is a sparse dataset with large uncertainties on many levels. It is contrasted in Ch. 9 with an analysis of monthly data from transient simulation of the last 21 thousand years.

Part I │ Methods

2 | Network approaches to climate data analysis

A network consists of a set of nodes and a set of links (or edges) that connect pairs of nodes. What makes networks so useful is that they enable us to investigate structures in the relationships between single entities in a simple, efficient and mostly intuitive way. Thus, one can identify key components of the system, study the efficiency of a graph (e.g., traffic flow in road networks) or detect changes in the dynamics of a complex system. In this chapter, we will just cover the basics of network theory used in this thesis. Excellent and comprehensive introductions into the topic can be found by Boccaletti et al. (2006) and Newman (2018).

As already mentioned in the introduction (Ch. 1), two network based approaches to study climate variability will be used in this thesis. Before we can discuss them in detail, we need to make some initial statements about the notation of time series analysis used in this thesis, as is done in the following Sec. 2.1. In addition, we define what a network is and introduce basic analysis methods in Sec. 2.2. An introduction into the method of visibility graphs follows in Sec. 2.3 and climate networks are discussed in Sec. 2.4.

2.1 Time series and moving windows

In this thesis, a time series of length L is denoted as $\mathbf{X} = \{x_t\} = \left(x_{t_1}, x_{t_2} \dots x_{t_L}\right)$, with observations at times $(t_1, t_3 \dots t_L)$ without prior assumptions about the nature and temporal sampling of the series. The set of indices is denoted as T. Ensembles consisting of M time series are denoted as $\{\mathbf{X}^i\}$, $i \in \{1, \dots, M\}$.

All applications in this thesis use moving window techniques. Here, any analysis is conducted for different time periods separately, using only observations from the these

(a) Regular graph (lattice)　　(b) Random graph　　(c) Complex network
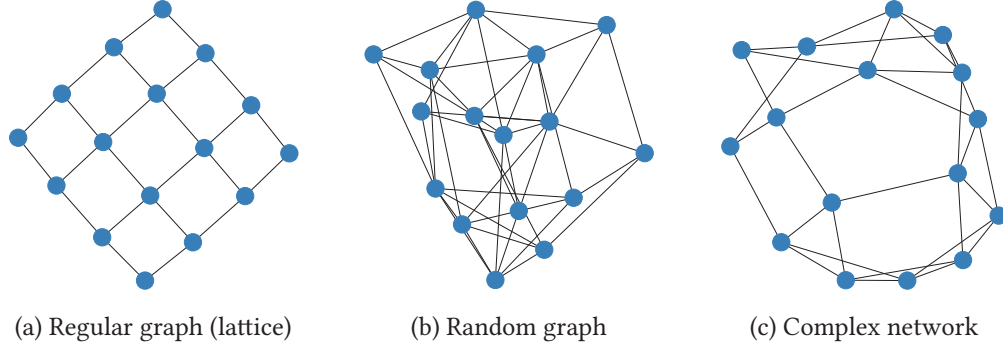
Figure 2.1: Three examples for different networks: (a) a regular graph (lattice), (b) a random graph and (c) a complex, small-world network.

time windows. We denote a time window as $\mathscr{W}$ and all results are assigned to the most recent point of each time window. In this way, we ensure that all points lay in the past of the assigned time and, thereby, no future observations influence the corresponding results. We denote all windowed measures by a subscript $t^{\mathscr{W}}$, as it is based on the subset of observations for which $\{t^{\mathscr{W}}\} = \{t' | t' \in T, 0 \leq t - t' \leq \mathscr{W}\}$. For example, $\mathbf{X}_{t^{\mathscr{W}}}$ denotes the truncated time series $\mathbf{X}_{t^{\mathscr{W}}} = \{x_{t'} | t' \in t^{\mathscr{W}}\}$.

2.2　Complex networks

A network is a graph G that is defined through two sets, that of nodes $\mathscr{N}$ and that of links or edges $\mathscr{E}$, combined as $G = (\mathscr{N}, \mathscr{E})$. The number of nodes is written as $N = |\mathscr{N}|$ and single nodes as n_i, $i \in \{1, \dots, N\}$. Each edge consists of a tuple of nodes (n_l, n_k).

Such a network can be fully described by an $N \times N$ matrix, the *adjacency matrix A*. In the simplest case, it is a symmetric, binary matrix that is defined through:

$$A_{ij} = \begin{cases} 1 & \text{if there is a link between nodes } n_i \text{ and node } n_j \\ 0 & \text{else.} \end{cases} \tag{2.1}$$

In most networks, self loops are not allowed, and, thus, $A_{ii} = 0 \; \forall i \in \{1, \dots, N\}$. The matrix representation allows the application of all the tools from linear algebra, which are computationally cheap and efficient.

There are some extensions of this notion of simple networks, in particular the edges can be weighted or directed. A *weighted network* is one at which each edge is assigned a real number, for example derived from geographical distance (Newman, 2004; Barrat et al., 2004). In other cases, the direction of links is important such that a link is present from node n_i to node n_j but not necessarily in the opposite direction. Such graphs are called *directed networks* and lead to a non-symmetric adjacency matrix. All networks considered in this thesis are undirected, but weighted graphs are used in Ch. 8.

The structure of a network is called *topology* and there are some general classes of networks to distinguish here. The most ordered case is that of a regular lattice, at which all nodes (except boundary nodes) have the same number of connections and all links are parts of closed loops (see Fig. 2.1a). On the other end of the spectrum are random networks, in which links between pairs of nodes are solely determined by some value

of probability. An example of this is shown in Fig. 2.1b. In general, complex networks are those graphs that lay somewhere in between these two extremes in that they do show a certain degree of stochasticity or complexity, but also exhibit structures that cannot be explained by chance alone. A very prominent example for this are so called *small world networks* (Watts and Strogatz, 1998), in which most nodes are connected by a low number of edges, as can be seen in Fig. 2.1c.

Most real world networks fall into the category of complex networks[1] and one of the goals of network theory is to find the deterministic structures in a network full of (apparent) randomness. One way to do so is to quantify characteristics of the network with so called *network measures.*

Network measures

In this thesis, we distinguish two types of network measures. If the whole network is assigned one scalar number, this is called a *global network measure.* In contrast, if a number is calculated for each node separately it is a *local network measure.* There are also measures that represent both local and global characteristics, for example different measures of *centrality*, but these are not considered in this thesis.

There are a multitude of methods to quantify structures in a network, but we will only cover some of them here. For a more comprehensive overview see Boccaletti et al. (2006).

Local measures try to quantify the importance of a specific node in the whole network or try to quantify degrees of regional organization. The simplest, and most used, measure is that of the *network degree k*, which gives the number of connections each node has as

$$k_i = \sum_{j \in \mathcal{N}} A_{ij}. \tag{2.2}$$

Many measures rely on higher orders of the adjacency matrix, for example the local clustering coefficient C_i, defined as

$$C_i = \frac{1}{k_i (k_i - 1)} \sum_{j \in \mathcal{N}} \sum_{k \in \mathcal{N}} A_{ij} A_{jk} A_{ki}. \tag{2.3}$$

The local clustering coefficient quantifies to what degree neighbours of n_i are also connected and, hence, if n_i is part of a highly connected cluster of nodes, in which there are many closed triangles.

Some global measures are simple arithmetic means over local network measures, for example the *mean degree*

$$\langle k \rangle = (1/N) \sum_{i \in \mathcal{N}} k_i \tag{2.4}$$

Another measure that will be used extensively in this thesis is the global *transitivity*, that is similar to the clustering coefficient in that it gives the fraction of closed triangles, but averaged over the whole network:

$$T = \frac{3 \times \# \text{ of triangles in graph}}{\# \text{ of connected triplets in graph}} = \frac{\text{Tr}\left(A^3\right)}{\sum_{i \neq j} \left(A^2\right)_{ij}} \tag{2.5}$$

---

[1]Note that they are not necessarily small-world networks.

(a) Visibility graph

(b) Horizontal visibility graph
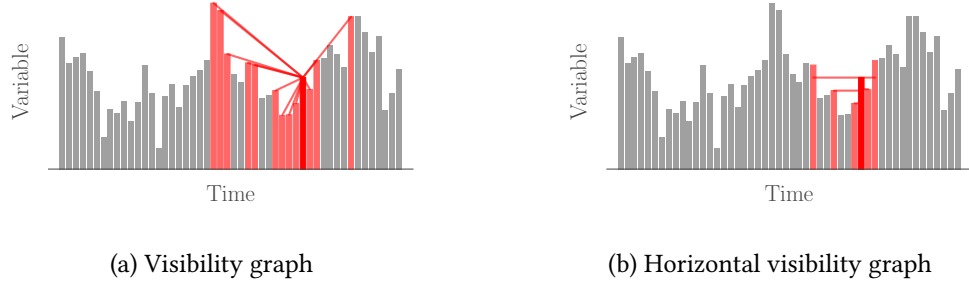
Figure 2.2: Visualization of the construction rules for (a) visibility graphs and (b) horizontal visibility graphs, shown for one node (dark red). All neighbours of this node are shown in light red.

with Tr denoting the trace of a matrix. A low transitivity means that links are spread out throughout the network, which is typical for random graphs, while a high value indicates the presence of regions with high connectivity.

There are also other measures that are not direct functions of *A*, like the average shortest path length, defined in the Appendix Ch. B. In the aforementioned section all network measures used in this thesis are summarized.

2.3 Visibility graphs

Several methods have been proposed to represent a time series as a network. Some are motivated by dynamical systems theory and aim to quantify the topology of the reconstructed phase space of a time series (Donner et al., 2010b). Others follow a geometric approach, like the method of visibility graphs that is discussed here. In most methods, the individual observations of the time series make up the set of network nodes. The main difference lays in the dimensionality of the data and in the criteria used to draw links between observations.

Visibility graphs (VG) have been introduced as a tool for time series analysis by Lacasa et al. (2008) and have gained popularity in the geosciences in the last years (Elsner et al., 2009; Lacasa et al., 2009; Telesca and Lovallo, 2012) due to their conceptual simplicity and low requirements on data. In-depth discussions of visibility graphs and their applications are given by Nuñez et al. (2012) or Zou et al. (2018).

The general idea of visibility graphs is to see a time series as a landscape of values, plotted as a bar plot. Points in this landscape are connected to each other if one can draw a straight line between them without interference of other points, i.e. if they are *visible* to each other. Mathematically, the rule of network construction is thus given as:

$$A_{ij} = \begin{cases} 1 & \text{if} \quad x_k < x_i + \left(x_j - x_i\right) \frac{t_k - t_i}{t_j - t_i}, \quad \forall k, \ i < k < j. \\ 0 & \text{else} \end{cases} \tag{2.6}$$

An example is presented in Fig. 2.2a where all neighbours of one observation are shown.

A visibility graph is hence thought to represent the distribution of peaks and troughs in a time series as nodes of high and low degrees. If the time series is drawn from a
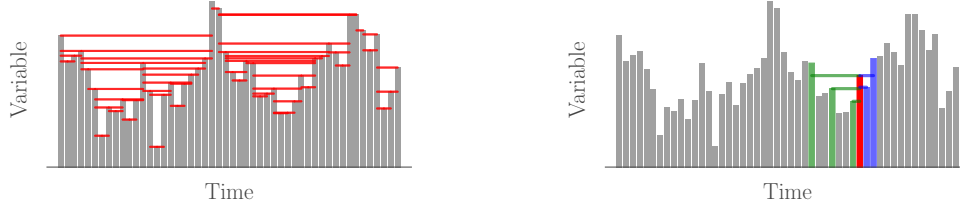
(a) The full HVG representation of the time series.

(b) Forward (blue) and backward (green) connections of one node (red).

Figure 2.3: (a) A full HVG of the same time series as used in Fig 2.2 and (b) the forward (blue) and backwards (green) links for one node (red).

random process, these peaks and troughs would be equally distributed along the time series, as would the intermediate values. Each deviation from such a behaviour would hence point towards a longer-scale components in the signal. The visibility graph has a number of properties, that make it particularly suitable for time series analysis: For example, it is always connected, as each node can at least see its neighbours. In addition, it is invariant under affine transformations, in particular rescaling or translations on both axes. The latter is particularly useful when analysing time series with time uncertainties.

A computationally and analytically more accessible version of this construction algorithm is that of *horizontal visibility graphs* (HVGs). Here, only those nodes are considered connected, which are visible to each other along a horizontal line, meaning that no value in between them is larger than any of the two. The adjacency matrix is thus given as

$$A_{ij} = \begin{cases} 1 & \text{if} \quad x_i, x_j > x_k \quad \forall k \ : \ i < k < j \\ 0 & \text{else.} \end{cases} \tag{2.7}$$

The HVGs are subgraphs of the corresponding VGs with a lower number of edges. An example for a single node is shown in Fig. 2.2b. The full HVG of the depicted time series can be seen in Fig. 2.3a.

It has been claimed that the degree distribution (and in particular its slope) of a HVG is characteristically different for time series originating from stochastic or chaotic processes (Lacasa et al., 2009; Luque et al., 2009) even though this has been put into question recently (Ravetti et al., 2014; Zhang et al., 2017b). The discrimination of stochastic time series from those that stem from non-linear, but deterministic processes has since been one of the prime applications of this method (e.g., Liu et al., 2010; Telesca and Lovallo, 2012; Yang et al., 2009). Others plot measures of the degree of randomness, complexity or information content in a graph against each other and compare different graphs on the respective planes (Ravetti et al., 2014).

An alternative approach is to focus on time-reversibility, a characteristic of stationary, linear, and stochastic time series, and test for this feature using visibility graphs, as discussed in the next section.

Testing time-reversibility using visibility graphs

A time series is called *time-reversible* if any multi-point statistical characteristic has one value (in the limits of estimation uncertainty), independent of the direction of time (Weiss, 1975). This is a necessary feature of any stationary, linear, stochastic process (Lawrance, 1991; Weiss, 1975). Hence, a violation of time-reversibility implies that the time series in question is either non-stationary, non-linear or non-stochastic. Such a time series is called *time-irreversible*. Besides simple explanations like trends, which can be eliminated beforehand, there are different mechanisms which can cause time-irreversibility, for example, non-linear dynamics or linear responses to complex forcings.

Lacasa et al. (2012) proposed that visibility graphs can be used to detect such violations of time-reversibility by introducing a time directionality to links in the network. For each mode, outgoing links are distinguished into forward and backward connections, depending on if the link corresponds to an observation before or after the node. Note that this does not mean that the network becomes a directed graph, it is still a symmetric network, but an edge that is a forward link for one node is a backward link for the other. Based on this classification, directional local network measures can be defined and each node has assigned not one, but two values, one forward and one backward in time. Example for these are the directed degrees or the directed local clustering coefficients (Donges et al., 2013). For a single node these are defined as:

$$k_i^{\mathrm{f}} = \sum_{j>i} A_{ij} \quad \text{and} \quad k_i^{\mathrm{b}} = \sum_{j<i} A_{ij} \tag{2.8}$$

and

$$C_i^{\mathrm{f}} = \frac{1}{k_i^f\left(k_i^f - 1\right)} \sum_{j>i,k>i} A_{ij}A_{jk}A_{ki} \quad \text{and} \quad C_i^{\mathrm{b}} = \frac{1}{k_i^b\left(k_i^b - 1\right)} \sum_{j<i,k<i} A_{ij}A_{jk}A_{ki}. \tag{2.9}$$

Considering the whole graph, one can then compare the sampling distribution of these forward and backward measures with each other. If these two distributions are the same, the time series is said to be (H)VG time-reversible, otherwise it is (H)VG time-irreversible. While Lacasa et al. (2012) have initially proposed to use the directed degree for this test, Donges et al. (2013) argue that the time directed local clustering coefficient shows a higher sensitivity and should thus be used. In this thesis, the forward and backward distributions are compared using a Kolmogorov-Smirnov (KS) test (Hollander et al., 2014) as has been recommended by the aforementioned publication. The KS-test is a non-parametric test that compares two distributions with each other. It results in a p-value that describes the probability, that the estimated value occurs if the two sample distributions are the same. It should be stressed that a violation of Gaussianity of the underlying process does not lead to HVG time-irreversibility, since the test is independent of the probability distribution from which observations are drawn.

It should be noted that one of the main disadvantages of the HVG based test for time-reversibility, in particular when using the local clustering coefficient, is the high rate of false positives of the method (Donges et al., 2013). This has to be accounted for when applying the test to multiple time series and when interpreting the results.

Often, we are not interested if the full time series is time-irreversible, but are looking for specific time periods which show dynamics that differ markedly from the rest of the data. To detect these phases of dynamical anomalies, we use moving windows and apply the HVG based test for time-reversibility to each window separately. To ensure robustness of the results, it is advisable to follow this procedure for a larger array of window sizes. Hence, for a single time series we obtain a plane of p-values of the KS-test with time on the x-axis and window sizes on the y-axis. An example of these results can be seen in Fig. 5.2.

We emphasize that there is no strict correspondence between HVG time-reversibility and general time-reversibility (see, e.g., Lacasa and Flanagan, 2015). While there are processes that are time-irreversible that might show no signs of HVG time-irreversibility, those that do are time-irreversible by definition.

HVG based testing for time-irreversibility has multiple advantages compared to other methods of non-linear time series analysis. First, it is computationally cheap and algorithmically simple and it does not require complicated ways of testing, like surrogate tests. In addition, it has very low requirements on data, it works well with short time series and those that are irregularly sampled. This is very important when dealing with paleoclimate time series, which suffer from these problems in most cases. The only condition for HVG construction is that the values are ordered in time, which in the case of paleoclimatology is ensured by the law of superposition[2]. Still, indirect effects of irregular sampling and boundary effects of short samples are still not fully understood and require further study (Donner and Donges, 2012).

2.4 Climate networks

In 2004, Tsonis and Roebber introduced a novel method to analyse large datasets of spatially distributed climate time series, the method of climate networks (Tsonis et al., 2006). The general idea of this method is to give a representation of the spatial co-variability among observations that can be analysed in an efficient and intuitive way. When used together with moving windows it is furthermore possible to trace changes in the co-variability structure which might point towards shifts in climate dynamics, an extension that is called *evolving climate networks*. As we are always dealing with evolving climate networks, we are mostly dropping the term *evolving*. If we want to relate to a network corresponding to a specific time window, we denote the adjacency matrix as $A_{ij,t\mathcal{W}}$.

For an introduction to climate networks and their applications, see Donner et al. (2017). Climate networks are a special case of *functional networks*, in which links are drawn by any statistical similarity measure possibly reflecting some kind of functional relationship between nodes. Climate networks are spatial networks (Barthélemy, 2011), as nodes are always embedded in a geographical space, often the two dimensional surface of the Earth, but three dimensional embeddings are also possible as discussed in Ch. 8 for networks in the Atlantic Ocean.

---

[2]This is one of the basic assumptions of Geology and states that for any two layers in one sequence, the deeper one is older (Tarbuck and Lutgens, 2014).

In detail, a climate network is a graph-theoretical representation of the similarity structure among a set of time series $\{\mathbf{X}^i\}$ with $i = 1, \dots, M$ [3]. Each time series is represented as one node and links are drawn between the nodes if the corresponding time series are sufficiently similar to each other. Hence, the network is constructed as

$$
A_{ij} = \begin{cases} 1 & \text{if } \mathbf{X}^i \text{ and } \mathbf{X}^j \text{ are similar} \\ 0 & \text{else.} \end{cases} \tag{2.10}
$$

This definition does not depend on any specific way to assess similarity, other than many other methods of spatial analysis that are limited to linear correlation, e.g. EOF analysis (Storch and Zwiers, 2003). Besides Pearson correlation coefficients, there are more complex measures of similarity, for example mutual information (Paninski, 2003), rank based correlation (Kendall's τ or Spearman's ρ Kendall, 1970) or event synchronization (Quian Quiroga et al., 2002; Malik et al., 2012). For a discussion of these measures and their differences, see Rehfeld and Kurths (2014).

It is also possible to assign a weight each link proportional to the strength of the similarity estimate in order to obtain weighted climate networks. This is for example done in Ch. 8.

An evolving climate network framework is a sequence of time ordered climate networks, where each is based on the similarity matrix calculated over a specific time window. These can be analysed either visually (Nocke et al., 2015) or by applying network measures as discussed in Sec. 2.2.

Applications are, for example, changes in the number of triangles (Eq. 2.5), which for recent decades are often related to the El Niño Southern Oscillation (Wiedermann et al., 2016b) or changes in single links that indicate changing monsoon patterns (Rehfeld et al., 2013).

Climate networks are often contrasted with other methods of spatial analysis, in particular Empirical Orthogonal Functions/Principal Component analysis (EOF/PCA, for paleoclimate applications, see, e.g., Gouirand et al., 2008; Mann et al., 1998). Even though they are all based on the similarity matrix, there are some notable differences. First, climate networks are less restrictive in the measure of similarity, whereas conventional EOFs are only well defined for linear correlations. The assumptions of linearity and/or orthogonality of modes in EOF analysis might yield spurious dipole patterns that do not have a physical correspondence (Hurrell et al., 2003; Monahan et al., 2009). In contrast to most classical measures, climate networks also enable a look at higher-order structures of co-variability, as for example via the triangle structures or betweenness measures. A general comparison of climate networks with EOF analysis is given by (Donges et al., 2015b).

In most cases, the method of climate networks has been restricted to data of recent observations or reanalysis data, rarely going beyond the 20th century. Consequentally, applications have focused on phenomena of inter-seasonal to inter-decadal climate variability, for example the El Niño Southern Oscillation (Tsonis and Swanson, 2008;

---

[3]Note that in a paleoclimate context, the number of nodes often varies in time, as different record cover different times.

Yamasaki et al., 2008; Wiedermann et al., 2016b) or the monsoon systems (Boers et al., 2013; Stolbova et al., 2016).

When it comes to paleoclimate, applications have been rare and focused on a low number of records related to the Asian and Australian monsoon system (Rehfeld et al., 2013; McRobie et al., 2015; Oster and Kelley, 2016). This is related to some specific problems one has to deal with when analysing paleoclimate records. First, paleoclimate data is sparse and geographically biased to locations at which suitable archives for a particular time and climate variable can be found (see, e.g., the map of proxies in Rehfeld et al., 2018). Second, all methods of similarity assessment rely on concurrent observations for all time series. This is almost never the case in a paleoclimate context due to age-model uncertainty (Goswami et al., 2014; Trachsel and Telford, 2017) and irregular sampling (Rehfeld et al., 2011). How this issue can be treated has been discussed previously by (Rehfeld and Kurths, 2014). A Bayesian approach is furthermore discussed in Ch. 3.

3 | Probabilistic similarity estimation of age-uncertain paleoclimate data

As discussed in the last chapter, the method of climate networks relies heavily on the assessment of similarity among time series. If two time series are similar determines if a link is drawn and, hence, the overall topology of any climate network. This is not a problem for most contemporary time series, which are available at high and regular resolution, so that any appropriate measure of similarity can be applied to them. With reservations, this is also true for many datasets for the late Holocene, which derive from well dated, often annually resolved archives like tree rings, varved lake sediments or ice core records. It is for this reason that we use mainly classical Pearson correlation in Ch. 6, which uses such data.

For earlier time periods, the picture looks more difficult. Here, sampling intervals are often large and irregularly distributed. In addition, there is a considerable amount of time uncertainty, coming from instrumental errors, dating uncertainty and additional effects like the variable reservoir effect for radiocarbon dated archives (Bradley, 2015). Therefore, a comparison is often done by eye alone (see, e.g. Zhang et al., 2008; Cheng et al., 2012; Waelbroeck et al., 2011). For a quantitative treatment of similarity, as is needed for climate networks, these uncertainties have to be taken into account, as they can lead to spurious correlations either by sampling size effects or by interpolation methods used to bring two records to the same time axis.

While different methods of approximation and similarity estimation have been compared in previous studies (Rehfeld and Kurths, 2014; Rehfeld et al., 2011), they were all based on classical point estimators. In contrast, we propose to use a Bayesian

framework to estimate correlations, as this is most suitable to deal with the different levels of uncertainty of not well dated paleoclimate records. From a Bayesian viewpoint, two time series are considered to be realizations of a bivariate stochastic process and the correlation is determined by the off-diagonal elements of the joint probability distribution (a more formal definition is given in Sec. 3.1). Estimating this model parameter, using methods like Markov Chain Monte Carlo sampling (MCMC), yields posterior distributions[1], that account for uncertainties that stem from sample sizes, model error etc. that have to be estimated in more complex manners, e.g., by the Fisher z-transform (Fisher, 1915) in classical statistics. Knowledge about data and model can be incorporated into the prior distributions. A major advantage of this approach is, that this also includes the structure of the covariance matrix, which needs to be positive semi-definite to be well defined. This is not always the case when using classical estimates together with interpolation (Babu and Stoica, 2010; Rehfeld et al., 2011), but can be ensured by using appropriate priors in a Bayesian approach. Another advantage of this approach is, that the assumptions of the underlying model are made explicit, which can prevent inappropriate applications to data that do not match these assumptions. Furthermore, (Behseta et al., 2009; Matzke et al., 2017) demonstrated that the Bayesian estimation is superior to classical approaches when measurement errors are present. As this topic has been covered extensively in these publications, we do not incorporate these sources of uncertainty here.

Still, even Bayesian methods rely on concurrent observations for the estimation of the model parameters from sample data and, hence, this joint distribution has to be approximated, either by some kind of interpolation or by other methods. A fully Bayesian framework for this problem might—and hopefully will—be developed, but is not available up to date. In this chapter, we aim to investigate, how different methods of approximation influence the probabilistic treatment of correlation and what role different levels of time uncertainty play. This is meant to set the stage for an application of climate networks to notoriously badly dated paleoclimate records in a more quantitative and reliable way by eliminating spurious correlations and gaining a proper estimation of uncertainty of derived knowledge, enabling a more meaningful interpretation of results.

Key Questions

- What uncertainty do different approximation methods to bring records to the same time scale add to correlation estimation?

- How do different levels of time uncertainty contribute to overall estimation uncertainty?

- Are meaningful correlations possible, given all these uncertainties?

---

[1]Most methods Bayesian data analysis do not yield single point estimates, but rather distributions for parameters. As these are the result of the analysis, they are called the *posterior* distributions. Different from classical statistics, one can also include prior knowledge into the analysis. This happens by suggesting distributions for all model parameters. These are called *prior* distributions.For an in depth discussion of Bayesian data analysis, see, e.g., von Toussaint (2011) or Gelman (2014).

This chapter largely follows the publication JF3. The remainder of the chapter is structured as follows. In Sec. 3.1, the Bayesian approach to correlation estimation is introduced. In the following Sec. 3.2 the problem of irregular sampling and common solutions are discussed. We use synthetic data, modeled after marine sediment records. The model by which these time series are generated is introduced in Sec. 3.3. The results are then discussed in Sec. 3.4, followed by an application to two benthic δ^{18}O records from the Atlantic ocean in Sec. 3.5. All these results are then put into a broader context in Sec. 3.6.

3.1 Bayesian correlation estimation

The aim of correlation analysis is to compare two time series $\mathbf{X}$ and $\mathbf{Y}$. A time series $\mathbf{X}$ is a set $\{x_i, t_{X,i}\}$, with observations $\vec{x} = \{x_i\}$ and observation times $\vec{t}_X = \{t_{X,i}\}$, $i = 1, 2, \ldots, N_x$, with N_x being the number of observations. The observations of a time series are drawn from a distribution $P(x)$.

If both sets of observation times are equal $\left(\{t_{X,i}\} = \{t_{Y,i}\}\right)$ a joint probability distribution $P(x, y)$ exists. The two sets of observations are statistically independent if and only if $P(x, y) = P(x)P(y)$, otherwise they are said to be dependent. The degree of dependence is often quantified by different statistical measures. In general, such measures are zero if $\mathbf{X}$ and $\mathbf{Y}$ are independent and non-zero otherwise, obtaining the maximum value, if both time series are identical.

Some methods, like mutual information (Paninski, 2003), try to quantify similarity from the joint and marginal probability distribution directly. These methods have the drawback that estimation of these distribution from limited sample sizes is difficult and can introduce considerable biases (Paninski, 2003; Papana and Kugiumtzis, 2009). If sample sizes are very small, it is thus more suitable to employ a simple statistical model, whose parameters can be estimated with higher confidence.

The most common model to describe $P(x, y)$ is the bivariate normal model (BNM)

$$P(x, y) \sim \mathcal{N}\left(\vec{\mu}, \underline{\Sigma}\right) \tag{3.1}$$

with

$$\vec{\mu} = \{\langle x \rangle, \langle y \rangle\} \quad \text{and} \quad \underline{\Sigma} = \begin{pmatrix} \sigma_X^2 & \rho \sigma_X \sigma_Y \\ \rho \sigma_X \sigma_Y & \sigma_Y^2 \end{pmatrix}. \tag{3.2}$$

Here, σ_X^2 and σ_Y^2 are the variances of the corresponding time series $\mathbf{X}$ and $\mathbf{Y}$, while ρ describes the shared variability (or *coupling strength*). As the relationship between the two time series is fully described by a linear term in the off-diagonal elements, this is called a linear model of correlation. The often used Pearson correlation ρ^p is an asymptotically unbiased and efficient point estimator for this coefficient (Lehmann and Casella, 1998). As we are dealing with low resolution paleoclimate data in this thesis, we will restrict our analysis to the problem of estimating the parameters of this BNM, considering the estimated parameter value of ρ as the measure of correlation.

For the estimation of statistical methods, Markov Chain Monte Carlo (MCMC) methods have been proven to be of great value (for an overview of Bayesian and in particular MCMC methods, see, e.g., von Toussaint, 2011; Gelman, 2014). As with all Bayesian methods, prior probability distributions that represent previous knowledge

about the data need to be defined before estimation. If θ denote the parameters of a statistical model, priors are denoted as $P_{pr}(\theta)$. They are defined for each parameter individually.

As we would like the results of this chapter to be as widely applicable as possible, we use very weakly informed priors, which are distributions with very broad variances. In the following it is assumed that each time series has been normalized to zero mean and unit variance before estimation. The mean μ_i and variances σ_i are assigned the priors $P_{pr}(\mu_i) \sim \mathscr{N}(0, 10)$ and $P_{pr}(\sigma_i) = \text{HalfCauchy}(2.5)$ (for a discussion of this distribution see, Polson and Scott, 2012).

The only thing that we know in general about the covariance matrix σ is that it needs to be positive semidefinite. Lewandowski et al. (2009) describe a prior to efficiently sample from the set of such positive semidefinite matrices, the so called LKJ prior, named after the initials of its inventors. This prior introduces an additional parameter η, for which we set a uniform prior of $P_{pr}(\eta) = \text{Uniform}(0, 5)$, again as a rather uninformed choice.

Using a Metropolis sampler, we draw 30,000 samples and discard the first third, as the sampler has not converged for these samples. We did not detect any non-convergence for this sample sizes when using the synthetic data introduced in this chapter. When applying the method to other data, convergence always needs to be checked. To save memory and storage, we keep only 1,000 values for each pair of time series.

The MCMC sampler yields posterior probability distributions for all model parameters, but the only one we are interested in here is the posterior distribution of the coupling parameter $\rho_{MCMC}(\mathbf{X}, \mathbf{Y}) \sim p(\{\rho_i, i = 1, \dots, 1000\})$. The corresponding point estimate $\hat{\rho}(\mathbf{X}, \mathbf{Y})$ is given by the value of highest probability in $\rho_{MCMC}(\mathbf{X}, \mathbf{Y})$.

3.2 Ways to deal with irregular sampling and age model uncertainties

As discussed before, two related problems make the estimation of correlation difficult in the case of paleoclimate records: irregular sampling and age model uncertainty.

A time series is *irregularly sampled* if $\Delta t_{X,i+1|i} := t_{X,i+1} - t_{X,i}$ is different for different i. Many paleoclimate archives have varying recording conditions (e.g., sedimentation rate) and, thus, even regular physical sampling intervals (e.g., equally spaced depths along a sediment core) will usually lead to irregular sampling times.

Two irregularly sampled time series $\mathbf{X}$ and $\mathbf{Y}$ are commonly *unequally sampled*, meaning that the observation times are unequal, $\{t_{X,i}\} \neq \{t_{Y,i}\}$. If this is the case, $P(x, y)$ cannot be estimated directly and has to be approximated.

Only a few paleoclimate archives, like tree rings or varved lake sediments, show a reliable relative or absolute time scale. In most cases, the attribution of times to observations is done in indirect ways, e.g., by making use of the radioactive decay of isotopes like ^{14}C (see, e.g., Bradley, 2015). The absolute observation times have to be estimated using so called age models which are models that relate these physical properties to calendar ages and extend these single age measurements to the full paleoclimate record. There is a broad range of age models, some using simple interpolation between aged points (Blaauw, 2010), while others build upon simulated sedimentation

histories combined with a probabilistic approach (Haslett and Parnell, 2008; Blaauw and Christen, 2011).

In this way, there are two ways in which age models introduce errors. First, they all make assumptions about the archive evolution (even linear interpolation assumes constant sedimentation rates between measurements) and, hence, all times between age measurements come with a large degree of uncertainty. Second, most age calibration techniques come with errors, which means that any time observation cannot be attributed to one specific point in time, but rather to a set of possible times. If one uses a probabilistic age model, the latter source of uncertainty can be taken into account by using different realizations of the age model.

All these issues add to the problem of unequal sampling and the need to bring two time series onto the same time scale by some way of approximation. In this study, we focus on three possible approaches: (i) interpolation of both variables to a shared time axis (ii) comparing averages over time intervals, and (iii) combining observations which are presumed to be close to each other. Specifically, the following four methods will be used:

Linear Interpolation (LI). Missing observations are assumed to lie on a straight line between the two neighbouring observations and, hence, the point on this imaginary line corresponding to the specific time is set as a new observation.

Gaussian Kernel Interpolation (G). Here, the unobserved value is set to a weighted mean of nearby observations in time, with close points having larger weights than those that are farther away in time. How many observations are taken into account depends on the bandwidth (h) of the weight function and has to be specified in advance. As we use different bandwiths, we denote the corresponding approximation as G(bandwidth), with the bandwidth values being scaled by the mean sampling time of a given pair of time series.

Nearest Value (NV). In this approach, values that are close to each other in time are considered to be concurrent. Values that don't have any close value in the other time series are discarded. Hence the effective number of observations is reduced while this method does not introduce additional data points like is done for interpolation.

Slotting (S). For this method, values are averaged over time slots for both time series and these mean values are then compared. This is efficiently a very basic low pass filter. This method will be denoted as S(slot width), where the slot width W is again scaled by the mean sampling time, similar to the Gaussian kernel based interpolation.

Mathematical details on each interpolation method are presented in the Appendix Sec. C.1.

3.3 Synthetic pseudoproxy data

For a systematic test of how different uncertainties influence the estimation of correlation, we construct pseudoproxies resembling marine sediment records. Here, I only want to discuss the general ideas that determine the different steps to generate these
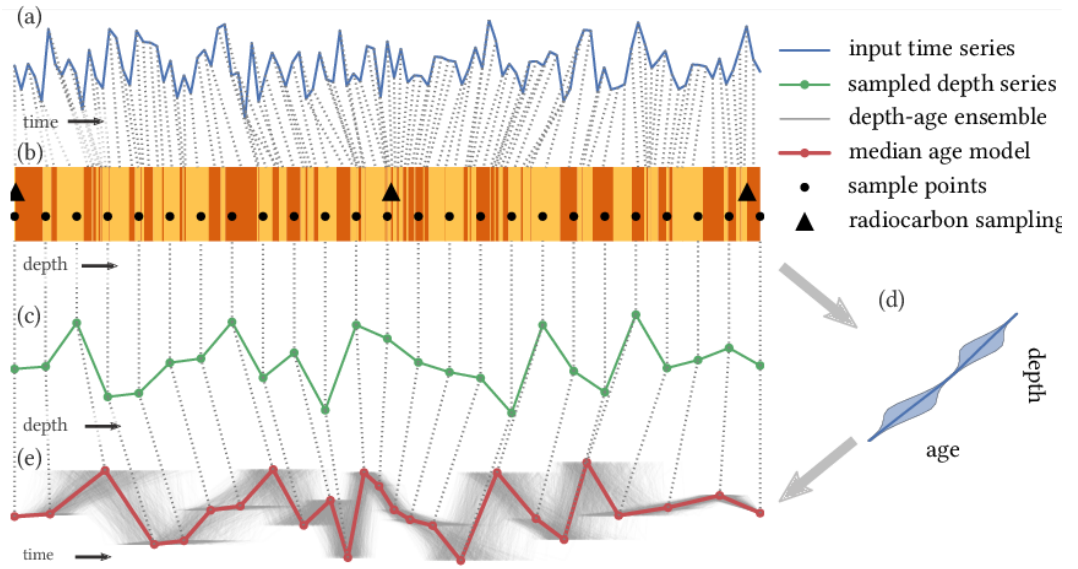
Figure 3.1: The procedure by which pseudoproxies are generated in this chapter. (a) At first, a regularly sampled time series is generated. (b) Each value corresponds to one layer of sediment, the thickness of each layer is independently drawn from a gamma distribution. (c) This sequence of layers of different thickness is then sampled at regular intervals, to mimic the physical sampling process. This yields an irregularly sampled time series. (d) A smaller number of calendar ages are converted to radiocarbon ages and these are then used to construct a depth-age model. (e) The result is a record with a different temporal sampling due to the age model related error and age uncertainty.

artificial time series. A more detailed description can be found in the Appendix Sec. C.2. The overall procedure is sketched in Fig. 3.1 and in the following paragraphs, we will walk through all steps shown here.

A first step is to generate a pair of coupled, regularly sampled time series for which the true correlation value is known (Fig. 3.1a). This true value is referred to as *coupling strength* and abbreviated as *c*. In parallel, a sedimentation history is simulated for each proxy individually and observations are assigned to layers of different width (Fig. 3.1b). Sampling at regular intervals of the sedimentation record then leads to an irregularly sampled time series of much lower resolution (Fig. 3.1c). We also simulate the effect of radiocarbon dating (Fig. 3.1d), which leads to shifted times and additional age uncertainty (Fig. 3.1e) as discussed in the previous section.

In our case, the pair of time series are generated using an Ornstein-Uhlenbeck process and a linearly dependent variable with a prescribed coupling strength *c*. The key parameter of this stochastic process is the drag parameter θ that determines the persistence structure of the generated time series. Example realizations of time series generated by this process are shown in the Appendix Fig. C.1.

In addition to the coupling strength, there are four more model parameters for each pair of pseudoproxy records: the length of the records, the drag parameter θ and the mean and skewness of the sedimentation rate μ_S and γ_S.
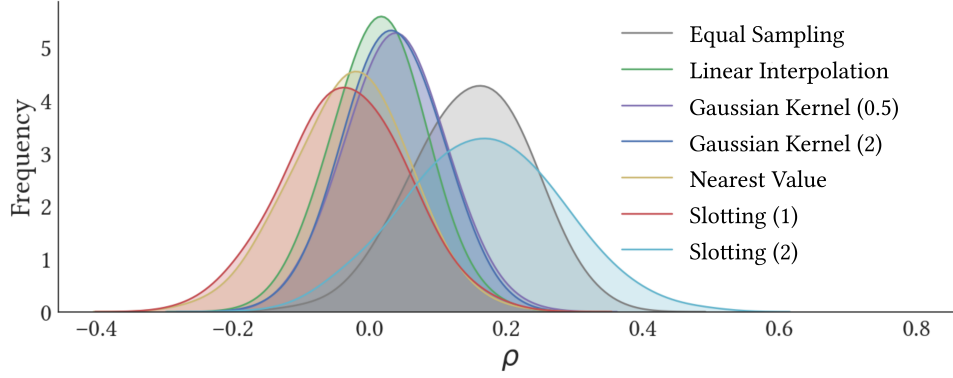
Figure 3.2: Example for the estimation of ρ using MCMC in combination with different approximation methods. The time series in this example is a realization of the pseudo-proxy described in Sec. 3.3 and Appendix Sec. C.2 (drag parameter $\theta = 0.85$). The true correlation value is $\rho_t = 0.3$.

3.4 Results of pseudoproxy experiments

Before discussing anything else, a first look at the different posterior estimates for one pair of pseudoproxy records in Fig. 3.2 is already instructive as it shows some general features.

At first, we see that due to the unequal sampling, the estimated coupling is much smaller than for the evenly sampled pair. In cases like this, with estimates close to zero, different approximation methods can even yield different signs of the estimate. This demonstrates the usefulness of the full posterior distribution as it puts such an estimate into a wider range of uncertainty. Another feature of the posterior distribution is that it becomes wider for those methods that reduce the number of observations (nearest values and slotting). A reduction of sample size is directly translated into an increase in estimation uncertainty.

For a more systematic investigation, we repeat this estimation of ρ_{MCMC} for 5,000 pairs of pseudoproxy records, with parameters randomly drawn from the intervals shown in the Appendix Tab. C.1. Each pair of realizations is tested in four different scenarios to represent different degrees of time uncertainty:

Equal sampling. At first, the true observation times are used which corresponds to the assumption that **Y** has the same sedimentation rates as **X**. As samples are concurrent, the dominant source of uncertainty is the finite sample size.

Unequal sampling/reference times. If the true ages are combined with separate sedimentation processes, uncertainties originate not only from finite sample size, but also from unequal sampling.

Age model median. The time axis of the age model is used, in particular the median age model $\{t^m\}$. In additional to sample size and unequal sampling, uncertainties also come from radiocarbon calibration.

method	abbreviation	parameter settings
Linear Interpolation	LI	
Gaussian Kernel Interpolation (0.5)	G (0.5)	$h = 0.5\Delta t$
Gaussian Kernel Interpolation (2)	G (2)	$h = 2\Delta t$
Nearest Value	NV	limit $0.5\Delta t$
Slotting (1)	S (1)	$W = \Delta t$
Slotting (2)	S (2)	$W = 2\Delta t$

Table 3.1: The different methods of approximation that are compared in this chapter, together with the parameters used, if any. The details of these methods are discussed in Sec. 3.2 and in the Appendix Sec. C.1.

Age model ensemble. Instead of using only the median time axis, we integrate over the range of realizations of both age models. This is approximated by drawing N_{ens} realizations from the age model and combining the resulting posterior distributions for each ensemble member as $\rho'_{MCMC} \approx \bigcup_{i=0,...,N_{ens}} \rho_{MCMC,i}$. This adds explicit time uncertainties. Usually, a small ensemble size of $N_{ens} \sim \mathcal{O}(10)$ suffices to yield stable results.

Given an interpolation method I, a time model T and a realization i the resulting estimate of the correlation is written as $\hat{\rho}^{I,T}_{MCMC,i}$. The point estimator for a realization i is the value at which the posterior distribution of ρ indicates the highest probability. The true value is considered to be c. The approximation methods and their corresponding parameters are summarized in Tab. 3.1 and detailed in the Appendix Sec. C.1.

We analyze the performance of correlation estimates for different parameters of the pseudoproxy generation. To do so, we differentiate between local and global measures. The former are defined on single realizations (e.g., bias), the latter on the whole ensemble of realizations (e.g., the root mean square error).

3.4.1 Local measures

We focus on two local measures, the bias (bias$_i$ = $\hat{\rho}_i$ − c) as a measure of accuracy and the interdecile range (IDR = Q_{95} − Q_5, with Q_i denoting the ith quantile) as a measure of precision. The distributions of values over all realizations are shown in Fig. 3.3, each scaled by the true coupling strength c for better comparability. In this way, a scaled bias of -1 means, that the two time series are erroneously considered independent. For the IDR, to scale the obtained results as well, we relate the width of the posterior distribution to the magnitude of the real coupling. A large IDR still yields reasonable results for large coupling strengths, but makes interpretation difficult for low coupling strengths. As the point of maximum probability is often close to the median of the posterior distribution, a scaled IDR of 0.5 and larger indicates, that a correlation of zero is likely within the interval $[Q_5, Q_{95}]$.

For equally sampled time series, the median bias is very close to zero and most of the spread is due to finite sample sizes. The largest fraction of the bias is confined between -0.5 and 0.5, indicating that while finite sample sizes introduce a bias, the
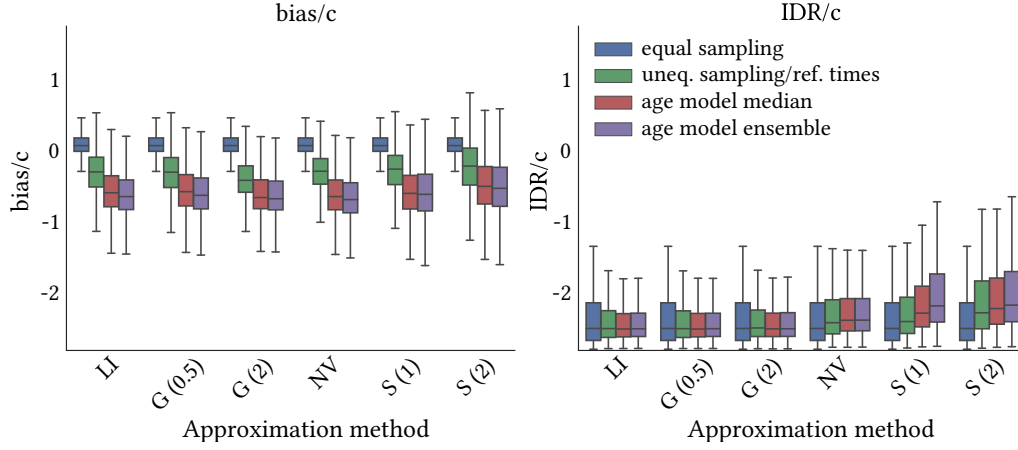
Figure 3.3: Distribution (box plots) of scaled bias and interdecile range (IDR) of all realizations for different approximation methods (left to right) and levels of time and sampling uncertainty (different colours). The values are scaled to the coupling strength in order to make them more comparable.

point-estimator still shows the sign of the correlation correctly. However, both unequal sampling and age models introduce considerable additional bias. These are mostly negative, with a tendency towards low or no correlations. Every approximation method deviates from the true variability, which can be interpreted as additional noise on the joint distribution weakening the effective coupling. The introduction of time uncertainty of the age model adds yet another bias, which is however rather small as compared to the other contributions. In general, the LI, G and NV methods show comparable results while the slotting methods exhibit larger variability but also slightly lower bias.

For the IDR we note, that the variability decreases with the introduction of additional sources of uncertainty for most approximation methods. This can be explained by the fact that interpolation methods effectively introduce new "observations" and thus the overall set of compared values gets larger, decreasing the estimation uncertainty. Furthermore, the posterior can peak around zero if no correlation is detected, narrowing the IDR. On the contrary, the NV and slotting methods show considerably higher IDR, which is due to the reduction of observations and, thus, higher estimation uncertainty.

To study the effects of varying parameters we focus on the realizations related to the lowest, middle and highest decile of each parameter. The corresponding results are shown in the Appendix Figs. C.3 and C.4. As changes in μ_S and γ_S do not result in much variation (not shown) we discuss here only the results for the effects of the time series length, coupling strength and drag parameter θ.

While the median bias does not change much with increasing time series length, its variability does reduce drastically. For short time series there are more realizations (especially when using an age model) for which the scaled bias falls below −1, thus indicating the wrong sign of correlation. This error is markedly reduced for longer time series. A similar effect is seen for the coupling strength. While the mean scaled bias does not change much, its variability increases for weak coupling. Finally, the model parameter θ is found to have a very strong impact on the correlation estimates. For low

values of θ all methods provide good estimates while for large values the introduction of unequal sampling alone leads to a scaled bias of around -1, so that no correlation is detected.

To understand the latter result, we recall that the parameter θ is responsible for the persistence of the considered Ornstein-Uhlenbeck process used for generating our pseudoproxies. The strength of persistence can also be estimated directly from the data, for example, via the lag-Δt autocorrelation of **X**. We estimate the latter property with the help of the Gaussian Kernel estimator (denoted as gACF, Rehfeld and Kurths, 2014). The results using the estimated persistence are almost identical to those using θ alone, with almost unbiased estimates for strong persistence and very large scaled bias for weak persistence. This is not unexpected, as persistence is known to increase the values of correlation among time series in general (Mudelsee, 2010). Also, a certain degree of persistence is necessary to be able to approximate unobserved data from close data. If there is no persistence, these close observations do not carry enough information and, hence, approximations effectively add a random signal to the time series which reduces correlation estimates.

By contrast, the IDR does not depend much on persistence. This results mainly the posterior is often peaked at zero, if no correlation is detected, resulting in a low IDR. Besides that, we see a strong decrease in IDR for increasing time series lengths and coupling strengths. Again, the IDR is considerably larger for the nearest value and slotting methods, while linear and Gaussian kernel interpolation yield similar results.

3.4.2 Global measures

For most of the following results the parameter ranges are discretized to a small number of subsets and measures are then applied to these subsets. We will concentrate on two global features, the root mean square error (RMSE) and the correct sign ratio.

The RMSE is shown in Fig. 3.4 in dependence on the persistence of the time series. Similar figures for the effects of time series length and coupling strength can be found in the Appendix Figs. C.5 and C.6.

Not surprisingly, we observe a decreasing RMSE for increasing persistence. The corresponding dependence on θ is very similar (not shown). Furthermore, there is a strong increase in RMSE with increasing coupling strength for all time models, mainly related to the increasing underestimation for large coupling strengths. However, the RMSE does not decrease much if increasing the sample size. Thus, globally, the accuracy does not depend too much on the length of the sample, which mainly influences the uncertainty of the estimate.

Again, the largest uncertainties are associated with unequal sampling and age model timescales. Additional time uncertainty does not render the observed estimates much worse.

In many cases, the matter of interest is not so much the exact strength of a correlation, but its presence and sign alone. From the posterior distribution ρ_{MCMC} one can determine the sign by introducing a threshold level α and assign a positive (negative) sign if at least a fraction $1 - \alpha$ of the posterior sample values are above (below) zero. If none of the two is the case, we say that the estimator is indifferent. At first, we study how well the different methods can detect the presence or absence of correlation in general. For this, we examine the receiver operating characteristic (ROC), in which the
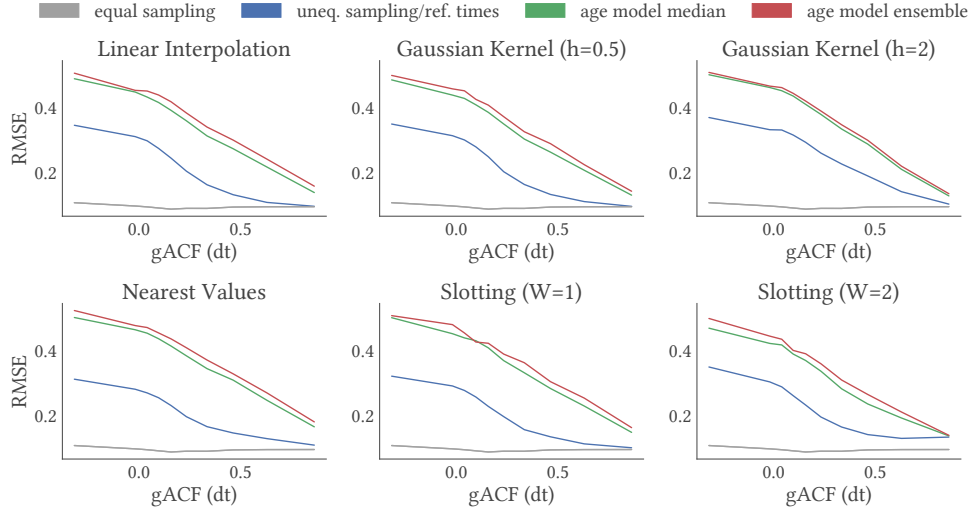
Figure 3.4: The influence of persistence on the root mean square error (RMSE), shown for different approximation methods (different panels) and different levels of time and sample uncertainty (different colours).

true and false positive rates are plotted against each other for different threshold values. The resulting ROC curves are shown in Fig. 3.5. While all approximation methods perform similarly well in the case of unequal sampling alone (left panel), the curves spread out when adding age model uncertainties (middle and right panel). Here, the Gaussian interpolation outperforms the other methods, in particular when using age model medians and ensembles.

Given a subset of realizations, we can study the fraction of realizations that show a particular sign as shown in Fig. 3.6 and the Appendix Figs. C.7 and C.8. In the case of weak coupling (below 0.2) about 50% of the estimates are indifferent, but the correlation is mostly detected successfully for stronger coupling (Appendix Fig. C.7). This is even true in ~ 85% of the cases when including age model uncertainties.

In Fig. 3.6 and the Appendix Fig. C.7 and C.8 we see that the rate of correctly identified signs in the presence of age model errors and uncertainty is lower for the slotting and nearest values methods than for the interpolation methods. In the Appendix Fig. C.8, a similar pattern is seen for the dependency on the time series length (and thus effectively the sample size). Not surprisingly, the sign is determined correctly more often for large sample sizes, but there seems to be a saturation after about 200 observations (more than present in many paleoclimate records).

Again, the persistence seems to be a good indicator of the performance of the estimator as seen in Fig. 3.6. For persistent time series, the sign is determined correctly in most cases, independent of sampling or time uncertainties. Low or negative autocorrelation is associated with a much lower fraction of correct signs.

When it comes to the determination of the sign, most methods agree reasonably well with each other, as can be seen in the Appendix Fig. C.9. Here, we show the fraction of realizations and time models for which pairs of approximation methods indicate the same sign. The highest agreement is between the LI and G (0.5) with 91%. These are
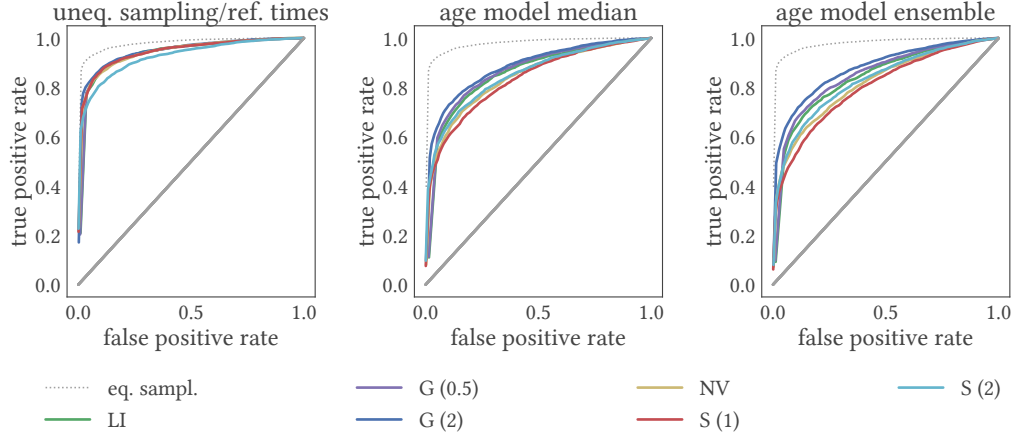
Figure 3.5: The receiver operation characteristic (ROC) curves for different levels of time uncertainty (from only unequal sampling on the left, to age model error in the middle and additional age model uncertainty in the right panel) and different approximation methods (shown as different colours). The dotted line is the corresponding ROC curve for equally sampled time series, for which limited sample size is the main source of uncertainty.
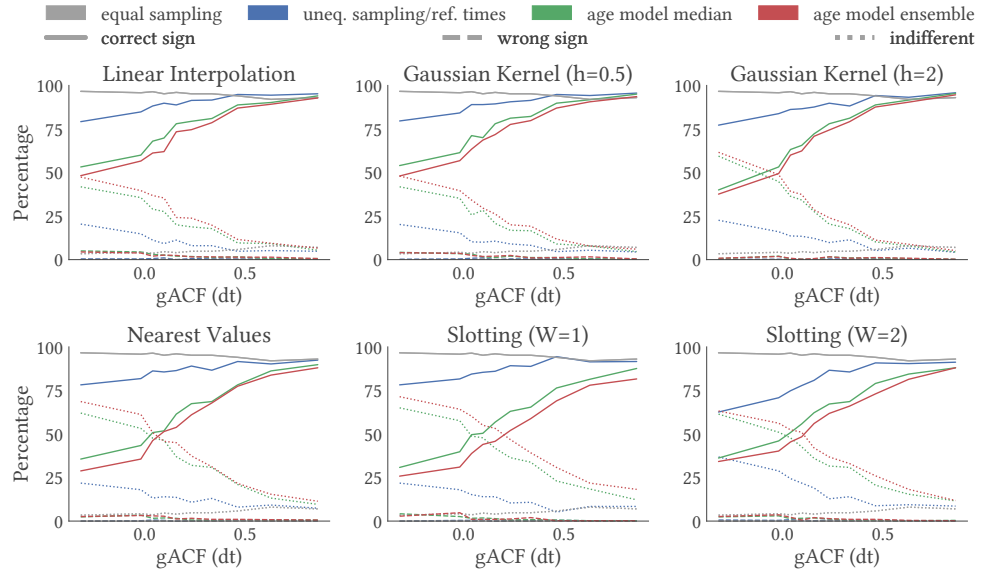
Figure 3.6: Fractions of correctly, wrong and indifferently estimated signs of correlation in relation to the persistence of the time series, shown for different approximation methods (subplots) and different levels of uncertainty (marked by colours).

also the two methods which are in highest agreement for the equally sampled time series. In general, most of the disagreement is due to one method showing a significant correlation while another one is indifferent. Disagreement on the sign of correlations is extremely rare. The linear and Gaussian kernel interpolation seem to perform better, as the percentage of indifferent estimates is lower than for all other methods.

3.5 Real-world application
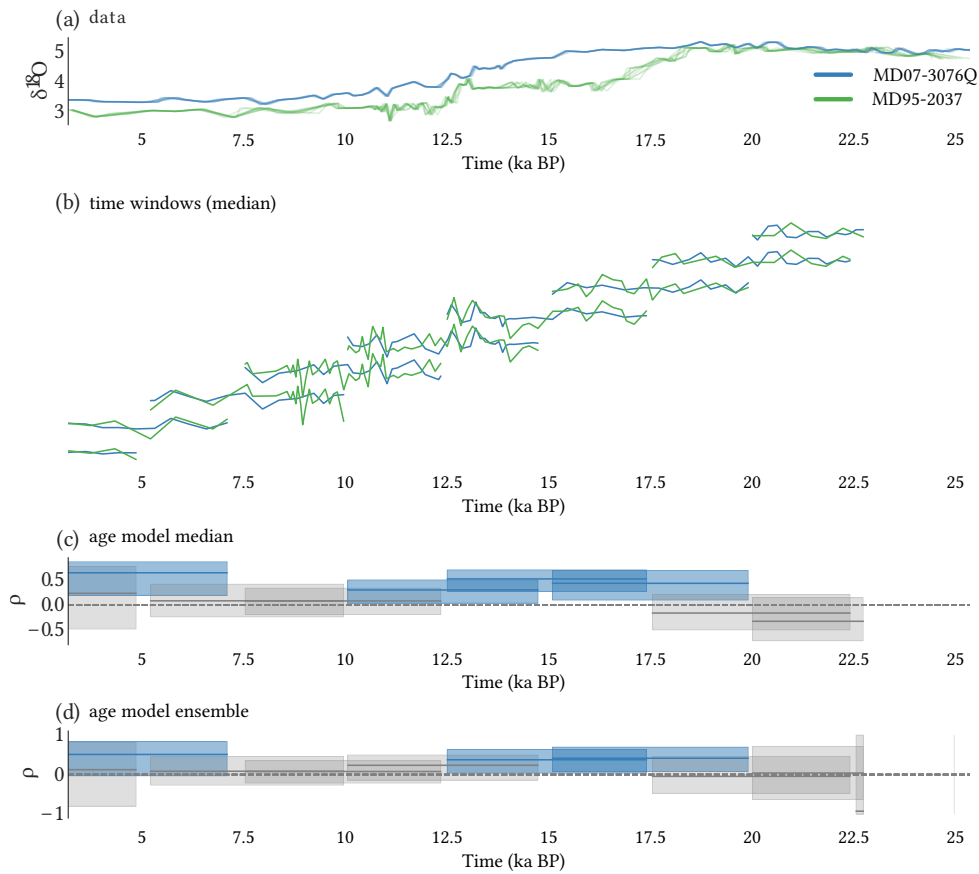
Figure 3.7: Application of the probabilistic correlation estimation discussed in the text to a pair of marine benthic $\delta^{18}O$ records from the South (MD07-3076Q) and North Atlantic (MD95-2037). (a) Different realizations of the age model for both proxies, adjusted by that time lag at which mutual correlation is maximal. (b) Filtered values used to estimate the correlation for each window. Here, the low frequency parts are removed using CEEMDAN decomposition (see main text and Appendix Sec. A.2). (c) Moving window correlation when only using the median of the age model ensemble. Shown are the median value and the interdecile range. The length of each line represents the duration of the time window. Those windows for which more than 95% of the ρ_{MCMC} samples are larger or smaller than zero are shown in blue, the rest in gray. (d) Same as for (c), but for correlations integrated over a number of realizations of the age model.

To demonstrate the usefulness of a Bayesian estimation of correlation, we take a look at two marine records of benthic δ^{18}O values from the Atlantic region. The cores are MD07-3076Q from the South Atlantic (Waelbroeck et al., 2011) and MD95-2037 from the North Atlantic (Labeyrie et al., 2005), both covering the last 30,000 years. In general, δ^{18}O is considered to be a proxy for both water temperature and salinity, but as the bottom water temperature is close to zero benthic δ^{18}O is mainly interpreted as predominantly representing salinity, which, on longer timescales, is mainly a function of the global sea ice volume (Maslin and Swann, 2006; Bradley, 2015).

Hence, these two records are generally thought to be correlated up to a possible lag due to reservoir effects and slow mixing of the ocean water. Both are radiocarbon dated and we construct the depth-age model as used for the pseudoproxies (detailed in the Appendix Sec. C.1) to have comparable age uncertainties. We use our own depth-age model, because both records were published using different, and now outdated, calibration curves, which show a large deviation of ~ 400a at the time of the deglaciation (~ 15 ka BP) from the more recent calibration curve Marine13 (Reimer et al., 2013).

MD95-2037 has a reported reservoir age effect of ~ 400a, while MD07-3076Q has been reported with variable reservoir effects between 1 ka and 3 ka. In this study, we use a relative time axis, by aligning the two records such, that the correlation is maximized, a procedure common in lead-lag estimation (see e.g. Chang et al., 1997; Klein et al., 1999; Boker et al., 2002). In this way, we do not include any reservoir effect into the age model. Any detected lag of the order of 1 to 3 ka could thus result from such reservoir effects.

For simplicity, we use linear interpolation in this application. We find a lag of 2100 years to yield a maximum correlation value. Nevertheless, the correlation posteriors are very similar for all lag values between 1.5 ka and 3.1 ka and, thus, the lag relationship shows a considerable degree of uncertainty.

In Fig. 3.7a one can see different realizations of the age models of the two records, adjusted for the mutual lag showing the maximum correlation. Even though both records exhibit a marked drop in δ^{18}O during the deglaciation, the shape of the transition is considerably different. Also, it is difficult to assess the similarity at shorter timescales. Waelbroeck et al. (2011) discussed, that benthic δ^{18}O records might not be correlated at sub-millennial timescales.

To concentrate on different time-scales of interest we apply Complete Ensemble Empirical Mode Decomposition with Adaptive Noise (CEEMDAN Torres et al., 2011, discussed shortly in the Appendix Sec. A.2)) to each time series and discard those intrinsic mode functions (IMFs) for which more than 10% of the instantaneous wavelengths are larger than 5 ka. This ensures, that no overlying trends and low-frequency variability alter the results obtained in the following.

For the time series reconstructed by superposition of the higher-frequency IMFs, the maximum correlation for the age model median and the age model ensemble are reached at lags of 2.1 ka and 2.05 ka, respectively, comparable with the results for the original unfiltered records.

Having adjusted the two decomposed time series on a shared timescale, we now use sliding windows of 5 ka length and mutual overlap of 2.5 ka to study changes in co-variability over time. The results are shown in Figs. 3.7c, d.

For the age model median, we see significant correlation over most of the last 22 millennia. Only at the beginning of the Holocene and towards the end of the records

(probably related to a lower number of samples) there are no significant correlations. If we take age uncertainty into account we generally find a similar pattern, but the estimator is now indifferent for one more time window. The uncertainty in observation times is rather small in our age model as compared to those produced by other age model algorithms like Bacon (Blaauw and Christen, 2011). Hence, when using such models it is possible that less time intervals will show significant correlations. We thus decided against using these more elaborate age model algorithms, as this would make comparison with the previous results difficult. Furthermore, we consider our age model to sit in between very simplistic and rather complex age models and, hence, the results can be more directly related to other models.

3.6   Conclusions

The aim of this chapter was to provide some guidelines for the estimation of correlations between (marine) paleoclimate records, in particular when dealing with unequal sampling and age model uncertainties. The main tool has been the probabilistic (Bayesian) estimation based on a bivariate normal model. While most results might not be surprising, they have rarely been addressed explicitly in previous works.

In cases of weak coupling, different approximation methods can show even different signs of the estimated correlation, but these are rarely significant. Thus, when different approximation methods with different parameters yield different signs for the point estimator it is crucial to take estimation uncertainty into account. This will probably lead to a non-significant correlation. Still, in most cases, the correct sign of a correlation can be detected even in the presence of a large bias of its absolute value.

Those methods which reduce the number of observations like slotting tend to highlight low-frequency variability and trends. In comparison, interpolation seems to be a better strategy to approximate the joint probability distribution. The best results were obtained using linear interpolation or a Gaussian kernel with small bandwidth. For small bandwidths, the directly neighboring observations dominate the approximation of missing values and thus these two methods are expected to be very similar. Our findings agree with other studies, that have reported the Gaussian kernel estimator to be superior (Rehfeld et al., 2011; Rehfeld and Kurths, 2014), even though the difference to linear interpolation is small. Hence, it seems reasonable to prefer the Gaussian kernel estimator with small bandwidth over other methods.

The characteristics of the time series under study are in many cases more important than the choice of the particular interpolation method. The most important features are the coupling strength, number of observations, and persistence of the signal.

The first factor is generally not accessible for real-world data, but the other two can be estimated. As mentioned in Sec. 3.4 persistence has been seen as a problem to correlation estimation due to its tendency to induce spuriously high correlations. Still, it is of advantage in the case of irregularly sampled time series, as it allows inference from neighbouring points on unobserved data.

Thus, in real-world applications, one should check, if a time series shows enough persistence to perform meaningful interpolation. While the sample length does not affect the error much, it increases the estimation uncertainty. Most time uncertainties mainly lead to indifferent estimates, but rarely produce false signs of correlation. If one

finds a significant correlation between unequally and age-uncertain time series one can hence accept them to reflect features of the time series. Large persistence nevertheless yields the same problems as in the case of regularly and evenly sampled time series. Thus, if a significant correlation is found, it should be investigated if it might be due to low-frequency variability (if the latter is not the time-scale of interest).

In most of the pseudoproxy experiments in this study, the additional error from time uncertainty has been much smaller than those originating from unequal sampling and age model calibration. From our real-world example we can see that many features are similar in both cases, even though sometimes significance is lost. In the past, only few authors have published explicit age uncertainties for each observation. In these situations, it might still be preferable to use the published age model, as a bad age model with quantified time uncertainties might introduce a larger error than ignoring time uncertainties.

We have finally discussed an example of two benthic δ^{18}O records, which are generally thought to be correlated on at least millennial timescales. Using the Bayesian estimation of correlation together with Gaussian kernel based interpolation we have seen that when adjusting to one time-scale we find similarities even at the sub-millennial scales. These correlations are not stationary and change over time, being significant only during some periods. Taking uncertainties into account can be helpful in assessing if two time series are similar to each other. In summary, we therefore conclude that it would be useful if data publishers would also report the age uncertainty given by their age model to each observation to make more accurate estimations possible.

Part II | Late Holocene

4 | Overview: Holocene climate variability

The term Holocene describes the current geological epoch that has started about 11.5 ka BP[1], following the retreat of ice sheets, sea ice and mountain glaciers all over the world. The Holocene marks the latest in a series of warm periods, the so called interglacials. It differs from most of these other periods in being remarkably long lasting, similar only to a low number of previous episodes, like Marine Isotope Stage 11.[2]

Understanding Holocene climate variability is a highly crucial undertaking, as it provides the context for recent anthropogenic warming, induced by greenhouse gas emissions, land cover change, etc. In order to quantify the effects of anthropogenic influences, we need to understand the different roles of forcing and feedback mechanisms in the past. Besides external forcings, there are also internal modes of variability, in particular in the atmospheric and ocean circulation. Understanding their variability and modes of operation under more or less constant Holocene background conditions is crucial to make statements about future climate change. These tasks demands proxy-based paleoclimate reconstructions, as the instrumental measurements do not cover multi-decadal and longer time-scales well.

The transition into the Holocene was accompanied by a drastic reduction in climate variability, with the largest changes in the mid- and high-latitudes, in particular in Greenland (Rehfeld et al., 2018). These features have led to the long lasting belief that the Holocene is a period of exceptional stability, linked to the rise of civilizations, in

---

[1]Remember that we use the ka BP convention for all times that are much before the year 0 CE.

[2]There are various detailed introductions to Holocene climate variability, for example by Cronin (2010), IPCC (2013), and Wanner et al. (2008), on which this chapter is largely based.

particular in the Fertile Crescent and Europe (deMenocal, 2001; Diamond, 1997). In contrast, episodes of unstable climate conditions have frequently been accompanied by cultural decline (Coombes and Barber, 2005; Marcott and Shakun, 2015).

This view has been challenged in recent years and there is now compelling evidence that many key components of the climate system evolve—in terms of both gradual changes as well as abrupt shifts—during the Holocene. Examples for such changes are a southward shift of the intertropical convergence zone (ITCZ), a weakening of the monsoon systems and increasing intensity of the El Niño Southern Oscillation (ENSO, see, e.g. Cronin, 2010). Still, the amplitude and rate of changes are much lower than those of millennial-scale variability during glacial times and, therefore, Holocene climate variability is considerably harder to assess.

4.1 Sources of climate variability during the Holocene

In general, climate variability is attributed to either external forcings or to internal variability. External forcings are boundary conditions to which the climate system responds, while internal variability can develop without any external interference. A prominent example for external forcing are the variations in incoming solar insolation due to orbital changes that shape the glacial-interglacial cycle (see, e.g. Paillard, 2015, and Ch. 7). Internal variability is often connected to patterns of ocean or atmospheric circulation like the Atlantic Meridional Overturning Circulation (AMOC), the North Atlantic Circulation (NAO) or ENSO.

Still, the two mechanisms cannot be distinguished as internal variability and external forcings are connected via feedback mechanisms. This is illustrated by the complex patterns of forcings and feedback loops that explain the glacial terminations (see Ch. 7) or the tendency of the NAO towards a positive phase in the years following a volcanic eruption (the NAO is discussed in more detail in Sec. 6.1).

The dominant external forcings during the Holocene are variations in solar activity and explosive volcanic eruptions, which are commonly made responsible for much of the Holocene climate variability (up to 64%, according to Crowley, 2000).

In contrast to glacial time-scales, solar insolation varies only slightly (in the order of permills) during the Holocene, mostly related to cyclic variations in solar activity. Still, this variability is visible in many paleoclimate proxies and minima of solar activity are related to extended cold periods, for example during the 16th century CE, which is related to the solar Maunder minimum. A physical understanding of how such minor solar variations can lead to changes in surface temperatures of this magnitude is largely missing, but it is clearly visible in climate models as well (Haigh, 1996; Ammann et al., 2007).

The second source of external forcing are explosive volcanic eruptions that inject large amounts of aerosols into the atmosphere (Robock, 2000). These aerosols block sunlight and, in this way, lead to a substantial stratospheric heating and surface cooling. If such an eruption occurs in the tropical region, it reduces the meridional temperature gradient and consequently changes the atmospheric circulation, in particular over the Northern Hemisphere. Volcanoes have long been known to influence the climate system, but normally their impact is of smaller magnitude and only lasts for a couple of years following the eruption. Still, very large eruptions or periods of clustered eruptions
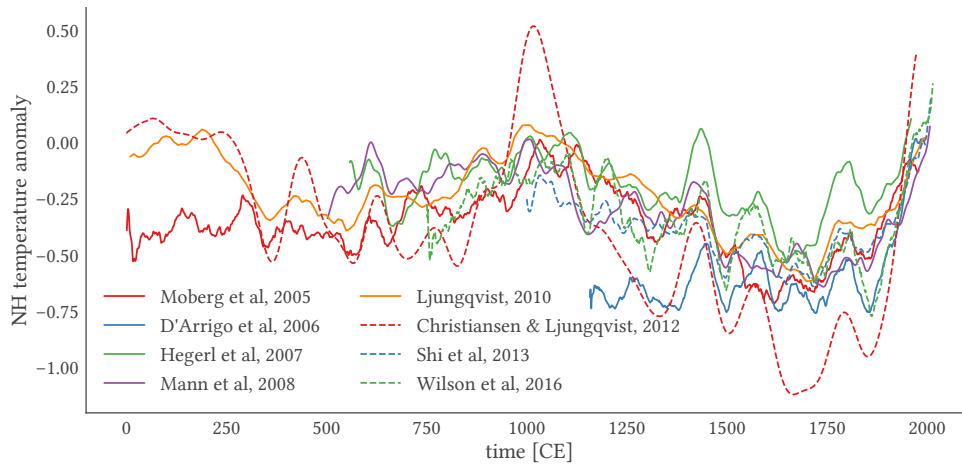
Figure 4.1: Northern Hemisphere temperature anomaly reconstructions for the late Holocene. This plot uses the reconstructions by Christiansen and Ljungqvist (2012), D'Arrigo et al. (2006), Hegerl et al. (2007), Ljungqvist (2010), Mann et al. (2008), Moberg et al. (2005), Shi et al. (2013), and Wilson et al. (2016).

might trigger climate changes on much longer time scales (Crowley, 2000; Büntgen et al., 2016).

Both solar activity and volcanism are connected to internal dynamics in various ways, mostly through changes in the radiation balance, for example through heat flux reorganization, land-cover and vegetation changes or albedo related feedbacks. One particular example of such an influence is the impact of volcanic eruptions on the NAO. The increased meridional temperature gradient in the years following an eruptions strengthens the mid-latitude westerlies and, therefore, causes a preference for a positive NAO phase (Robock, 2000).

4.2 The last two millennia or the Common Era

The period of interest in this part of the thesis are the last two millennia of the Holocene, also called the Common Era (CE). This is a key period in many recent discussions, as it provides the context in which anthropogenic climate changes are commonly discussed. This is due to the fact that external boundary conditions are close to today's and, hence, the range of natural decadal to centennial-scale climate variability is accessible. In addition, this is a time period for which a high number of well-dated and high-resolution paleoclimate proxies are available, mainly in the form of tree rings, varved lake sediments, ice cores and corals (Bradley et al., 2003). Even for this period, however, there is no consensus about the extent and causes of climate variability. This can be seen very clearly by the selection of Northern Hemisphere temperature reconstructions shown in Fig. 4.1[3].

---

[3]Due to its inconsistency, this type of plot has been coined a *spaghetti plate* (Frank et al., 2010).

There are nevertheless some key periods for which most reconstructions agree, marked by either anomalously warm or cold temperatures. These episodes are often connected to changes in other climate variables as well and constitute the subdivision of the Common Era. They are introduced in the next paragraphs.

Roman Warm Period (RWP)   The centuries around the year 0 CE were characterized by a warm and humid climate in Central and Western Europe (Luterbacher et al., 2016). This period coincides with the height of the Roman Empire and thus has been called the Roman Warm Period (Bianchi and McCave, 1999; Büntgen et al., 2011). Due to the lack of high-resolution records, the spatial extent of this period is not well known, but there is evidence for similar conditions at other regions, for example Florida (Wang et al., 2013) and China (Liu et al., 2006).

Late Antique Little Ice Age (LALIA)   This period has recently gained attention, mostly due to an increased number of high-quality proxies of volcanic forcing. While an extreme volcanic eruption around 536 CE has long been suspected (see e.g. Stothers, 1984), there has not been much knowledge about this time. This changed when a cluster of strong volcanic eruptions between 536 and 547 CE was found (Sigl et al., 2015) which, together with decreasing solar activity might have led to a cold period that lasted for about a century until 660 CE (Büntgen et al., 2016). These climate changes have been connected to societal changes and migration in Europe (Büntgen et al., 2011).

Medieval Climate Anomaly (MCA)   The Medieval Climate Anomaly (previously called Medieval Warm Period), is most pronounced as a period of relatively warm temperatures in Central and Northern Europe lasting from about 950 CE to 1250 CE (Hughes and Diaz, 1994; Bradley et al., 2003; Mann et al., 2009; Luterbacher et al., 2016). Temperatures in the Northern Hemisphere are thought to be comparable to those of the late 20th century. Still, this temperature signature is not the same globally, with colder than modern temperatures in other regions, for example over Central Asia or large parts of the Southern Hemisphere (Mann et al., 2009).

The MCA has been related to an extended period of stable atmospheric conditions, possibly caused by a tendency of the North Atlantic Oscillation towards its positive phase (Trouet et al., 2009; Ortega et al., 2015; Bradley et al., 2016), but also to the low number of large volcanic eruptions (Sigl et al., 2015) and the lack of strong solar minima (Steinhilber et al., 2009).

Little Ice Age (LIA)   The Little ice age comprises the centuries of colder temperatures that followed the MCA. Due to its complex spatial patterns there is no consensus about the exact timing of the LIA. While some authors propose a start already in the 13th (Miller et al., 2012) the peak period was likely between the early 16th and the 19th century. In many areas of the Northern Hemisphere, it was characterized by cold winters and strong precipitation, which is thought to have had an extensive influence on European societies (Fagan, 2000).

The LIA is now often considered not as a single period, but rather a sequence of cold periods. These correspond to different minima in solar activity, for example the Spörer minimum in the 15th century, the Maunder minimum in the 17th century and

the Dalton minimum around 1800 CE. Clusters of explosive volcanic eruptions have likely contributed to the cold temperatures in many regions (Briffa et al., 1998; Crowley, 2000; Ammann et al., 2007; Miller et al., 2012). Examples for such clusters of eruptions are the eruptions of Mt. Samalas and others in the 1250s, that of Kuwae in the 1450s and the large eruption of Tambora in 1815. The latter caused the year 1816 to be called *the year without summer* in Europe, due to the large reduction of incoming sunlight caused by ash and aerosols in the atmosphere (Luterbacher and Pfister, 2015).

It should be noted that while these intervals are found in most reconstructions of Northern Hemisphere temperatures, there is no agreement on the temporal extent of each period. Their names demonstrate a Eurocentric viewpoint, as they are rarely global signals, but most pronounced in reconstructions of European temperatures. As this region is the region of interest in this part of the thesis, we stick to these terms, while keeping in mind that they are not representative for other regions of the world.

5 | Dynamical anomalies in terrestrial paleoclimate records

Before looking into co-variability between records, it is useful to better understand the characteristics of paleoclimate records. In particular, we are interested in the question if and to what degree paleoclimate records from the late Holocene can be described by a simple linear, stochastic model, and, if this is not the case, what kind of dynamics might lead to anomalous signals in the archives.

Even though the climate system is a high-dimensional and deeply non-linear system, many climate variables can be described as stationary, linear, stochastic processes (e.g. autoregressive processes), when looking at annual and longer time-scales. While short time scales are dominated by the intrinsic chaotic dynamics of the atmosphere, these are aggregated to a more stochastic behaviour on longer scales, modulated by slower processes of the climate system, in particular the ocean (Bigg et al., 2003). This is not the case anymore if large-scale reorganizations of the (regional) climate system occur, possibly related to non-linear transitions caused by changes in external parameters (Strogatz, 2014). These types of transitions will be accompanied by transient dynamics, represented in the mean state or variability of a time series (Donges et al., 2011a; Schleussner et al., 2015; Donges et al., 2015a). Hence, any deviation from stochasticity might point towards dynamical changes in the climatic conditions.

The method of (horizontal) visibility graphs, introduced in Sec. 2.3, has recently been demonstrated to be a particularly useful tool for such an analysis of real-world data (Donges et al., 2013). In particular, it has been successfully applied to study the transition behavior of the North Atlantic subpolar gyre between the MCA and LIA

(Schleussner et al., 2015).

In the present chapter, we use this method to systematically test for time-reversibility in an ensemble of terrestrial paleoclimate records spanning the last millennia. Time-reversibility is a necessary feature of linear stochastic processes and, hence, a lack thereof points towards more complex dynamics. In this way, we test if the reported anomalies in Atlantic ocean circulation were accompanied by similar changes in atmospheric dynamics. One particular ambition is to overcome the large rate of false-positives, that has prevented a widespread use of this method so far. We propose that only those times should be regarded as anomalous that show consistent time-irreversibility over an ensemble of records. In this way, we differ from previous studies, which have focused on single records. One way to obtain such a consistent and reliable detection is introduced in this chapter, which largely follows the publication JF1.

Key Questions

- How can we obtain reliable signatures of anomalous climate dynamics using horizontal visibility graphs?

- Are there any periods of anomalous dynamics in Fennoscandia during the last two millennia?

The remainder of this chapter is organized as follows. In Sec. 5.1, we present the data used in our analysis and in Sec. 5.3, the results of our analysis are presented, further discussed in Sec. 5.4. We end the chapter with some concluding remarks in Sec. 5.5. Additional results supporting our main findings are provided in the Appendix Ch. D.

5.1 Data selection for this study

While the North Atlantic region is sensitive to external forcings, such as solar activity and volcanism, it also exhibits large-scale phenomena of internal variability, like the North Atlantic Oscillation (NAO) or the Atlantic Multi-decadal Variability (AMV). These phenomena play a key role for understanding climate dynamics in large parts of the Northern Hemisphere (as discussed in detail in the next chapter). As such, the area has been extensively studied and there are few other regions in the world with such a dense data coverage. These include long, high-resolution and well-studied tree ring (Helama et al., 2009; Gunnarson et al., 2011; Esper et al., 2012; Melvin et al., 2013) and lake sediment records (Tiljander et al., 2003). Many of these time series have been used in recent high-resolution, regional (PAGES 2k Consortium, 2013; McKay and Kaufman, 2014), hemispheric (Ljungqvist, 2010) and global (Mann et al., 2009) paleoclimate temperature reconstructions.

Site-specific processes and archive-specific restrictions to the recording of climate variations lead to different signals, even in high-resolution proxy records from the same region. This makes it difficult to obtain a coherent picture of the regional climate dynamics based on individual records alone. Rather, a paleoclimate record is a projection of the regional climate state on a variable of the recording archive (e.g. tree ring width). This variable is then assumed to be (linearly) related to one specific climate variable (e.g. summer temperature). Thus, records that are affected by similar regional conditions should in general share most of the climate dynamics, even though their

Figure 5.1: Geographical locations of the paleoclimate records used in this chapter. Tree ring records are shown in red, lake sediments in blue. The details of these records are presented in the Appendix Tab. D.1.

specific variability might differ. Although some of these assumptions might be up for discussion, we accept them as necessary approximations to the possibly more complex real-world processes. Hence, we consider paleoclimate records from close locations to be interrelated, especially on decadal to centennial time scales.

From this considerations, we select an ensemble of terrestrial paleoclimate records from Fennoscandia and Iceland, which is shown in Fig. 5.1. The (detrended) individual time series are shown in the Appendix Fig. D.3 and further details on the records are provided in the Appendix Tab. D.1. Notably, we only consider annually resolved paleoclimate records with at least 300 data points during the last two millennia. Hence, any problems related to uneven sampling can be avoided.

5.2   Ensemble based testing for HVG time-reversibility

The general concept of visibility graphs and how they can be used to study time-irreversibility has been introduced in Ch. 2. Here, we want to introduce, how the method can modified to achieve more robust results.

Donges et al. (2013) found that the KS-test is very sensitive, but leads to a relatively high false positive rates (i.e. finite sample tests showing HVG time-irreversibility in cases, which are analytically HVG time-reversible). To take this into account, we insist on coherence of a signal in multiple ways. First, for a single record, the p-value has to be below the threshold for time windows of different size and for many consecutive time windows. Second, only those signals are considered that are present in a significant portion of the proxies. In this way, we aim to minimize the effect of spurious signals and local dynamics.

5.2.1 Single record test

Large-scale trends, coming from multi-centennial dynamics, can also lead to time-irrversibility. Therefore, we subtract an exponentially smoothed moving average from each time series with a window length of 1 ka. The resulting detrended time series are displayed in the Appendix Fig. D.3.

For single records, we follow the procedure outlined in Sec. 2.3. Hence, we obtain a two-dimensional field of p-values of the KS-test indexed by time and window size. One example of such a plane is shown in Fig. 5.2.

In the following, we refer to a contiguous region with significant p-values as a *patch*, shown as contoured areas in Fig. 5.2. A patch has to fulfill at least one of the following criteria to be considered consistent:

(i) The average fraction of windows with significant p-values is at least equal to 1/3 of the temporal extent of the patch (in our case, this means that on average more than 33 window sizes simultaneously show HVG time-irreversibility).

(ii) The patch's size is larger than the minimum size of a patch which fulfills criterion (i) over a time span of at least 50 years (in our case, this means that the patch consists of at least 33 × 50 = 1650 significant p-values of the individual KS tests).

The first criterion allows for fragmented areas, while the second one aims at patches with a diagonal structure in the time-window size plane.

Time-irreversibility is a feature that does not depend on the sign of a time series. In contrast, Eq. (2.7) does not share this invariance. Hence, a time series **X** could be significantly HVG time-irreversible but −**X** is not. Furthermore, some archives (in particular lake sediment records) are negatively correlated to the associated climate variable (e.g. temperature). If this is the case, one might prefer using the negative time series −**X** even though these negative proxy values do not have a physical meaning (as is the case for example for negative varve thickness). To take this ambiguity into account, we perform the analysis for both signs and consider a time period to be HVG time-irreversible if there is a consistent patch for either one of the two, adjusting the assumed threshold value accordingly.

5.2.2 Group-wise significance testing

As discussed before, a paleoclimate record is a composite of both a regional or global climate signal and local effects. To filter out those signals that are purely local, we concentrate on intervals at which a consistent pattern of HVG time-irreversibility over a larger region is visible. The implicit assumption beyond this integration of information from different records is that all of them are subject to similar conditions, both in regional inter-annual climate variability as well as external forcings like explosive volcanic eruptions or changes in solar activity.

For this purpose, we introduce a group wise test for which we need to estimate the probability of a false positive, meaning that the forward and backward distributions are significantly different, even though the underlying process is time-reversible. This probability is in the following denoted as P. As a conservative estimate of this value, we use the significance threshold for the KS-test α (= 0.1 in this study), even though the
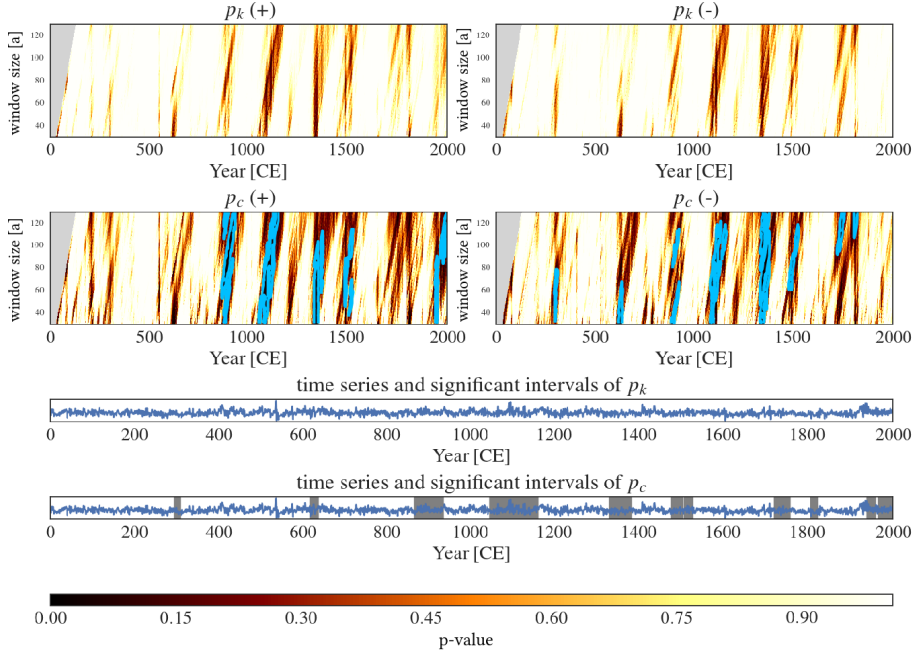
Figure 5.2: The results of the test for HVG time-reversibility, applied to one of the records used in this chapter (Finish Lapland). The upper left two panels show the results for the time directed degree and local clustering coefficients for the time series **X** and the upper right panels for the sign flipped time series −**X**. Areas contoured in blue are those for which the p-value of the KS-test is below 0.1. The lower two panels show the time series together with the detected intervals of HVG time-irreversibility for the degree (top) and local clustering coefficient (bottom). The much higher sensitivity of the clustering based test is clearly visible.

actual probability might be much below this value. If the probability is assumed to be the same for both **X** and −**X**, the joint probability of a false positive is $P_j = 1 − (1 − P)^2$. Here, we consider P to be independent for both signs, even though they are generally strongly correlated. This is again a conservative assumption, as the joint value for correlated probabilities would be considerably lower. Recall, that HVG time-irreversibility is a sufficient, but not necessary criterion for general time-irreversibility. A less conservative approach is not guaranteed to achieve less false negatives but provides higher confidence in the obtained signals.

We want to calculate the number of records S_α for which the probability of a signal by chance alone is less than a predefined threshold value α_m. This can be achieved using a one-sided binomial test to determine a multi-record significance level. As the number of records $N(t)$ varies with time, the resulting significance threshold

$$S_\alpha(t) = \min_{n \in \mathbb{N} \setminus \{1\}} \left\{ \sum_{k=n}^{N(t)} \binom{N(t)}{k} P_j^k \left(1 - P_j \right)^{N(t)-k} < \alpha_m \right\} \tag{5.1}$$

is time dependent. Only those times are considered, at which the number of records that show simultaneous patches with individually significant HVG time-irreversibility is higher than the corresponding $S_\alpha(t)$. In turn, if $n_{\mathrm{obs}}(t)$ out of $N(t)$ do show a signal

at a given time t, we can calculate the probability that this number occurred by chance as

$$p(t) = \sum_{k=n_{obs}(t)}^{N(t)} \binom{N(t)}{k} P_j^k \left(1 - P_j\right)^{N(t)-k}. \tag{5.2}$$

This constitutes the group-wise p-value and we are interested at times at which $p(t) < \alpha_m$.

5.3 Episodes of HVG time-irreversibility in Northern Europe

The single and multi-record analysis presented in the previous section is applied to the ensemble of 16 terrestrial paleoclimate records discussed in Sec. 5.1. The individual results for each time series are shown in the Appendix Fig. D.1 and those for the sign flipped time series are depicted in the Appendix Fig. D.2. We observe that HVG time-irreversibility normally occurs over a sufficiently large, consistent area, though the temporal extent of these intervals varies. By attributing significance to the full patch, we take this time uncertainty explicitly into account. The (detrended) raw data is shown in the Appendix Fig. D.3 together with the intervals that are considered significantly HVG time-irreversible for each record. In general, there is a large variety of patterns. While some records show many periods of HVG time-irreversibility, others seem to be sufficiently described by a linear, stochastic model and show almost no signals. These figures highlight the need for the group wise testing, as some of these many intervals are certainly the result of an overly sensitive test.

The results of the multi-record significance test are shown in Fig. 5.3 together with two significance levels of 5% and 10%. For comparison, we have added two reconstructions of temperature for the Arctic and European region provided by Luterbacher et al. (2016) and PAGES 2k Consortium (2013) respectively. Many of the records used in this chapter have also been included in the Arctic reanalysis, but as our study region lays at the border of the two regions, a similarity to the European climate variability is also expected.

At most times, at least one or two of the records show significant HVG time-irreversibility. In contrast, peaks that are significant under the group-wise test are limited to six time intervals. These intervals are summarized in Tab. 5.1 together with their respective group-wise p-values.

All of these periods coincide with known changes in regional climate:

Interval I1 precedes a decline of European temperatures starting at about 280 CE and accumulating in a cold period that lasted for several centuries. This decline is commonly interpreted as the end of the Roman Warm Period (RWP).

Interval I2 in the 7th century CE follows the Late Antique Little Ice Age (LALIA) from about 530 CE to 660 CE.

Interval I3 coincides with the beginning of the MCA, which is mostly considered to start between 900 CE and 950 CE.
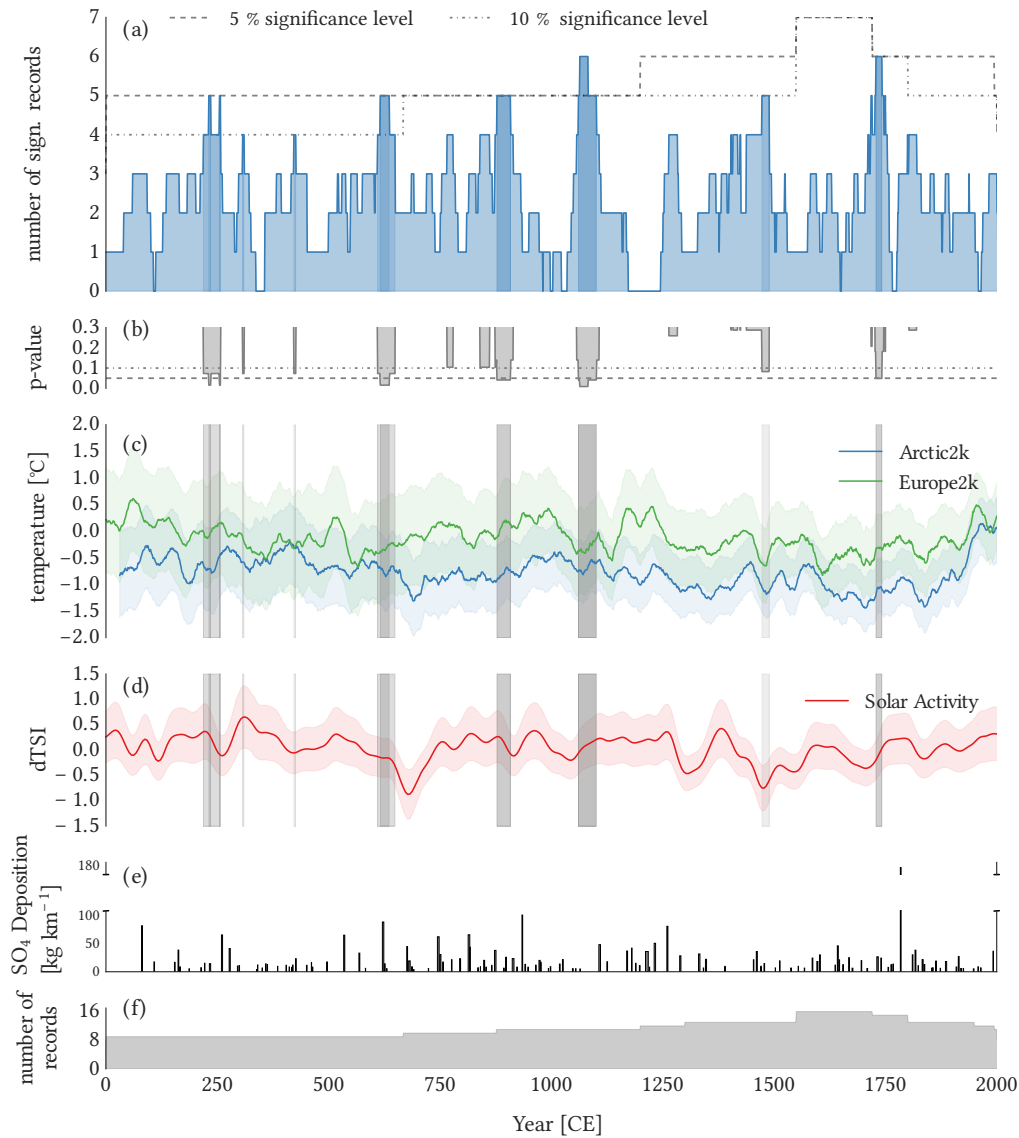
Figure 5.3: Combined results for the HVG time-irreversibility test: (a) The number of proxies that show HVG time-irreversibility per point in time together with the expected number corresponding to significance levels of 5% and 10%. (b) The group-wise p-value that this number of records show HVG time-irreversibility if all time series were realizations of normal, linear and stationary processes. (c) Two regional temperature reconstructions from Europe and the Arctic sector. For comparison, the periods of significant HVG time-irreversibility as determined by the multi-records test are shown as gray bars. (d) Same as in (c), but with a reconstruction of solar activity (Steinhilber et al., 2009). (e) Volcanic activity throughout the Common Era, based on Sigl et al. (2015). (f) Number of records available at each point in time.

Interval	Year [CE]	$n\,(N)$	p-value	Episode
I1	219–257	4–5 (8)	0.016–0.073	End of RWP
I2	610–649	4 (8)	0.016	LALIA/1.4k event
I3	878–908	5 (11)	0.041	Onset of MCA
I4	1064–1101	6 (11)	0.009	Cold episode during MCA/Oort minimum
I5	1473–1489	5 (13)	0.082	Onset of LIA
I6	1729–1742	6 (15)	0.049	Late Maunder mininum

Table 5.1: Intervals with group-wise significant HVG time-irreversibility and coinciding climate related phenomena.

Interval I4 corresponds to an episode of colder temperatures during the MCA in the 11th century.

Interval I5 precedes the onset of the LIA (IPCC, 2013).

Interval I6 follows the late Maunder minimum (1675–1715)

5.3.1 Robustness

Our analysis comprises of several steps and multiple levels of testing for a comparably low number of records. Hence, it is crucial to ensure that results are robust under changes of test parameters or the set of records included. For this purpose, we studied three different kinds of modifications to our analysis:

1. We consider a stricter significance level of $\alpha = 0.05$ for the KS-test, leaving the rest of the analysis unchanged. The corresponding results are shown in the Appendix Fig. D.4. The intervals I1–I4 remain significant, but I5 and I6 do not.

2. We repeat the analysis after removing individual records, as well as pairs of records from the set of time series. These leads to the results shown in the Appendix Figs. D.5, D.6 and D.7. In the leave-one-out case, only the intervals I1, I2 and I4 remain significant in all cases, while the others lose significance for some records removed. In the Appendix Fig. D.6 we show the fraction of cases at which the multi-group test shows significant results for different threshold values. The aforementioned intervals stay significant in all, I3 and I6 at most, but I5 only in few cases, even for the $\alpha_m = 0.1$ threshold value. The same is true—with overall lower fractions—when leaving two records out, as depicted in the Appendix Fig: D.7. In addition, some time intervals, between 300 and 450

CE and between 750 and 850 CE, that are not regarded significant in the full test, become significant for some reduced sets of records.

3. Finally, we study the effect of adding a single, artificial record with no significant intervals of HVG time-irreversibility, by increasing $N(t)$ by one. As can be seen in Fig: D.8 the intervals I5 and I6 fall below the significant threshold, while the rest stays robust.

In summary, the intervals I1, I2 and I4 show robust HVG time-irreversibility. The interval I3 loses significance at the removal of some records. The intervals I5 and I6 are not robust under all three tests and are thus to be considered only marginally significant.

5.4 How are these intervals related to large scale climate changes?

As already mentioned in Sec. 5.3, all of the six intervals that show HVG time-irreversibility can all be linked to distinct periods of climate variability. Still, direct attribution for causes of time-irreversibility is difficult, as all records result from an interplay of local and archive effects with climate dynamics. Even when neglecting the former, one is still confronted with both highly non-linear internal dynamics and possibly non-stationary external forcings. The latter factor can be discussed when considering the Appendix Fig. D.9, where we see that a reconstruction of solar activity itself shows episodes of time-irrversibility. These periods coincide with the intervals I2, I5 and I6 and, hence, these periods might not stem from internal dynamics, but also be linear responses to complex forcing conditions. The second major forcing contribution on the time scale of interest is that of volcanic activity. A HVG analysis of this data is much more difficult, due to the highly intermittent character of eruptive volcanism. In general, reliable and high-resolution reconstructions of external forcing are largely missing at this time and, hence, a connection to driving mechanisms can only be highly speculative.

In the following we discuss the different climate periods and how previous knowledge of the causes of said periods might explain the presence of HVG time-irreversibility at some transitions. For an introduction of these periods, see Sec. 4.2.

5.4.1 Roman warm period

Our results indicate that the shift towards a pronounced cold period in the third century CE is visible not only in the regional reconstructions (Bianchi and McCave, 1999; PAGES 2k Consortium, 2013), but also identified as a dynamical anomaly in the paleoclimate records. These results indicate that the RWP was a distinct warm state of the regional climate system, which ended in a period of anomalous dynamics, followed by colder conditions.

5.4.2 Late antique little ice age

In our analysis, we connect both I1 and I2 with the LALIA. The first marks the beginning of cooling at the end of the RWP, while I2 coincides with the recovery of regional temperatures at the end of the LALIA. At both times, we see HVG time-irreversibility

when low solar activity coincides with strong volcanic eruptions. For the interval I2, we further see anomalous solar activity in the Appendix Fig. D.9, which might have contributed to the complex dynamics at this time.

5.4.3   Medieval Climate Anomaly

Using the HVG test, two intervals are related to the MCA, one around the initiation phase at about 900 CE (I3) and another one between 1050 and 1100 CE (I4). We interpret I3 as indicating a transition period between the colder conditions of the LALIA towards warmer temperatures and hydrological anomalies in the North Atlantic region. Notably, I4 does not correspond to the onset of another transition, but rather to a recovery phase from temporarily reduced temperatures during the 11th century. This cold period corresponds to a minimum in solar activity and is a consistent feature in many reconstructions (Moberg et al., 2005; Mann et al., 2009; IPCC, 2013; Luterbacher et al., 2016) and model simulations (Ammann et al., 2007). It is even more pronounced in some proxy records from Fennoscandia (Gouirand et al., 2008), possibly indicating a particularly strong local response to solar variability changes (Bradley et al., 2003; Mann et al., 2009). The recovery from this cool decades is followed by a persistent state of stable atmospheric conditions, probably supported by an absence of relevant dynamical anomalies in the solar forcing.

5.4.4   Little Ice Age

In our analysis, the less robust intervals I5 and I6 correspond to two of the cold episodes of the LIA, coinciding with the Spörer (I5) and the Maunder minimum (I6) of solar activity.

During the Spörer minimum, cooling due to reduced solar activity was amplified by two large volcanic eruptions in 1452 and 1458 CE (Sigl et al., 2015). Camenisch et al. (2016) describe an increased seasonality during this time, which they argue cannot be explained by external forcing alone and is thus the result of internal variability.

The late Maunder minimum can be considered to be the climax and key period of the LIA. Luterbacher et al. (2016) also attribute it to a combination of solar and volcanic forcings and internal dynamics of the North Atlantic.

The confidence of the intervals I5 and I6 is lower than for the other times. Still, our results are in agreement with a similar analysis by Schleussner et al. (2015), who applied the HVG based test to two marine records. In addition, they coincide with periods of anomalous solar activity as seen in the Appendix Fig. D.9. Hence, they might be the result of a local response to external forcing, leading to a less consistent signal.

While strong volcanic eruptions have occurred frequently during the LIA, they are accompanied by HVG time-irreversibility only at those times at which solar activity is low and possibly anomalous itself.

5.5   Conclusions

In this chapter, we have extended and applied a recently proposed test of time-reversibility, based on horizontal visibility graphs (HVG), to a set of terrestrial paleoclimate records from across Northern Europe, spanning the last two millennia. A time series that is

HVG time-irrreversible cannot be described by a stationary, linear stochastic process. Therefore, these signals point to times at which non-stationary, possibly non-linear dynamics were recorded in the archives.

The onsets of both the MCA and the LIA are associated with dynamical anomalies, most likely triggered by possibly nonlinear atmospheric dynamics. The LIA has previously been studied by Schleussner et al. (2015) for two marine records. They find indications of HVG time-irreversibility and connect it with changing circulation following strong volcanic eruptions. In this regard, our results show a terrestrial manifestation of the previously discussed dynamical changes.

To understand the causes of such dynamical anomalies can, at this stage, only be the subject of speculations. Paleoclimate proxies are a complex filter of climate dynamics and, thus, an unambiguous attribution of specific causes to a given signal is difficult and requires further research. Model based experiments together with proxy forward models might lead to further insights into which mechanisms can lead to such signals, but they have been beyond the scope of this study. It is noticeable that the events I2, I4, I5 and I6 coincide with periods of combined low solar activity with strong explosive volcanism. Hence, we argue that the time-irreversibility does not result solely from internal dynamics but rather reflect complex recovery processes following strong external perturbations of the regional climate system. Regarding time interval I3, this interpretation is less applicable, as the MCA has been considered a period of exceptionally low perturbations (Bradley et al., 2016) and more robust internal variability (see Ch. 6). Furthermore, the onsets of both the LALIA and the LIA have been influenced by complex variations in solar variability, as the results in the Appendix Fig. D.9 show.

A common problem when analysing paleoclimate data is the low number of high-resolution records available for a region. Here, the method of (horizontal) visibility graphs can fill a gap, as it provides an assumption poor analysis tool. It can be applied to a broad range of time series, even those that cannot be approached with most other methods from nonlinear time series analysis, for example due to to irregularly sampled data or low numbers of observations.

Other than previous studies, we have applied the HVG based test to an ensemble of records, to overcome the high error rate of the method. In this way, we obtain results that are more consistent and reliable than when using single time series alone. This is demonstrated in Fig. 5.3, as there are one or two records with significant HVG time-irreversibility at most times. Some of these will clearly be false positives, either due to the high sensitivity or due to multiple testing effects. In this chapter we have shown, how a group-wise significance test can help to get consistent results for a larger region. As more high-quality records become available, the method of ensemble based HVG time-irreversibility testing can be expected to become a useful tool to study anomalous dynamics in a broader range of regions and proxies.

In summary, we have obtained reliable results using a multi-record test, which indicate that the regional climate system in Northern Europe can be regarded as a dynamical system that has been repeatedly driven out of equilibrium by a combination of reduced solar activity, explosive volcanism and internal feedbacks, followed by complex recovery dynamics which are visible as HVG time-irreversible periods.

6 | Using climate networks to reconstruct the multi-decadal North Atlantic Oscillation

Winter conditions in the North Atlantic region are largely determined by the regional leading mode of atmospheric circulation, the North Atlantic Oscillation (NAO), characterized by a pressure dipole between the Azores and Iceland. Through it's influence on heat and moisture transport, the NAO affects temperatures, precipitation and many other weather phenomena at surrounding land masses. As already suggested by the name, the dipole is not static, but changes in time between a strong gradient, called a positive phase (NAO+) and a weak gradient, the negative phase (NAO-). The state of the North Atlantic Oscillation can be quantified by a scalar, the NAO index, a value proportional to the strength of the gradient between the two centers of action.

The NAO varies on all time scales, and there is no clear preference for any frequency. While inter-seasonal to inter-decadal variations are often considered to be purely stochastic, variability on decadal and longer time scales need some kind of memory mechanism that the atmosphere itself cannot provide. This indicates an influence of external forcings or feedback mechanisms that could allow for some degree of predictability. In addition, understanding multi-decadal NAO variability is particularly important, as it is a major source of uncertainty in projections of climate change. As climate models indicate a tendency towards positive NAO phases with increasing concentrations of greenhouse gases in the atmosphere, it is imperative to understand the impacts and feedback mechanisms of multi-decadal NAO variability better than is done today.

As instrumental observations only go back for approximately 150 years (Vinther

et al., 2003), a meaningful discussion of multi-decadal variability is only possible with re-liable reconstructions from paleoclimate data. While there have been multiple attempts to reconstruct the NAO index (Trouet et al., 2009; Olsen et al., 2012; Ortega et al., 2015), there is a considerable degree of disagreement between these reconstructions, as can be seen in Fig. 6.2. The common approach in these publications is to find a reasonable set of paleoclimate records and then apply linear regression to an instrumental NAO index. This approach can be problematic as it assumes a stationary, linear relationship between the proxy variations and the NAO, which is likely not the case for most proxies (Schmutz et al., 2000; Zorita and González-Rouco, 2002; Lehner et al., 2012). For example, growth of tree rings is affected by very strong winter precipitation, related to a positive NAO phase in Fennoscandia, but largely unaffected by winters with less snow fall (Linderholm and Chen, 2005). Similar effects appear across many other regions and archives.

These issues serve as a motivation to develop a method to reconstruct the NAO index that does not suffer from this lack of non-stationarity, but instead uses it. The framework of evolving climate networks is a prime candidate for such a purpose, as they are explicitly designed to trace non-stationary changes in the covariance structure of multivariate data. Our main assumption is, that different types of archives in different geographic locations are affected by the NAO by different mechanisms for each phase. If regions that are normally unrelated show high similarity, this might hence point towards a shared influence of atmospheric conditions and thereby a specific NAO phase. The results discussed in this chapter have been published in the paper JF2.

Key Questions

- How can we use evolving climate networks to reconstruct climatological indices without relying on a stationary relationship between the index and the paleoclimate proxies?

- How did the NAO vary during the last two millennia and what were possible impacts of those variations?

The remainder of this chapter is structured as follows: At first, the NAO and its effects are discussed in detail in Sec. 6.1. The data used in this study is then introduced in Sec. 6.2. The way from multivariate proxy data to a scalar climate index is discussed step-by-step in Sec. 6.3. The corresponding results are then shown in Sec. 6.4 and discussed further in Sec. 6.5.

6.1 North Atlantic Oscillation

As mentioned in the introduction, the NAO is characterized by a dipole between a high-pressure region around the Azores and a low-pressure system around Iceland and can be quantified by a scalar NAO index[1].

---

[1] A comprehensive discussion of the NAO can by found in Hurrell et al. (2003). If not stated otherwise, information in this section stem from this publication.

(a) Patterns of the positive NAO phase.

(b) Patterns of the negative NAO phase.
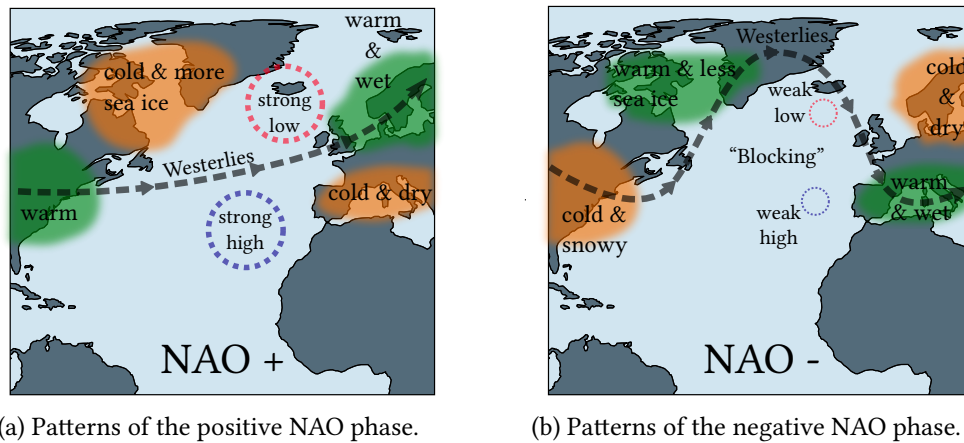
Figure 6.1: A schematic sketch of the two phases of the North Atlantic Oscillation. In the positive phase, there is a strong pressure gradient over the North Atlantic, leading the Westerlies towards Fennoscandia. When the pressure gradient is low, the Westerlies are blocked over the Atlantic, leading to heavy meandering and reverse effects.

The gradient determines the strength and the path of the strong prevailing westerly winds—the *Westerlies*—which leads to changes in heat and moisture transport to the surrounding land masses. This influence is largest in winter and, thus, the NAO is normally considered a winter phenomenon, even though it is also visible at other times of the year (Folland et al., 2009). The general pattern of climate variability associated with the NAO phases is shown in Fig. 6.1. During a positive NAO phase, the Westerlies are generally stronger and follow a straight, zonal path over the Atlantic with a northward tilt. In this way they bring warm, moist air into Fennoscandia while allowing cold, Arctic air to flow into the areas around the Labrador sea. The Mediterranean region does not receive much moisture and, therefore, winters there are cold and dry. A different pattern is characteristic for a negative NAO phase, with warm and wet winters around the Labrador Sea and the Mediterranean. Fennoscandia is blocked from these air masses and, thus, Arctic air flows southward, leading to cold conditions and low precipitation.

Multi-decadal variability of the NAO is seen as a large factor in determining Northern Hemisphere temperatures (NHT), in particular over the continents (Li et al., 2013; Delworth et al., 2016; Iles and Hegerl, 2017). The effect of the NAO on large scale temperatures is thought to be mediated via induced changes in the Atlantic circulation, via the Atlantic multi-decadal variability (AMV, Delworth et al., 2016) and the Atlantic Meridional Overturning Circulation (AMOC Delworth and Zeng, 2016). In addition, is also related to ocean-atmosphere-sea-ice feedbacks and the slow time scale of the ocean leads to a 15-20 year lag of temperatures to the NAO. The NAO has been made responsible for up to 45% of the winter warming of the second half of the 20th century in the continental Northern Hemisphere (Wallace et al., 2012; Iles and Hegerl, 2017). This impact is expected to continue with a projected tendency towards positive NAO phases in the future.

Besides direct impacts of the NAO on weather and climate, it is also a determining factor for other environmental processes, like heat waves (Wang et al., 2011), droughts (López-Moreno and Vicente-Serrano, 2008; Cook et al., 2016), tracks and strength of

storms (Rogers, 1997), lightning (Piper and Kunz, 2017) or growth of glaciers (Bjørk et al., 2018). In addition, it has profound impacts on ecology by determining the growth and development of both single animals (Yom-Tov et al., 2017) as well as whole populations (Hurrell et al., 2003). Furthermore, it leads to a large scale synchronization of populations of plants and animals alike via the *Moran effect* (Post and Forchhammer, 2002; Ascoli et al., 2017).

Even besides extreme events, human lives are also directly affected by the NAO via climate impacts on agriculture, for example, wheat production (Kettlewell et al., 1999) or viticulture (Esteves and Manso Orgaz, 2001; Grifoni et al., 2006), energy markets (Hurrell et al., 2003) or direct impacts on human heath (McGregor, 2005; Almendra et al., 2017).

The NAO shows variability on all time scales, without any preferred scale (with a slight tendency towards a red spectrum). On short time scales, it is commonly regarded as resulting mainly from internal dynamics of the atmosphere[2]. There is a very low rate of persistence at time scales from weeks to seasons, where it behaves largely stochastic and, hence, unpredictable.

In contrast, the pronounced variability on decadal time scales might point towards external forcings or slow feedback mechanisms that might be pathways to at least some predictability. Candidates of driving mechanisms are ocean circulation (Rodwell et al., 1999), volcanic eruptions, solar activity, or greenhouse gas concentrations (Gillett et al., 2003), Woollings et al. (2015) argue that multi-decadal NAO is physically different from short time scale NAO in that it is not only related to a shift in the jet and storm track, but also in strength of the Westerlies, hence, the dynamical mechanisms differ at both scales. Still, the exact nature of multi-decadal NAO variability is debated and no consensus has been reached.

As mentioned in the introduction, there have been several attempts to reconstruct the NAO from proxy data. Some of them are based on single records (Olsen et al., 2012; Faust et al., 2016), others on ensembles (Trouet et al., 2009; Ortega et al., 2015; Deininger et al., 2016), but all are rely on linear regression of the proxy variable on some time series of NAO variability. There is a considerable disagreement among these reconstructions, in particular for the first millennium CE, as can be seen in Fig. 6.2. Reasons for this mismatch could be the aforementioned non-stationary relationship between proxy variables and the NAO, but also different instrumental time series as target variables. This missing consensus about variability of the NAO has, so far, limited a conclusion about mechanisms and impacts of multi-decadal NAO.

6.2 Data used in this study

The North Atlantic region is one of the most extensively studied regions in the world and thus offers a broad variety of high-resolution paleoclimate records, in particular for the late Holocene. These include long-ranging tree ring chronologies from the Scandinavian mountains, the Alps and other mountain ranges, varved lake sediments,

---

[2]In models, it can be reproduced without changes in ocean circulation, sea surface temperature, sea ice, land cover or other external forcings.
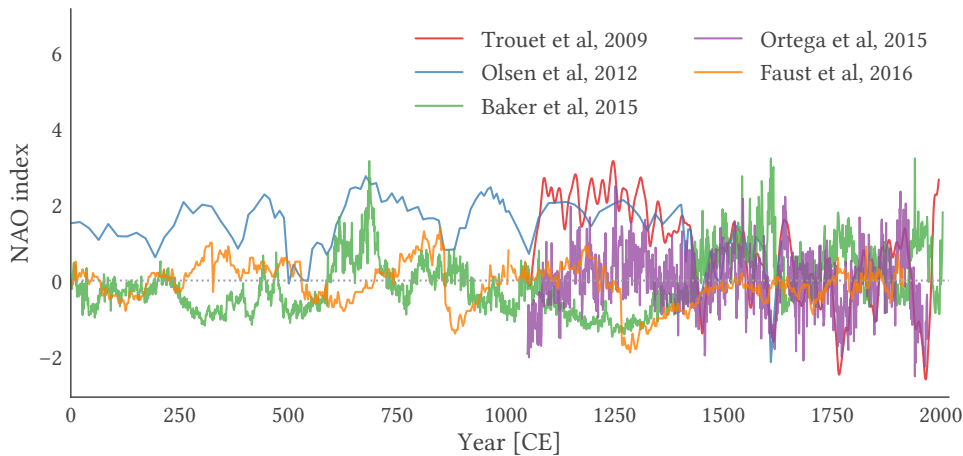
Figure 6.2: Previous paleoclimate reconstructions of the NAO by Baker et al. (2015), Faust et al. (2016), Olsen et al. (2012), Ortega et al. (2015), and Trouet et al. (2009).

and ice core records from the Greenland ice shelf and Svalbard. In addition to natural archives, there are also long historical temperature records from early instrumental measurements.

We limit ourselves to one climate variable, atmospheric temperature, as most archives in the region are considered to be temperature dependent. The number of records that cover a certain time period decreases as one goes back further in time, but there are a few high-quality records that span the whole Common Era. We furthermore only consider records that span more than 300 years with close to annual resolution so that they retain all time scales of interest.

Based on these requirements, we end up with an ensemble of 37 records from different archives, which are shown in Fig. 6.3. Detailed information about the individual records are given in the Appendix Tab. E.1. Out of these 37 records, 12 cover the full Common Era. Most of the time series are strongly correlated to seasonal or annual temperature variability and some have been used in regional (PAGES 2k Consortium, 2013; Luterbacher et al., 2016; Werner et al., 2018) and hemispheric (Mann et al., 2008; Ljungqvist et al., 2012) temperature reconstructions.

There are different ways the NAO can influence these archives. Ice core records from Greenland for example are dominated by winter conditions (Appenzeller et al., 1998; Vinther et al., 2010) and are thus directly related to the NAO. In contrast, tree ring records are mainly related to summer temperatures, but extreme winter precipitation can also affect the tree growth (Vaganov et al., 1999; Lindholm et al., 2001; Linderholm and Chen, 2005). Varves in lake sediments are directly related to winter precipitation and duration as well as runoff strength, all of which are partly controlled by the NAO.

It should be noted, that we did not include several records that have been used in previous reconstructions of the NAO, as they did not meet our selection criteria (e.g. Deininger et al., 2016). In particular, they were neither temperature sensitive nor did they have a sampling resolution high enough. All records included in this study are from well dated archives (tree rings, varved lakes, ice cores and historical documents)
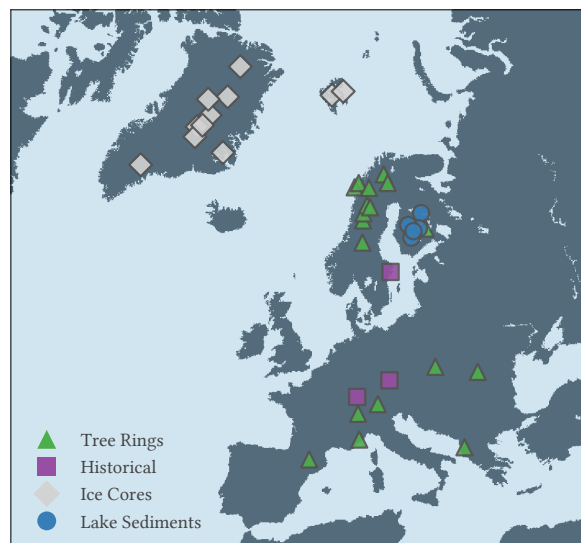
Figure 6.3: Geographical locations and types of the paleoclimate records used in this study. Different markers indicate different paleoclimate archives, as indicated by the legend. Detailed information on the individual data sets can be found in the Appendix Tab. E.1.

and, thus, age uncertainty can be largely neglected. Unfortunately, there is no detailed information about proxy and measurement uncertainty available for most records. Hence, we cannot address these sources of uncertainty explicitly in our analysis.

6.3   How to reconstruct the NAO from networks

The method of evolving climate networks has been introduced in Sec. 2.4. In this chapter, we want to relate inter-regional co-variability to the phases of the NAO. To achieve this, we expand the original idea of climate networks in a number of steps, also illustrated in Fig. 6.4:

1. We collect data, that we consider to be related to the NAO, at least temporarily. For consistency reasons, we limit ourselves to one variable, atmospheric temperature. The data selection and the time series considered have been discussed in Sec. 6.2.

2. Using this set of time series, we construct evolving climate networks.

3. As a way to deal with proxy uncertainty and a varying number of records, we introduce groupings of records and calculate connectivities between groups. This reduces the complexity of the obtained information and makes the analysis more robust.

4. The connections between different groups of records are linearly related to the climate index via regression analysis.
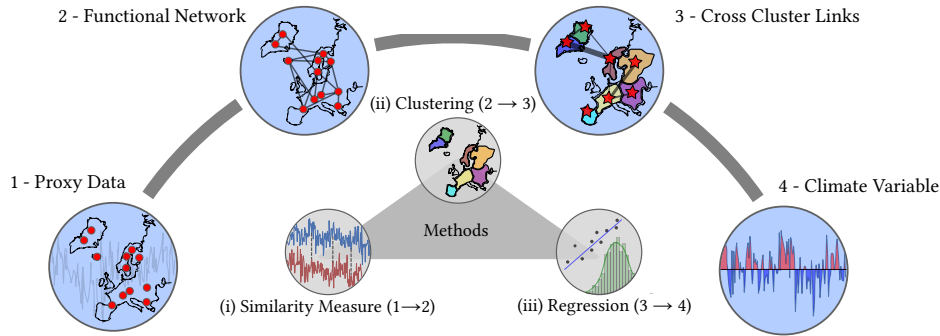
Figure 6.4: Schematic overview of the method introduced in this chapter. First, evolving climate network are constructed from paleoclimate proxy records, in order to encode the co-variability among the different time series. By grouping records together in clusters we simplify these network structures and obtain quantitative measures of inter-cluster linkages as key characteristics of the networks. These values are then related to an established long-term reconstruction of the NAO index via linear regression.

6.3.1 Climate network construction

In general, we follow the procedure discussed in Sec. 2.4, using the notation introduced in Sec. 2.1. We will hence, only shortly recapitulate the construction of evolving climate networks. The aim is to obtain a time ordered sequence of climate networks, each being assigned to a specific time window $\mathcal{W}$. Each time coordinate corresponds to the end point of the corresponding time window. It should be noted, that the window width determines the temporal resolution of our analysis. Short time windows would increase resolution but would in turn also raise uncertainty. Here, we decide for a window size of 50 years (=50 data points per time window), which is short enough for a meaningful analysis, but long enough to enable robust correlation estimation.

In principle, a climate network can be based upon any similarity measurement. Here, we decide for the simplest, the linear Pearson correlation measure. As some of the records have data gaps, we use a Gaussian kernel based variant, as discussed in Ch. 3 and the Appendix C.1.

Each archive is recording its environmental conditions in a specific way and, hence, time series originating from the same archive are expected to share certain characteristics. An example of this would be the large spikes in lake sediment records, coming from exceptional flooding events, or the absence of long-term variability in tree ring records due to calibration procedures. These archive specific variations have to be taken into account when comparing records from different archives in a shared framework. This is in particular related to the issue of (shared) persistence in records, leading to inflated correlation estimates (Guez et al., 2014). There are different ways to tackle this problem, be it high-pass filtering, pre-whitening or surrogate testing. Here, we pick the latter method, using amplitude adjusted Fourier transform (AAFT) surrogates (Schreiber

and Schmitz, 2000). The AAFT method provides permuted copies of the original time series that keep the spectrum (and, thereby, the auto-correlation structure) intact. For each pair of records, we draw 1000 of these alternative versions of the records and calculate the same correlation measure[3]. In this way, we calculate the probability that the correlation value was obtained by chance alone, given the specific autocorrelation structure of each record. This probability is the pair wise *p*-value and a correlation is considered significant if this *p*-value is lower than a threshold value α_{pr}.

The network is then constructed by nodes corresponding to the different paleoclimate proxies and links are drawn between each pair, if the *p*-value of the corresponding correlation is below α_{pr}.

6.3.2 Network analysis

Networks made out of paleoclimate proxy time series involve some specific problems, that make a straight-forward analysis difficult. First, the number of records varies between different time windows, as not all archives cover the same time period. This makes comparing networks from different times difficult. Second, while a set of archives might be related to the same climate variable, they are also subject to local and proxy specific effects. This means that the pair-wise similarity assessment can fluctuate, independently from the real shared signal.

Furthermore, the number of nodes in a paleoclimate network is often considerable lower than in most other applications of networks. In a way, paleoclimate networks sit between very simple and sufficiently complex networks. While there are too many possible connections to allow for a intuitive climatic interpretation by eye, there are often not enough nodes to apply more sophisticated methods from complex network theory, in particular higher-order measures (network transitivity, betweenness centrality, community detection) that are very useful in large, complex networks (Donner et al., 2017).

As we cannot increase the number of nodes, and with it the complexity of the network, at will, we move towards the other extreme in reducing the number of nodes even further. We do so by combining records into clusters and consider the overall connectivity between clusters. In this way, we obtain smaller networks, which are more robust in time.

A *cluster* is a subset of records $C^K \subset \left\{\mathbf{X}^i\right\}_{i \in \{1,\dots,M\}}$ with $M \subset \{1, 2, \dots N^r\}$. The number of members of each clusters, its cardinality, is denoted as $|C^K|$ and we discard all clusters with only one member. As the different records cover different times the number of members can vary and we denote the cluster of a specific time window as $C^K_{t\mathcal{W}}$.

How we assign a record to a specific cluster is discussed in the next section. Note that the assignment of a record to a cluster is kept fixed. Hence, the existence and size of a given cluster depends only on the (non-)availability of data from the pre-defined proxies during the time window in question.

---

[3]Note that among the considered set of archives, all but four records are annually resolved. As the AAFT method demands regular sampling, we apply linear interpolation to these few records before drawing surrogates.

Given a grouping of records into clusters, we define the *cross-link* density (CLD) between any two clusters $C_{t\mathscr{W}}^{K}$ and $C_{t\mathscr{W}}^{L}$ as

$$CLD_{t\mathscr{W}}^{K,L} \quad := \frac{\text{\# links between } C_{t\mathscr{W}}^{K} \text{ and } C_{t\mathscr{W}}^{L}}{\text{\# possible links between } C_{t\mathscr{W}}^{K} \text{ and } C_{t\mathscr{W}}^{L}}$$

$$= \frac{\sum_{i \in K} \sum_{j \in L} A_{t\mathscr{W}}^{i,j}}{|C_{t\mathscr{W}}^{K}| \cdot |C_{t\mathscr{W}}^{L}|}. \tag{6.1}$$

As we consider evolving networks, the CLDs varies in time. Still, they are expected to be more robust measures of the covariance structure than single links between records, since they combine information from various links and are normalized by the (time-dependent) number of records. If paleoclimate archives were perfect recorders of climate variability, these inter-regional links would be representations of larger teleconnection patterns. For real world proxy data however, the attribution of a specific physical process to a network structure is far less clear, but a link between regions should still indicate some shared variability.

If S_C denotes the number of clusters with at least two members, we can define a $S = \binom{S_C}{2}$ dimensional vector of cross-link densities

$$\chi_{t\mathscr{W}} = \left\{ CLD_{t\mathscr{W}}^{K,L} \middle| K, L \in \{1, \dots S_C\}, K \neq L \right\}.$$

This vector describes a network with fewer nodes and weighted links (the CLD values). Any information of intra-cluster connectivity is discarded, as we consider each cluster to be homogeneous and all differences resulting largely from local and archive effects. If one was to combine the cross cluster connections with intra-cluster links, one could follow a "network of networks" approach, which has been employed in a few studies on recent climate variability (Donges et al., 2011b; Wiedermann et al., 2016a). In the present study it would make the analysis much more difficult and be dominated by statistical noise.

6.3.3 Spacial clustering of records

When grouping the records into clusters, we aim to (i) combine spatially close data and (ii) obtain clusters that are large enough to reduce the impact of individual records to ensure a robust representation of large-scale spatial co-variability.

As the different archives and records have very distinctive, partly non-stationary characteristics, it is difficult to perform any cluster analysis directly to the set of observations, as this leads to highly fragmented clusters, violating both criteria. Instead, we define clusters by regions that share inter-annual temperature variability over the modern (instrumental) period. For this purpose, we use the gridded ERA-20C reanalysis summer temperature data that covers the whole 20th century (Poli et al., 2016). This data set is used to generate a single climate network, based on absolute Pearson correlations of boreal summer (JJA) temperatures for each grid point over land in the study region. Links are drawn only for the strongest correlations, which are those above a threshold value α_C[4]. From this network representation of the ERA-20C data set, we identify

---

[4]Due to the high number of nodes, we do not use the surrogate testing here, but apply the threshold to the correlations directly, as is commonly done for high-dimensional data.

regions of high coherence by applying the Louvain community detection algorithm[5]. The paleoclimate records are then assigned to different clusters, depending on their locations.

It should be pointed out, that this procedure introduces an additional parameter α_C. In general, small values of α_C result in a high number of small clusters, while larger values lead to a few larger ones (not shown). The main differences between the groupings based on different values of α_C from a reasonable range of values (those that result in $\mathcal{O}(10)$ clusters) are the division of Greenland and the location of the border between Central and Eastern Europe. This is also the main difference in using different climate variables for the clustering, e.g. different seasonal averages. This can be seen in the Appendix Fig. E.4.

6.3.4   Statistical modeling by linear regression

While the networks with a reduced number of nodes can generally be analysed by eye, we want to obtain a more quantitative link to the NAO index $\text{NAO}_{\text{Ortega}}$, in particular to the moving average, using the same window length $\mathcal{W}$, denoted as $\overline{NAO}_{\text{Ortega},\mathcal{W}}$. The simplest model to describe such a relationship between a vector of values $\chi_{t\mathcal{W}}$ and some variable Y is the linear model

$$Y_{t\mathcal{W}} = \mathbf{D}_{t\mathcal{W}} \chi_{t\mathcal{W}} + \epsilon_{t\mathcal{W}} \tag{6.2}$$

with a coefficient vector $\mathbf{D}$ and a zero-mean noise process $\epsilon_{t\mathcal{W}}$. The model implies that the degree of similarity among regions is linearly proportional to the amplitude and sign of the NAO. This formulation is mainly motivated by its simplicity and computational reasons, even though a more physical model would treat the CLDs as variables of the NAO and not vice versa. Furthermore, it might make sense to include additional variables into the model. For a detailed discussion of regular vs. inverse linear regression models and their implications for paleoclimate reconstructions, we refer to Christiansen (2014) and Christiansen and Ljungqvist (2017) and references therein.

Our analysis has two free parameters, the threshold values α_{pr} of the paleoclimate networks and α_C of the reanalysis network used for spatial clustering. We aim to find those values that maximize the information about the NAO into the cross-cluster links. Hence, we vary the values of both α_{pr} and α_C over a broad range, resulting in different paleoclimate networks and spatial clusterings. We perform a multiple linear ordinary least-square (OLS) regression of model Eq. 6.2 between the CLDs and $\overline{NAO}_{\text{Ortega},\mathcal{W}}$ for each pair of values individually. Performance of the model with a given pair of parameters is tested by calculating the percentage of variability in $\overline{NAO}_{\text{Ortega},\mathcal{W}}$ described by the regression model, the r^2 value. The parameter combination that describes most variability is used for all further analysis. The full range of values is shown in Fig. E.3. In general, the results are robust for different window sizes.

For the final regression, we switch from simple OLS regression to a Bayesian approach, based on Markov Chain Monte Carlo (MCMC) regression (see the Appendix Sec. A.4). Unlike OLS regression, this approach does not only provide single point estimates, but joint probability distributions for the full set of model parameters. Thereby,

---

[5]See a short discussion in the Appendix Sec. A.3.

question	decision	comment	reference
Which records to use?	37 records	high resolution records, related to (summer) temperature	see the Appendix Tab. E.1
How to assess similarity?	gXRF	linear correlation	Rehfeld and Kurths, 2014
How to group?	ERA-20c (JJA)	high resolution reanalysis of 20$^{\text{th}}$ century	Poli et al., 2016
How to find relationship to NAO?	linear model	regression by MCMC method	Eq. (6.2)

Table 6.1: Overview of the methodological decisions taken for this study.

one can study the intrinsic uncertainty resulting from the model and the limited number of observations. Since not all clusters cover the full two millennia, we can use the full set of clusters over the calibration period as a prior distribution for reduced sets of CLD values to be used for previous times. In this way we utilize the knowledge of the full data set for times of lower data availability. For the MCMC regression, we rely on a NUTS sampler (Hoffman and Gelman, 2014) with 10^4 samples, one quarter of which are discarded as burn-in.

6.4 Spatial networks and the corresponding reconstruction of the NAO phase

The procedure discussed in the last section has been applied to the data introduced in Sec. 6.2, using time windows of 50 years length and a mutual overlap of 1 year between successive windows. The threshold values have been determined as described in the Sec. 6.3.3, yielding α_{pr} = 0.46 and α_C = 0.0104. The resulting spatial clusters and the assignment of records to clusters are shown in Fig. 6.5. All methodological choices used in this chapter are summarized in Tab. 6.1.

Fig. 6.6 shows the simplified networks and the dominating cross-cluster links for some exemplary time windows. For illustrative purposes, we have used a lower threshold value of α_{pr} = 0.1 to focus on the strongest correlations. During the first millennium CE, two different states can be distinguished, one at which Fennoscandia (FS) is connected to the other two clusters (Fig. 6.6a,c) and another one with strong links between Southern Greenland (SG) and Central Europe (CEu) (Fig. 6.6b,d). The second millennium CE offers considerably more records, which allow us to clearly see periods of dominant West-East connections (between Greenland, Svalbard and Fennoscandia, Fig. 6.6f, i) change with times at which North-South connections involving Central Europe are more prominent (Fig. 6.6e,g,h). The latter is commonly the case when $\overline{NAO}_{\text{Ortega},\mathscr{W}}$ indicates a negative mean NAO index, while the North Atlantic sector is more interconnected during positive NAO phases.

As this way to analyse networks is highly subjectivity and ambiguous, we apply the linear model (Eq. 6.2) discussed in Sec. 6.3.4. The most relevant regression coefficients
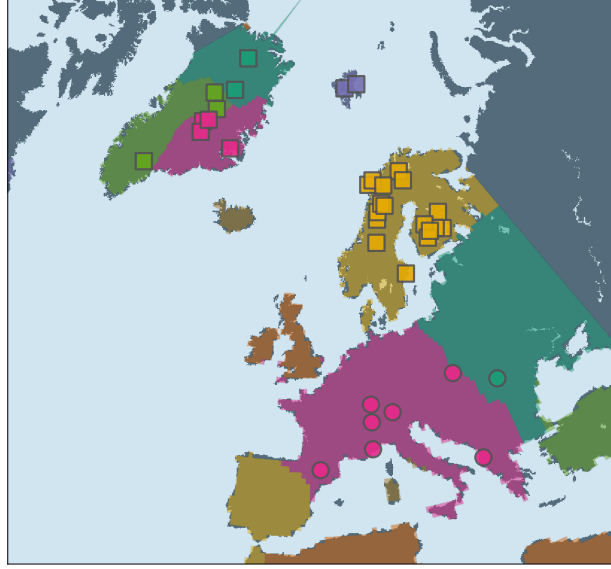
Figure 6.5: Division of the study area as obtained by cluster analysis of the ERA-20C summer mean temperatures, together with the paleoclimate archives used in this study ($\alpha_C \approx 0.01$). Non-adjacent regions of the same colour represent different clusters, as are indicated by different symbols (squares vs. circles) showing the spatial locations of the considered archives. All coloured areas are used for the clustering analysis.

are summarized in the Appendix Tab. E.2 and their strengths and signs are illustrated in Fig. 6.7. Here, thick, red lines indicate that positive (negative) NAO phase is associated with relatively many (few) inter-regional links. Blue lines indicate the opposite. The most informative clusters are those with the highest regression coefficients and are located in Southern Greenland (SG), Fennoscandia (FS) and Central Europe (CEU), all of which cover the full Common Era. The time-evolution of the six CLDs associated with the largest regression coefficients are shown in the Appendix Fig. E.5. The resulting mean regression coefficients of the model support the general patterns discussed before. West-East connections are linked to positive NAO phases, while North-South connections involving Central Europe dominate during negative NAO phases.

To see how well the estimated linear model can explain NAO variability, we split the $\overline{NAO}_{\mathrm{Ortega},\mathscr{W}}$ time series into two parts of equal size. We use one part as a training period and the other half for validation. The resulting r^2 values are very low (0.15 when using the first half and 0.28 when using the second half as training period) meaning that much of the shorter time-scale variability cannot be described by our model. Nevertheless, the sign of the NAO phase is identified correctly in 68% and 71% of the considered time windows respectively. In the following, we refer to this quantity as the true sign ratio (TSR). Notably, using the second, more recent half as a training period results in higher values of both r^2 and TSR. This suggests that using additional records, even if they do not cover times outside of the calibration period, can still lead to better predictions as they make existing links more meaningful.

(a) 150 to 200 CE

(b) 350 to 400 CE

(c) 650 to 700 CE

(d) 710 to 760 CE

(e) 1100 to 1150 CE

(f) 1200 to 1250 CE

(g) 1400 to 1450 CE

(h) 1620 to 1670 CE

(i) 1896 to 1946 CE

Figure 6.6: Simplified functional paleoclimate networks for different exemplary time windows illustrating the great variety of spatial connectivity patterns during the covered time interval. The red circles indicate the center of each group of records (only shown any record in a cluster covers the specific time window). The thickness of each link is proportional to the CLD of that connection. The time intervals have been chosen such that they demonstrate the general patterns of zonal and meridional connectivity.
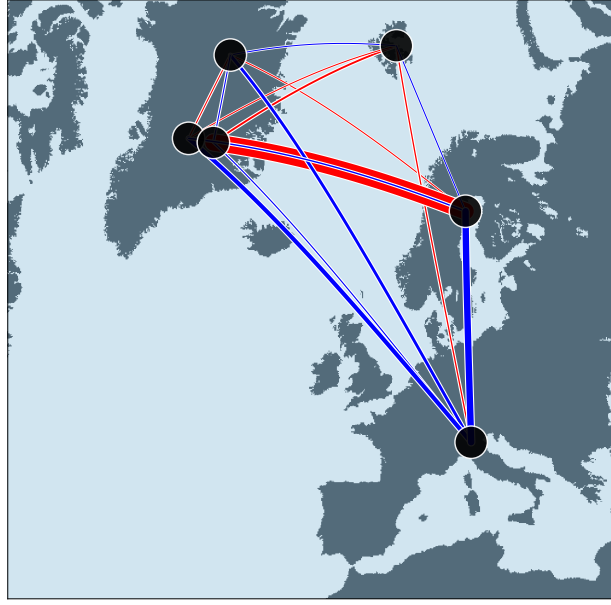
Figure 6.7: The 15 cross-link densities (CLD) between different regions, weighted by their corresponding regression coefficients. Black circles mark the centers of each group of records. Red (blue) colours indicates a positive (negative) coefficient and, therefore, that a correlation is associated with a positive (negative) phase of the NAO. The width of the drawn links is proportional to the mean coefficient value as given in Appendix Tab. E.2. Note that these linkages represent statistical relations and do *not* necessarily relate to (temperature) teleconnections between different regions, as they may also reflect other shared influences on the archives.

While the observed TSR is significantly better than a random guess (TSR~ 50%), it is still relatively low, compared to what would commonly be required for a predictive model. To better understand the 30% of time windows at which the sign is not determined correctly, we take shorter, 50 year long, time slots as validation periods and the remainder for calibration. The results of this piece-wise validation is shown in the Appendix Fig. E.8. There, we can see that at time windows where the TSR is below the mean value of 0.7 the original time series $\overline{NAO}_{\mathrm{Ortega},\mathscr{W}}$ is either close to zero or exhibits an abrupt transition between the two phases. At some times, in particular the 17$^{\mathrm{th}}$ century, our model description differs considerably from $\overline{NAO}_{\mathrm{Ortega},\mathscr{W}}$. For the values close to zero there is no clear preference in sign and our model predicts both negative and positive phases. At most of these times, our reconstruction is also close to zero with large parts of the posterior distribution of the NAO being at both signs. In case of rapid transitions it should be noted that the same transitions are still seen in our reconstruction, but with a time lag, leading to a disagreement in sign. Hence, the exact timing of transitions comes with a large degree of uncertainty, which should be kept in mind when interpreting the results.

As four of the geographical clusters of paleoclimate records cover the full Common Era, the model allows us to expand the 50 year-averaged reconstruction $\overline{NAO}_{\mathrm{Ortega},\mathscr{W}}$ to
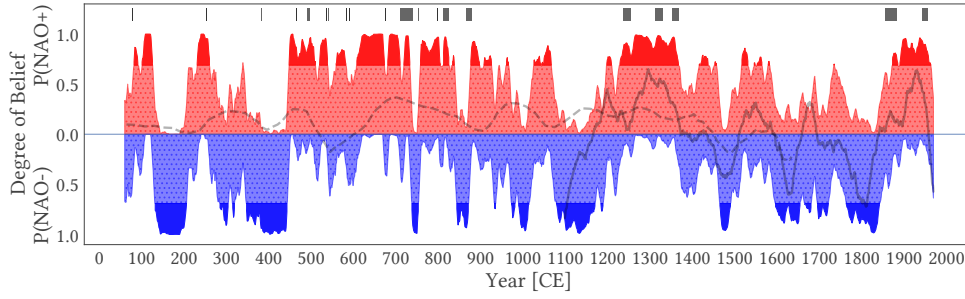
Figure 6.8: Degree of belief (probability) that the NAO is in a specific (positive vs. negative) phase during each 50-year time window. The figure has been smoothed by a 10-year moving-average filter to enhance its readability. Times for which more than 66% of the MCMC sample members agree upon the sign of the NAO are indicated by dark colouring, all values below are shaded. Gray bars correspond to known major drought episodes in the Western Mediterranean as discussed in Sec. 6.5.2. For comparison, the NAO reconstruction by Ortega et al. (2015) is shown as a black line, indicating a general agreement with our probabilistic reconstruction over the common period, as expected. In addition, the long lasting reconstruction by Olsen et al. (2012) is shown as a dashed line.

the first millennium CE. To do so, we draw 10,000 realizations of the regression model posterior distributions based on the available CLDs and calculate the corresponding NAO indices. The probability of each NAO phase is then determined by the percentage of members in the posterior distribution that are above and below zero. This value is subject to several proxy and model uncertainties and is called the *degree of belief* that a specific NAO phase was present. To prevent a misrepresentation of times with low NAO variability as positive or negative phases, we only consider those times at which more than 66% of the posterior are of one sign. In this way, we account for the ambiguity of low NAO amplitudes, while correctly identifying strong NAO phases. The results of this probabilistic reconstruction are shown in Fig. 6.8.

During the Common Era, there have been both periods of persistent positive (e.g. during the migration period and the late medieval times) and negative (e.g. during the Little Ice Age) NAO phases. In addition, there are times of high variability (e.g. the late Roman period or the centuries around 1000 CE) which might point towards more unstable conditions.

As there have been multiple choices of parameters in this analysis, we need to test the results for robustness. Fig. E.7 shows the reconstructed NAO phases based on different values of α_C (similar variations of α_{pr} did not alter the results much and are not shown here). Besides a few exceptions, most of these alternative reconstructions are very close to the one using the predetermined optimal parameter value. A particular remarkable difference is seen in the second half of the 5th century, where an abrupt transition from a negative to a positive NAO phase is exhibited. In some cases, the exact timing of this transition differs. This observation underlines the uncertainty of our model in the timing of transitions, which has to be accounted for by varying the

model parameters.

6.5   Critical assessment of the results, further evidence and implications on human societies

The discussion of the results presented in the previous section focuses on two aspects, first the spatial patterns of co-variability associated with specific NA0 phases and second the probabilistic reconstruction of the NAO based on the linear model (Eq. 6.2).

The preferred presence or absence of CLDs during certain NAO phases agrees well with the known impact the NAO has on European climate variability during the instrumental period. A positive NAO phase is related to a northward shift of the westerlies, causing mild, but wet winters in Northern Europe. During a negative NAO phase, a similar pattern is seen in Central Europe and the Western Mediterranean region. As tree ring records have been shown to be strongly influenced by intensive winter precipitation, we expect records in Fennoscandia to be particularly affected by positive NAO phases and those in Central Europe by negative ones. The non-stationary relationship between records and the NAO is illustrated in Fig. E.2. While some ice core records (which were instrumental in the reconstruction by Ortega et al., 2015) show a persistent negative correlation to NAO_{Ortega} , there is much more variability for the other records. The most important feature here is the absence of a linear relationship at most times. The records are co-varying with the NAO only at certain times, but are unaffected for others. This exemplifies the need for a reconstruction method that does not rely on a stationary, linear link between proxy variables and the NAO.

A reference time series with a stationary relationship with the "true" NAO, as the aforementioned Greenland ice cores, can then act as a filter for the remaining time series. If the variability of any other record shows a strong similarity to these reference time series, we can expect the record to carry significant information about the NAO. As the influence of the NAO is differs between regions, this is the case at different times, therefore, leading to variable patterns of co-variability. Besides these reference records, other regions play an important role as well. If two regions have been shown to be influenced similarly by the NAO, a co-variability among them does provide valuable information about the NAO phase.

The median value of the regression model based NAO index correlates well with $\overline{NAO}_{Ortega,\mathcal{W}}$ (r^2 = 0.58). However, this value could simply result from overfitting, as indicated by the low r^2 values in the cross-validation. Thus, we do not rely on these quantitative values of the NAO index, but solely on the qualitative description of the most likely dominant NAO phase of the specific time periods.

Besides the NAO, there are a number of other factors that determine multi-decadal temperature variability on a regional level. These include other modes of internal variability, like the Atlantic multi-decadal variability, changes in solar activity or explosive volcanism (Crowley, 2000; Schurer et al., 2014; Bothe et al., 2015). Hence, the observation of high temperatures during the Roman and Medieval times and lower ones during the Late Antique (PAGES 2k Consortium, 2013; Luterbacher et al., 2016) do not contradict the reconstruction of NAO phases, which would be related to different effects on temperatures. Instead, there might actually be common causes for such apparently contradictory observations. Volcanic eruptions, for example, have been discussed to

cause cold periods like the Late Antique Little Ice Age (Büntgen et al., 2016), but at the same time, they are known to trigger positive phase NAO conditions for the years following strong eruptions (Robock, 2000). Even though this is a very short-lasting effect, a higher number of strong eruptions clustered together, as present during the Late Antique (Sigl et al., 2015), might lead to a more persistent impact.

We have to emphasize a number of limitations of the framework presented in this chapter. First, as a consequence of the decreasing number of records back in time, most of the CLDs show a downward trend and decreasing variance over the Common Era, as seen in the Appendix Fig. E.5. This non-stationarity of the CLDs might be a considerable bias to any application going beyond the Common Era or to regions which are less well covered with data. In our study, it might favour positive NAO phases, since the largest regression coefficient (between South-Eastern Greenland and Fennoscandia) is related to such a CLD. Furthermore, our results are an extension of a previous reconstruction, based on paleoclimate proxies itself and is thus object to all related uncertainties. A reconstruction can only be as reliable as the "reference truth" that it is calibrated to, which is of questionable quality in our case. In addition, the cross-validation showed that the linear model disagrees considerably with $\overline{NAO}_{\text{Ortega},\mathscr{W}}$, mainly at times of low variability or abrupt transitions. We have tried to address this model uncertainty by using a MCMC regression, leading to a more probabilistic result. Hence, when $\overline{NAO}_{\text{Ortega},\mathscr{W}}$ is close to zero, no particular phase is preferred in general, as can be seen in Fig. 6.8.

As there are considerable uncertainties in our probabilistic reconstruction we need to put our results into a broader context with previously published reconstructions of the NAO as well as with additional lines of evidence.

6.5.1 Comparison with other NAO reconstructions

The linear model is able to reproduce most larger features of the reconstruction by Ortega et al. (2015), in particular a dominant positive phase during the MCA, a tendency towards negative values but higher variability during the LIA and more positive values during the 20$^{\text{th}}$ century, also in accordance with instrumental records (Vinther et al., 2003).

Trouet et al. (2009) have argued, that the whole MCA was characterized by a positive NAO phase, leading to mild and stable conditions in Central Europe. While we do find stronger trans-Atlantic connectivity during the late medieval times, this is not the case for the early MCA, which is more variable.

Olsen et al. (2012) have related a more than 5000 years long lake sediment record from Southern Greenland to the NAO. For the overlapping time, our reconstruction does not correlate with this record ($r^2 = 0.04$), even though it seems that some long term variability is shared (see Fig. 6.8). This disagreement is probably a result of the large time uncertainty in both reconstructions, as Olsen et al. (2012) report dating uncertainty of multiple decades during the first millennium CE. In addition, their record has been calibrated to the reconstruction published by Trouet et al. (2009), which disagrees with the one by Ortega et al. (2015) at many times.

A recent study by Deininger et al. (2016) uses 11 European speleothem records and relate their mutually coherent dynamics to long-term North Atlantic circulation regimes. Similar to Trouet et al. (2009), they report a persistent positive NAO during the entire

MCA and a tendency towards negative NAO phases during the LIA, the first being in partial disagreement, the second in accordance with NAO$_{\text{Ortega}}$ and our reconstruction. They also show a dominant negative NAO between 250 and 500 CE and a neutral-to-positive NAO thereafter. This agrees well with our probabilistic reconstruction.

6.5.2 Historical Droughts and the NAO

As mentioned in Sec. 6.1, drought conditions are one of the many climate phenomena that are linked to the NAO through the corresponding precipitation anomalies and its effects on soil moisture and river discharge (López-Moreno and Vicente-Serrano, 2008; Cook et al., 2016).

Due to their severe impact on agricultural productivity and, hence, societies as a whole, droughts belong to the best documented weather extremes in historical times. Hence, existing reports of historical droughts can be used as an independent test of any NAO reconstruction. While the relationship between the NAO and droughts is rather ambiguous at many regions, it is well pronounced in the western Mediterranean. Fortunately, this region was home to several book-keeping societies and, therefore, we can rely on multiple sources. McCormick et al. (2012b) collected climatic evidence from the period of the Roman Empire up to 800 CE. He reports 8 large droughts for the Western Empire (accessible through McCormick et al., 2012a). Domínguez-Castro et al. (2014) summarized historical records from Muslim Al-Andalus in present day southern Spain, a region exceptionally vulnerable to NAO related droughts (Cook et al., 1998). These reports cover the time between 711 and 1010 CE and three major drought events are discussed therein. The last millennium is discussed in detail by Cook et al. (2016), based on the Old World Drought Atlas (OWDA Cook et al., 2015). The drought index reconstructed for the Western Mediterranean correlates well with $\overline{NAO}_{\text{Ortega},\mathscr{W}}$. Hence, we only include the five strongest drought events, shown in Fig. 5 of their publication.

The major drought periods discussed in the aforementioned publications are shown as gray bars in Fig. 6.8. There is a clear tendency towards a positive NAO phase at times of drought. 17 out of the 20 events coincide with times at which P(NAO+) > 0.5 and for 12 of them P(NAO+) > 0.66 holds. Thus, most of the severe drought events found in historical documents support the qualitative results of our analysis.

It should be emphasized that even though droughts are strongly related to the precipitation extremes associated with the dominant NAO phase, they are complex phenomena with multiple causing factors. Furthermore, societies can react differently on climate extremes of similar magnitude. A stable and rich society might be resilient to a drought which is catastrophic for others. Thus, a rise in reported droughts might also be an indicator of a more vulnerable society that found them more worth reporting. Hence, we cannot expect all droughts to be reported equally and no particular NAO reconstruction can explain the timing of all droughts.

6.5.3 Possible impacts on European societies

Droughts are just one of many climatological effects of persistent NAO phases, and not the only one with impacts on human societies. In general, the NAO influences temperature and precipitation patterns throughout Europe and has consequences for many natural and agricultural ecosystems (see Sec. 6.1). Here, we want to discuss

further implications of our qualitative reconstruction of the NAO phase in the context of European history of the last two millennia. Since the patterns of changes vary geographically, we restrict our considerations to two key regions, the Western Roman Empire and to Norse colonies in the North Atlantic.

It has to be kept in mind that climatic conditions are never the sole reason for societal changes and most often not even a dominant one. Geographical factors, human decisions, man-made conflicts and pure chance are usually much more important factors that shape the path of societies. However, climatic conditions can be either beneficial or disadvantageous for a society, also depending on how vulnerable it is to environmental disruptions (Diaz and Trouet, 2014; Diamond, 2005; Weiss and Bradley, 2001). Because of the complex relationship of human societies with environmental and climatic changes (Engler, 2012; Engler and Werner, 2015) any approach onto causal links is highly speculative, so that we explicitly refrain from making any conclusive claims.

The first centuries until about 450 CE see a predominant negative NAO phase with shorter NAO periods in between, which corresponds to milder and wetter winters in the western Mediterranean. This is in line with previous descriptions of the corresponding period as warm (Luterbacher et al., 2016) and humid (Desprat et al., 2003; García et al., 2007; Martín-Chivelet et al., 2011). Still, there is considerable disagreement about when this period ended in different paleoclimate archives. These conditions would have been generally beneficial for the Western Roman Empire. In turn, decreasing temperatures and more frequent droughts following the RWP added stress to societies that were already weakened by internal conflicts, plagues, invasions and other factors at this time (McCormick et al., 2012b; Diaz and Trouet, 2014; Drake, 2017). As an example, López-Moreno and Vicente-Serrano (2008) argue that the Balkan region is subject to NAO related hydrological anomalies in a similar fashion as the Western Mediterranean. During prolonged negative NAO phases, these regions receive higher precipitation. During the 4th and 5th century CE, this might have made them a target for invading Huns, who might have been escaping drought conditions in Central Asia (McCormick et al., 2012b). This in turn has been related with the mass migrations of the Late Antique (Halsall, 2007). A similar argument has been made by Drake (2017), who links negative NAO phases to droughts at the areas of origin of populations migrating to the Roman Empire.

While precipitation is the dominant feature in the Mediterranean region, societies in the Northern parts of Europe are more dependent on changes in temperature and wind patterns. Patterson et al. (2010) discuss the impact of seasonality on Norse colonies based on δ^{18}O values of mollusk off the coast of Iceland. This proxy is associated with ocean circulation, which is also related to NAO changes. They report cold periods around 410 CE and between 1380 and 1420 CE and warm periods from 230 BCE to 140 CE and 600 to 1000 CE. The last finding is in line with Werner et al. (2018) who assign the maximum of the MCA to 960 until 1060 CE in the Arctic. All of these findings match well with the effects that would be expected from the NAO phases as determined by our reconstruction.

A positive phase of the NAO leads to generally warmer temperatures and less sea ice and is thus more favourable to marine ecosystems around Iceland. While a positive NAO would be beneficial for settlement and sustained population on the island, it is also related to enhanced storm activity and increased wave heights in the North Atlantic

(Serreze et al., 1997; Bader et al., 2011). This makes sailing conditions and, hence, a colonisation more difficult. The first evidence of settlements on Iceland dates back to around 870 CE (Zori, 2016), a time at which our reconstruction indicates a short period of negative NAO phase. This implies, that while the overall positive NAO phase caused conditions that made settlement successful, short negative NAO phases helped to establish these settlements by allowing longer expeditions across the North Atlantic. Settlement on Greenland follows a similar pattern, as it also coincides with a negative NAO phase in the late 9th century. Different from Iceland such a negative NAO is associated with warmer conditions and, hence, the early MCA would be advantageous for settlement in Southern Greenland. This changes in the 14th century, when a period of prolonged positive NAO and, hence, lower temperatures set in. This coincides with the abandonment of most Greenland colonies, which has been related to environmental changes (Diamond, 2005).

In summary, some key periods and processes in the history of those parts of Europe that are influenced by North Atlantic climate seem to be closely related to environmental changes in agreement with our NAO reconstruction. This provides additional evidence for the general validity of the obtained long-term patterns.

6.6 Conclusions

In this chapter, we have demonstrated that evolving climate networks based on paleoclimate proxy records offer great potential to reconstruct spatial patterns of atmospheric circulation and their long-term variability. Specifically, we have reached a new, 2000 year-long probabilistic multi-decadal reconstruction of the leading mode of atmospheric circulation in the North Atlantic, the North Atlantic Oscillation (NAO). We achieved this by combining visual inspection of changing patterns in the simplified networks with regression of a linear model to the inter-regional connectivity. We have presented a climatologically consistent interpretation of the relationship between single cross cluster links and the NAO and how they change with time. In general, we relate strong East-West links with a positive NAO phase and North-South connections with a negative one. While the linear model does not trace the high-frequency variability of the reconstructed NAO index by Ortega et al. (2015) very well, it is in good agreement when it comes to the sign of the phase.

Our expansion of $\overline{NAO}_{\text{Ortega},\mathscr{W}}$ shows that there is a great deal of multi-decadal variability of the NAO during the Common Era. Some periods are dominated by a specific NAO phase, be it a positive NAO during most of the migration period, the late medieval times or the 20th century, or a negative phase, which was prevailing during the late Roman times and the Little Ice Age. Other times show considerably more variability, for example during the Roman and early medieval times. These long-term changes of the NAO might have had substantial impacts on European societies, as the NAO influences both regional temperature and precipitation and can increase the likelihood of droughts, all of which directly affect agricultural productivity. Therefore, specific phases have supported some European societies, while negatively affecting others.

The relatively low skill of the probabilistic reconstruction (sign in agreement with NAO$_{\text{Ortega}}$ in ~ 70% of the cases), points to the limitations of the model. Rather than

a conclusive framework for the reconstruction of climate indices, we have presented a first step towards a novel tool, based on an innovative set of assumptions. Previous reconstructions of climate variables mostly assume a stationary, linear relationship between a proxy and the target variable. For the NAO, this has been shown to be violated for many archives and our method explicitly targets this non-stationary relationship. What we assume to be stationary instead is the influence of the NAO on different regions. If a positive NAO phase is bringing warm and wet winters to Fennoscandia today, we assume that it also did so two thousand years ago. If this was not the case, the very idea of reconstructing a climate index itself would be pointless, as it would render any interpretation or application of such an index useless.

There are many uncertainties in the obtained NAO reconstructions. They arise mainly from possible biases induced by a varying number of records (in particular as one goes back in time), pre-existing uncertainties in the target variable $\overline{NAO}_{\mathrm{Ortega},\mathscr{W}}$, which is a proxy based reconstruction itself, but also from the inability of a simple linear model to describe the complex interactions among records sufficiently.

The first source of error can be expected to become less important in the future, as more long, high-resolution records are published. For a better performance of this model, high-quality records from Greenland, Svalbard and Eastern Europe would be desirable, as they are yet only sparsely covered.

Standard methods of similarity estimation like Pearson correlation are not feasible to be used with short time windows. Because of this, we were not able to calibrate the model against instrumental data, as the longest instrumental record of the NAO goes back to 1821 only (Vinther et al., 2003). Hence, there would not be enough independent data points available for a proper calibration and cross-validation when using multi-decadal time windows. This issue could be attacked, by either using less demanding measures of similarity, like rank based correlations, or by building upon the Bayesian approach discussed in Ch. 3, which would then explicitly trade off resolution against precision. Still, lowering the resolution itself would add considerable levels of uncertainty. These approaches could also be part of a larger effort to develop the framework presented in this chapter into a full Bayesian Hierarchical Model, modeling uncertainties directly at every level and thus leading to a more reliable estimate. This has not been achieved so far, as one would need to deal explicitly with a changing number of records and missing data, something that was beyond the scope of this study.

It would be desirable to test the presented framework in a controlled environment, consisting of gridded model or reanalysis climate data and proxy system models. This requires advanced forward models that are capable to model non-stationary influences of a multitude of climate variables to all the archives used in this study. Sadly, these are not available yet for most proxies.

The framework presented in this chapter could be applied to other large-scale patterns of climate variability, for example the Atlantic Meridional Variability (AMV Knight et al., 2006). We have performed the same analysis, using the same set of proxies and a reconstruction of the AMV published by Mann et al. (2009) as a reference time series. Unlike the results presented in this chapter, we did not yield a reconstruction that was substantially better than guessing the phase. This highlights the importance of proxy selection for this procedure, as most of the records are arguably not related to the AMV directly, or not in such a spatially diverse manner that is necessary for our reconstruction method to work. Hence, a consistent procedure of proxy selection and

clustering is one of the main challenges for the future application of the reconstruction framework presented here.

Part III | Last Deglaciation

7 | Overview: Glacial terminations

The last 2.5 million years have been characterized by a succession of cold and warm periods, marked by a growth and decline of vast continental ice shelves, sea ice and mountain glaciers on both hemispheres. These shifts between the cold glacials and the warm interglacials are related to changes in solar insolation caused by varying orbital parameters of the planet. This theory has been conceptualized in the 19th century and made popular in the beginning of the 20th century (Milanković, 1930, therefore called Milanković theory). For a historical discussion of the study of glacial cycles and the most common physical theories, see Paillard (2015).

Even though this theory has been proven very successful, there remain some open questions that could not be answered yet, for example, why most glacials in the late Pleistocene (starting from ~ 800ka ago) re-occur approximately every 100 thousand years, although this corresponds to only a minor peak in the spectrum of solar insolation changes.

What causes glacial terminations and which mechanisms are involved in the process is another open question. Many variables co-vary and have complex interrelationships and possible leads and lags, the estimation of which are made difficult by the dating uncertainties of most quaternary paleoclimate proxies. While Milanković theory can explain the pacing of glacial-interglacial cycles, it does not inform about the dynamics that unfold during these cycles. The terminations are often accompanied by insolation maxima, but not all of these maxima lead to terminations. There are opposing theories of deglacial mechanisms (see, e.g., Cronin, 2010, and references therein; Denton et al., 2010; Paillard, 2015), however all agree that terminations are related to the maximum extent of ice sheets, rising atmospheric CO_2 levels and changes in ocean circulation, in particular in the Atlantic.

Much of our knowledge about glacial terminations stems from the transition from the last glacial maximum (LGM) to the recent Holocene epoch, the last deglaciation.

7.1 The last deglaciation
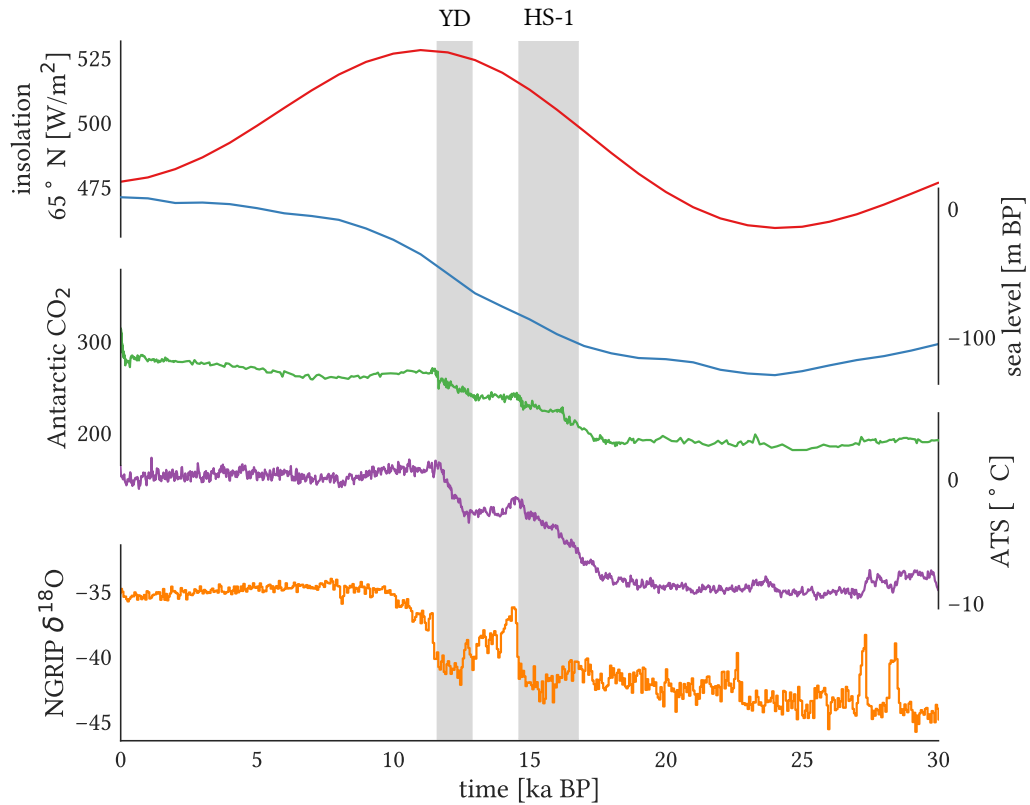
Figure 7.1: Different climate variables during the last deglaciation, in particular solar insolation at 65° N (red, Laskar et al., 2004), relative sea level as measured in Barbados (blue, Peltier and Fairbanks, 2006), atmospheric CO_2 as measured in a composite of Antarctic ice cores (green, Bereiter et al., 2015), air temperature in Antarctica from the Antarctic temperature stack (ATS, purple, Parrenin et al., 2013) and Greenland, as measured in the NGRIP ice core (orange, NGRIP members et al., 2004).

The last deglaciation is one of the most studied periods of Earth's climate history. It is represented in many paleoclimate archives and has been studied using climate models of various levels of complexities. Therefore, it is a prime candidate to study network based methods, but it also poses severe challenges in terms of data availability and quality.

A first overview of key variables is shown in Fig. 7.1 with reconstructions of solar insolation, atmospheric CO_2 concentrations, sea level (related to global ice volume) and atmospheric temperatures at both poles in Greenland and Antarctica.

Temperatures in Antarctica seem to follow the increasing insolation during the early deglaciation closely, together with the CO_2 concentrations and sea level (Parrenin et al., 2013). In contrast, after a small initial increase, Greenland temperatures stay at a

(a) AMOC glacial mode   (b) AMOC interglacial mode   (c) AMOC off mode
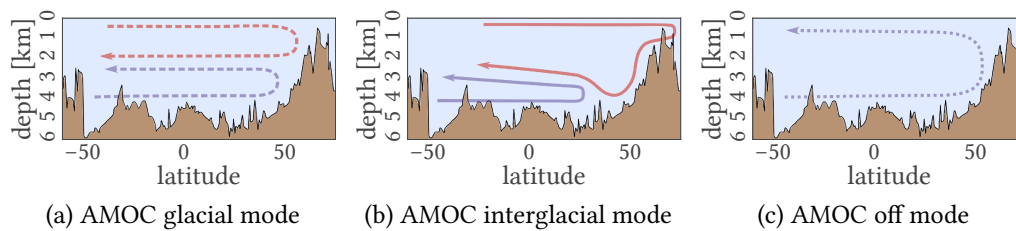
Figure 7.2: The three states model of the Atlantic Meridional Overturning Circulation (AMOC). (a) During cold glacial times, North Atlantic Deep Water (NADW) formation occurs south of the Scotland-Iceland ridge and the warmer water (red) flows southward at intermediate depths. (b) During warm interglacials, NADW forms further north and fills the bottom of the North Atlantic, rising to intermediate waters in the tropical latitudes. (c) At some times, e.g. during Heinrich events, NADW formation is reduced drastically so that the colder and denser Antarctic Bottom Water (AABW, blue) fills most of the Atlantic.

low level until a rapid warming occurs around 14.6ka BP, the so called Bølling-Allerød warming. This connection to solar insolation does not uphold during the Holocene, as all the shown variables stay at an about constant level with very low variability until the most recent decades.

The picture is even more complex, when focusing on the North Atlantic region, represented by the Greenland temperature record. Besides the delayed, but abrupt warming, there are other features of millennial scale variability, most pronounced the cooler Younger Dryas about 12ka BP. The cooling, which is in contrast to warming in Antarctica, is related to a period of enhanced iceberg discharge in the North Atlantic, characterized by large debris found in sediment cores throughout the Atlantic. These phases are called Heinrich Events. Those cold periods during which iceberg discharge events occur are called Heinrich Stadials (HS).

7.2 The role of the ocean

One key element of glacial-interglacial dynamics (corresponding to a multi-millennial time-scale) is the global ocean circulation, in particular, the one in the Atlantic ocean. Marine sediment records reveal large changes in the Atlantic Meridional Overturning Circulation (AMOC) that are believed to have influenced the distribution of heat on a global scale. The AMOC refers to a part of the global thermohaline circulation, in which ocean currents are driven by changes in temperature and density, related to the salinity of the water.

A model with three states has been established (Rahmstorf, 2002) to describe the different modes of circulation during warm and cold periods as well as during Heinrich Events. In modern times (Fig. 7.2b), warm water from the tropics is transported along the surface to the North Atlantic. As it cools through evaporation, the water becomes denser and at some point sinks below other, less dense water masses to form the North Atlantic Deep Water (NADW). This water flows back southward, only to return to intermediate depths when it meets the even denser and colder Antarctic Bottom Water (AABW), which flows northward from the Southern Ocean. It gradually rises until

it reaches the surface again in the South Atlantic. This formation of NADW occurs further south during the cold glacials (Fig. 7.2a) and the NADW flows southward at intermediate depths. The deep water basin of the Atlantic is thus entirely filled by AABW.

During Heinrich events, NADW formation is suggested to have been slowed down drastically or even stopped temporarily due to massive influx of freshwater into the North Atlantic. Hence, the entire Atlantic ocean is largely dominated by the cold AABW.

In both the glacial and the interglacial mode, the AMOC transports heat from the tropics into the northern hemisphere and, thus, results in an interhemispheric heat balance. In case that the AMOC slows down, heat accumulates in the Southern ocean basins, while the North Atlantic cools down. This mechanism is called the *bipolar seesaw* and is made responsible for the often asymmetric changes between Greenland and Antarctic climate records.

Furthermore, the AMOC is thought to be an efficient transport mechanism by which changes in one hemisphere can be transported to have impacts globally, which is crucial for most explanations of glacial terminations.

8 | Functional networks of past ocean circulation

While the Atlantic ocean plays a key role in deglacial dynamics as discussed in Ch. 7, it is also one of the most challenging component of the climate system to study in terms of co-variability in general and for applying climate networks in particular. The main reasons for this are the large degree of time uncertainties related to radiocarbon dating and to complex patterns in lead and lag relationships.

When comparing atmospheric data, it is rational to assume correlations on a fast time scale, as atmospheric processes are often faster than the sample resolution of paleoclimate records. In contrast, when dealing with marine sediment records, the relative time scales are almost arbitrary, as there is not only the age model uncertainty discussed in Ch. 3, but also the state dependent reservoir effects (see Sec. 8.1.2). In addition, the slow mixing of the ocean leads to multi-centennial to millennial scale lags between records, so that they have to be aligned in some way. Out of these issues, the reservoir effect poses the biggest problems for comparing radiocarbon dated marine records, as it introduces an age offset between the radiocarbon dates and the age of the dated material, which is directly related to the state of the ocean circulation itself (discussed in detail in Sec. 8.1.2). Therefore, any assumption about this variable offset already incorporates assumptions about the underlying circulation.

In this chapter, I want to investigate if climate networks, despite these challenges, can still yield meaningful statements about the past circulation of the oceans. Even though many structures among records are visible by eye, climate networks are expected to provide a more quantitative and reliable representation of past circulation.

For this purpose, we focus on stable isotope measurements from bottom dwelling benthic foraminifera from the Atlantic basin that cover the transition from the last glacial maximum (LGM) to the Holocene. In particular, we use oxygen (δ^{18}O) and

carbon (δ^{13}C) isotope ratios, which are commonly related to global ice volume and ocean ventilation.

As a precondition for climate networks, we need to find a shared time axis. Our approach is to assume synchrony between the oxygen records for major events, to be specific for the onset of deglaciation, seen in almost all records.

As a first step, we construct our own age models for all selected records, treating the reservoir effect as an additional source of uncertainty, with estimates coming from an independent isotope enabled ocean circulation model. Then, we align all records in such a way, that the onset of deglaciation occurs synchronously. Note that in this way, we do not assign these lags to the reservoir effect, but expect them to tell us something about the proxies, the circulation and the signal transport itself. The relative timing of events is an interesting question in itself. Zhang et al. (2017a) argue that there is a temperature signal in the oxygen data in addition to that of salinity and the asynchronous onset of deglaciation is caused by variable heat diffusion in different parts of the ocean basin. This is one of the hypotheses that we can test when analysing the leads and lags between different records.

After the time scales are fixed, the relative correlations can be estimated, using the procedure discussed in Ch. 3 and climate networks in which different sources of uncertainty are accounted for can be constructed. In this way, we expect to see more robust links and thus a reliable network structure. This chapter corresponds to the manuscript JF4.

Key Questions

- Given the independent age models of the records, what can we learn about the timing of the onset of the deglaciation?

- Are quantitative statements about correlations still possible in this combination of time uncertainties besides major transitions? If so, what do they tell us about changes in the Atlantic ocean's circulation?

This chapter is structured as follows: In Sec. 8.1 the data used in this chapter are introduced and the construction of age models is discussed in depth. In Sec. 8.2 the relative timings between these records are considered and related to ocean circulation. This is followed by the results of evolving climate network analysis, which are discussed in Sec. 8.3. The chapter closes with some concluding remarks in Sec. 8.4.

8.1 Benthic stable isotope records of the last deglaciation

8.1.1 Selection of records

Oxygen and carbon isotopes were among the first marine paleoclimate proxies studied and thus, a large number of high quality records have been published. It is often assumed that benthic oxygen isotope ratios mainly represent global ice volume and show the same signal globally (Bradley, 2015). This synchronicity has been utilized for the development of both global (Lisiecki and Raymo, 2005) as well as regional (Lisiecki and Stern, 2016) benthic δ^{18}O stacks. However, these records cannot be assumed to be

1: ENAM93-21	12: KNR159-5-17JPC	23: KNR166-2-GGC73
2: EW9209-1JPC	13: KNR159-5-20JPC	24: M35003-4
3: EW9302-24GGC	14: KNR159-5-30GGC	25: MD03-2707
4: EW9302-25GGC	15: KNR159-5-33GGC	26: MD07-30760
5: EW9302-26GGC	16: KNR159-5-36GGC	27: MD95-2010
6: GIK13289-2	17: KNR159-5-63GGC	28: MD95-2037
7: GeoB-1711-2	18: KNR159-5-78GGC	29: MD99-2339
8: GeoB1720-2	19: KNR159-5-90GGC	30: NA87-22
9: GeoB9508-5	20: KNR166-2-26JPC	31: ODP984
10: GeoB9526-4	21: KNR166-2-29JPC	32: RAPiD-15
11: KNR159-5-125GGC	22: KNR166-2-31JPC	33: RAPiD-17

Figure 8.1: The locations of the sediment records used, both in a transect of the Atlantic ocean (upper left) and geographically (right). The details of the records are given in the Appendix Tab. F.1.

synchronized at all time scales, as they are probably dominated by local dynamics at shorter scales (Waelbroeck et al., 2011).

In addition to oxygen isotopes carbon isotope ratios ($\delta^{13}C$) are also of interest as proxies for nutrients and ocean ventilation. This ventilation can yield information about the sources of water and thus indicates changes in the ocean's circulation.

We use these two proxies together as we expect the oxygen isotopes to inform us about relative timings between different records which helps us to compare the carbon isotopes in a meaningful way.

We selected marine sediment records of benthic foraminifera that fulfil the following criteria:

1. They have measurements of both oxygen and carbon isotope ratios.

2. They cover the transition from the LGM to the Holocene as a transition from low to high $\delta^{18}O$ values.

3. They provide independent radiocarbon dates and are not aligned to other records. This is necessary to account for comparability and further discussed in Sec. 8.1.2.

4. The onset of the transition is abrupt enough to be detected by the change point detection algorithm discussed in the Appendix Sec. A.1.

The records that fulfil these criteria are summarized in Tab. F.1 and their locations and depths are shown in Fig. 8.1. The time series of $\delta^{18}O$ values are shown in Fig. F.1 and those for $\delta^{13}C$ in Fig. F.2.

8.1.2 Age models

As many paleoclimate proxies, marine sediment records do only encompass relative and indirect information about the times of observations. For the period of the deglaciation the prevailing method to determine ages is radiocarbon dating. Stable isotopes have been analysed for several decades and the published records are therefore based on a multiplicity of age-depth models. In particular many different calibration curves have been used, which is problematic as even the two consecutive marine calibration curves IntCal09 and IntCal13 differ for multiple centuries, especially during the Heinrich Stadial 1 and the deglaciation.

Reservoir ages pose a major problem when dealing with radiocarbon dated marine records. The reservoir effect describes the fact that the radiocarbon in shell building organisms used for dating often appears to be older than the actual animal. Most age models rely on radiocarbon measurements from surface dwelling planktic foraminifera, which absorb carbon from the surrounding surface water. However, this carbon is of variable age[1]. "Young" carbon gets absorbed by surface waters from the atmosphere and is mixed with "old" carbon that is upwelled by advection or diffusion from deeper layers of the ocean. Hence, the age of the carbon at the time of absorption is associated with the balance between ocean-atmosphere interactions and the strength of upwelling, which depends on the state of ocean circulation itself. Thus, it varies both spatially and temporally, ranging from centuries in low latitudes during the Holocene to multiple millennia in higher latitudes during Heinrich Stadials (Balmer et al., 2016). The time difference between the true age of the organism and the age of the carbon is called the reservoir age. This effect means, that any argument about co-variability between radiocarbon dated marine sediment records is in some sense circular, as assumptions about the dynamical process are already inhibited in the construction of the age models themselves[2].

Oxygen isotopes in foraminifera are controlled by the temperature and the salinity of the surrounding water. As the water temperatures at the bottom of the ocean are very cold and show low variability, benthic oxygen isotopes are commonly related to global ice volume, in particular on long time scales (Lisiecki and Raymo, 2005). They are thus thought to be synchronous to a certain degree. In general, the dating of benthic records is mostly considered somewhere between two extremes. One can regard radiocarbon dates as correct and interpret all differences in timings of events as information about circulation, mostly assuming constant reservoir ages. The other extreme is to assume co-occurrence of events to synchronize ("wiggle-match") benthic data, efficiently explaining all mismatch by the reservoir effect. Most studies lay

---

[1]The method of radiocarbon dating is related to processes in the upper atmosphere, where carbon interacts with cosmic radiation and the different isotopes have a fixed ratio to each other. When the carbon is incorporated into an organism, this interaction stops and the ratio between stable and unstable isotopes gives information about the time of absorption. Atmospheric carbon is well mixed and, hence, the ratio between the isotopes is almost constant there. This carbon is referred to as "young" carbon, whereas carbon that was isolated from the atmosphere for a longer time is called "old" carbon. For an in depth discussion of radiocarbon dating, see Bradley (2015).

[2]Note, that even the common assumption of constant radiocarbon dates is a very strong assumption about a static ocean circulation, that is not supported by the data (see, e.g. Skinner et al., 2010).

somewhere in between, such that at least regional coherence is assumed. In some cases, the oxygen records are synchronized to terrestrial proxies, most prominently Greenland ice cores or speleothems. While being problematic in itself (see e.g. Blaauw, 2012, for a deeper discussion) this inhibits the danger of circular logic as well, as different records might be aligned to the same record.

In addition almost no available record provides information about the age uncertainty of single observations. Hence, the effect of age-model uncertainty cannot be tested appropriately, even though this can have a crucial impact on the estimation of correlations or other measures.

For these reasons we decide to construct new age models for all records used in this study. Doing this, we want to ensure comparability and employ a more elaborate treatment of reservoir ages than commonly done. The aim is to have more faith in the individual chronologies. We estimate the age-depth relationship using the Bayesian software Bacon (Blaauw and Christen, 2011) and the latest calibration curve IntCal13 (Reimer et al., 2013).

We use different reservoir ages for each record, all of which vary in time, based on carbon cycle modelling by Butzin et al. (2017). This method has been shown to be in accordance with the few measurements of reservoir ages based on carbon plateaus (Balmer et al., 2016). We use the data for 50-200m depth and for each record we consider the grid-cell closest to the record's location. For each calender year we thus have an estimate about how old the radiocarbon at the corresponding location has been when it was incorporated into the shells of foraminifera. We add these reservoir ages onto the IntCal13 calibration curve and use the combined curve for calibration. To account for the uncertainties related to the reservoir ages we impose an additional uncertainty of 400 years onto the calibration curve which is the typical order of the maximum difference between the model and published reservoir age data in Butzin et al. (2017).

Thus, we have an independent estimate of the ages of observation for the different records, which also takes changes in reservoir ages into account. This enables us to interpret differences in the timing of events in a more physical way, as coming from regional dynamics and delayed transport of a signal through ocean currents.

In most cases, the proposed settings, in particular priors for accumulation rates, are used. In some cases, we decided to use normal distributions instead of student-t to include radiocarbon measurements which would have otherwise been treated as outliers. These records are marked in Tab. F.1.

8.2 Construction of a shared time axis

Studying co-variability between two records depends on two factors: a common time scale and an measure to quantify similarity. In this section, we will deal with the first of the two.

Due to slow transport times in the ocean and interference with local processes we do not expect major events to occur simultaneously in all records, even if the absolute time scale was perfect. Hence, a—possibly variable—time delay between records has to be considered. In this study, we use single anchors to fix the time scales to each other, while keeping the rest of the records to be determined by the age-depth models.
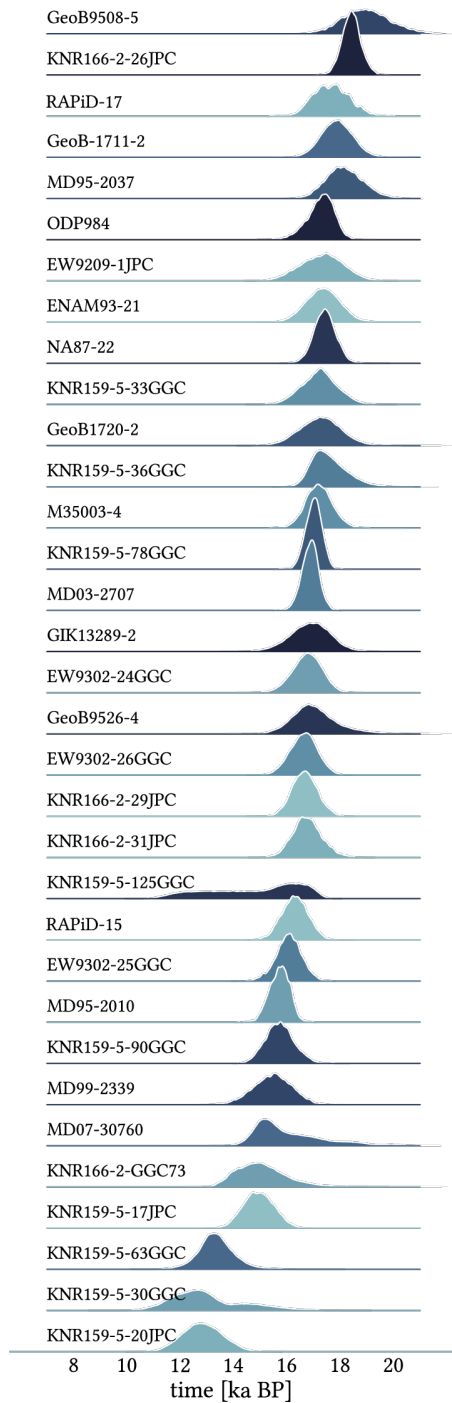
Figure 8.2: The posterior distribution for the onset of deglaciation for all records, sorted in descending order of the point of highest probability. The gray bars are, from right to left, meltwater pulse (MWP) 19 ka and 1A.

The onset is determined by a change point detection algorithm, discussed in detail in the Appendix Sec. A.1. In this context, a change point is a point in time at which a simple linear model is not sufficient to describe data on both sides of that point at once and, hence, a piecewise linear model is applied. The algorithm gives an estimate of the probability that a change occurred at each individual observation point. For most records, there is more than one change point, but we only consider that part of the change point posterior distribution which can be assigned to the onset of deglaciation by eye, meaning the transition from an elevated plateau of δ^{18}O values towards lower values. We argue that a transition is not necessarily occurring exactly at the observation, but at some time between it and the following observation. Hence, we consider all values in between these two observations to be equally probable change points. An example of the (not truncated) change point posterior distribution can be seen in Fig. A.1.

This builds upon the idea that major events like meltwater pulses will lead to global signals while centennial and millennial variability is mainly determined by regional dynamics. As an anchor we chose the onset of deglaciation that is present in all benthic δ^{18}O records, commonly interpreted as a signal of increased freshwater input from melting ice shields in the North Atlantic. In a second step, the time axes are shifted such that the anchor event occurs simultaneously. Correlations are then estimated for time windows, chosen relative to this anchor.

The posterior distributions for the timing of the onset of deglaciation in the oxygen records are shown in Fig. 8.2 and the regional pattern of timings is shown in Fig. 8.3. We see that the onset occurs around 19 ka BP in some cores while others stay at glacial values until almost 13 ka BP. Some distributions are very broad, often spanning more than one millennium. This shows the high uncertainty in time of these estimates, which is mainly
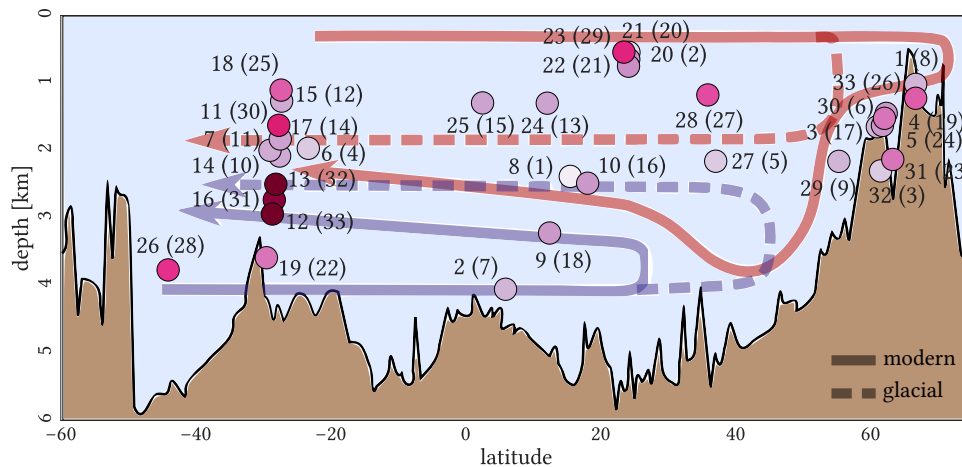
Figure 8.3: The timing of the onset of deglaciation for the different proxy locations, when considering the point of highest probability for each change point distribution. The darker the color of the circle the later the onset occurs. The numbers are the same as in Fig. 8.1, while the numbers in brackets indicate the nominal ordering of the onsets with the lowest number indicating the record that shows the earliest onset.

coming from the uncertainties of the age-depth model. Furthermore the imposed 400yr reservoir age uncertainty and the low sampling resolution play a role.

In general, a transition provides the first evidence of increased meltwater flux and rising sea level, also called meltwater pulse (MWP) 19 ka. This onset is also clearly present much before the more drastic meltwater pulse 1A. Still, some records are showing a transition very close to MWP 1A, hence, it is possible that they do not encounter MWP 19 ka at all and the deglaciation is really just setting in along with MWP 1A.

In Fig. 8.3 we see that the first records to undergo a transition are those at intermediate depths, while some very shallow and very deep cores are delayed by several millennia. The intermediate depths are those of the mixed zone between newly formed North Atlantic Deep Water (NADW) and the colder and more saline Antarctic Bottom Water (AABW). This mixed zone is thought to have deepened during the deglaciation as the NADW is able to sink deeper and is upwelling at lower latitudes.

We argue that this deepening of the mixed zone is the first sign of deglaciation recorded in the benthic oxygen record. While the amplitude of delay is likely too large (caused by the large time uncertainties), this pattern fits well the view, that the signal of onset is mainly driven by insertion of fresh meltwater in the high latitudes, deepening the NADW flow. The signal of lowered salinity is then transported and recognized first by the newly formed NADW. It then propagates to deeper and shallower cores by up- or downwelling and diffusion.

This interpretation is limited by the heterogeneous pattern, which makes strong statements somewhat more difficult. Still, it is not in accordance with the view, that the onset is dominated by temperature sensitivity as proposed by Zhang et al. (2017a), as this kind of signal would in general propagate from shallow to deeper cores.

8.3 Climate networks based on anchored correlations

As discussed in the previous section we can construct a shared time axis by shifting all the time series such that the signatures related to the onset of deglaciation coincide. Correlations are then estimated for these shifted time series.

As discussed in more depth in Ch. 3, the main obstacle for a quantitative analysis of co-variability between paleoclimate time series is the irregular and age uncertain sampling of the proxies. We follow the procedure discussed in said chapter, using Markov Chain Monte Carlo (MCMC) methods to estimate the coupling factor in a bivariate normal model as a probabilistic estimate of the common Pearson correlations. For the approximation of the joint distribution, we use the Gaussian kernel based interpolation, as it showed to be slightly superior to the other methods.

To take all uncertainties into account we do not only integrate over all possible age models, but also over the change point distribution. We approximate this by drawing one realization from the age model at a time. The distribution for the onset of the deglaciation is estimated for each time series and one realization is drawn of it. We then shift both time scales such that these two anchor points are concurrent. Lastly, we estimate the correlation using the MCMC estimator. We repeat this procedure 100 times and stack the distributions of ρ together, which estimates the integrated correlation values. For computational reasons we draw 20.000 independent samples from this stacked distribution.

We estimate correlations both for the full 30,000 year time period centred around the onset of deglaciation as well as for moving windows of 5000 year length each. The number of possible links is shown in Fig. F.4. We see that around the onset of deglaciation the proxies provide most data, not surprisingly given our selection criteria. During the LGM and the Holocene, the number of possible links reduces due to a lower number of records and lower temporal resolutions.

8.3.1 Oxygen Isotopes

For the full 30,000 year long time period, the oxygen isotopes show generally high correlations, dominated by the shared step-like transition. This is illustrated by the network shown in the Appendix Fig. F.3a, which shows only strongly positive links with small uncertainties. Therefore, the assumption of shared signals in oxygen isotope records is generally justified on long time scales, if time differences are taken into account.

The functional networks for shorter time windows are shown in Fig. 8.4 and the Appendix Fig. F.5. The only time period that exhibits marked, consistent correlations throughout the Atlantic are the 10 ka that follow the onset of the deglaciation, as the shared trend to lower values dominates the correlation estimates.

For other times, there are mainly meridional connections, but few between deep and shallow cores. These few meridional connections might indicate a stronger stratification during the LGM before the onset, while the ocean appears to be more mixed during the Holocene. Still, the number of connections is by far too low to draw reliable conclusions from them. Hence, besides major transitions like the deglaciation, most benthic $\delta^{18}O$ records used in this study are not synchronized significantly. At times farther away
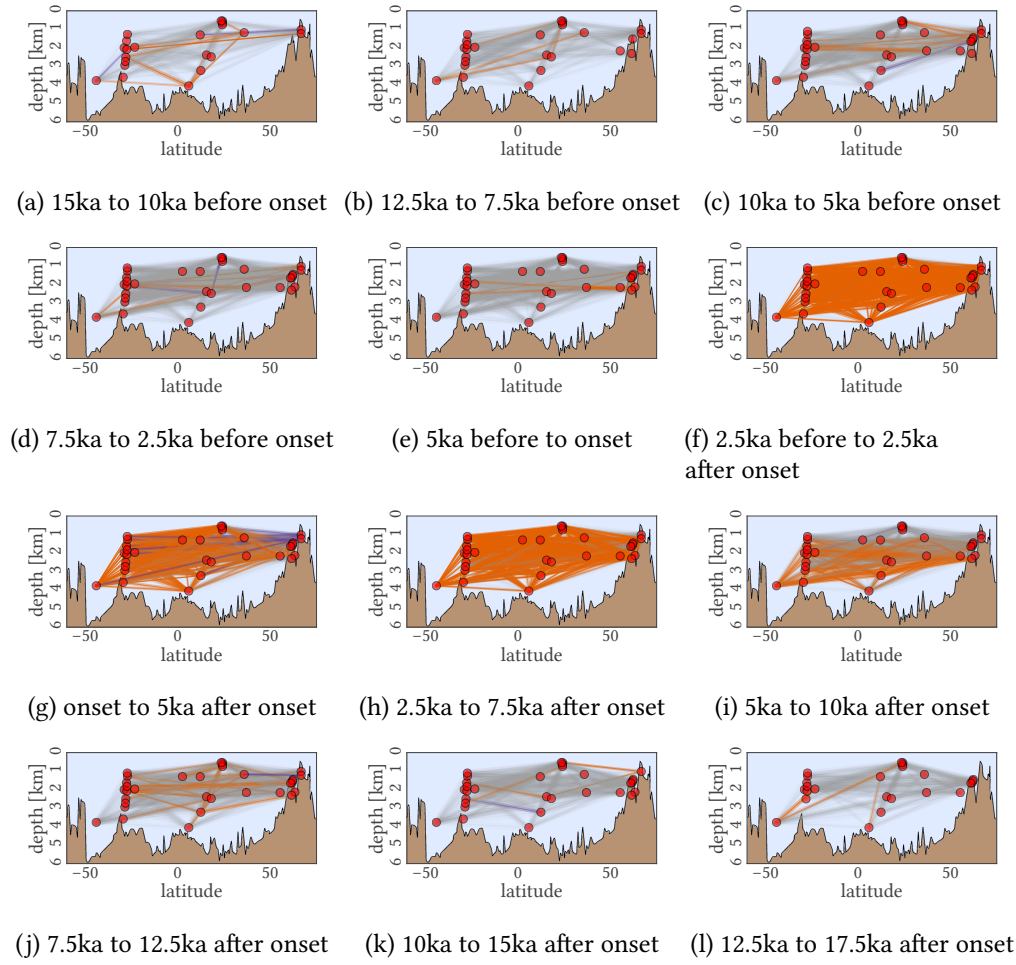
(a) 15ka to 10ka before onset (b) 12.5ka to 7.5ka before onset (c) 10ka to 5ka before onset

(d) 7.5ka to 2.5ka before onset (e) 5ka before to onset (f) 2.5ka before to 2.5ka after onset

(g) onset to 5ka after onset (h) 2.5ka to 7.5ka after onset (i) 5ka to 10ka after onset

(j) 7.5ka to 12.5ka after onset (k) 10ka to 15ka after onset (l) 12.5ka to 17.5ka after onset

Figure 8.4: Evolving networks of δ^{18}O data. A link is drawn orange or purple if 95% of the samples of the posterior distribution of ρ lay above or below zero, respectively. It is shown in gray, if neither is the case. The width of each link is proportional to the width of the central 90% range of the posterior. This means, that precise estimates are shown as thin lines. The red dots mark the locations of the records.

from transitions, local and regional variability, varying patterns of temperature, and proxy related processes like bioturbation dominate the oxygen isotope signal.

Since each link between two locations is not represented by a single number, but a probability distribution, one can apply all methods of network theory in a probabilistic way. One way to do this is using the correlation between records as weights and combining weighted network measures with samples from the distributions. This yields network measures with uncertainty estimates, as shown in Fig. 8.5a. Here, we show the absolute weighted network density, which is the sum of all link weights divided by the number of possible links[3]. Given all the uncertainties that enter this analysis, these

---

[3]Note that in this case, the number of possible links is smaller than the classical $N(N-1)$ as we

(a) Absolute weighted network density.
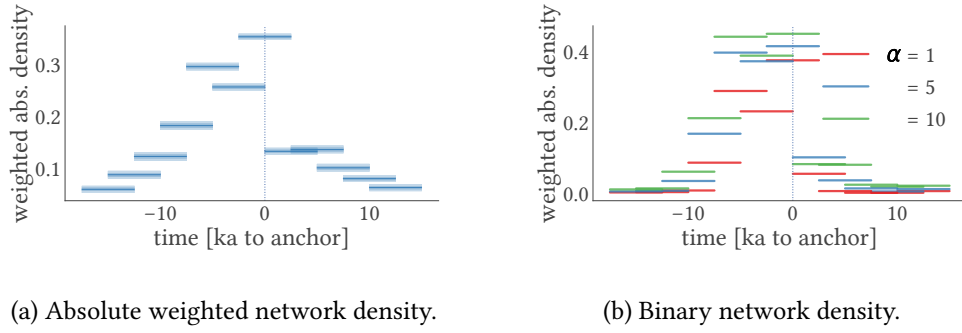

(b) Binary network density.

Figure 8.5: Two ways to quantify a network with probabilistic link weights, in this case, the absolute link density of the network. (a) The probabilistic absolute link density, calculated by repeatedly drawing realizations from the posterior distributions and, hence, obtaining a range of possible values. (b) The link density after binarizing the adjacency matrix, setting those links to 1 that show correlations significant at different levels of α and all others to 0. The length of each bar represents the duration of the time window. Different from classical measures, we have removed links that are not possible due to low data coverage from the normalization of the density.

measures are remarkably precise, as uncertainties in different links balance each other out in most cases.

An alternative approach is to construct an unweighted graph by only considering those links for which the correlation distribution is significantly of one sign, determined via a significance level α. An example for this type of measures is shown in Fig. 8.5b.

In this way we see that both the values as well as the number of significant correlations are increasing during the deglaciation and that this is a robust feature for different significance levels. We do also see an increasing trend in the millennia before the transition, which might indicate an early influx of freshwater leading to higher synchronicity. This signal is mainly determined by the shared trend of values during the deglaciation. The results for detrended time series are shortly discussed in Sec. 8.3.3.

8.3.2 Carbon Isotopes

The carbon isotope time series show a somewhat more complex pattern, already visible for the network of the full 30,000 year time period, shown in the Appendix Fig. F.3b. There are both positive and negative correlations, in particular between the North and the South Atlantic. For a more quantitative analysis, we apply a community detection based on modularity maximization, as discussed in the Appendix Sec. A.3. In this way, we can find groups of records that are strongly connected to each other, but weakly to the rest of the graph. We use a binarized graph by only considering those links that are significant at a 5% confidence level. The resulting groups of records are shown in Fig. 8.6a.

---

discard links if the number of observations is too small after interpolation.. Hence, the number of links does not only depend on the number of records, but also the relative timings between them.
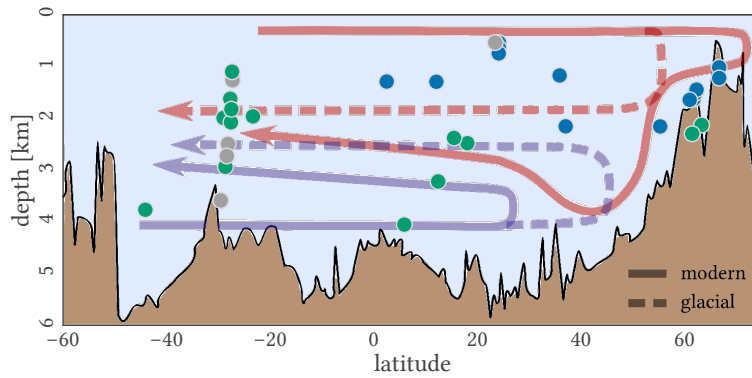
(a) Geographical distribution of communities on a transect of the Atlantic Ocean.
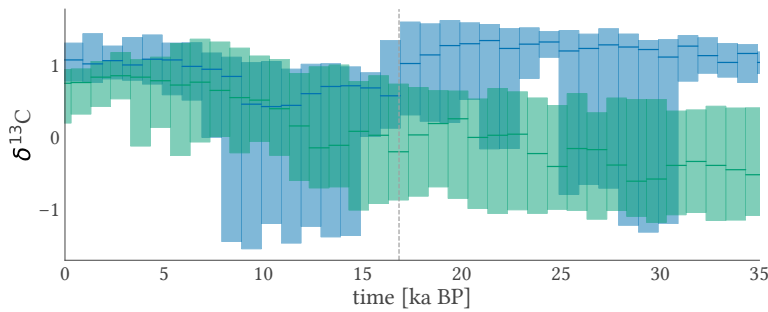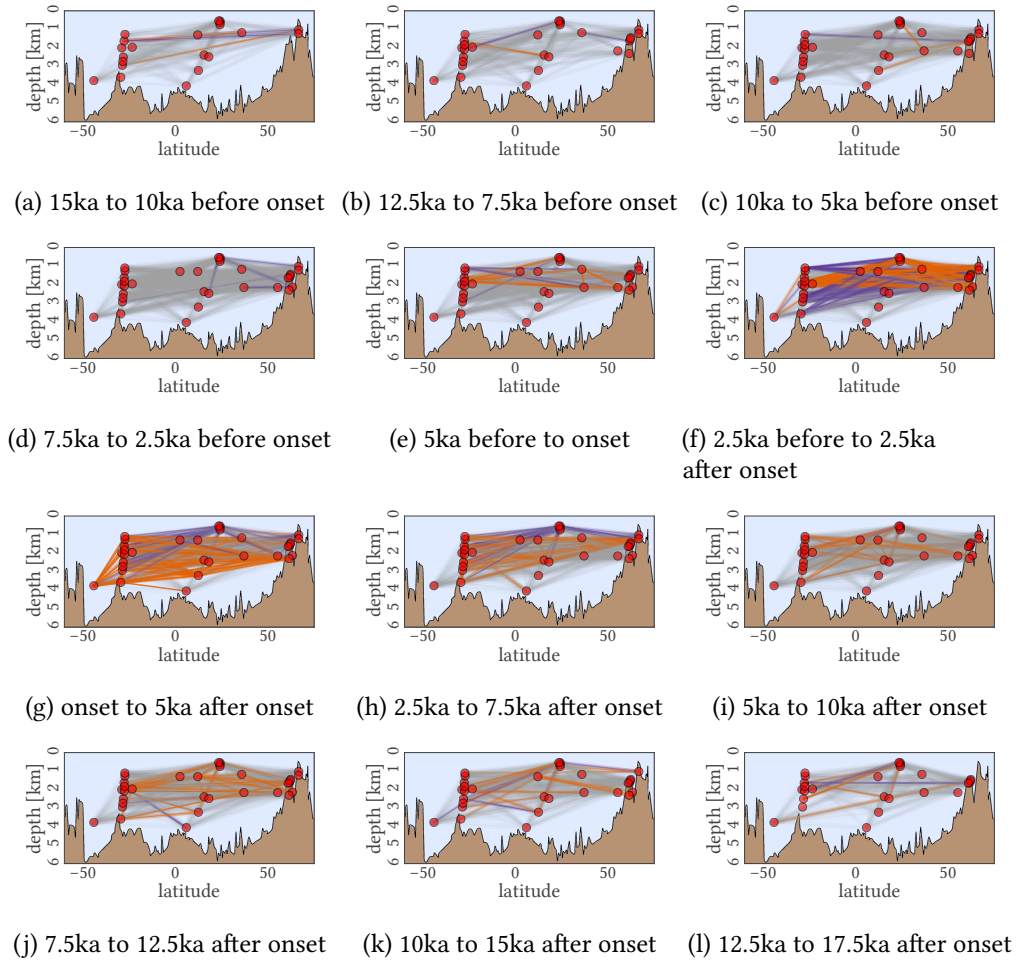

(b) Stacked δ^{13}C values for the different communities.

Figure 8.6: Grouping records of δ^{13}C data together based on similar dynamics. This grouping is based on the Louvain algorithm for community detection in networks (discussed in the Appendix Sec. A.3). (a) The allocation of each record to a cluster, each colour corresponds to one cluster. Clusters with less than 3 members are shown in gray. (b) Averaged values for the different communities, the colours correspond to the ones of communities in (a). Vertical lines show the extent of each time slot over which the values were averaged. The shaded areas show the spread in each community, marking the lowest and highest values during the corresponding time period.

As we can see, there are two groups of records, one in the upper Northern Atlantic shown in blue and the rest in the South Atlantic and in intermediate and deep waters shown in green. To understand the differences between these groups, we calculate separate stacks by averaging over 1ka time windows. These stacks are shown in Fig. 8.6b. The green cluster is depleted during the LGM and shows an enrichment in ^{13}C following the deglaciation, the onset of which is marked by the dashed line in the plot. In contrast, the blue cluster shows high values of δ^{13}C during the LGM, a sign of strong ventilation. These values drop after the onset of deglaciation, marking the Heinrich event 1, as a large volume of freshwater is flushed into the ocean. The values are still higher than those of the green cluster, which shows that the AMOC did not stop completely, but rather slowed down. The following short recovery period is again interrupted by a period of lower values, probably corresponding to a similar freshwater pulse during the Younger Dryas.

(a) 15ka to 10ka before onset (b) 12.5ka to 7.5ka before onset (c) 10ka to 5ka before onset

(d) 7.5ka to 2.5ka before onset (e) 5ka before to onset (f) 2.5ka before to 2.5ka after onset

(g) onset to 5ka after onset (h) 2.5ka to 7.5ka after onset (i) 5ka to 10ka after onset

(j) 7.5ka to 12.5ka after onset (k) 10ka to 15ka after onset (l) 12.5ka to 17.5ka after onset

Figure 8.7: As in Fig. 8.4, but for the δ^{13}C time series

During the Holocene, both communities reach similar, high values that indicate a generally high ventilation rate of the whole Atlantic Ocean, consistent with the warm mode of the three state model (Fig. 7.2b).

Similar to those for oxygen isotope ratios, the evolving networks of carbon isotopes, shown in Fig. 8.7, do not show many significant links before the deglaciation, which itself is dominated by the pattern discussed in the previous paragraphs. While the shallow, northern cores get depleted in carbon most of the others become enriched resulting in strong connectivity among deep and Southern cores and strong negative correlations between the two large clusters. We see that the events of freshwater influx mainly impact the Northern surface water, while the rest of the ocean is well connected. This is in accordance with most observations about the bipolar seesaw mechanism, which is a dipole between the surface layers of the North Atlantic and the rest of the ocean (Pedro et al., 2018). This pattern prevails for about 10,000 years. Following the deglaciation, we see mainly positive links, as all records get enriched in ^{13}C, but the number of significant links is decreasing gradually.

8.3.3 Decomposed signals

The time series used for the previous analysis show remarkable slow variability, which is likely to be responsible for most of the correlations. To test this hypothesis, we filter out long time scale variability and apply the same analysis using only the fast components of each signal. To do so, we use the complete ensemble empirical mode decomposition with adaptive noise (CEEMDAN Torres et al., 2011, see the Appendix Sec. A.2), an algorithmic variant of empirical mode decomposition (Huang et al., 1998). This method decomposes a time series into a set of empirical modes, for which the instantaneous frequency can be determined using the Hilbert transform. We decide to only consider those modes whose instantaneous frequency has a median below 2500 years.

For both isotopes, there are only occasional significant correlations, which can result from chance alone. This is not unexpected, as the filtered signal is likely dominated by local dynamics besides major transitions. Furthermore, by removing the slow components, we also removed serial correlation in the data. It has been discussed in Ch. 3 that missing serial correlation makes it difficult to infer correlations when the data is irregularly sampled and demands interpolation.

8.4 Conclusions

In this chapter, we have studied co-variability between marine sediment proxies, while taking into account the obstacles presented by age-model uncertainty, reservoir effects and the time delays stemming from slow transport through ocean circulation. In contrast to previous studies, we have not simply assumed the records to be synchronous bona fide, but only during major transitions as the deglaciation. From this assumption we have learned that the onset of deglaciation is recorded at significantly different times throughout the Atlantic Ocean. This transition is first recorded at intermediate depths, which is expected if the signal is coming from a decline in salinity, induced by freshwater input in the region of NADW formation. From here on, the anomaly in salinity is transported to deep and shallow core sites by either direct circulation or diffusion. The large time difference and the fact that low latitude records experience the onset earlier than some high-latitude southern records which lay in the general flow direction is an argument for a prominent role of diffusion in this process.

We have seen, that synchronicity on glacial-interglacial time scales is a justified assumption for oxygen isotopes, as they are all highly correlated when anchored to the same transition point. Still, when considering moving windows on the same anchored time series, we see that besides the transition itself, there are few significant correlations. Thus, we argue that wiggle-matching benthic oxygen isotope ratios on these millennial time scales introduces artificial correlations where there are none (an illustrative example for this is provided by Blaauw, 2012).

As we have demonstrated for the carbon isotopes, major transitions can be used to anchor time series to provide a meaningful analysis. Here, the anchored time series show different clusters of similar dynamics that demonstrate the changes in ocean circulation during the deglaciation. During the LGM, there has been a with strong ventilation visible in the northern, shallow cores and low ventilation elsewhere. This changes during Heinrich Event 1, with low ventilation throughout the whole Atlantic, pointing

towards a massive slowing down of the AMOC. All records show increasing ventilation during the late deglaciation and high rates during the Holocene, demonstrating the enhanced strength of the AMOC. The evolving networks derived from carbon isotopes show negative correlations between shallow northern cores and the rest of the graph. This corresponds to the general pattern of the bipolar seesaw (Pedro et al., 2018). In general, links between these two regions seem to be indicative of the different states of the AMOC. During the LGM state, there are few significant links between the different communities of sites, while the off mode is marked by a negative correlation. The warm mode is accompanied by positive links between both communities. This hypothesis could be tested with longer time series, for example to investigate how the Atlantic circulation changed during Dansgaard-Oeschger events.

In conclusion, we have demonstrated that the climate networks constructed for the Atlantic ocean do represent previous knowledge about circulation changes in a robust way, despite all levels of uncertainty that is present in these date sets. Hence, the method can be expected to yield new insights into spatial patterns of past ocean circulation in other oceans in the future.

9 | Climate networks of a transient simulation of the last deglaciation

As we have seen in the last chapter, climate networks built from paleoclimate proxy data for the last deglaciation suffer from a variety of problems, in particular sparse spatial coverage, low data resolution and all types of uncertainties related to radiocarbon dating. Complementary to proxy data, there are efforts to understand the dynamics of the deglaciation using coupled global circulation models (GCMs). The most comprehensive attempt so far is the TraCE-21ka project, using the NCAR Community Climate System Model 3 (Liu et al., 2009; He, 2011). In contrast to other model experiments this is not a simulation of short snapshots in an equilibrium state, but a transient simulation of the full last 21 thousand years, covering the complex transition from the last glacial maximum (LGM) to the warm Holocene.

This simulation gives us the opportunity to apply climate networks to a time period that is characterized by abrupt and probably highly non-linear transitions in many parts of the climate system. These are features of complex, non-linear systems that are largely missing from previous applications of large-dimensional climate networks, all of which focused on the dynamics of the late Holocene, a period with much less variability and certainly no transitions as extreme as the glacial terminations.

While the results of the TraCE-21ka simulation have been discussed extensively (see, e.g., Liu et al., 2012; He et al., 2013; McGee et al., 2018), the global statistical characteristics of the simulation have not been studied so far. Hence, using climate networks to analyse spatial co-variability of the model output can not only help us understand the potentials of the method, but can also point towards features and

characteristics of the climate model itself. This chapter is based on the manuscript JF5.

Key Questions

- How do climate networks change at global and abrupt transitions of large magnitude?
- What do they tell us about the structure of atmospheric dynamics in the TraCE-21ka simulation?

The TraCE-21ka simulation is introduced in Sec. 9.1, followed by a discussion about the way climate networks are constructed and analysed in this chapter in Sec. 9.2. Different ways to look at the evolving structures of the climate networks are discussed in Sec. 9.3. These dynamics are put into a larger context and interpreted in Sec. 9.4. We close with some concluding remarks in Sec. 9.5.

9.1 The TraCE-21ka simulation

The TraCE-21ka simulation is a transient simulation of the last 21,000 years using the Community Climate System Model 3 (CCSM3), a coupled atmosphere-ocean-sea ice-vegetation model. It covers the last parts of the Last Glacial Maximum (LGM), most of the Holocene and the complex transition period between these two periods. The simulation uses the T31_gx3v5 resolution, which corresponds to ~ 3.7° at both latitude and longitude. The atmosphere and ocean components consist of 26 and 25 vertical levels, respectively.

The model has been forced with a set of boundary conditions, in particular changing solar insolation, greenhouse gas concentrations, and land ice cover, to trigger a transition between a cold and a warm state. The millennial-scale variability seen in proxies during the deglaciation is commonly attributed to a complex pattern of freshwater input, altering the AMOC and leading to abrupt shifts in regional and global climate. To account for this, freshwater input has been prescribed explicitly at different regions with variable flow rates. The regions of meltwater forcing are shown in Fig. 9.1 and the specific meltwater forcings together with the AMOC strength in Fig. G.1.

While the model provides many different climate variables, we focus on the atmospheric temperature at a reference height of 2m on a monthly resolution.

9.2 Climate network construction and analysis

In this chapter, we use the method of climate networks as introduced in Ch. 2. To track changes in co-variability, we use sliding, non-overlapping windows of 10 years, leaving 120 values for the estimation of correlations in each window. The seasonal cycle has been removed to ensure an unbiased estimate by calculating the mean value for each month over the whole time window and subtract it from all data for that month. In order to prevent spurious correlations coming from shared trends, we removed linear trends from the anomalies by fitting a straight line to each time series in each time window and remove it from the anomaly values. In this way, we end up with monthly residuals, possibly modulated by more complex decadal variability. The correlation matrix is
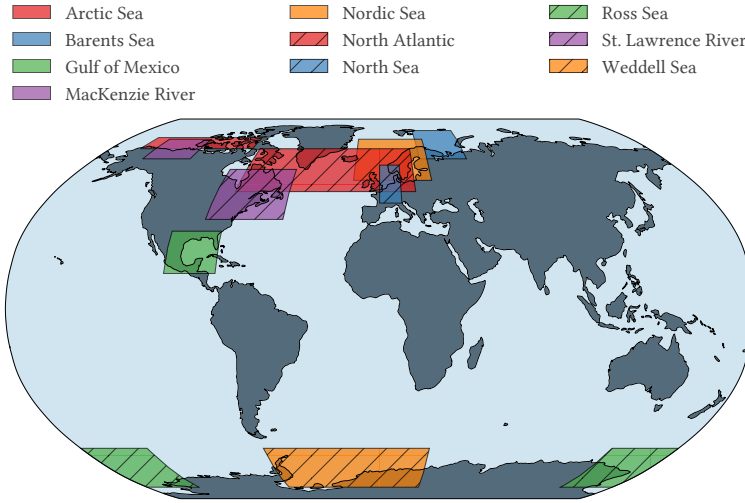
Figure 9.1: The regions to which the freshwater forcing is applied in the TraCE-21ka study.

based on Pearson's correlation coefficient. To take the possibility of long ranging teleconnections into account, we use the absolute correlation value. As discussed in Sec. 2.4, the network is constructed by setting links between those nodes which show the strongest correlations. In this study, we impose a threshold value of 0.6, for which about 1% of the possible links are realized at most times (see Fig. 9.2).

The model is calculated on a close-to-regular grid, which means, that the spatial distance between nodes is much larger on the equator than in the polar regions. Hence, the tropical nodes represent larger areas. Heitzig et al. (2012) proposed node splitting invariant (n.s.i.) measures that are designed to correct for this possible bias by introducing weights to each node, proportional to the area that it represents. Based on this, modified versions of most network measures can be defined. In the following we only consider n.s.i. versions of network measures.

To quantify the changes in any scalar network measure, we apply Bayesian change point detection and if no change is detected, linear trend estimation. The change point detection is described in the Appendix Sec. A.1. If no change point is found, we consider the simplest alternative, the linear model. We consider the data Y as being drawn from the distribution $Y \sim \mathcal{N}(\beta t, \sigma)$, with time t, variance σ and the trend β. The parameters of this model are estimated using a Markov Chain Monte Carlo (MCMC, see the Appendix Sec. A.4) estimator and the corresponding fits are shown as horizontal lines in Fig. 9.2. We only show those fits that have a significant trend (more than 95% of the posterior of β is below or above 0). Furthermore, we ignore those trends, where changes between the beginning and the end of the time series are less than half of the standard deviation of the time series.
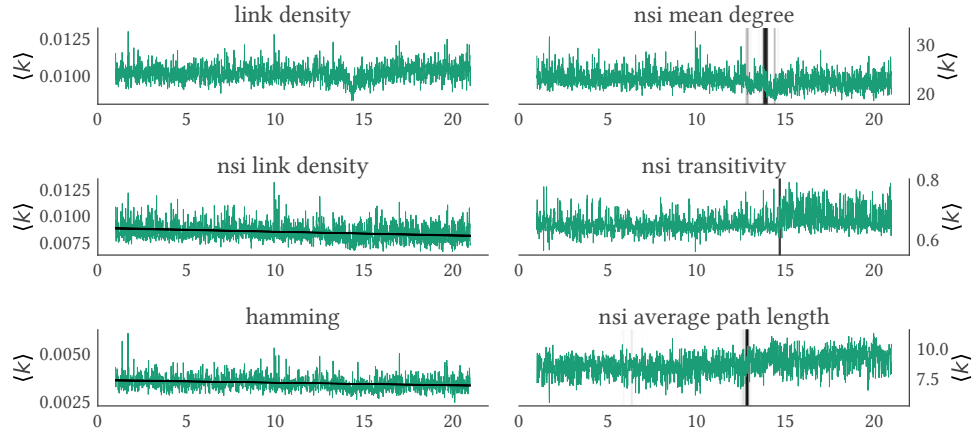
Figure 9.2: Global network measures for the whole time period. Vertical lines show change points, with darkness being proportional to the probability of change. Vertical lines show significant trends, that extend to more than 50% of the variables' standard deviations (only if no change point is detected).

9.3 Results

In this study, we distinguish between three different kinds of measures applied to the networks:

Global measures, for which one scalar value is calculated from the whole network, for example, the proportion of closed triangles, the transitivity $\mathscr{T}$. These are discussed in Sec. 9.3.1.

Local measures, which are assigned to each node individually. An example for this is the number of links originating from a node, the degree k. These are shown in Sec. 9.3.2.

Zonal measures are averages over all longitudes of a local measure and shown in Sec. 9.3.3.

9.3.1 Global network features

We start with the scalar network measures that are defined on the whole network, as shown in Fig. 9.2. The change points and estimated trends for each measure are shown in the Appendix Tab. G.1. The definitions of network measures are summarized in the Appendix Ch. B.

As we keep the threshold value constant, the number of links can change with time, depending on the covariance structure. The proportion of pairs that are linked to the number of all possible pairs is referred to as the link density. Remarkably, it is rather constant throughout the whole time period, except for a small excursion following the Bølling-Allerød warming. If one applies n.s.i. weights to each node, the corresponding n.s.i. link density informs us about the global distribution of links. This measure shows
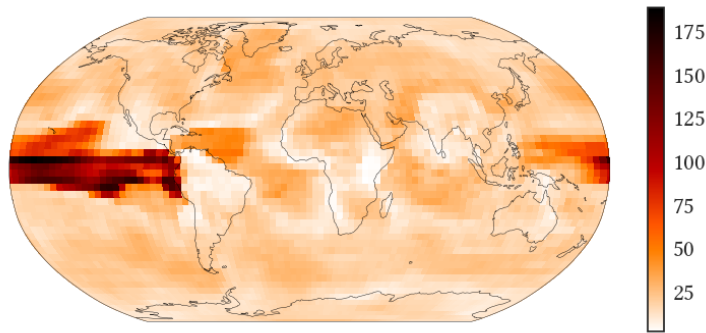
Figure 9.3: The n.s.i. degree for the example time window from 17.31 to 17.30 ka BP.

a significant upward trend throughout the whole time period. As the unweighted link density is constant, this means that links are shifted to nodes with higher node weights, i.e. away from the poles towards the equators.

The Hamming distance is the percentage of nodes that change between consecutive networks. It too shows an upward trend, meaning that consecutive networks are getting less similar with time. Remarkably, this is unrelated to any of the major transitions as it also continues during more stable periods, like the Holocene.

The simple arithmetic mean over the n.s.i. degree of all nodes shows the same upward trend until 12.86ka BP and then settles at a stable level. A detailed discussion of the n.s.i. degree fields is given in the next sections.

The transitivity gives the ratio of closed triangles in relation to possible triangles. High values are typical for clusters of highly interconnected clusters, while low values indicate that the links are spread out through the network. Here, we see a break at the onset of the Bølling-Allerød at which variability decreases drastically. While most links seem to be present in highly connected clusters for some parts of the LGM, the network links are more distributed after the disruption of meltwater input.

A path is a set of links which connect two nodes with each other. The average path length is the mean length of the shortest paths among all nodes. This measure shows a decrease until ~ 9ka BP, when the values become stable. These lower values indicate a network in which nodes are connected more efficiently, probably due to the dispersion of nodes and the shift towards equatorial nodes, which connect to both hemispheres.

9.3.2 Local network measures

While there is a lot of variability in space and time for most local network measures, there are few consistent, large-scale changes that are directly visible. The main patterns, shown in Fig: 9.3 and in the Appendix Fig. G.2, seem to stay stable at most times. Often, the differences between successive time windows are to be of a similar magnitude as those between the LGM and the Holocene.

One reason for this is that most measures are dominated by the tropical Pacific region, with most other variability of much smaller magnitude. Example can be seen for the n.s.i. degree and the maximum link density in Figs. 9.3 and G.2b. This is a common
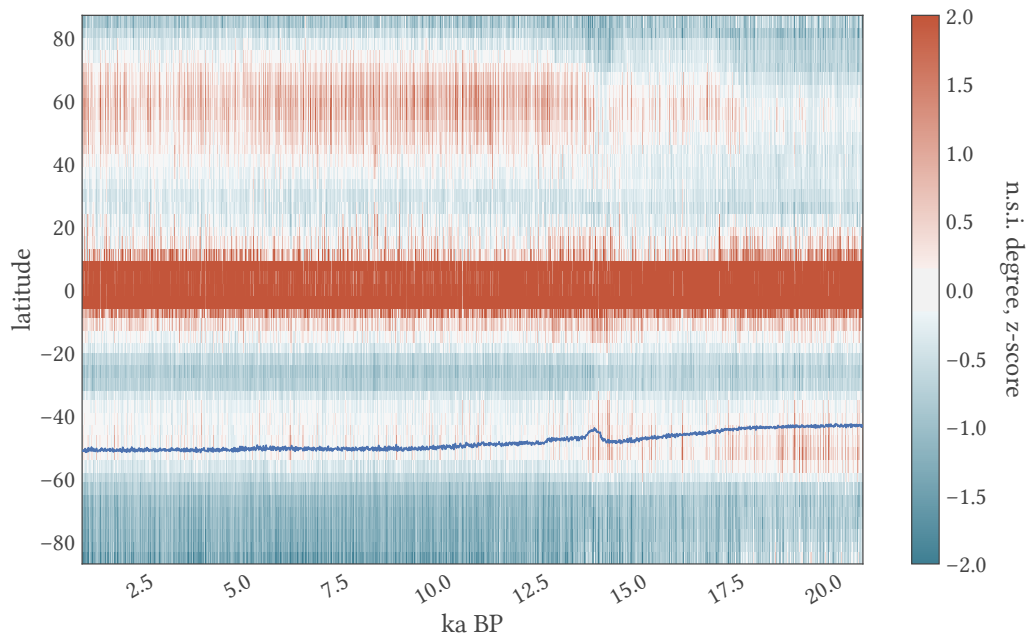
Figure 9.4: The zonal average over the n.s.i. degree for the whole study period. Shown are the z-scores, normalized to zero mean and unit variance, calculated for each time window. The blue line indicates the latitude of the mean northern boundary of the Antarctic ice sheet.

pattern in climate networks, as this region constitutes a large and strongly correlated area.

Outside of this region, we see a few further spots of higher degrees in the tropical Atlantic, the Indian Ocean and south of Greenland, but these patterns are much less robust in time. In general, degrees are higher over the ocean. This is expected, as the spatial correlation length is often considered to be larger over water (Briffa and Jones, 1993; North et al., 2011) and thus, the chance of a distant link is higher.

The local clustering coefficient describes the degree to which neighbours of a node are connected to each other. This is an indicator of highly connected regions, similar to the global transitivity. In the Appendix Fig. G.2a we see, that for most nodes more than 50% of their neighbours are also connected. These values tend to be higher in the equatorial region.

If each link is weighted by the geographical distance between the two nodes one can find regions that show particularly long connections. One way to look at this is the maximum link distance, that represents the longest link of each node. Figure G.2b shows an example of this measure. Again, the tropical Pacific shows the largest values and in general, the same areas as for the degree are more pronounced, in particular over the oceans.

9.3.3 Zonal measures

As most processes during the deglaciation are related to a redistribution of heat between different latitudes we investigate the distribution of links evolving in time. For this, we
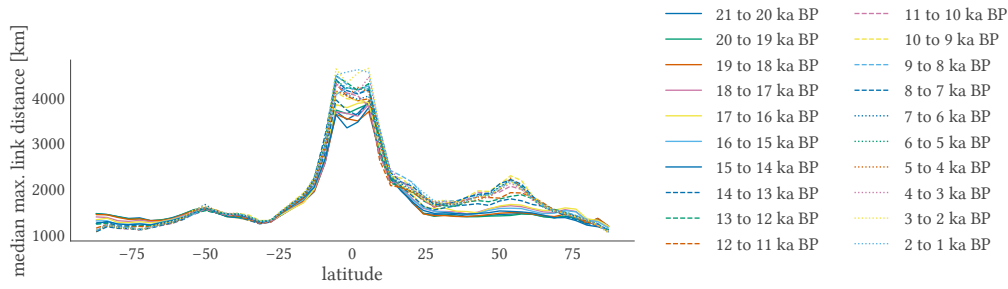
Figure 9.5: The maximum link distance, averaged over all longitudes and all time-windows for each millennium.

plot the zonally averaged n.s.i. degree for all latitudes for each time window, as shown in Fig. 9.4.

In general, we see a trimodal structure with maxima at the tropics and at the mid-latitudes. The highest degrees of the network are clearly found in the tropics, most of them in the tropical Pacific. Outside of the tropics, a clear shift in the degree distribution is happening during the deglaciation. At glacial times, the southern mid-latitudes are much stronger connected than the northern ones. This changes with an increasing influx of meltwater into the North Atlantic starting at 19ka BP, when extra-tropical connections are shifted from south to north. This is shortly interrupted by the strong pulses of meltwater forcing around 14ka BP, the Antarctic Cold Reversal, which leads to a short return to the glacial state and is followed by a dominance of the Northern hemisphere for the remainder of the simulation.

Given this distribution of links, it is of interest if these are local or long ranging teleconnections. This can be investigated using the maximum link distance, which is shown as an average over all longitudes and sets of time windows in Fig. 9.5. Three features are immediately visible. The by far longest connections arise in the tropical regions, with link distances up to 4500km. This is not surprising, as the region of high connectivity in the tropical Pacific itself measures about 5000km zonally. Indeed, when looking at the neighbourhood of the nodes inside the tropical Pacific, almost all neighbours lay within the box, as can be seen in Fig. G.4. A second feature is the trimodal structure with two small local maxima around 50° in both hemispheres. While the southern peak stays more or less constant throughout the whole time period, the northern nodes become connected to more distant nodes towards the Holocene, but rarely exceeding distances of 2500km. Thus, instant teleconnections are an exception and not visible in any of the averaged measures.

9.3.4 Regional degree fields

As the local measures are difficult to interpret due to the size of the dataset and the high rate of fluctuations, we need to simplify their complex structures to gain some insights about regional dynamics. For this purpose, we define boxes of 10° width in latitude and longitude, each of which contains around 10 grid cells. We average the n.s.i. degree over these boxes for each time window. We thus retain 647 time series of n.s.i. degrees at which local fluctuations are averaged out. We are interested in
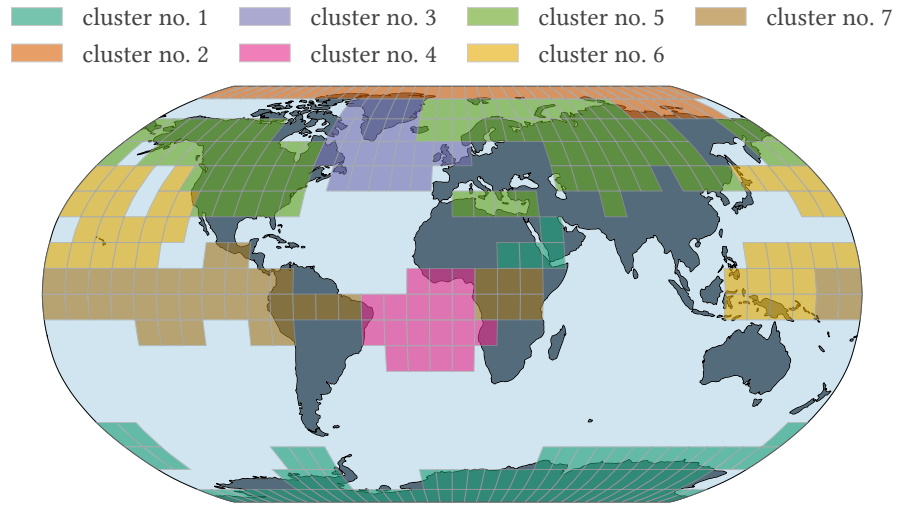
Figure 9.6: Clusters of coherent n.s.i. degree changes. Only those clusters with at least 18 boxes are shown. The corresponding mean n.s.i. degrees are shown in Fig. 9.7.

regions that show coherent linkage structures as these might indicate shared dynamical changes. This coherence can be investigated by applying a clustering algorithm. Here, we use classical hierarchical clustering, based on average inter-cluster distances (see the Appendix Sec. A.3). If C is the correlation between the n.s.i. degree time series of two boxes, their distance is defined as $1 - C$. We focus on clusters that are large enough to allow meaningful interpretation, but do not show too large internal variability. As a trade-off, we set a threshold of 0.74 that leaves the key clusters intact (the corresponding dendrogram is shown in the Appendix Fig. A.2), but limits the number of large clusters. The general structures of clusters are very robust for different clustering algorithms, with only small changes in the extent of clusters. To focus on large-scale structures, we only consider clusters with at least 18 boxes in them, which leaves us with 7 clusters. These are shown in Fig. 9.6 and the corresponding n.s.i. mean degrees are shown in Fig. 9.7. Most of the other (smaller) clusters do not show much variability, except for a group in the Southern Ocean, which will be discussed in the next section. This is also true for cluster no. 4 in Fig. 9.7, which is hence ignored in the following discussion. It should be noted, that these clusters do not mean, that nodes in these regions are necessarily connected to each other, but that the number of links of the nodes varies in a similar fashion. As can been seen in the Appendix Fig. G.4, most connections are to neighbouring grid-cells.

The two polar regions (clusters no. 1 & 2) show a decrease until the Northern Hemisphere Bølling-Allerød warming leads to a drop in the Arctic and a small rise in Antarctica. This resembles the opposing signs in temperature changes. After this short period, the mean degrees stay stable until the end of the Holocene. Similar degree changes can be found for a number of small clusters over the southern mid-latitudes (see the Appendix Fig. G.3), but these do show much stronger local signals and are poorly correlated among each other.

The North Atlantic region (cluster no. 3) shows by far the most variability, with an
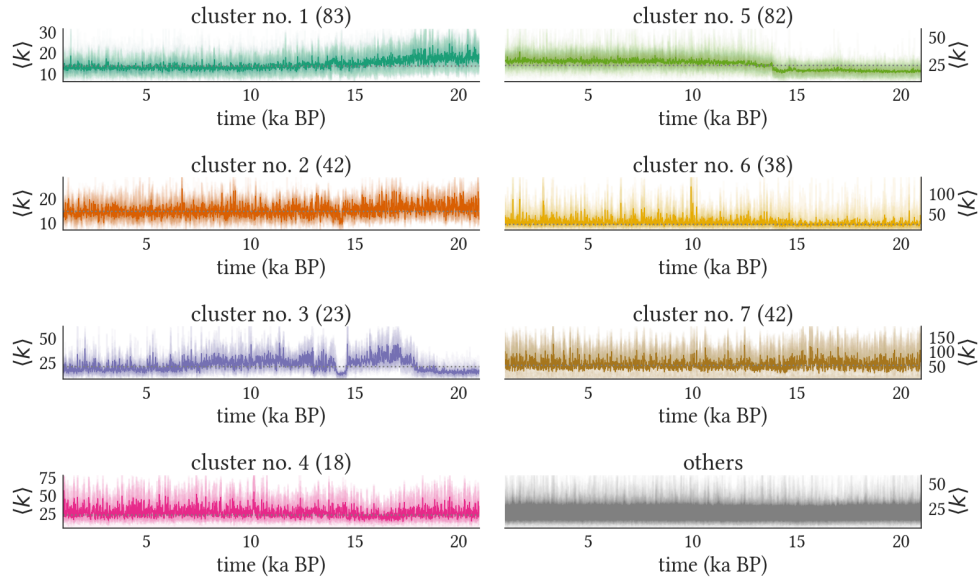
Figure 9.7: The n.s.i. degrees of the boxes for each cluster with their median values (bold). The colors and numbers correspond to those clusters shown in Fig. 9.6.

initial rise of n.s.i. degrees at 18ka BP, a plateau of high values until the Bølling-Allerød followed by a short drop to very low degrees. After the Bølling-Allerød warm period, the region exhibits high values, with more variability and a stepwise decrease towards the late Holocene.

Another large cluster lays over most of the land masses of the northern mid-to-high latitudes and some marginal seas around the North Atlantic (cluster no. 5). There is an abrupt transition towards higher mean n.s.i. degrees following the Bølling-Allerød warming. The n.s.i. degree stays stable at this higher level until the end of the simulation period.

The Pacific region is marked by two clusters (no. 6 & 7). Both show a small shift in variability and magnitude at ~ 14.5 ka BP, with the links in the eastern equatorial Pacific decreasing while those in the surrounding regions increase. As this dipole behaviour is of very low magnitude, we will not discuss it further in this chapter.

9.4 Climatological interpretation of network structures and dynamics

The last deglaciation, as modelled by the CCSM3 model, shows a marked reorganization of the covariance structure of the atmosphere that can be seen in most network measures. Some features, like most global network measures, change gradually, while others show abrupt changes of large magnitude. The latter is particularly the case when we look at a regional level as some features are averaged out when only taking the global network into account.

9.4.1   Global features

It is remarkable that the link density remains almost constant throughout the whole simulation period. This means, that even though large parts of the Earth system are reorganized, the strengths of correlation remains largely the same. It is not immediately clear if this is a physical feature of the climate system or an artifact of model parametrizations.

The gradual changes of most global network measures, in particular the Hamming distance and the n.s.i. average path length, show that throughout the model run, the links become less localized and more smeared out. This indicates that the initial conditions of the simulation are far from equilibrium.

In general, the network degrees exhibit a trimodal structure, with the largest number of links in the tropics and two side peaks at the Southern and Northern mid-latitudes. This can be explained by the fact that the tropics are the area with the largest correlation length (Christiansen and Ljungqvist, 2017). The network degrees in the mid-latitudes are influenced by the strong westerlies jet streams, an effect visible in other applications of climate networks as well (Wolf et al., 2018).

9.4.2   Regional dynamics

We see a meridional redistribution of links from the Southern mid-latitudes and the poles towards the Northern mid-latitudes. While this transition happens gradually throughout the early deglaciation, there is a marked shift during the Bølling-Allerød that leads to a dominance of the Northern Hemisphere throughout the rest of the model run.

At first, the pattern of anti-phase hemispheric changes resembles that of the bipolar seesaw, but in contrast to this hypothesis, the system stays at a stable state following the Bølling-Allerød warming. Liu et al. (2009) already mentioned that the bipolar seesaw hypothesis seems to hold only until the Bølling-Allerød, but not afterwards. Hence, the redistribution of heat alone does not explain the shifts in connectivity. Rather, we see most changes in the network topology persist even after the Bølling-Allerød warming.

As the popular mechanism of interhemispheric coupling via the bipolar seesaw does not seem to explain this transition sufficiently, we need to investigate the key regions of the network in detail, mainly the regional clusters that were defined via the n.s.i. degree.

For some regions, changes in the regional mean n.s.i. degree are accompanied by a change in variability in temperatures. For these regions, a strong one-to-one correspondence between a high standard deviation of the anomaly time series and the mean degree can be found. This is for example the case for the Antarctic and Northern continental regions, but not for the Antarctic region (see the Appendix Fig. G.5). This relationship might indicate a shift in the signal-to-noise ratio, meaning that a larger variability corresponds to a larger influence of regional climate dynamics, leading to higher coherence among grid cells. While this seems to be a viable pathway of different climate variables to alter the network structure, the specific dynamics can differ significantly between regions, as is discussed in the following sections.

Polar regions

The similar behaviour at both poles points at the issue of polar amplification, a term describing the fact that changes in radiation produce larger changes in temperature around the poles than at lower latitudes.

Overall, the changes over Antarctica are much more pronounced than those over the Arctic ocean. This is not surprising, as there is an Antarctic lead in the early deglaciation with stronger warming, accompanied by an initial rise in CO_2 concentrations and sea level. The period from 20ka BP until the Bølling-Allerød is marked by large changes in most climate variables and, hence, it is difficult to pin down a single cause for the changes in n.s.i. degree. It is more likely the result of many interacting changes and feedback mechanisms.

Still, the dynamics in n.s.i. mean degree closely resemble the amount of sea ice and regional temperature, which are closely related to each other by melting, CO_2 emissions and ice-albedo feedbacks (Curry et al., 1995). In the case of Antarctica, the extent of sea ice also leads to changes in atmospheric circulation.

In general, Antarctica is rather isolated from many atmospheric phenomena by the strong Southern Westerly Winds (SWW), the Antarctic Circumpolar Current (ACC) and the katabatic winds transporting cold air from the massive ice shield seaward (Parish and Bromwich, 1987; Fyke et al., 2018). This isolation strengthens when the northern edge of the sea ice migrates towards the pole, as the SWW follow and strengthen over the Southern Ocean (Toggweiler, 2009), leading of a larger isolation of a smaller region. In combination with large changes of radiative forcing, these changes lead to a decreasing coherence of temperatures over the early deglaciation until an equilibrium is reached at the beginning of the Holocene. The relationship between the regional n.s.i. degree and the extend of the sea ice shelf is shown in Fig. 9.8a.

We suggest that this process also plays a role for the decrease in n.s.i. degree at the Southern mid-latitudes. In Fig. 9.4 we compare the zonal n.s.i. degree with the mean position of the northern edge of the Antarctic ice shelf. We see that the band of high connectivity is located at the edge of the ice shelf and the degrees get lower as the ice shield decreases. As the surface cover changes from sea ice to open ocean, the connectivity decreases as well.

Still, the extent of sea ice cannot explain all dynamics, as the n.s.i. degrees rise again even before the sea ice extents during the Antarctic Cold Reversal. This might point to a lagged response of the sea ice to a change in ocean dynamics, most likely the overshoot of the AMOC during the Bølling-Allerød warming or freshwater input into the Weddell and Ross seas.

North Atlantic

The influence of the AMOC on the network structure is best seen in cluster no. 3 (Fig. 9.6). When plotting the mean degree of this region together with the AMOC strength (defined as the maximum water flux below 500m over all grid cells in the Atlantic northern of the equator), we see a strong correspondence on long time scales, as shown in Fig. 9.8b. At most times, major changes of the AMOC are mirrored by the mean degree, resulting in strong negative correlations between both variables. This link seems to be limited to a specific regime, as the connectivity does not increase any
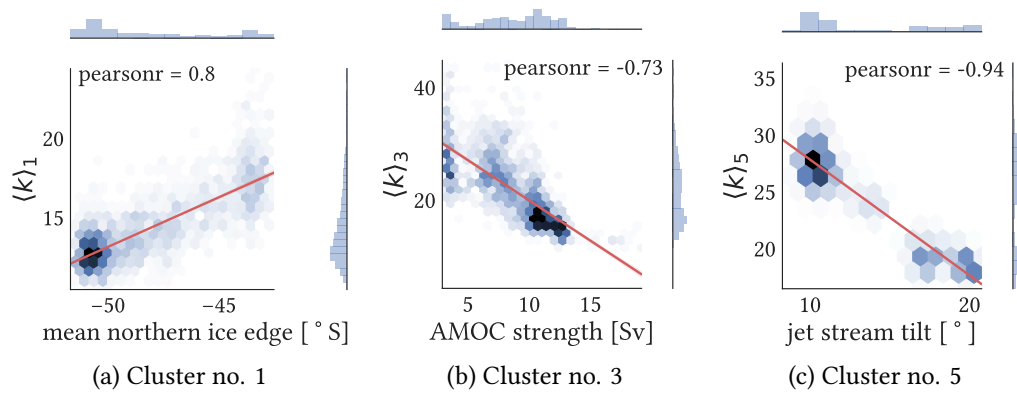
Figure 9.8: The mean degree $\langle k \rangle_i$ (with $i = 1, 3, 5$ for the three clusters no. 1, 3 and 5) with the largest changes in variability, together with explanatory variables as discussed in the text. Cluster no. 1 is related to the extent of sea ice in the Southern Ocean, whereas cluster no. 3 is driven by AMOC variability. Cluster no. 5 is related to the state of the jet stream, with low degrees during a zonally directed flow and higher degrees in the presence of large meanders, corresponding to either low or large tilt, as defined by Löfverström and Lora (2017).

further after a certain AMOC strength is surpassed. Furthermore, correlations are low at times of an almost constant AMOC (in particular during Heinrich Event 1), which shows that other dynamics dominate at stable AMOC conditions.

Continental Northern Hemisphere

The continental Northern mid-latitudes, even though surrounding the North Atlantic to a large degree, do not resemble the AMOC pattern in their covariance structure, as indicated by cluster no. 5 (Fig. 9.6). There are rather two stable regimes of low and high mean n.s.i. degree, with a transition happening between them around 14.8 ka BP, during the Bølling-Allerød. Even though it happens during the time of a large AMOC overshoot, it does not seem to be related to the AMOC at other times. Hence, we argue that this transition has less to do with changes in oceanic, but more with atmospheric circulation.

At the time of the transition, the Laurentide Ice Sheet broke up into two ice sheets, the Laurentide and the Cordilleran ice sheets. This event has been termed the (Laurentide Ice Sheet) *saddle collapse*. This collapse of the ice masses connecting the two large ice shelves of the North American continent led to a massive surge of meltwater into the Atlantic (Gregoire et al., 2012; Gomez et al., 2015) and to changes in both ocean and atmospheric circulation (Ivanovic et al., 2017). The saddle collapse has also been discussed in the context of the TraCE-21ka simulation by Löfverström and Lora (2017), who attribute a large-scale, abrupt transition in the atmospheric dynamics to the collapse. In particular, they find a shift in the Northern Hemisphere westerly jet stream, from a strong, zonal regime to a weaker, but strongly meandering circulation. Before the saddle collapse the extensive ice sheet forced the Westerlies to a straight path at the southern edge of the ice sheets, whereas the collapse lead to a new stationary wave source, resulting in a strongly tilted flow. This new circulation regime incorporates

influences of a larger range of latitudes, leading to larger variability in the underlying regions. This shift in variability is visible in our network as an increased regional coherence, shown by the linear regression between the tilt of the jet stream[1] and the mean degree in cluster no. 5 in Fig.9.8c.

Pacific ocean

Even though changes in the Pacific ocean are small, they occur in the region of highest connectivity and, hence, they can have a noticeable impact on the rest of the network. This is best seen in the transitivity, that shows a similar drop in both magnitude and variability at ~ 15 ka BP. The transitivity has been connected with ENSO (Radebach et al., 2013; Wiedermann et al., 2016b), using daily data. Some authors have described an abrupt intensification of ENSO in the TraCE-21ka model, occurring around 14ka BP, a lag of multiple centuries to the regional mean degrees and transitivity. Due to the large time difference, we argue that the shift in regional n.s.i. degree and transitivity is not related to a change in ENSO, but rather to the Bølling-Allerød warming happening at the same time. The exact mechanism is not clear to this point.

9.5   Conclusions

In this chapter, we have analysed how the network representation of the TraCE-21ka simulation changes during the last deglaciation. The spatial co-variability structure changes significantly throughout the simulation period. In general, we see a redistribution of links from the Southern to the Northern Hemisphere, a transition that happens gradually in some regions, but abruptly in others, in particular in the Northern Hemisphere.

We have demonstrated, that the regional n.s.i. degree is strongly affected by transitions in the regional climate system (e.g. the tilt of Westerlies in the Northern Hemisphere or changes in the AMOC), but these changes differ from place to place. While freshwater forcing, through induced changes in the AMOC, is often seen as the dominant driver of deglacial dynamics, it can only explain a small part of the changes that we see in the functional network representation. Different mechanism seem to dominate in different regions and during different times. It is not clear which variables are driving these changes in the network structure or are merely co-varying due to shared controls. To study the exact influences of different state variables and forcings, one would need a larger array of sensitivity runs with single variables held constant. The global network measures might overrate a global or interhemispheric explanation like the bipolar seesaw during periods at which a regional one is more appropriate. This highlights the need for a mechanistic understanding to interpret climate networks.

Another crucial feature of our analysis is the lack of long-range teleconnections. The maximum link distance varies both in space and time, but always stays at a low level. This has multiple implications. First, it points to a lack of long-range connections

---

[1]Following Löfverström and Lora (2017), we define the tilt of the jet stream as the difference in wind strength between two boxes, one extending from 25°N to 45°N and 80°W to 90°W, the other from 20°N to 70°N and 20°W to 10°W

in the climate model used at monthly scales, as the method of climate network has been shown to detect these connections for recent data (Tsonis et al., 2011). Second, it has implications for the interpretation of paleoclimate proxy data. Not only are different locations representative for areas of different size, but these areas also change over time. A Northern Hemisphere record from the Holocene is similar to a significantly larger area than one from the LGM. This non-stationarity of the spatial correlation length is a crucial feature that might be included in future reconstructions of spatial paleoclimate conditions.

Part IV | Conclusions

10 | Conclusion and outlook

I have considered a number of different approaches to use network theory to analyse paleoclimate data. The goal has been to further develop existing methods to allow for more quantitative and reliable results in light of particularities of paleoclimate proxy data. The different case studies presented in this thesis are intended to stimulate a wider application of these methods and to promote their further usage by a larger audience.

In this chapter, I want to look back and recapitulate the work that I have presented in this thesis. When looking back, there are mainly three questions: What have I done in the thesis? What are the key achievements of this work? And, where do we go from here? I will try to answer these questions in the following sections.

10.1   What have I presented in this thesis?

All chapters of this thesis are related to a key area of global climate dynamics, the Atlantic ocean and the surrounding continents. Despite the long history of research on this region, it has rarely been studied using network techniques, in particular for pre-instrumental times.

I have focused on two periods of the late Quaternary, the last two millennia of the recent Holocene and the transition from the last cold to the recent warm period, the last deglaciation. I selected these two time periods as they are very distinct, so that the characteristics of network based techniques in very different environments can be seen. The Holocene is commonly considered to be exceptionally stable and, thus, networks can be used to detect structures that are not visible to the eye immediately. In contrast, the last deglaciation is marked by massive changes in almost every part of the Earth system. In this setting, I am interested in the related changes in the topology of the network representations during these transitions.

For each of these time periods I conducted two case studies, either with different methods or with different data types. The two methods that I have used in this thesis were visibility graphs in Ch. 5 and evolving climate networks in Ch. 6, 8 and 9.

In the following I want to shortly summarize the key results that were presented in the corresponding chapters.

Methods   The methods on which this thesis are based were discussed in Ch. 2. These are the theory of complex networks and two applications, that of visibility graphs and of correlation based climate networks.

As the estimation of correlations lays at the core of climate networks, I have dedicated Ch. 3 to the issue of estimating correlations in the presence of time uncertainty, which is typical for paleoclimate records. The aim of this chapter was to study how different interpolation algorithms react to different levels of time uncertainty in a systematic way. For this purpose, I have implemented a model of synthetic pseudoproxy data, resembling marine sediment records with radiocarbon dating. I studied 5 different methods of interpolation in combination with four stages of increasing time uncertainty in the time series, starting with evenly sampled time series and then successively adding unequal sampling, age model error and age model uncertainty. Different from similar previous studies, I have focused on a Bayesian approach, which provides reliable estimates of the estimation uncertainty, incorporating different levels of both time and measurement uncertainty. In contrast to classical estimates, a covariance matrix estimated with the Bayesian framework is always well defined, as it can be ensured to be positive-semidefinite, even in combination with interpolation.

I have found that in most cases most estimation errors originate from uneven sampling and from age model errors while the single observation time uncertainties do only play a minor role. In addition, the statistical features of a time series, in particular its persistence, are crucial for a meaningful estimation. Which method is used to bring both time series to a shared time axis only plays a minor role. This probabilistic treatment of correlations is later used in Ch. 8.

Holocene 1: Dynamical anomalies in terrestrial paleoclimate records   In Ch. 5, I have focused on a visibility graph based test of time-reversibility, a characteristic indicative for complex, possibly non-linear dynamics in the underlying process.

Due to the notoriously high rate of false positives of the method, I have extended this originally univariate method to an ensemble based approach, using area- and group-wise significance testing.

I have shown that this ensemble test yields reliable results that are in accordance with previous results for marine records and with known, large-scale changes in climate dynamics in Northern Europe, in particular transitions between warm and colder periods. It is remarkable, that one can detect anomalous dynamics in the inter-annual time series, even though, these large-scale changes operate on a multi-decadal to centennial time-scale. Most of these periods are related to times of both low solar activity and strong volcanic eruptions. Therefore, these results might point towards a destabilization of the regional climate system in response to external forcings and related changing atmospheric patterns, recorded in the paleoclimate proxies.

Holocene 2: Using networks to reconstruct the NAO   In Ch. 6, I have proposed a novel method to reconstruct multi-decadal variability of the leading mode of atmospheric circulation in the North Atlantic region, the North Atlantic Oscillation (NAO). Contrary to previous methods, the new approach does not rely on a stationary relationship between the target variable and the proxy time series. Instead, it is based on the idea that paleoclimate archives do only record variability in the NAO during specific phases, while being unaffected by others. If distant regions show more coherence at one time, but less at others, this might point towards large scale influences and the state of atmospheric circulation, in particular the NAO.

The presented method can be used to reconstruct the phases of the NAO for the full Common Era by extending a previous reconstruction by a thousand years. This extended reconstruction is supported by further evidence from historical records of drought events. It shows a large degree of multi-decadal variability of the NAO throughout the last two thousand years, with long periods of predominantly positive NAO phases in late medieval times and the late Antique and negative phases prevailing during Roman times and the Little Ice Age. Recent anthropogenic warming is expected to shift the NAO towards a positive phase and, therefore, studying this multi-decadal to centennial variability of the NAO is crucial for the understanding future climate variability.

Last deglaciation 1: Climate networks for marine sediment records and their uncertainties   I have furthermore explored the use of climate networks for ocean sediment records for the last deglaciation in Ch. 8. These are some of the most challenging records to study co-variability, due to the low sampling rates and the high uncertainty in observation times that come with radiocarbon dating of marine cores.

Due to this high degree of uncertainties in the records, I proposed to use the Bayesian framework introduced in Ch. 3 to construct networks in this setting. In this way, the quality of the results can be estimated, which makes them more reliable than those of classical approaches.

To test this method, I have chosen a well studied system, the circulation of the Atlantic ocean during the last deglaciation. As proxies, I use stable isotope ratios of benthic foraminifera, as these are long studied and well understood proxies, so that one can focus on the characteristics of probabilistic climate networks in such a setting.

As a prerequisite, I needed to bring all the records to a shared time axis, which was achieved by shifting all time series in such a way that the onset of deglaciation occurred simultaneously. From the relative timing of the onset of deglaciation one can see the transport of information in the Atlantic, as the earliest records lay in the path of newly formed deep water.

The climate networks of oxygen isotope ratios have shown a general synchronicity of the aligned time series, but the evolving networks have shown that this is limited to the transition period of the deglaciation. Only few features are significant further away from this transition, for example the isolation of the North Atlantic records from the rest of the ensemble during the last glacial maximum.

Carbon isotopes were shown to form two communities in a climate network, one comprising shallow cores in the North Atlantic and another one filling the deep Atlantic and the South Atlantic. This is well in accordance with the known circulation changes during the deglaciation, which mainly influence deep water formation and, hence, the

origin of water masses in the North Atlantic. The anti-phasing of climate variability in these two regions is known as the bipolar seesaw and is also visible as strong negative connections between both regions during Heinrich Event 1 in the evolving networks.

Last deglaciation 2: Combining climate networks and long, transient model simulations The last chapter, Ch. 9, differs from all the others, as it does not use paleoclimate proxy data, but relies on model output from a transient simulation of the last 21,000 years. In this way, I could study the behaviour of climate networks in the case of large-scale transitions on a global scale, without artifacts deriving from proxy sampling, resolution and local proxy effects.

While most global network features stayed rather constant, there were heterogeneous dynamics when comparing different regions. In general, there is a shift of links from the southern to the northern mid-latitudes. This shift is not connected to the bipolar seesaw mechanism of interhemispheric coupling, but rather to two different transitions that are not directly related. In particular, changes in the north are related to a reorganization of the westerly jet stream towards a more tilted path in response to the melting of continental ice sheets, while the southern connectivity decreases with decreasing sea ice cover, probably related to changes in surface-atmosphere interactions. The influence of a changing AMOC is directly visible only in the North Atlantic itself, even though it changes the temperatures globally.

This chapter shows that climate networks, applied to global model output, can be used to detect and characterize shifts in climate dynamics not only on a global, but also on a regional scale.

10.2   What has been achieved by this?

The three main novelties presented in this thesis are the reconstruction method for climate indices presented in Ch. 6, the ensemble based approach to visibility graphs in Ch. 5 and the probabilistic construction of climate networks studied in Ch. 8.

The reconstruction method for climate indices, presented in Ch. 6 is an innovative approach to meet the challenge that most records are not related stationary to the NAO. While this feature increases uncertainty in classical reconstruction methods, it is a key feature on which this method is built upon. If all the records were related to the NAO at all times, the network would likely be more stationary and, hence, could not be used to reconstruct the NAO index. This method opens a broad range of possibilities to study not only singular climate variables like temperature and precipitation, but integrative measures of climate variability, which are much more informative about large scale atmosphere or ocean dynamics.

Still, this method has many limitations, for example, a comparatively low predictive skill, in particular when it comes to transitions between different phases. In addition, the time resolution of the reconstruction is comparatively low. The latter has prevented a use of instrumental data as a calibration target so far, which would be needed to provide a fully independent reconstruction. Therefore, the method presented here should be seen as a complementary method to classical linear regression and not as a replacement.

In other parts of the thesis, I aimed to overcome some of the drawbacks that have hindered a widespread use of visibility graphs and climate networks by the paleoclimate community.

Most methods of non-linear time series analysis have a rather high demand on the length and resolution of the time series, in contrast to paleoclimate records that are typically short and unevenly sampled. The method of visibility graphs is well suited to fill this gap, but suffers from over-sensitivity. In this thesis, I have proposed a combination of an area-wise and an ensemble significance test to overcome the problem of high false positive rates. Using this ensemble approach one can find coherent signals, that allow a wider application of the method.

When applying climate networks to paleoclimate records beyond the Holocene, I suggest that the probabilistic estimation of similarity is the appropriate way to go. The main reason for this is that a Bayesian framework can naturally integrate the many levels of uncertainties present in paleoclimate data, either directly via explicit modeling or by integrating over different realizations of uncertain variables. A network structure obtained in this way is more reliable, as the uncertainties that go into each link have been considered in its construction. While this renders many links insignificant, some structures are still visible in the network topology and, thus, climate networks can be used for a wider field of analysis in a meaningful way.

This is demonstrated by the results of Ch. 8, as these climate networks resemble known changes in past ocean circulation, despite all uncertainties associated with radiocarbon dated sediment records. This motivates a wider application of the method to other regions that are less well studied.

Using these methodological developments, I have provided case studies that demonstrate that large scale changes in the climate system can be analysed efficiently and reliably in a network representation. As more and more paleoclimate records are published, the need for reliable multivariate and spatial analysis methods increases. With this thesis, I have provided different ways in which networks can be a part of this trend.

10.3   Where do we go from here?

The methods and case studies presented in this thesis are not final frameworks for network based paleoclimate analysis, but rather starting points for further developments and applications. I hope that they motivate other researches to consider network based techniques when trying to make sense out of larger sets of paleoclimate records.

For each of these studies, there are multiple pathways of further study, some of which I want to discuss in this section.

In the case of visibility graphs, a more analytical treatment of the area-wise significance test, as has been conducted for other methods, is desirable. Furthermore, the effects of uneven sampling should be studied more systematically.

Together with the study of probabilistic correlations in Ch. 3, the method of network based climate index reconstruction could be developed into a fully Bayesian Hierarchical Modeling approach. In this way all physical relationships between different variables would be represented in a more appropriate way. In addition, uncertainties on different levels could be included more easily. This would also allow the inclusion of more records, in particular those that did not pass our selection criteria. Therefore, the method could

be applied to any integrated climate index that show a spatially heterogeneous response, in particular, other modes of atmospheric circulation, like the Southern Annual Mode or the El Niño Southern Oscillation.

The treatment of uncertainty, that was introduced in Ch. 3 could be developed further to explicitly model unequal sampling between records in a Bayesian way and, hence, take distortions due to interpolation better into account.

All methods need further testing with the help of climate model output and proxy model systems to systematically study their characteristics and drawbacks. While such forward models exist for some archives, they have not been developed for others, for example lake sediment records. The goal of such an analysis would be, to include proxy specific processes to see, how they can change the network structures and thus the results.

Part V | Appendices

A | Additional methods used in this thesis

A.1 Change point detection

The main idea behind change point detection is to find times at which a simple linear model is not sufficient to describe the time series at both sides of that specific point together. In this case the next simplest option, a piecewise linear model, is more appropriate. For a survey of classical change point detection methods see, e.g. Aminikhanghahi and Cook (2017).

In this thesis, I use the Bayesian change point detection algorithm introduced by Ruggieri (2013). This algorithm provides a probability for each observation time that a change is occurring at this time. The number of change points is one of the estimated variables and does not need to be prescribed like in other methods.

An example result is shown in Fig. A.1, for which the change point detection is applied to one of the records discussed in Ch. 8, namely oxygen isotopes in core M35033-4. We see that there are two change points and each has a wide distribution, related to the high uncertainties in observation times for this record (see the detailed discussion in Sec. 8.2).

It should be noted that this definition of change points does not only relate to changes in trend, but also in variability. The exact timing of the change point should be treated with caution, as it merely indicates the point at which a linear model is not sufficient any more, even if a change has already set in before.
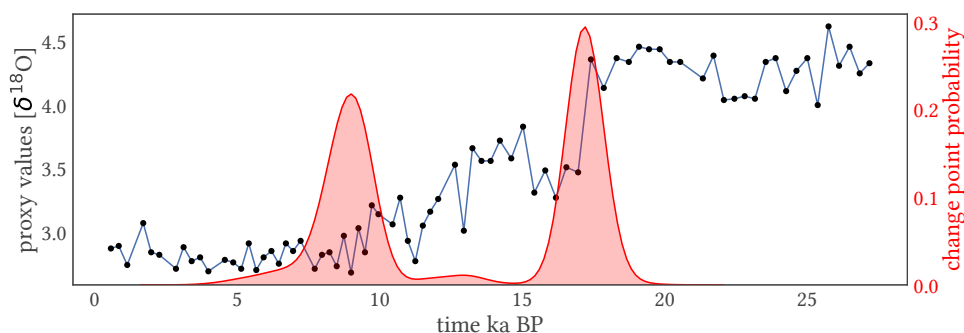
Figure A.1: Example of a time series exhibiting multiple change points (record M35033-4, see Ch. 8) and the estimated change point probability posterior distribution shown in red.

A.2 Empirical mode decomposition

Spectral decomposition tries to separate different components of a time series that vary on different time scales and might thus be related to different processes. Most applications focus on techniques of spectral analysis, in particular Fourier transformation or wavelet analysis (Castagna and Sun, 2006). Most of these methods rely on long and regularly sampled data, even though some progress has recently been made to apply them to unevenly sampled time series (Lenoir and Crucifix, 2018a,b).

Empirical Mode Decomposition (EMD), closely related to the Hilbert-Huang transform, is a more heuristic method, in which time series are decomposed into different modes, the so called Intrinsic Mode Functions (IMFs). For an overview of this method, see the discussion by Huang and Wu (2008). All modes added together restore the original time series. As the spectrum of each mode can be analysed, one can hence combine only those modes that correspond to a specific spectral range, to filter out those components that one is interested in. In this thesis, this is mostly done, by using the Hilbert transform to estimate the instantaneous frequencies and filter via the median instantaneous frequency of each mode.

Several extensions of EMD analysis have been proposed, most prominently ensemble EMD (EEMD Wu and Huang, 2009) or complete ensemble empirical mode decomposition with adaptive noise (CEEMDAN Torres et al., 2011). In these variants, noise is added to the time series repeatedly and the decomposition is repeated for many realizations of these perturbed time series. In this way, the different modes can be distinguished better. The main differences between EEMD and CEEMDAN is the time at which modes are averaged over the ensemble and in the type of noise added at each stage of the algorithm. In this thesis, CEEMDAN is used.

A.3 Clustering algorithms

Cluster analysis describes a set of algorithms to form subgroups out of a large set of objects, based on mutual distance to each other. There is a multitude of algorithms,
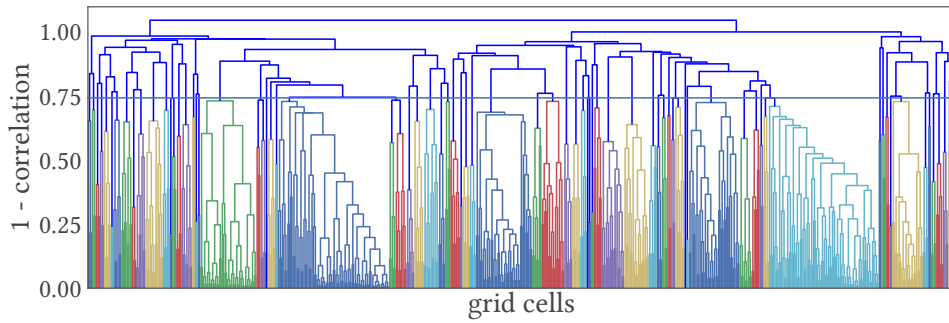
Figure A.2: An example of a dendrogram for average-linkage clustering. This dendrogram corresponds to the cluster analysis applied to the n.s.i. degrees in Ch. 9. The distance matrix is constructed as 1−correlation and the horizontal line marks the threshold used in Ch. 9. Different colours indicate grid cells, that form a cluster up to the threshold value (a so called leaf). As one can see, there is a small number of large leaves and many smaller ones.

depending on the kind of structures that one is interested in and the definition of distance that one considers to be important (Kaufman and Rousseeuw, 1990).

In this thesis, I rely mainly on classical hierarchical cluster analysis. Here, one starts with each object forming its own cluster. Then, a threshold value is successively increased and all clusters that are closer to each other according to some kind of cluster based distance measure are merged. This continues until another prescribed threshold value is reached. This procedure is commonly visualized in a dendrogram, as the one in Fig. A.2.

This method requires three choices: (i) a measure of distances between the different objects, (ii) a measure of distance between different clusters and (iii) a threshold value at which to stop merging clusters.

While decisions (i) and (iii) can be chosen more or less freely by the researcher, there are a few standard options for decision (ii), which then give the name to the particular method used. Common choices are to use the average, the minimum or the maximum distance between objects in each cluster. These are then called *average, single* and *complete*-linkage clustering.

In this thesis, I use hierarchical clustering in combination with correlation matrices C (with a derived distance matrix $D = \mathbb{1} - C$), together with either average or complete clustering. The threshold is chosen for each application.

Another method to detect clusters used in this thesis is network based community detection. In a network, a community is a group of nodes that are stronger connected among each other than they are to the rest of the network (Newman, 2018). There is no unique and generally agreed upon definition and, hence, detecting communities in a network is a complex issue. The method I use in this thesis is the Louvain algorithm (Blondel et al., 2008), in which the network is split into communities in such a way that its modularity is maximized. The modularity is a global network measure, which measures the degree to which a network is separated into subgroups (Newman, 2006). The higher the modularity is, the more links are inside communities and few connecting

different groups. This method is used in Ch. 6 and Ch. 8. Network based community detection tends towards including most records in some cluster, even though this might not be justified in some cases. An example for this is the clustering in Ch. 9 where most grid cells do not show any similarity to other cells. In these cases, a threshold based hierarchical clustering is advantageous.

A.4 Markov Chain Monte Carlo methods

Markov Chain Monte Carlo (MCMC) methods describe a class of algorithms to sample high-dimensional integrals in an efficient way and have become some of the main tools for Bayesian inference. Here, I will only present the main idea of these algorithms, for the technical details I refer to Gelman (2014), Gilks et al. (1995), and von Toussaint (2011).

Monte Carlo methods are those methods in which a (possibly high-dimensional) parameter space is randomly sampled to obtain approximate results for integrative measures over this space. MCMC methods combine this approach with Markov Chains, in which each sample is related to the previous one. Starting from any position in the parameter space, the next sample point is selected in such a way that it contributes most to the integral to be solved, allowing for a more informed and efficient sampling.

There are different sets of rules to decide which sample points are selected at each step and these rules are the main difference between different MCMC algorithms. In this thesis, we use the classical Metropolis-Hasting sampling and a newer algorithm, called NUTS sampling (Hoffman and Gelman, 2014).

As the first sample points are often highly correlated and might sample regions of the parameter space that are not important for the overall integral, they are often discarded as so called *burn-in*. The main challenge when applying MCMC methods is to decide at which point the distribution of samples has converged sufficiently against the true integral. In general, convergence cannot be proven, but lack of convergence is often clearly visible, both by numerical tests, but also by visual inspection. An example for the latter is start the same estimation from different starting points and compare the resulting chains. If the distributions differ, convergence has not been reached.

B | Network measures used in this thesis

In this chapter, we summarize the measures to quantify network structures used in this thesis. We distinguish two types of network measures. Those that assign values to each node separately are called local measures and those that yield one scalar for the whole network are global measures.

B.1 Local network measures

Degree The node degree k_i is the number of all edges that originate from a node n_i, determined as

$$k_i = \sum_{j \in \mathcal{N}} A_{ij}. \tag{B.1}$$

Local clustering coefficient This is the degree to which neighbours of a node n_i are themselves connected to each other. It is given by

$$C_i = \frac{1}{k_i (k_i - 1)} \sum_{j \in \mathcal{N}} \sum_{k \in \mathcal{N}} A_{ij} A_{jk} A_{ki}. \tag{B.2}$$

Link distance If a network is embedded in a physical space, each link can be assigned a distance and a $N \times N$ distance matrix D can be introduced. These distances can be analysed in different ways, for example by looking at the maximum value for each node as

$$d = \max_{j \neq i, A_{ij} \neq 0} D_{ij}. \tag{B.3}$$

B.2 Global network measures

Mean degree All local measures can be averaged over the whole network. In this thesis, we use for example the mean degree, defined as

$$\langle k \rangle = (1/N) \sum_{i \in \mathcal{N}} k_i. \tag{B.4}$$

Link density The link density is the number of links in a network in proportion to the number of possible links. For an undirected graph it is

$$\rho = \frac{2|E|}{N(N-1)}. \tag{B.5}$$

Transitivity

$$T = \frac{3 \times \text{\# of triangles in graph}}{\text{\# of connected triplets in graph}} = \frac{\text{Tr}\left(A^3\right)}{\sum_{i \neq j} \left(A^2\right)_{ij}} \tag{B.6}$$

Hamming distance The Hamming distance measures the overall difference between two networks. Let A^α and A^β describe the adjacency matrices of two different networks. The Hamming distance is then given by

$$H\left(A^\alpha, A^\beta\right) = \frac{1}{N(N-1)} \sum_{i,j,i \neq j} \left| A_{ij}^\alpha - A_{ij}^\beta \right| \tag{B.7}$$

Shortest path length If a path is any set of edges that connects two nodes with each other one can define a matrix L whose elements L_{ij} are given by the lowest number of edges that connect n_i and n_j, the *shortest path lengths*. The *average path length* is then the average over these distances as

$$l = 1/(N(N-1)) \sum_{i,j \in \mathcal{N}, i \neq j} L_{ij}. \tag{B.8}$$

C | Appendix to chapter 3

C.1 Methods to approximate the joint probability distribution

Without loss of generality we discuss most of the following for the time series $\mathbf{X}$, implying that the same steps are applied to any other series $\mathbf{Y}$ as well.

For all methods, we define a shared time axis $\{t_s\}$ and approximate values for times $t_{X,s} \notin \{t_X\}$ from the given observations. We then obtain a new time series $\tilde{\mathbf{X}} = \{\tilde{x}_s, t_{X,s} | x_i, t_{X,i}\}$. As most approximation methods are functions on pairs of time series, we denote them as $I(\mathbf{X}, \mathbf{Y}) = (\tilde{\mathbf{X}}, \tilde{\mathbf{Y}}) = (\{\tilde{x}_s, t_s\}, \{\tilde{y}_s, t_s\})$.

We furthermore define the reference sampling time Δt as the larger of the mean sampling times of the two records: $\Delta t = \max\{\langle\{t_{X,i+1} - t_{X,i}\}\rangle, \langle\{t_{Y,i+1} - t_{Y,i}\}\rangle\}$ and a neighborhood as $T_{X,s} = \{t_{X,i} | |t_{X,i} - t_s| < \tau\}$, with a threshold τ.

C.1.1 Linear Interpolation

The most common way to infer values between observations is that of linear interpolation. Here, the missing observation is assumed to lie on a line between the two neighboring observations. Thus, the shared time axis is given by $\{t_s\} = \{t_X\} \cup \{t_Y\}$. For a given time t_s the neighboring observations are $t_l = \max\{t_i \in \{t_{i,X}\} | t_i < t_s\}$ and $t_u = \min\{t_i \in \{t_{i,X}\} | t_i > t_s\}$. If there is no t_l or t_u, we remove t_s from the shared time axis. The corresponding value $\tilde{x}_s$ is then given as

$$\tilde{x}_s = a + bt_s \tag{C.1}$$

with $b = \frac{x_u - x_l}{t_u - t_l}$ and $a = x_l - bt_l$.

C.1.2 Gaussian kernel interpolation

While being conceptually similar to linear interpolation, kernel based methods use a larger range of observations around t_s. The new value is assumed to be a weighted average of these neighboring observations, the weights K being determined by their distance to t_s:

$$\tilde{x}_s = \frac{\sum_{i \in T_s} K(t_s - t_i) x_i}{\sum_{i \in T_s} K(t_s - t_i)}. \tag{C.2}$$

Here, the kernel function $K(\cdot)$ is given by

$$K(t_s^y - t_i^x) := \frac{1}{\sqrt{2\pi h}} e^{-(t_s^y - t_i^x)^2 / 2h} \tag{C.3}$$

with the bandwidth h, as discussed by Babu and Stoica (2010) and Rehfeld et al. (2011). Here, this bandwidth is denoted as a fraction of Δt, so $h = 0.5$ means $h = 0.5\Delta t$. To reduce the effect of observations too far away from t_s, the kernel is set to zero outside of a neighborhood T_s with $\tau = 3\Delta$. If there are less then 3 observations in T_s we remove t_s from $\{t_s\}$.

Nearest values

Without lack of generality we assume that $N_y \leq N_x$. This method considers observations which occur close to each other in time to be concurrent (Mudelsee, 2010). Thus, if for any $t_s \in \{t_{Y,i}\}$ the corresponding value of $\mathbf{X}$ is given as

$$\tilde{x}_s = x_i, \quad i = \min_j \{|t_s - t_j| | t_j \in T_s\}. \tag{C.4}$$

To omit combining observations which are far from being simultaneous, we set $\tau = 0.5\Delta t$. If there are no observations in T_s we discard t_s.

Slotting

One way to deal with both unequal sampling and to a certain degree time uncertainty is to average over time slots and compare the averages of both time series (Mudelsee, 2010). This procedure is very similar to low-pass filtering, but has a wider applicability, due to a lack of assumptions. For $\{t_s\} = \{t_X\} \cup \{t_Y\}$, $N := |\{t_s\}|$ and a slot width W define a new timescale consisting of sets of times as

$$\{t_{W,i}\} = \{\{t_{s,i} \mid t_{s,0} \geq t_{s,i} \geq t_{s,0} + W\}, \{t_{s,i} \mid t_{s,0} + W \geq t_{s,i} \geq t_{s,0} + 2W\},$$
$$\dots, \{t_{s,i} \mid t_{s,0} + nW \geq t_{s,i} \geq t_{s,N_s}\}\}. \tag{C.5}$$

New observations are then given as the averages over time windows $\tilde{x}_{W,s} = \langle \{x_i | t_i \in T_{W,s}\} \rangle$. The number of pairs of averaged observations can be significantly lower than the ones in each time series, leading to higher uncertainty of estimates. Here, we prescribe W as a multiple of Δt, so that $W = 2$ means $W = 2\Delta t$.

C.2 Pseudoproxy construction

As a first step, we generate a regularly sampled time series $X_r = \{x_{r,i}, t_{r,i}\}$, interpreted as annual values, the intuition being that most archives are representative of a particular season of the year (including seasonality would be straight-forward, e.g., by superimposing a sine to the signal). Then, we define a dependent variable **Y** which is generated as

$$y_i \sim \begin{cases} \mathcal{N}(0, 1) & \text{if } i < \ell \\ \mathcal{N}(cx_{i-\ell}, \sigma_c) & \text{else} \end{cases} \tag{C.6}$$

with the coupling c and $\sigma_c = \sqrt{1 - c^2}$ so that y_i has unit variance. We chose this separation into one dynamic (x) and one dependent variable (y) because it makes the analysis easy. For once, the number of parameters of the model is low. Furthermore the Pearson correlation converges to the true value c and thus, it is very straight-forward to determine biases in the estimates, which might not be the case in other models (see, e.g., the discussion by Runge et al., 2014). In this way, one can use any kind of data for X_r, for example, any stochastic process, but also real-world data.

For constructing our pseudoproxies, we use an evenly sampled Ornstein-Uhlenbeck process, defined as

$$dx_t = \theta(\mu - x_t) + \sigma \, dW \tag{C.7}$$

with θ, μ and $\sigma > 0$ and W being a Wiener process. θ is a drag parameter, indicating the speed at which the process returns to the mean after a deviation and the main free parameter we consider here. In general, the process is more persistent for very low values and resembles a stochastic process with no persistence for high values of θ. Example realizations are shown in Fig. C.1. Without loss of generality we set $\mu = 0$ and $\sigma = \sqrt{2\theta}$ so that the long term variance $\mathrm{var}(x_t) = \dfrac{\sigma^2}{2\theta}$ is 1.

In a marine environment sedimentation happens at variable rates. Hence, we consider the thickness of an annual sedimentation layer S to be drawn from a gamma distribution $p(d) = d^{k-1} \dfrac{e^{d/\vartheta}}{\vartheta^k \Gamma(k)}$ (examples of this distribution are shown in Fig. C.2).

The two moments of the gamma distribution that we vary in this study are its mean S_μ and skewness S_γ. The parameters k and ϑ are then determined as

$$k = 4S_\gamma^2 \quad \text{and} \quad \vartheta = S_\mu/k. \tag{C.8}$$

For our pseudoproxy construction, a sequence of sedimentation layers S_t is drawn from this distribution, implying a monotonically rising sequence of depths $d_t = \sum\limits_{t'=0,\ldots,t} S_{t'}$, as illustrated in Fig. 3.1. Each layer S_t at depth d_t is assigned one value of the time series x_t. As an additional parameter, we introduce the length of the sediment record L, discarding all layers above the cumulative length of L. Thus, the record is now limited to $\vec{d}_{L,t} = \{d_t | d_t <= L\}$.

The sequence $\vec{d}_{L,t}$ is regularly sampled at a unit length interval with sampling depths at $SD_i = i$. All other lengths are interpreted in the units of the sampling interval, for example $S_\mu = 0.2$ means that on average there are 5 layers between two sampling points. What follows is a shorter time series with samples at times $\{t_i'\} = \{t | \max d_{L,t} \leq SD_i\}$. This leaves us with a set of observations O, including depth, time and values: $O_i = \{d_{L,t_i'}, t_i', x_{t_i'}\}$

So far, we have only introduced irregular sampling originating from varying sedimentation rates. For most sediment records one also encounters time uncertainty due to age model uncertainty. To take this into account as well, we add a number of radiocarbon measurements, shown as triangles in Fig. 3.1b. The number of radiocarbon samples be N_{RC}. While t_i corresponds to the (true) calendar ages we will denote radiocarbon ages as $t_{RC,i}$. We chose N_{RC} such that we have ~ 10% of the sampling points as radiocarbon sampling points (but a minimum of 3) and set a measurement uncertainty of $\sigma_{RC} = 10a$ (varying this does not alter the results much, so we reduce the number of free parameters). We have thus obtained radiocarbon samples $RC_j = \{d_{RC,j}, t_j\}$.

We decided to impose the time uncertainty to the calendar ages, as the same value can have different implications at different times in radiocarbon ages, depending on the location on the calibration curve.

The true calendar ages at $d_{RC,j}$ are then transformed to radiocarbon ages by using the marine IntCal13 calibration curve (Reimer et al., 2013). For each sample point i we draw samples from $\mathcal{N}(t_i, \sigma_t)$ and transform them to radiocarbon ages to get the sample radiocarbon time $t_{RC,i}$ and $\sigma_{RC,i}$. This completes the generation of a pseudoproxy series, consisting of depths, observations and radiocarbon samples as $RC_i' = \{d_{RC,i}, t_{RC,i}, \sigma_{RC,i}\}$.

For our analysis, an age model is constructed from these samples to yield radiocarbon ages for each sampling point of O_i with associated calibrated ages and age uncertainties. We use the MoTaBaR algorithm (Heitzig, 2013) to fit a quadratic depth-radiocarbon age curve through the radiocarbon samples RC_i, incorporating the uncertainties (see Fig. 3.1d). The radiocarbon age for each observation O_i is denoted as $t_{RC,i}$ and the uncertainty in age as $\sigma_{RC,i}$.

As there are uncertainties in the calibration curve and due to its non-monotonicity there is a set of calendar ages that correspond to a single radiocarbon age t_{RC}, denoted as $S(t_{RC})$. To yield calendar ages, we hence first draw a sample t_{RC}' from the possible radiocarbon ages $\mathcal{N}(t_{RC,O_i}, \sigma_{RC,O_i})$, and then use $S(t_{RC}')$ to detain possible values of the calendar age. We denote this procedure in short as $C(t_{RC}, \sigma_{RC})$ We repeat this 1000 times for each observation i, hence we have an $|\{O_i\}| \times 1000$ calendar age matrix $\underline{A}_{i,j} = C(t_{RC,i}, \sigma_{RC,i})$

Any realization of this age model has to fulfill monotonicity to prevent age reversals along the modelled sequence. To effectively draw such realizations, we start with the median time-scale as $t_{cal,O_i}^m = \text{median}_j(A_{i,j})$ and perturb it by sampling for each observation a value from A while imposing as an upper limit the median time of the following observation. A sampled time for observation i is $t_{cal,O_i}^r \in \{A_{i,j} | A_{i,j} < t_{cal,O_{i-1}}^m\}$.

The same procedure is then repeated for the dependent time series **Y**. In Fig. 3.1e, a median age model and a set of realizations from the age model for one pseudoproxy are illustrated.

To study the effect of the systematic uncertainty due to calibration we use the median age model $\{t_{cal,O_i}^m\}$. To additionally incorporate calibration uncertainties we use the full ensembles of realizations $\{t_{cal,O_i}^r\}$. These synthetic records are created at a multi-centennial time scale. Due to the many non-monotonic features of the calibration curve at this time scale we expect it to lead to more ambiguous distributions than similar curves for longer time scales. Hence, we expect our results to be valid for different time scales as well.

parameter	abbreviation	sample interval
time series length		$[25, 300]$
coupling strength	c	$[0.1, 0.9]$
drag parameter	θ	$[0.01, 0.9]$
sedimentation rate mean	μ_S	$[0.2, 0.5]$
sedimentation rate skewness	γ_S	$[1, 2]$

Table C.1: Intervals out of which the parameters are drawn for the pseudoproxy experiments. Their meaning is discussed in Sec. 3.3 and Appendix Sec. C.2. All lengths are considered to be given in a dimensionless unit. The length of a time series corresponds to the number of observations.

C.3 Additional figures
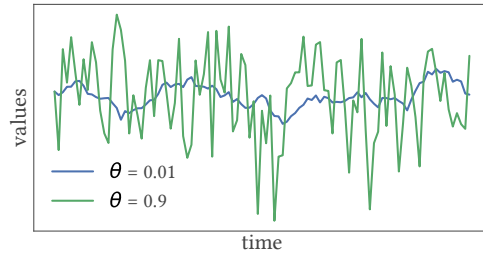
Figure C.1: Two example realizations of the Ornstein-Uhlenbeck process with different drag parameters. The different autocorrelations are clearly visible, with a low drag parameter leading to a highly persistent time series.
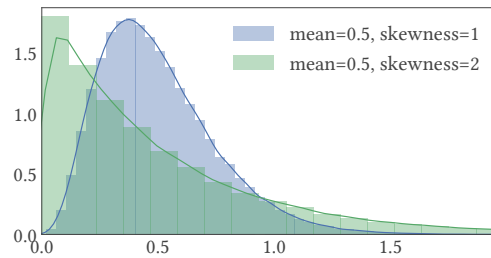

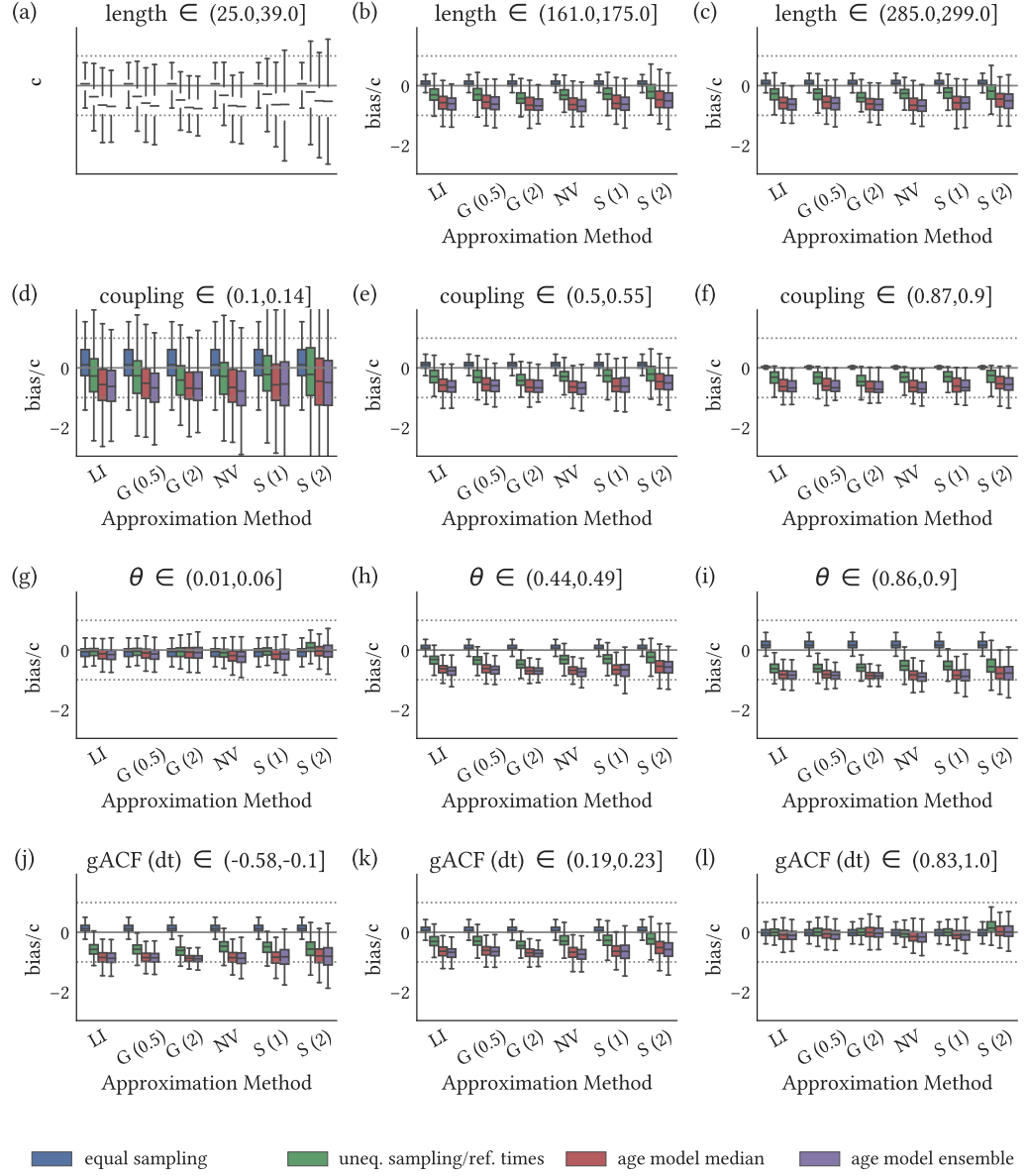Figure C.2: The gamma distribution for two different values of skewness.

Figure C.3: Distribution (box plot) of scaled bias in dependence of different experimental parameters, grouped into different approximation methods and levels of time and sampling uncertainty. The values are scaled to the coupling strength to make them comparable. For the experiment parameters, we only show three parameter ranges, the lowest and highest decile and one from the middle of the tested values
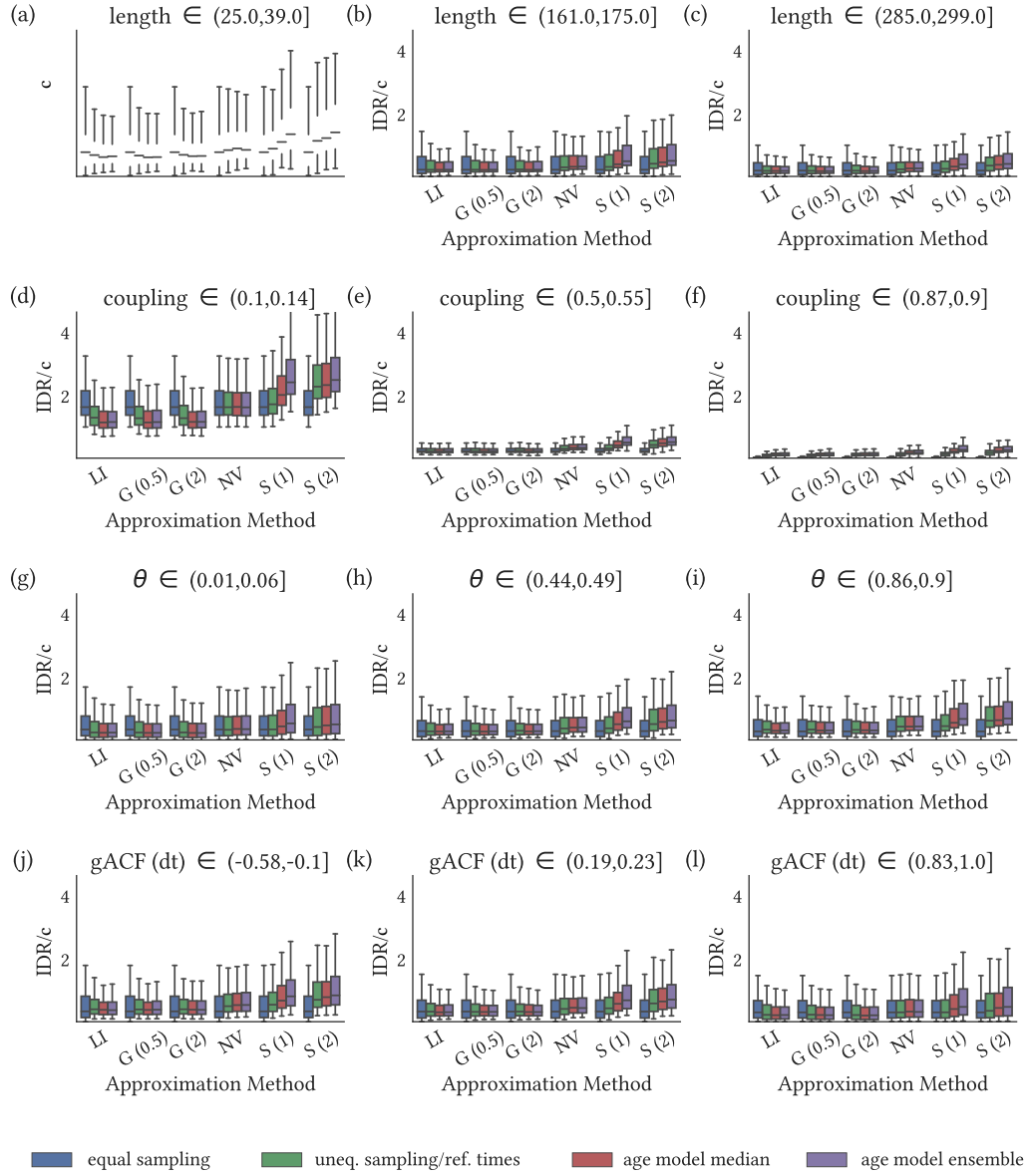
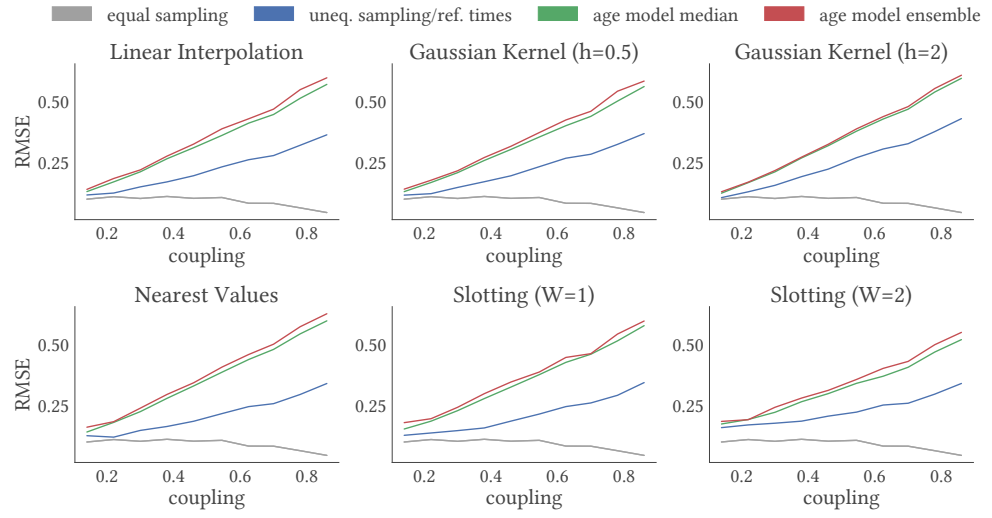Figure C.4: Same as in Fig. C.3, but for the scaled interdecile range (IDR).

Figure C.5: Root mean square error (RMSE) in relation to the true coupling strength, shown for different approximation methods and different levels of time and sample uncertainty.
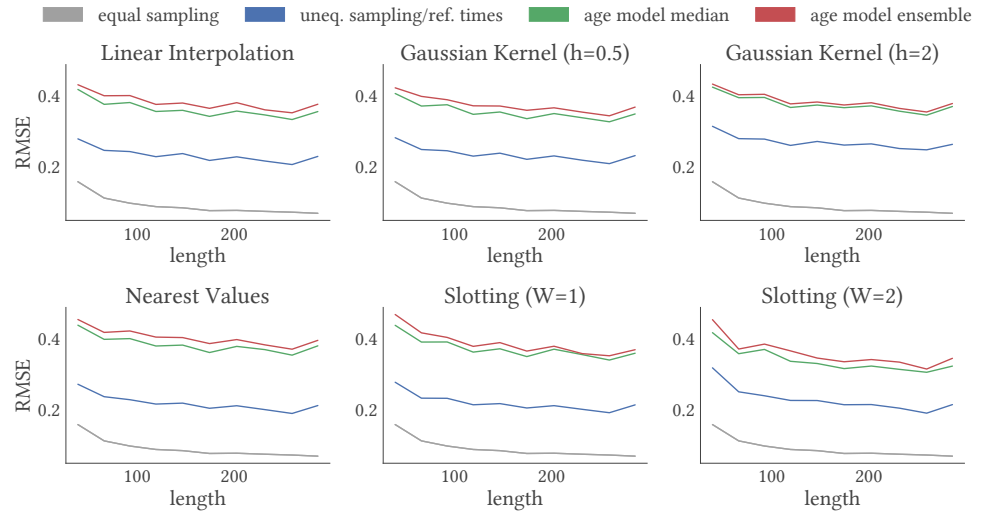

Figure C.6: Same as in Fig. C.5, but for the dependence on the time series length.
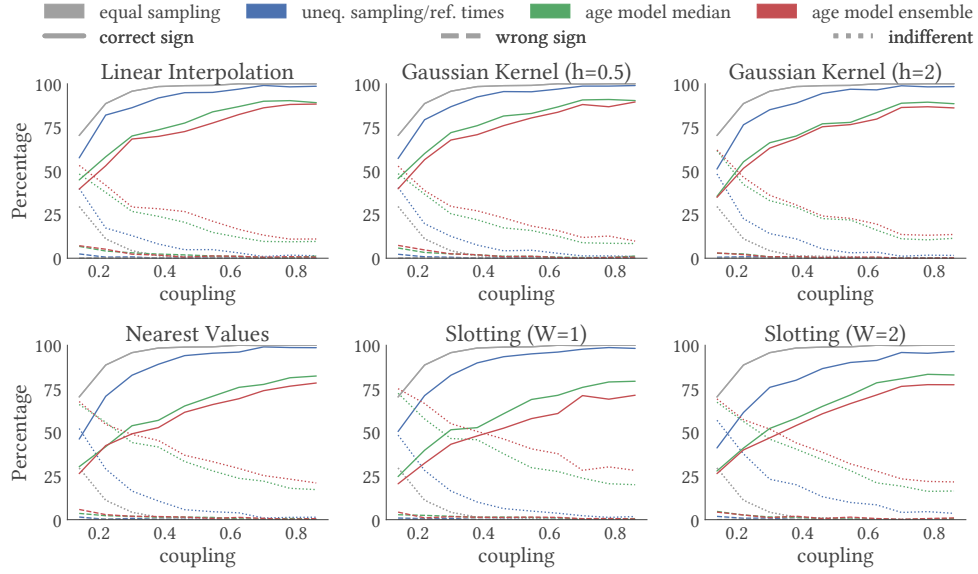
Figure C.7: The fraction of correctly, wrong and indifferently estimated signs of correlation in relation to the true coupling strength, shown for different approximation methods (subplots) and different levels of uncertainty (marked by colours).
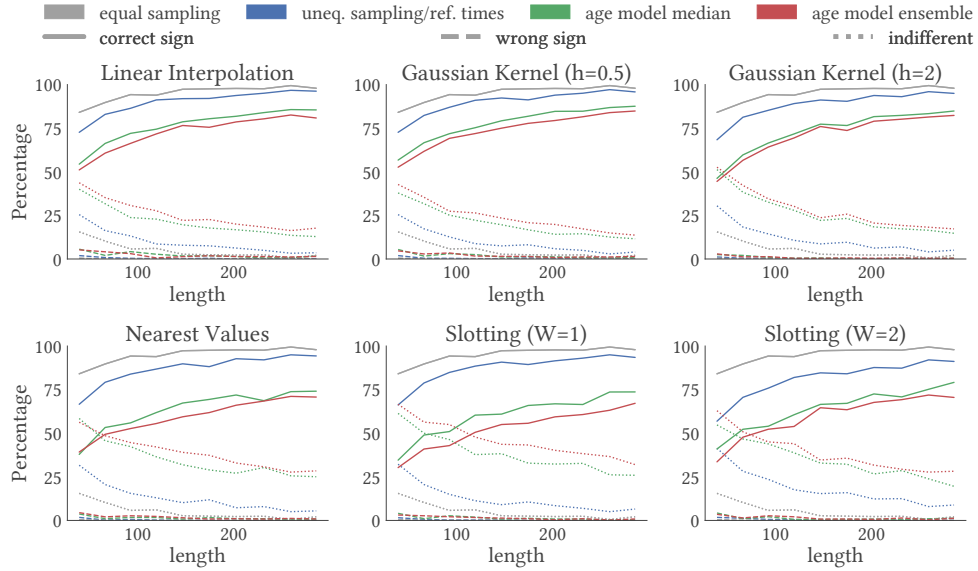

Figure C.8: Same as in Fig. C.7, but for the dependence on the time series length.
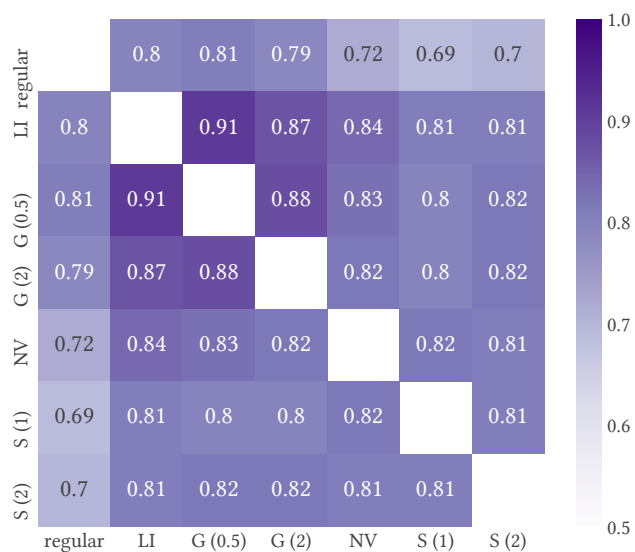
Figure C.9: Fraction of agreement in estimated sign between different approximation methods.
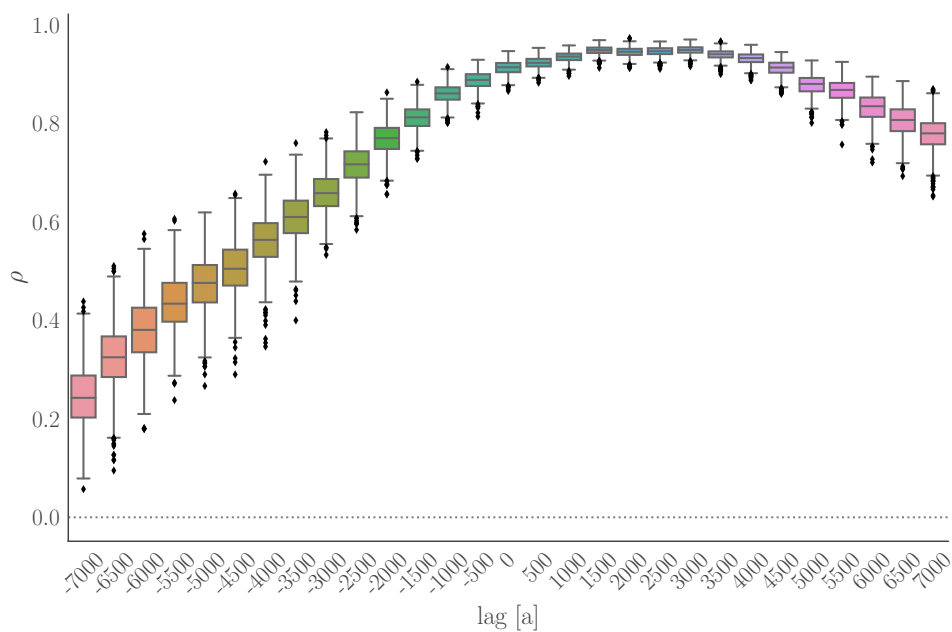

Figure C.10: Posterior distributions of ρ for different time lags between the two marine paleoclimate records.

D | Appendix for Chapter 5

name	latitude	longitude	archive	proxy	variable	reference
Amarnaes	66°3′N	16°1′E	tree ring	BI	RSF_i	Björklund et al. (2015)
Arjeplog	66°3′N	18°2′E	tree ring	BI	RSF_i	Björklund et al. (2015)
Finish Lapland	69°N	25°E	tree ring	TRW	Temp.	Helama et al. (2009)
Forfjorddalen	69°8′N	17°22′E	tree ring	TRW	TRSGI	Kirchhefer (2001)
Hvitárvatn	64°6′N	19°9′E	lake sediment	TOT	TOT	Larsen et al. (2011)
Jämtland	63°5′N	15°5′E	tree ring	BI	RSF_i	Gunnarson et al. (2011)
Kittelfjaell	65°2′N	15°5′E	tree ring	BI	RSF_i	Björklund et al. (2013)
Korttajärvi	62°33′N	25°68′W	lake sediment	Dens.	Dens.	Tiljander et al. (2003)
Kallio-Kourujärvi	62°33′N	27°E	lake sediment	TOT	TOT	Saarni et al. (2015)
Kalliojärvi	63°13′N	25°22′E	lake sediment	TOT	TOT	Saarni et al. (2016)
Laanila	68°31′N	27°2′E	tree ring	BI	HIindex	Larsen et al. (2011)
Lehmilampi	63°62′N	29°1′W	lake sediment	TOT	TOT	Haltia-Hovi et al. (2007)
Nautajärvi	61°81′N	24°68′W	lake sediment	OI	OI	Ojala and Alenius (2005)
N-Scan	65°5′ – 69°5′N	19°8′ – 32°E	tree ring	MXD	Temp.	Esper et al. (2012)
Tjeggelvas	66°6′N	17°6′E	tree ring	BI	RSF_i	Björklund et al. (2013)
Torneträsk	68°26′N	19°6′E	tree ring	MXD	Temp.	Melvin et al. (2013)

Table D.1: The records considered in this study. There are three types of tree ring records, namely those based on tree ring width (TRW), maximum latewood density (MXD) and blue intensity (BI). The tree ring variables are (summer) temperature (Temp.) as well as indices based on tree ring with (TRSGI), tree growth (HIindex) and a individual signal-free RCS approach (RSF_i). The lake sediments' observables are total varve thickness (TOT), relative density (Dens.) and an organic index (OI).
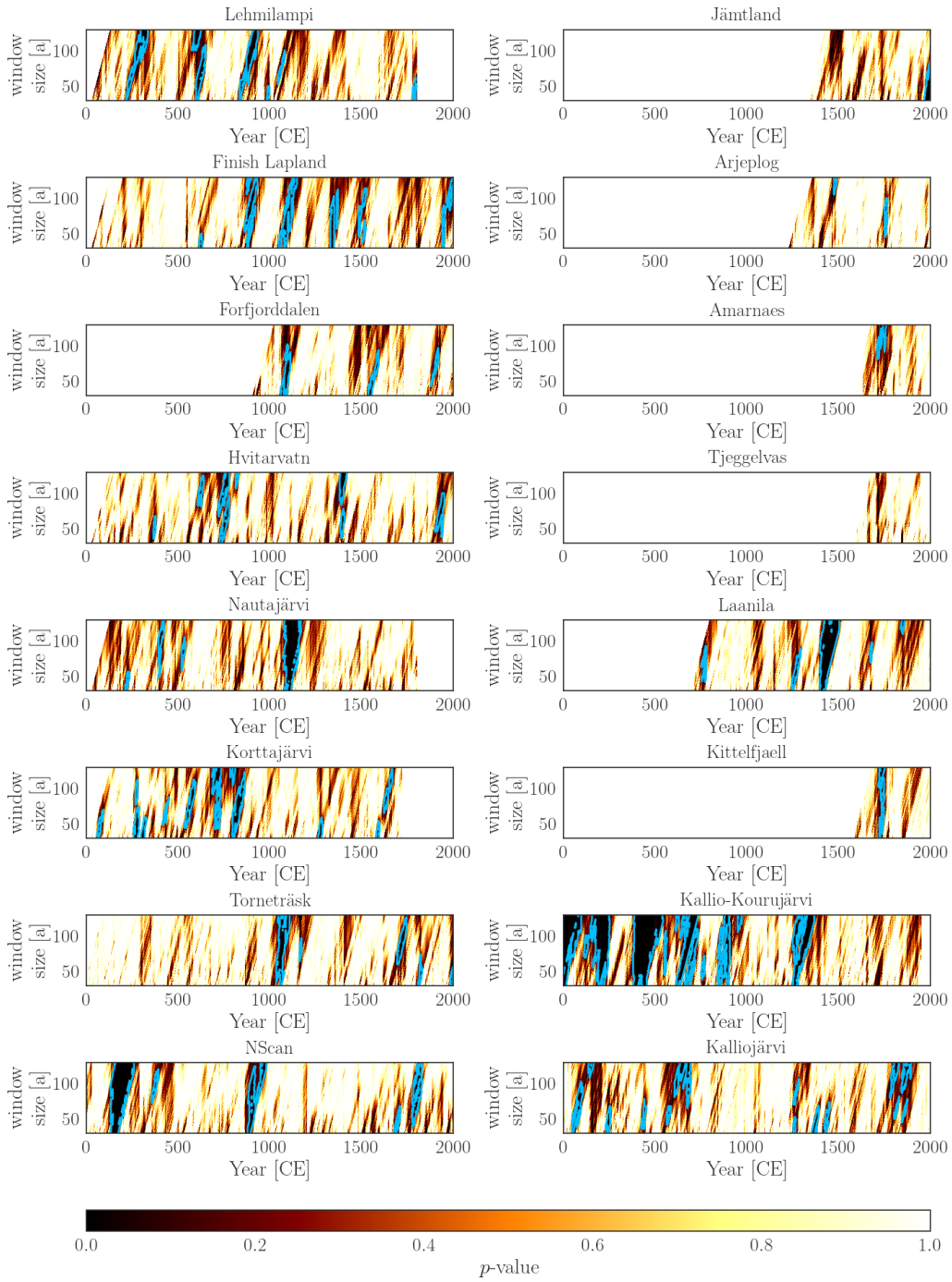
Figure D.1: The results of the single record HVG based tests for time-reversibility on the time-window-size plane. The color indicates the *p*-value of the KS-test. Those areas with *p*-value below 0.1 are considered significant and contoured in blue.
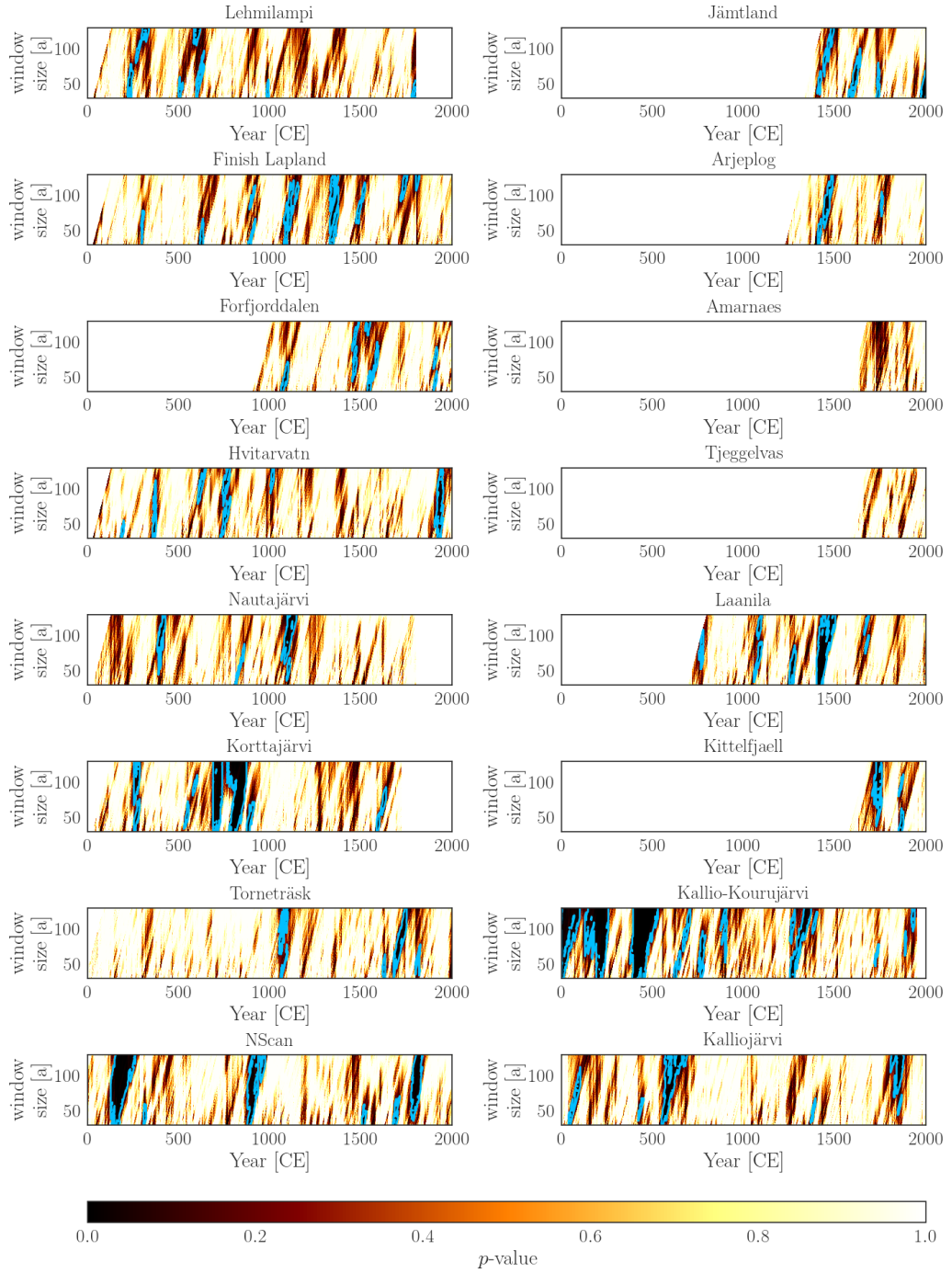
Figure D.2: Same as in Fig. D.1 but for the sign-flipped time series $\{-x_t\}$.
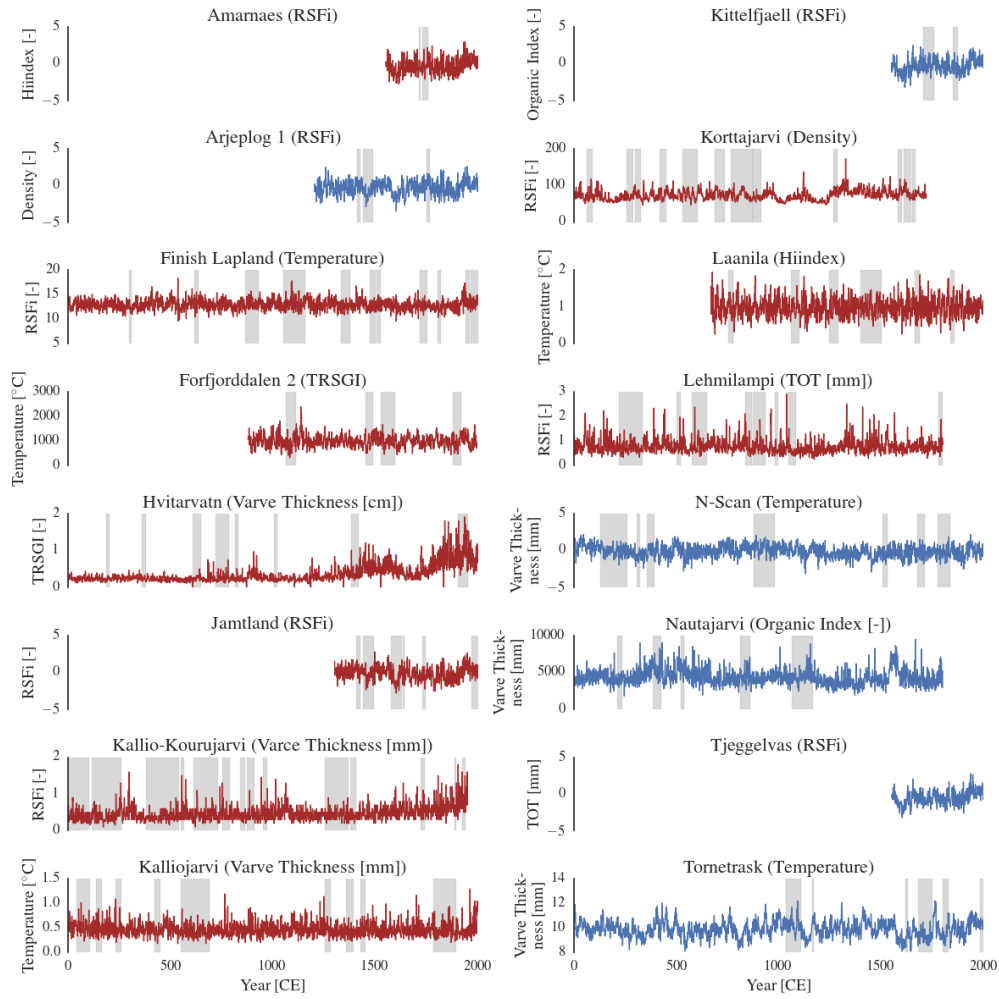
Figure D.3: The paleoclimate records considered in this study after millenial-scale detrending. Tree ring records are shown in red, lake sediments in blue. Grey-shaded periods indicate time intervals which are found to be time-irreversible by our testing procedure.
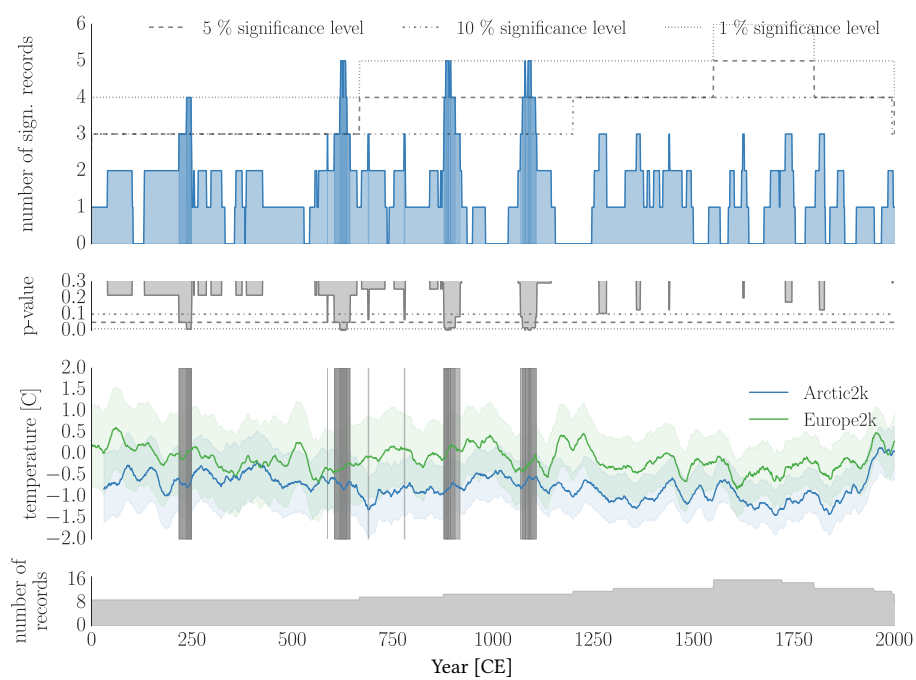
Figure D.4: Summary statistics using KS tests with a significance threshold of $\alpha = 0.05$.
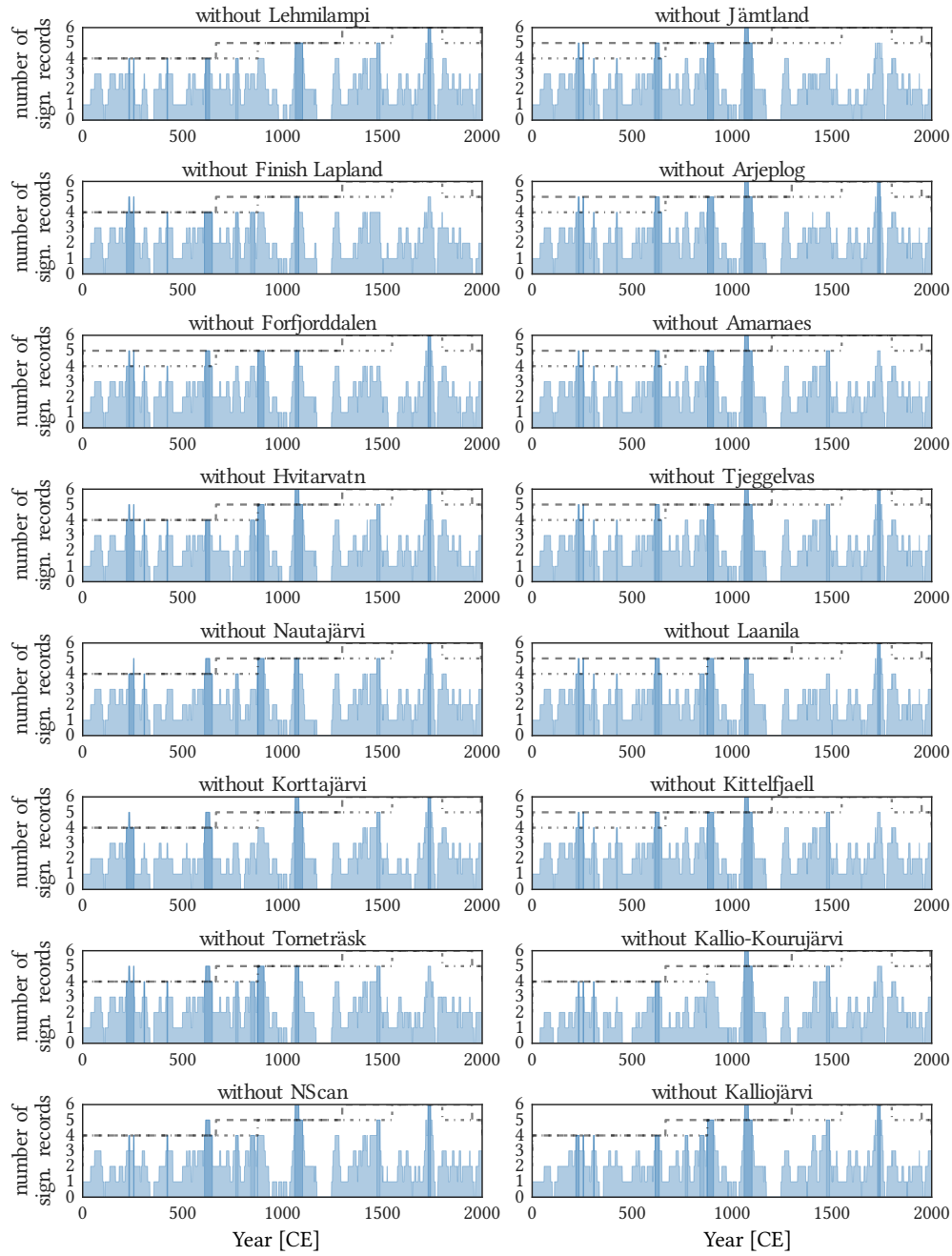
Figure D.5: Number of significantly time-irreversible records when one record is removed. The long (short) dashed line indicate the 5% (10%) confidence level.
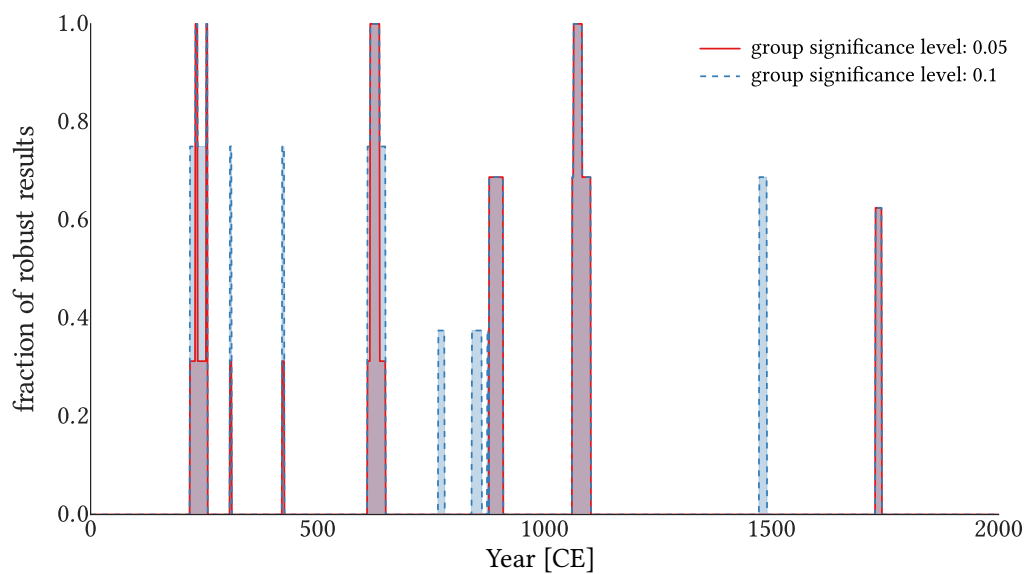
Figure D.6: Fraction of reduced (leave-one-out) ensembles that show significant HVG time-irreversibility according to our group significance test.
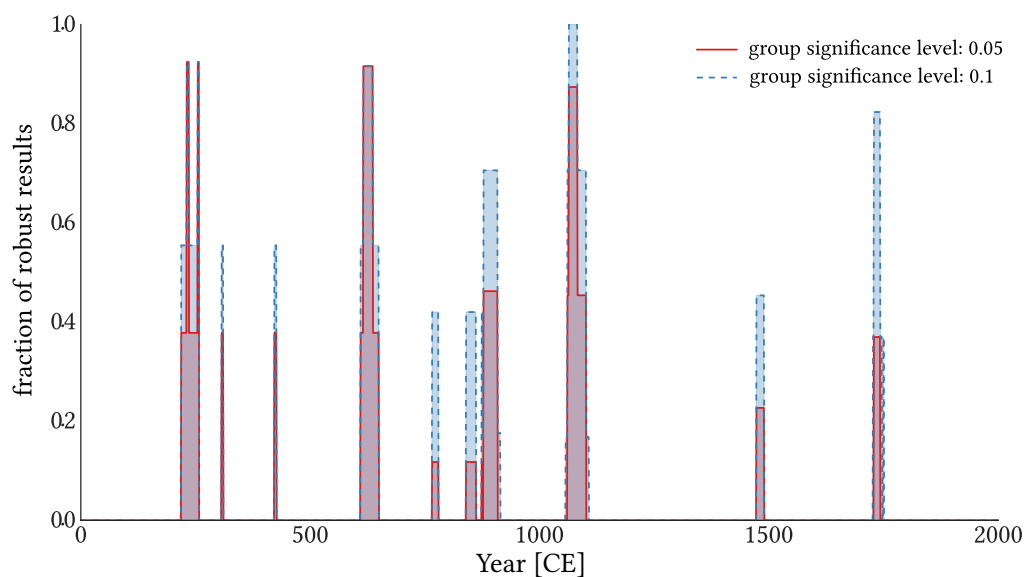
Figure D.7: As in Fig. D.6 for the leave-two-out case.
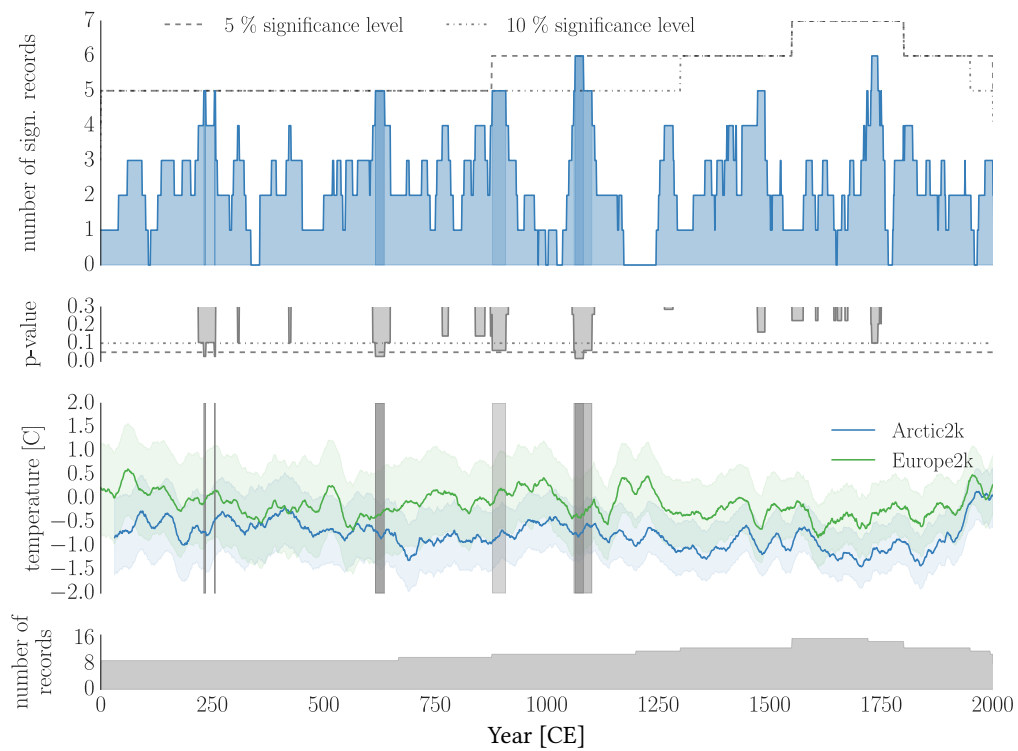
Figure D.8: Summary statistics with one artificial record without significant intervals of HVG time-irreversibility being added to the ensemble.
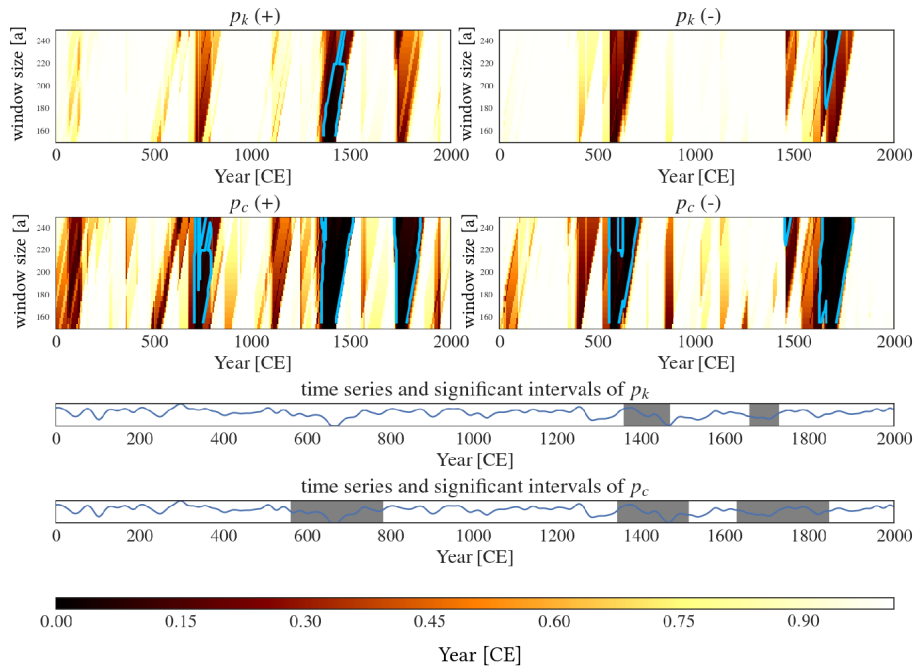
Figure D.9: An example of a test for HVG time-reversibility, applied to the reconstruction of solar activity by Steinhilber et al. (2009). The upper left two pannels show the results for the time directed degree and local clustering coefficients. Areas contoured in blue are those at which the *p*-value of the KS-test is below 0.1. On the upper right panels the same is shown for the time series with flipped sign, the motivation for this analysis is discussed in Sec. 5.2. The lower two panels show the time series with the thus detected times of HVG time-irreversibility for the degree (top) and local clustering coefficients (bottom).

E | Appendix to Chapter 6
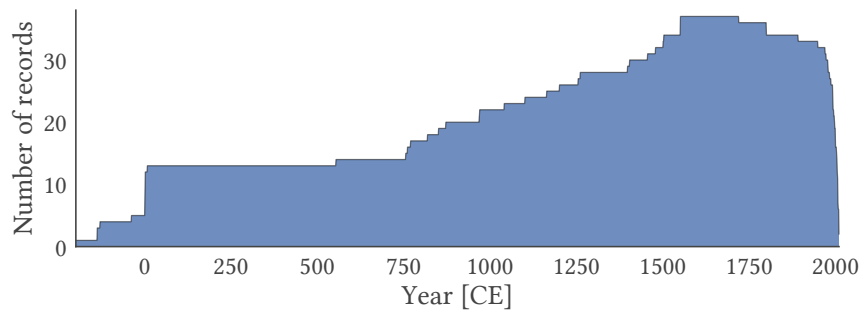
Figure E.1: Number of records covering a given year.
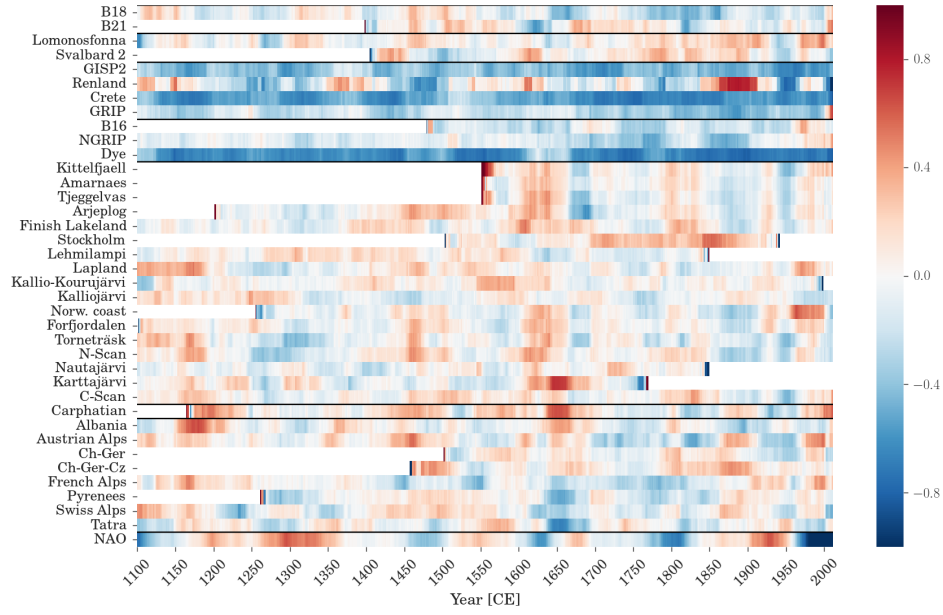
Figure E.2: Correlations between the different records used in our study and the NAO reconstruction by Ortega et al. (2015), averaged over 50-year running windows. Spatial clusters as discussed in the main text are separated by black lines.
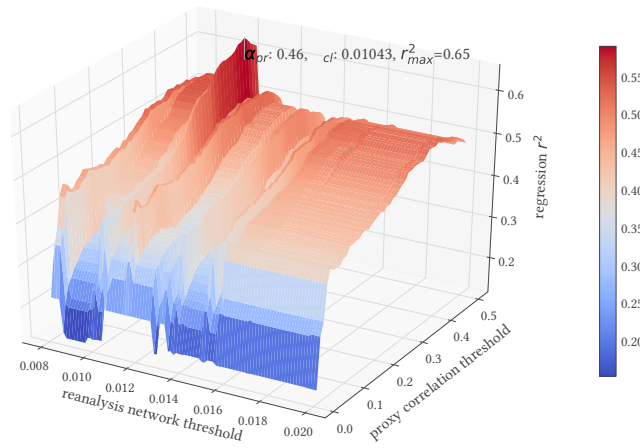
Figure E.3: r^2 values between the NAO reconstruction $\overline{NAO}_{\mathrm{Ortega},\mathscr{W}}$ and the OLS regression models obtained for different parameter combinations of α_{pr} and α_C. The resulting clusters of each pair of parameters have been used to fit a linear model (see main text for details) based upon the cross-link densities to the 50 year-averaged NAO reconstruction by Ortega et al. (2015). The parameter values used in this study are those that maximize r^2.
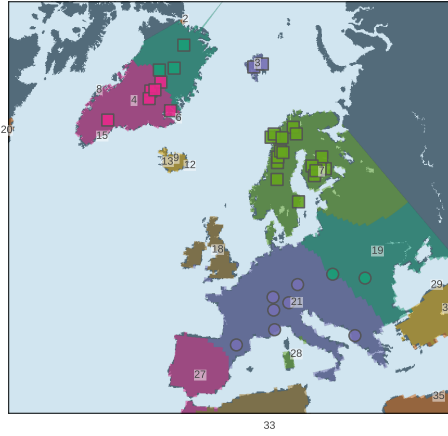
(a) JJA temperature, $\alpha_C = 0.008$
(b) DJF temperature, $\alpha_C = 0.007$
(c) annual temperature, $\alpha_C = 0.008$
(d) all seasonal temperatures, $\alpha_C = 0.0115$
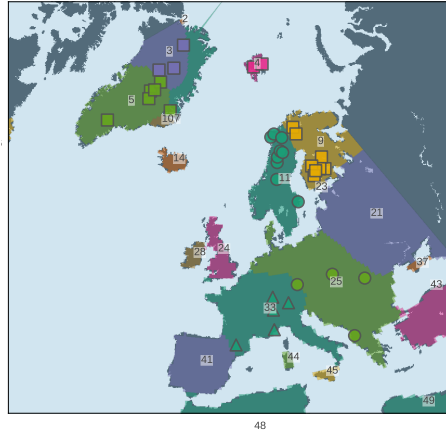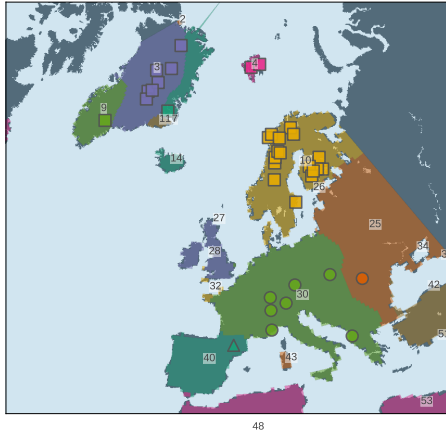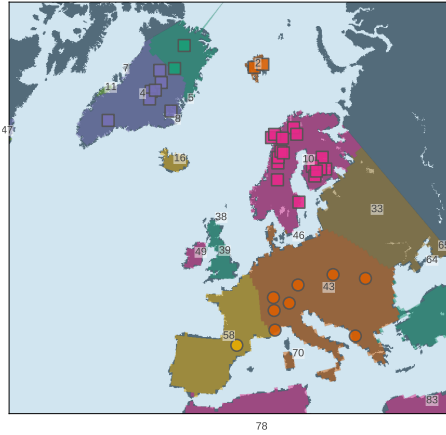
Figure E.4: Geographical clusters based on different temperature-related variables from the ERA-20C reanalysis. The threshold values were selected as described for Fig. E.3.
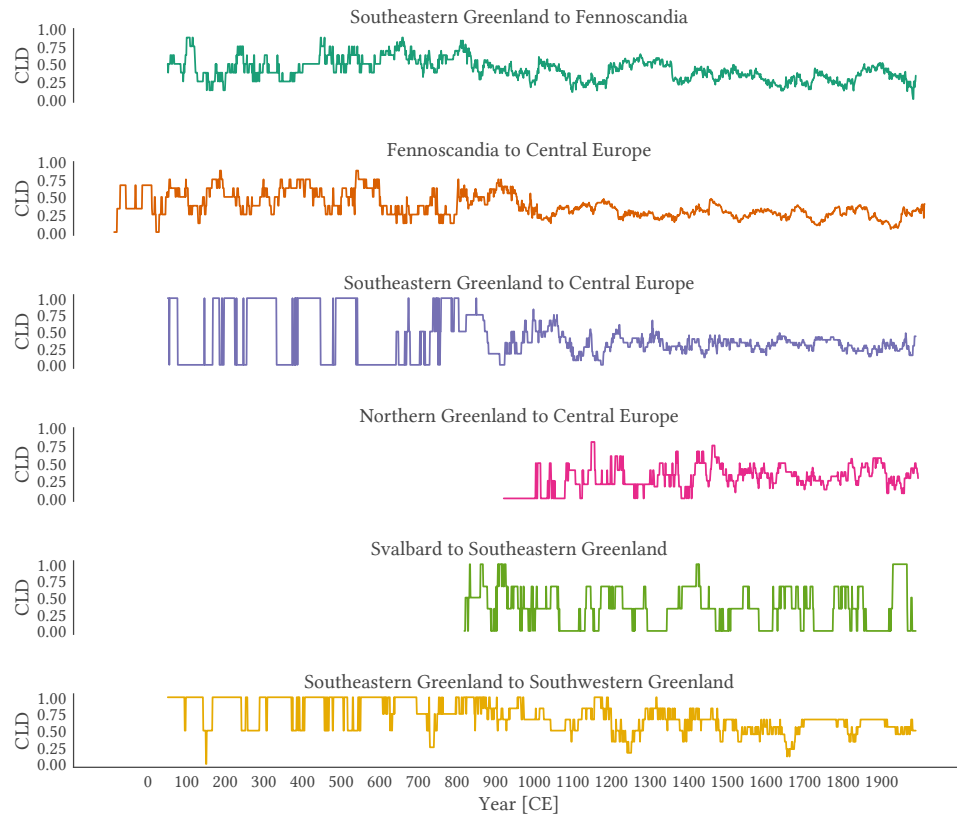
Figure E.5: Evolution of the six cross-link densities with the largest regression coefficients in the linear model (see Tab. E.2).
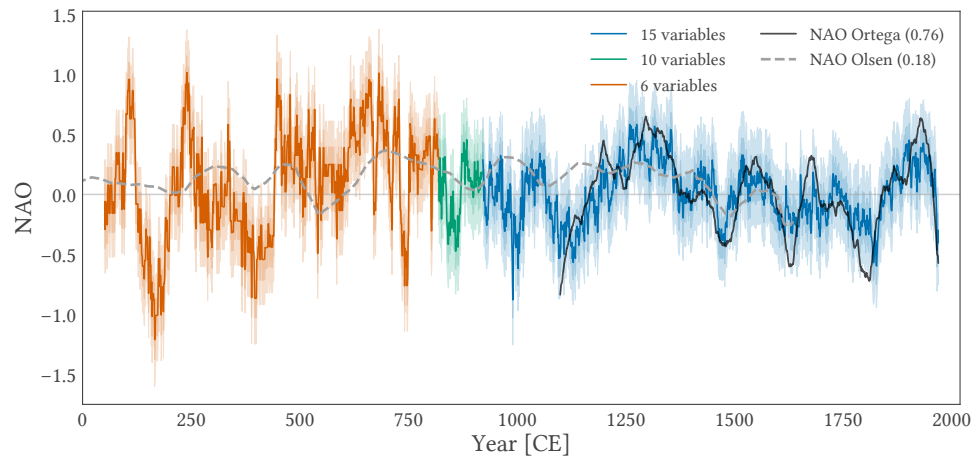
Figure E.6: The reconstructed NAO index, using the linear model fitted to $\overline{NAO}_{\text{Ortega},\mathscr{W}}$: The latter reconstruction is shown as a black line, while another multi-millennial reconstruction by Olsen et al. (2012) is shown as a dashed line.
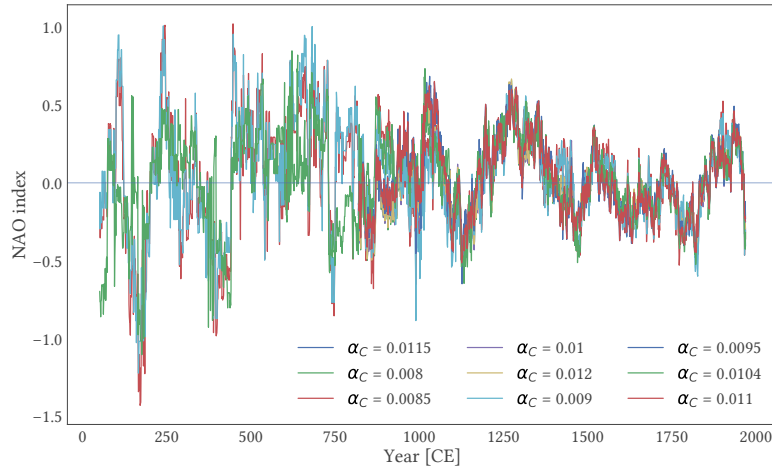
Figure E.7: Reconstructions of the NAO index obtained with different parameters of α_C. Changes in α_{pr} did not change the results much.
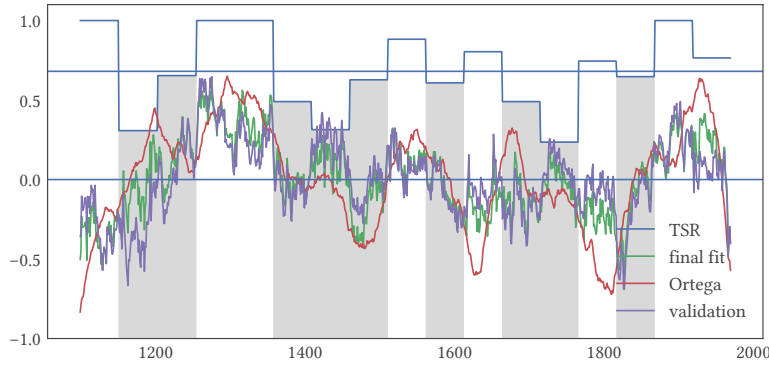
Figure E.8: Testing the regression quality by using (mutually exclusive) 50-year time windows as validation and the rest as training data for the linear regression model. The red line corresponds to the regression target, the 50-year running average of the NAO reconstruction by Ortega et al. (2015). The purple line indicates the values predicted by our model for each individual time window, the green line denotes the median of the final regression model, and the blue line shows the true sign ratio (TSR) for each window. The horizontal line marks the mean value of TSR (0.69); periods with lower values are shaded in gray.

name	long. [°W]	lat. [°N]	archive	proxy	variable	first [CE]	last [CE]	reference
Albania	41	20	TR	TRW	TRW index [-]	968	2008	Seim et al. (2012)
Amarnaes	65.9	16.1	TR	MXD	RSF_i	1550	2010	Björklund et al. (2013)
Arjeplog	66.3	18.2	TR	BI	$BRSF_i$	1200	2010	Björklund et al. (2013)
Austria*	47	10.7	TR	TRW	T [°C]	1	2003	Büntgen et al. (2011)
B16	73.94	-37.63	IC	$\delta^{18}O$	$\delta^{18}O$ [‰]	1478	1992	Fischer et al. (1998)
B18	76.62	-36.4	IC	$\delta^{18}O$	$\delta^{18}O$ [‰]	871	1992	Fischer et al. (1998)
B21	80	-41.14	IC	$\delta^{18}O$	$\delta^{18}O$ [‰]	1397	1992	Fischer et al. (1998)
Ch-Ger	48	8	hist.		T [°C]	1454	1970	Wetter and Pfister (2011)
Ch-Ger-Cz	49	13	hist.		T [°C]	1500	2007	Dobrovolný et al. (2010)
Carphatian	47	25.3	TR	TRW	T [°C]	1163	2005	Popa and Kern (2009)
Crete	71.12	-37.32	IC	$\delta^{18}O$	$\delta^{18}O$ [‰]	553	1973	Vinther et al. (2010)
CScan	63	14.05	TR	MXD	T [°C]	850	2011	Zhang et al. (2016)
Dye	65.18	-43.83	IC	$\delta^{18}O$	$\delta^{18}O$ [‰]	1	1978	Vinther et al. (2010)
Forfjordalen	69.08	17.22	TR	TRW/MXD	trsgi	1100	2007	McCarroll et al. (2013)
French Alps	44	7.5	TR	TRW	TRW index [-]	969	2007	Büntgen et al. (2012)
GRIP	72.58	-37.64	IC	$\delta^{18}O$	$\delta^{18}O$ [‰]	850	2011	Vinther et al. (2010)
Lehmilampi	63.62	29.1	LS	VT	VT [mm]	1	1800	Haltia-Hovi et al. (2007)
Lapland	69	25	TR	TRW	T [°C]	0	2000	Helama et al. (2009)
Kallio-Kourujärvi	62.33	27.04	LS	VT	VT [mm]	-129	149	Saarni et al. (2015)
Kalliojärvi	63.13	25.22	LS	VT	VT [mm]	-137	2000	Saarni et al. (2016)
Korttajärvi	62.33	25.68	LS	XRD	XRD	0	1720	Tiljander et al. (2003)
Kittelfjael	65.2	15.5	TR	MXD	RSF_i	1550	2007	Björklund et al. (2013)
Lomonosfonna	78.87	17.425	IC	$\delta^{18}O$	$\delta^{18}O$ [‰]	769	1997	Divine et al. (2011)
Nautajärvi	61.81	24.68	LS	OM	OMA	0	1800	Ojala and Alenius (2005)

NGRIP	75.1	-42.32	IC	$\delta^{18}O$	$\delta^{18}O$ [‰]	0	1995	Vinther et al. (2006)
Norw. coast	68.78	15.75	TR	TRW	TRW index	1254	1993	Kirchhefer (2001)
NScan	68	25	TR	MXD	T [°C]	1	2006	Esper et al. (2012)
Pyrenees	42.5	1	TR	MXD/TRW	T [°C]	1260	2005	Dorado Liñán et al. (2012)
Renland*	71.27	-26.73	IC	$\delta^{18}O$	$\delta^{18}O$ [‰]	3	1993	Vinther et al. (2008)
Stockholm	59.32	18.06	hist.		T [°C]	1502	1892	Leijonhufvud et al. (2010)
Svalbard 2*	79.83	24.02	IC	$\delta^{18}O$	$\delta^{18}O$ [‰]	1400	1998	Isaksson et al. (2005)
Swiss Alps*	46.4	7.8	TR	MXD	T [°C]	755	1892	Büntgen et al. (2006)
Tatra	49	20	TR	TRW	T [°C]	1040	2011	Büntgen et al. (2013)
Tjeggelvas	66.6	17.6	TR	BI	BRSF$_i$	1500	2010	Björklund et al. (2013)
GISP2	72.1	-38.8	IC	$\delta^{18}O$	$\delta^{18}O$ [‰]	818	1987	Grootes and Stuiver (1997)
Torneträsk	68.26	19.6	TR	TRW/MXD	T [°C]	-39	2010	Melvin et al. (2013)

Table E.1: The data used in this analysis. The corresponding references and data citations can be found in Tab. S2. Those records also used in the reconstruction by Ortega et al. (2015) are printed bold. Records marked with a star do not have annual resolution at all times.

connection	mean value	standard deviation
SE Greenland to Fennoscandia	1.9	0.09
Fennoscandia to Central Europe	- 0.73	0.1
SE Greenland to Central Europe	-0.59	0.09
N Greenland to Central Europe	-0.26	0.05
Svalbard to SE Greenland	0.23	0.05
SE Greenland to SW Greenland	0.21	0.05
Svalbard to Central Europe	0.14	0.04
SE Greenland to Central Europe	-0.13	0.08
N Greenland to SW Greeland	0.11	0.03
N Greenland to SE Greenland	-0.11	0.03
SW Greenland to Fennoscandia	-0.11	0.09
N Greenland to Svalbard	-0.04	0.02
N Greenland to Fennoscandia	0.04	0.08
Svalbard to SW Greenland	-0.03	0.03
Svalbard to Fennoscandia	- 0.003	0.05

Table E.2: Mean values and standard deviations of the regression coefficients corresponding to the individual cross-link densities used in this study.

F | Appendix to Chapter 8

Table F.1: The proxy records used in this chapter. Those marked by an asterisk are records for which we use a normal distribution for the radiocarbon dates.

core	lat. [°N]	lon. [°E]	depth [m]	reference
ENAM93-21	66.68	-4	1020	Rasmussen et al., 1996; Rasmussen et al., 1998
EW9209-1JPC	5.91	-44.2	4056	Curry and Oppo (1997)
EW9302-24GGC	61.76	-21.67	1629	Oppo et al. (2015)
EW9302-26GGC*	62.32	-21.46	1450	Oppo et al. (2015)
EW9302-25GGC*	62.06	-21.47	1523	Oppo et al. (2015)
GeoB-1711-2*	-23.32	12.38	1967	Little et al. (1997), Vidal et al. (1999), and Waelbroeck et al. (2006)
GeoB1720-2	-28.99	13.84	1997	Dickson et al. (2009)
GeoB9508-5	15.5	-17.95	2384	Mulitza et al. (2008)
GeoB9526-4	12.44	-18.06	3223	Zarriess and Mackensen (2011)
GIK13289-2	18.07	-18.01	2485	Sarnthein (2004) and Sarnthein et al. (1994)
KNR159-5-17JPC	-27.7	-46.49	1627	Tessin and Lund (2013)
KNR159-5-20JPC	-28.64	-45.54	2941	Tessin and Lund (2013)
KNR159-5-30GGC	-28.13	-46.07	2500	Tessin and Lund (2013);

KNR159-5-33GGC	-27.57	-46.18	2082	Lund et al. (2015) and Tessin and Lund (2013)
KNR159-5-36GGC	-27.27	-46.47	1268	Sortor and Lund (2011)
KNR159-5-63GGC	-28.36	-45.84	2732	Lund et al. (2015)
KNR159-5-78GGC*	-27.48	-46.33	1829	Tessin and Lund (2013)
KNR159-5-90GGC	-27.35	-46.63	1105	Curry and Oppo (2005) and Lund et al. (2015)
KNR159-5-125GGC*	-29.53	-45.08	3589	Hoffman and Lund (2012) and Lund et al. (2015)
KNR166-2-26JPC*	24.1951	-83.15	546	Came et al. (2008)
KNR166-2-29JPC	24.17	-83.16	648	Came et al. (2008)
KNR166-2-31JPC	24.13	-83.18	751	Came et al. (2008)
KNR166-2-GGC73	23.45	-79.26	542	Lynch-Stieglitz et al. (2009)
M35003-4	12.09	-61.24	1299	Rühlemann et al. (1999)
MD03-2707	2.502	9.395	1295	Weldeab et al. (2016)
MD07-3076Q	-44.09	-14.13	3770	Waelbroeck et al. (2011)
MD95-2037	37.05	-32.02	2159	Gherardi et al. (2009) and Labeyrie et al. (2005)
MD99-2339	35.89	-7.53	1177	Voelker et al. (2006)
NA87-22	55.3	-14.41	2161	Vidal et al. (1997) and Waelbroeck et al. (2006)
ODP984	61.0	-24.0	1648	Lund et al. (2015) and Praetorius et al. (2008)
RAPiD-15*	63.29	-17.13	2133	Oppo et al. (2015) and Thornalley et al. (2010)
RAPiD-17 *	61.48	-19.54	2303	Oppo et al. (2015) and Thornalley et al. (2010)
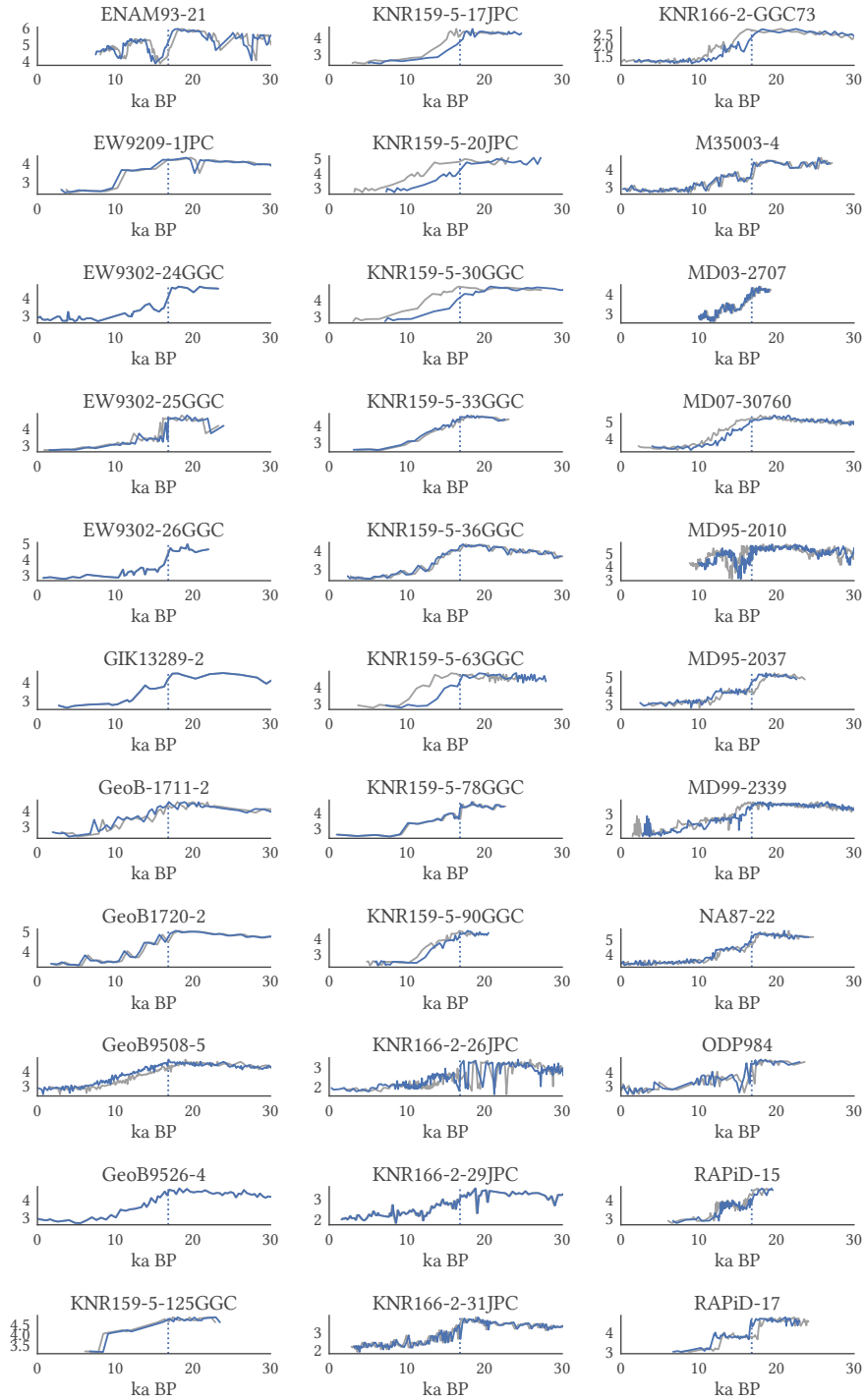
Figure F.1: The raw data of δ^{18}O values shifted to the transition onset. The timing of the onset of deglaciation is determined as the median over all records used in this study, considering the point of highest probability in the change point distribution for each record. The gray time series are the unshifted age models. The most likely transition onset is marked by the dashed line.
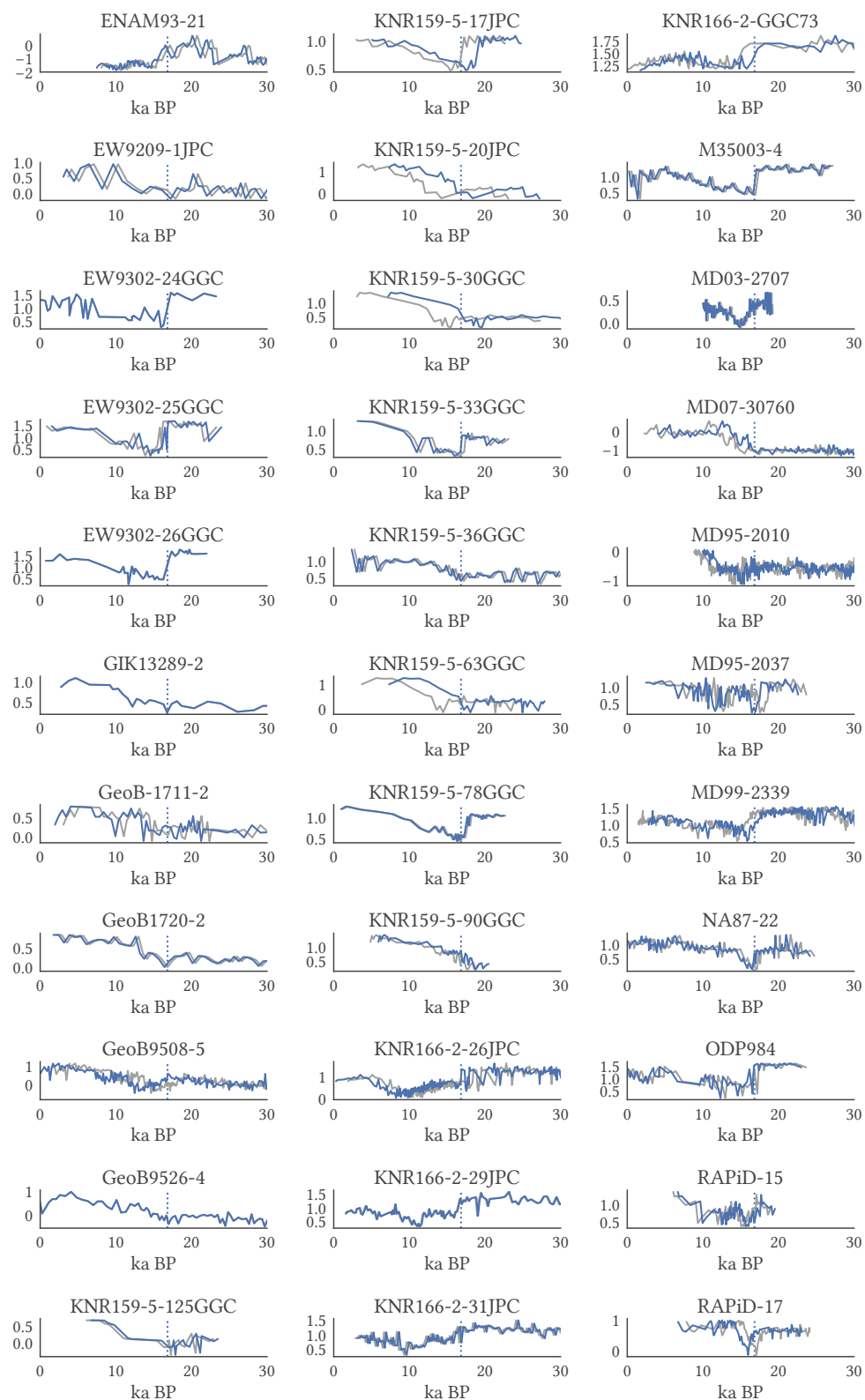
Figure F.2: Same as in Fig. F.1, but for the δ^{13}C time series.
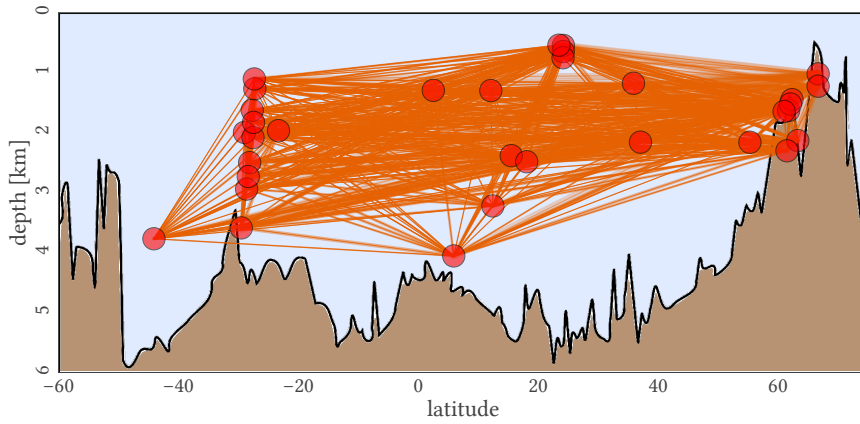
(a) Full 30ka period climate network for δ^{18}O data.
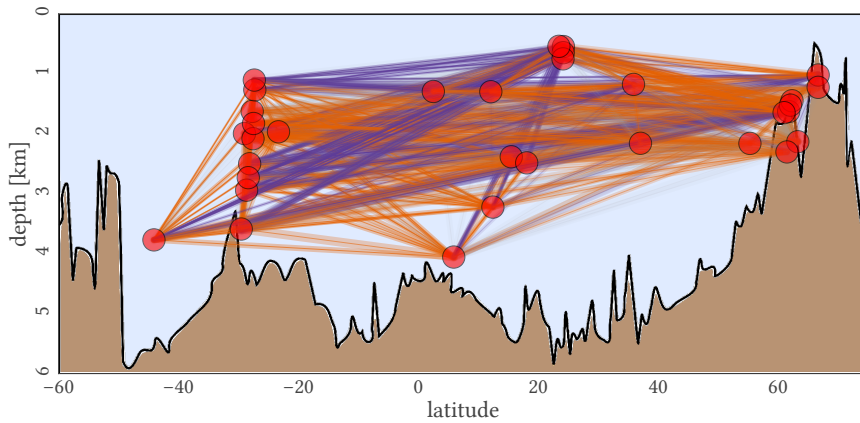
(b) Full 30ka period climate network for δ^{13}C data.

Figure F.3: Climate network for (a) δ^{18}O data and (b) δ^{13}C data for the full 30ka period. A link is drawn orange or blue if 95% of the samples of the posterior of ρ lays above or below zero respectively. It is shown in gray, if neither is the case. The colour strength is proportional to the peak of the correlation distribution and the width of each link is proportional to the width of the central 90% range of the posterior.
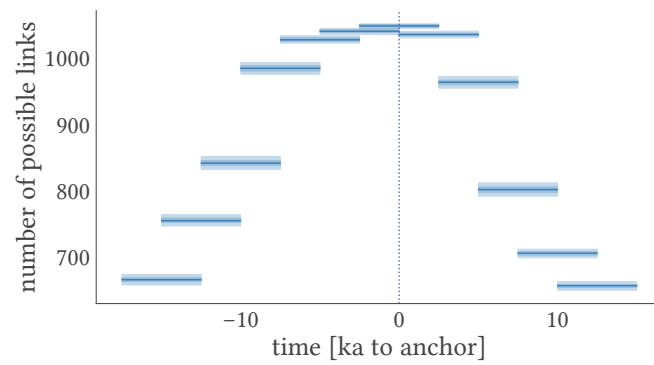
Figure F.4: The number of possible links for each time window. Note that this number is identcal for both isotope ratios, as they are measured at the same intervals. If there are too few data points for comparison after (<10 data points), a link is considered to be not possible and the weight is set to NaN. Therefore, the number of possible links changes with time, as different records cover different time periods with different resolution.

(a) 15ka to 10ka be-
fore onset

(b) 12.5ka to 7.5ka be-
fore onset

(c) 10ka to 5ka before
onset

(d) 7.5ka to 2.5ka be-
fore onset

(e) 5ka before to on-
set

(f) 2.5ka before to
2.5ka after onset

(g) onset to 5ka after
onset

(h) 2.5ka to 7.5ka af-
ter onset

(i) 5ka to 10ka after
onset

(j) 7.5ka to 12.5ka af-
ter onset

(k) 10ka to 15ka after
onset

(l) 12.5ka to 17.5ka af-
ter onset
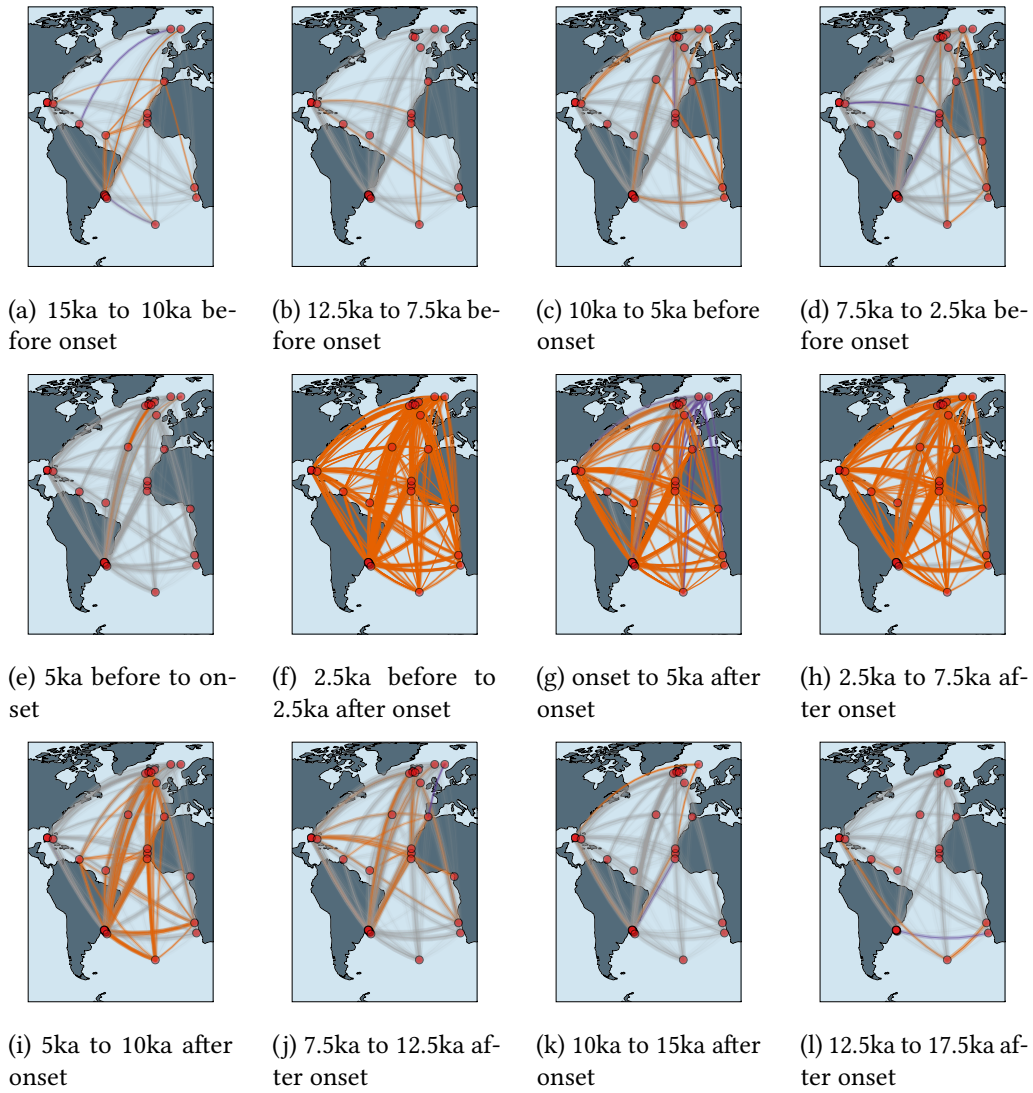
Figure F.5: Same as in Fig. 8.4, but showing the geographical locations of the records.

(a) 15ka to 10ka before onset

(b) 12.5ka to 7.5ka before onset

(c) 10ka to 5ka before onset

(d) 7.5ka to 2.5ka before onset

(e) 5ka before to onset

(f) 2.5ka before to 2.5ka after onset

(g) onset to 5ka after onset

(h) 2.5ka to 7.5ka after onset

(i) 5ka to 10ka after onset

(j) 7.5ka to 12.5ka after onset

(k) 10ka to 15ka after onset

(l) 12.5ka to 17.5ka after onset
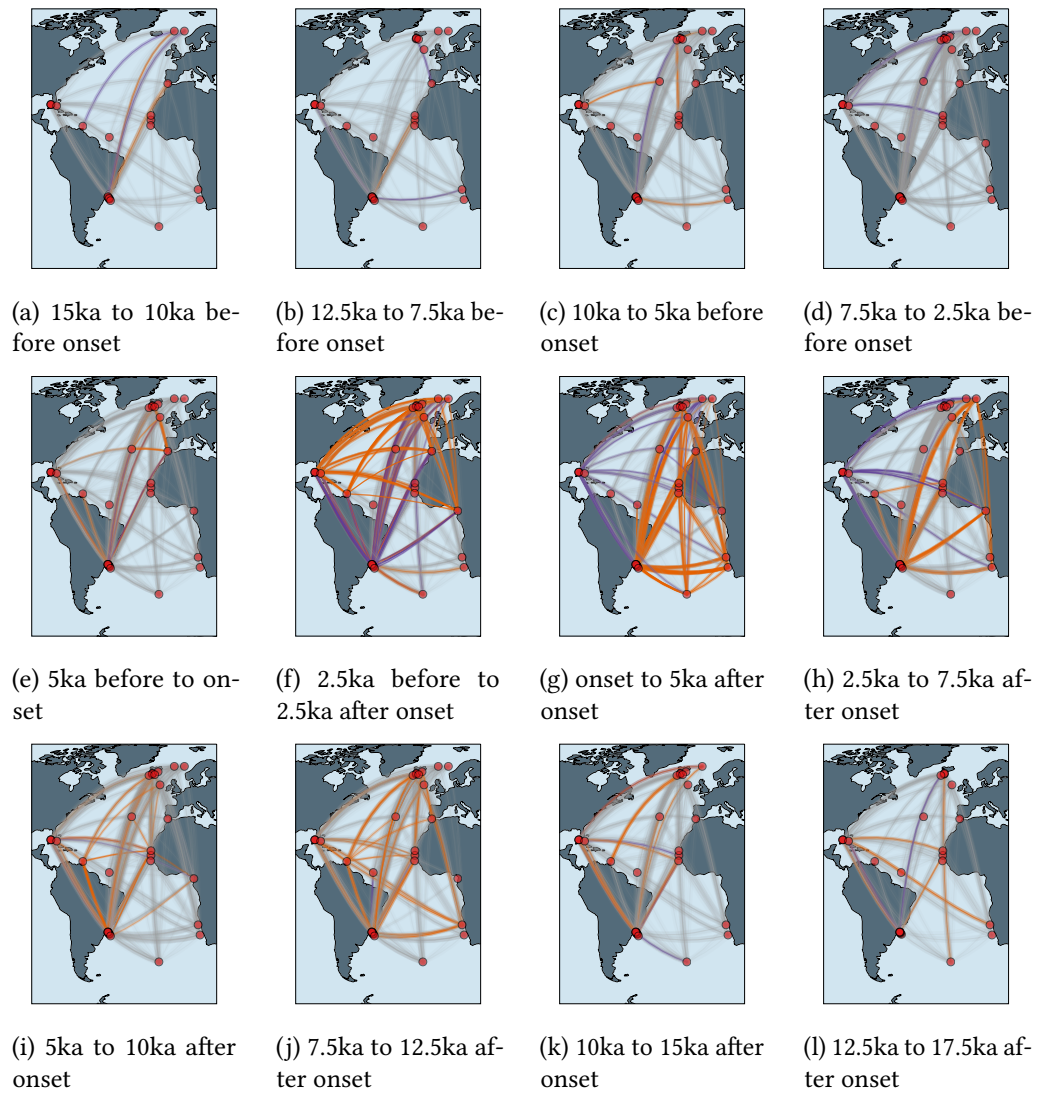
Figure F.6: Same as in Fig. 8.7, but showing the geographical locations of the records.

G | Appendix to Chapter 9

measure	change points [ka BP]	trends [per ka]
link density	-	-
n.s.i. link density	-	-0.036
hamming distance	-	-0.013
n.s.i. mean degree	12.86	-
n.s.i. transitivity	14.72	-
n.s.i. average path length	8.94	-

Table G.1: The detected change points and linear trends detected for the global network measures.
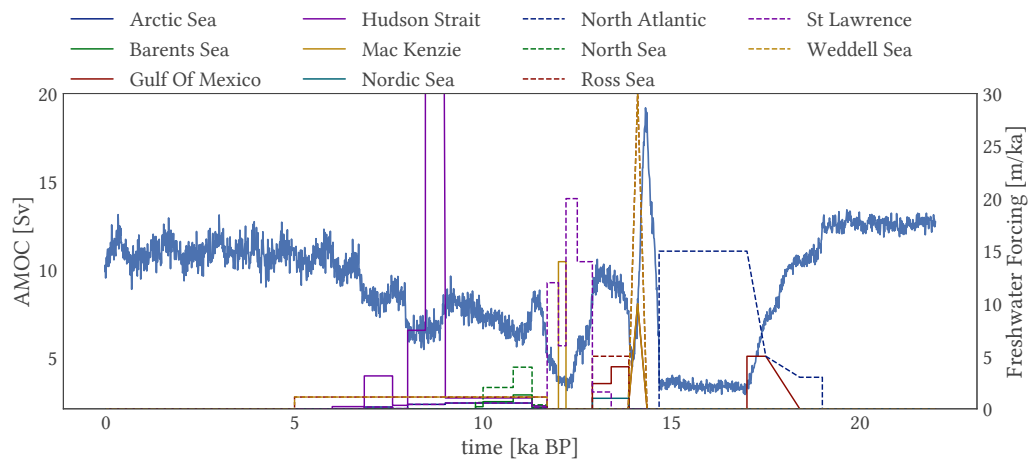
Figure G.1: The AMOC strength shown together with the freshwater forcing applied to the model.

(a) n.s.i. local clustering

(b) max. link distance [km]
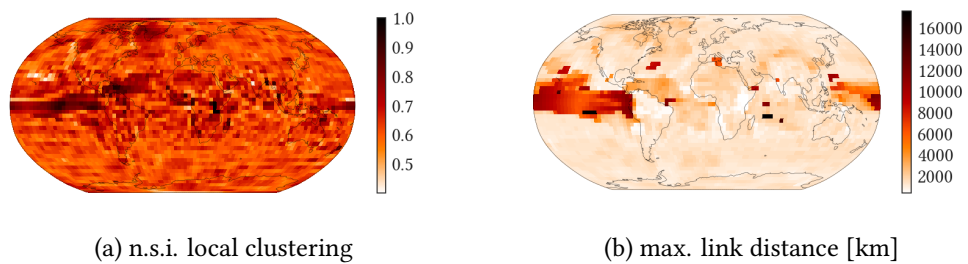
Figure G.2: Local network measures for the example time window from 17.31 to 17.30 ka BP. In particular the (a) local n.s.i. degree, (b) the n.s.i. local clustering and (c) the maximum link distance.
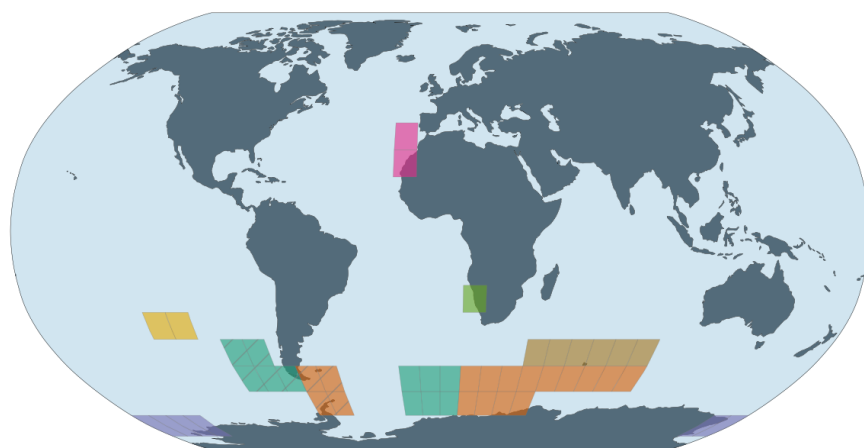
Figure G.3: Clusters that show a gradually decreasing n.s.i. mean degree during the deglaciation, but are too small to be considered along the large ones in the main text.

Figure G.4: In this plot, the degrees are plotted for a network in which only links that originate from the black box are considered and all others are removed. Most remaining links are either inside the box or with the surrounding areas.

(a) Cluster no. 1   (b) Cluster no. 3   (c) Cluster no. 5
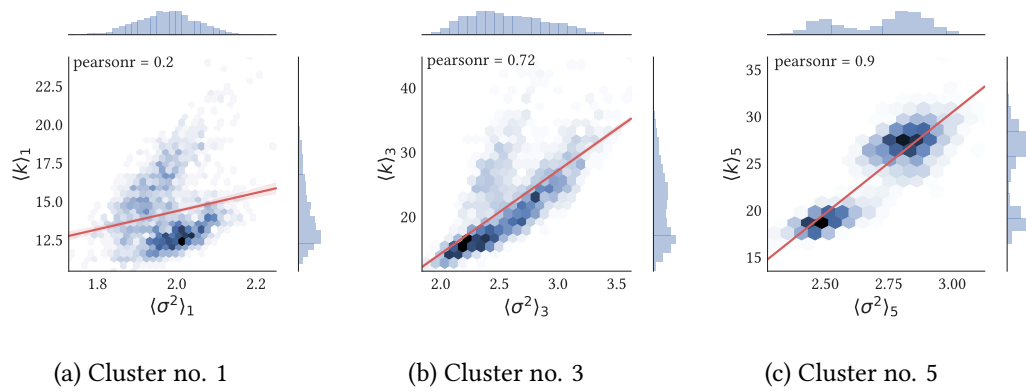
Figure G.5: The relationship between the mean n.s.i. degree over the three clusters no. 1, 3, and 5 and temperature variability. The latter is measured as the spatial mean over the standard deviations of all time series inside the cluster for each time window.

Bibliography

Almendra, R., P. Santana, J. Vasconcelos, G. Silva, F. Gonçalves, and T. Ambrizzi (2017). "The Influence of the Winter North Atlantic Oscillation Index on Hospital Admissions through Diseases of the Circulatory System in Lisbon, Portugal". In: *International Journal of Biometeorology* 61.2, pp. 325–333. DOI: 10.1007/s00484-016-1214-z.

Aminikhanghahi, S. and D. J. Cook (2017). "A Survey of Methods for Time Series Change Point Detection". In: *Knowledge and Information Systems* 51.2, pp. 339–367. DOI: 10.1007/s10115-016-0987-z.

Ammann, C. M., F. Joos, D. S. Schimel, B. L. Otto-Bliesner, and R. A. Tomas (2007). "Solar Influence on Climate during the Past Millennium: Results from Transient Simulations with the NCAR Climate System Model". In: *Proceedings of the National Academy of Sciences* 104.10, pp. 3713–3718. DOI: 10.1073/pnas.0605064103.

Appenzeller, C., T. F. Stocker, and M. Anklin (1998). "North Atlantic Oscillation Dynamics Recorded in Greenland Ice Cores". In: *Science* 282.5388, pp. 446–449. DOI: 10.1126/science.282.5388.446.

Ascoli, D., G. Vacchiano, M. Turco, M. Conedera, I. Drobyshev, J. Maringer, R. Motta, and A. Hacket-Pain (2017). "Inter-Annual and Decadal Changes in Teleconnections Drive Continental-Scale Synchronization of Tree Reproduction". In: *Nature Communications* 8.1. DOI: 10.1038/s41467-017-02348-9.

Babu, P. and P. Stoica (2010). "Spectral Analysis of Nonuniformly Sampled Data – a Review". In: *Digital Signal Processing* 20.2, pp. 359–378. DOI: 10.1016/j.dsp.2009.06.019.

Bader, J., M. D. S. Mesquita, K. I. Hodges, N. Keenlyside, S. Østerhus, and M. Miles (2011). "A Review on Northern Hemisphere Sea-Ice, Storminess and the North Atlantic Oscillation: Observations and Projected Changes". In: *Atmospheric Research* 101.4, pp. 809–834. DOI: 10.1016/j.atmosres.2011.04.007.

Baker, A., J. C. Hellstrom, B. F. J. Kelly, G. Mariethoz, and V. Trouet (2015). "A Composite Annual-Resolution Stalagmite Record of North Atlantic Climate over the Last Three Millennia". In: *Scientific Reports* 5.1. DOI: 10.1038/srep10307.

Balmer, S., M. Sarnthein, M. Mudelsee, and P. M. Grootes (2016). "Refined Modeling and ^{14} C Plateau Tuning Reveal Consistent Patterns of Glacial and Deglacial ^{14} C Reservoir Ages of Surface Waters in Low-Latitude Atlantic". In: *Paleoceanography* 31.8, pp. 1030–1040. DOI: 10.1002/2016PA002953.

Barrat, A., M. Barthelemy, R. Pastor-Satorras, and A. Vespignani (2004). "The Architecture of Complex Weighted Networks". In: *Proceedings of the National Academy of Sciences* 101.11, pp. 3747–3752. DOI: 10.1073/pnas.0400087101.

Barthélemy, M. (2011). "Spatial Networks". In: *Physics Reports* 499.1-3, pp. 1–101. DOI: 10.1016/j.physrep.2010.11.002.

Behseta, S., T. Berdyyeva, C. R. Olson, and R. E. Kass (2009). "Bayesian Correction for Attenuation of Correlation in Multi-Trial Spike Count Data". In: *Journal of Neurophysiology* 101.4, pp. 2186–2193. DOI: 10.1152/jn.90727.2008.

Bereiter, B., S. Eggleston, J. Schmitt, C. Nehrbass-Ahles, T. F. Stocker, H. Fischer, S. Kipfstuhl, and J. Chappellaz (2015). "Revision of the EPICA Dome C CO $_2$ Record from 800 to 600 Kyr before Present: Analytical Bias in the EDC CO2 Record". In: *Geophysical Research Letters* 42.2, pp. 542–549. DOI: 10.1002/2014GL061957.

Bianchi, G. G. and I. N. McCave (1999). "Holocene Periodicity in North Atlantic Climate and Deep-Ocean Flow South of Iceland". In: *Nature* 397.6719, pp. 515–517. DOI: 10.1038/17362.

Bigg, G. R., T. D. Jickells, P. S. Liss, and T. J. Osborn (2003). "The Role of the Oceans in Climate". In: *International Journal of Climatology* 23.10, pp. 1127–1159. DOI: 10.1002/joc.926.

Bjørk, A. A. et al. (2018). "Changes in Greenland's Peripheral Glaciers Linked to the North Atlantic Oscillation". In: *Nature Climate Change* 8.1, pp. 48–52. DOI: 10.1038/s41558-017-0029-1.

Björklund, J. A., B. E. Gunnarson, P. J. Krusic, H. Grudd, T. Josefsson, L. Östlund, and H. W. Linderholm (2013). "Advances towards Improved Low-Frequency Tree-Ring Reconstructions, Using an Updated Pinus Sylvestris L. MXD Network from the Scandinavian Mountains". In: *Theoretical and Applied Climatology* 113.3-4, pp. 697–710. DOI: 10.1007/s00704-012-0787-7.

Björklund, J., B. E. Gunnarson, K. Seftigen, P. Zhang, and H. W. Linderholm (2015). "Using Adjusted Blue Intensity Data to Attain High-Quality Summer Temperature Information: A Case Study from Central Scandinavia". In: *The Holocene* 25.3, pp. 547–556. DOI: 10.1177/0959683614562434.

Blaauw, M. (2010). "Methods and Code for 'Classical' Age-Modelling of Radiocarbon Sequences". In: *Quaternary Geochronology* 5.5, pp. 512–518. DOI: 10.1016/j.quageo.2010.01.002.

— (2012). "Out of Tune: The Dangers of Aligning Proxy Archives". In: *Quaternary Science Reviews* 36, pp. 38–49. DOI: 10.1016/j.quascirev.2010.11.012.

Blaauw, M. and J. A. Christen (2011). "Flexible Paleoclimate Age-Depth Models Using an Autoregressive Gamma Process". In: *Bayesian Analysis* 6.3, pp. 457–474. DOI: 10.1214/11-BA618.

Blondel, V. D., J.-L. Guillaume, R. Lambiotte, and E. Lefebvre (2008). "Fast Unfolding of Communities in Large Networks". In: *Journal of Statistical Mechanics: Theory and Experiment* 2008.10, P10008. DOI: 10.1088/1742-5468/2008/10/P10008.

Boccaletti, S., V. Latora, Y. Moreno, M. Chavez, and D. Hwang (2006). "Complex Networks: Structure and Dynamics". In: *Physics Reports* 424.4-5, pp. 175–308. DOI: 10.1016/j.physrep.2005.10.009.

Boers, N., B. Bookhagen, N. Marwan, J. Kurths, and J. Marengo (2013). "Complex Networks Identify Spatial Patterns of Extreme Rainfall Events of the South American Monsoon System". In: *Geophysical Research Letters* 40.16, pp. 4386–4392. DOI: 10.1002/grl.50681.

Boker, S. M., J. L. Rotondo, M. Xu, and K. King (2002). "Windowed Cross-Correlation and Peak Picking for the Analysis of Variability in the Association between Behavioral Time Series." In: *Psychological Methods* 7.3, pp. 338–355. DOI: 10.1037/1082-989X.7.3.338.

Bothe, O., M. Evans, L. F. Donado, E. G. Bustamante, J. Gergis, J. Gonzalez-Rouco, H. Goosse, G. Hegerl, A. Hind, J. H. Jungclaus, et al. (2015). "Continental-Scale Temperature Variability in PMIP3 Simulations and PAGES 2k Regional Temperature Reconstructions over the Past Millennium". In: *Climate of the Past* 11, pp. 1673–1699.

Bradley, R. S. (2015). *Paleoclimatology: Reconstructing Climates of the Quaternary*. 3. ed. Amsterdam: Academic Press/Elsevier. 675 pp.

Bradley, R. S., M. K. Hughes, and H. F. Diaz (2003). "Climate in Medieval Time". In: *Science* 302.5644, pp. 404–405. DOI: 10.1126/science.1090372.

Bradley, R. S., H. Wanner, and H. F. Diaz (2016). "The Medieval Quiet Period". In: *The Holocene* 26.6, pp. 990–993. DOI: 10.1177/0959683615622552.

Briffa, K. R., P. D. Jones, F. H. Schweingruber, and T. J. Osborn (1998). "Influence of Volcanic Eruptions on Northern Hemisphere Summer Temperature over the Past 600 Years". In: 393.6684, pp. 450–455. DOI: 10.1038/30943.

Briffa, K. and P. Jones (1993). "Global Surface Air Temperature Variations during the Twentieth Century: Part 2 , Implications for Large-Scale High-Frequency Palaeoclimatic Studies". In: *The Holocene* 3.1, pp. 77–88. DOI: 10.1177/095968369300300109.

Büntgen, U., D. C. Frank, D. Nievergelt, and J. Esper (2006). "Summer Temperature Variations in the European Alps, a.d. 755–2004". In: *Journal of Climate* 19.21, pp. 5606–5623. DOI: 10.1175/JCLI3917.1.

Büntgen, U., D. Frank, T. Neuenschwander, and J. Esper (2012). "Fading Temperature Sensitivity of Alpine Tree Growth at Its Mediterranean Margin and Associated Effects on Large-Scale Climate Reconstructions". In: *Climatic Change* 114.3-4, pp. 651–666. DOI: 10.1007/s10584-012-0450-4.

Büntgen, U., T. Kyncl, C. Ginzler, D. S. Jacks, J. Esper, W. Tegel, K.-U. Heussner, and J. Kyncl (2013). "Filling the Eastern European Gap in Millennium-Long Temperature Reconstructions". In: *Proceedings of the National Academy of Sciences* 110.5, pp. 1773–1778. DOI: 10.1073/pnas.1211485110.

Büntgen, U. et al. (2011). "2500 Years of European Climate Variability and Human Susceptibility". In: *Science* 331.6017, pp. 578–582. DOI: 10.1126/science.1197175.

Büntgen, U. et al. (2016). "Cooling and Societal Change during the Late Antique Little Ice Age from 536 to around 660 AD". In: *Nature Geoscience* 9.3, pp. 231–236. DOI: 10.1038/ngeo2652.

Butzin, M., P. Köhler, and G. Lohmann (2017). "Marine Radiocarbon Reservoir Age Simulations for the Past 50,000 Years: Marine Radiocarbon Simulations". In: *Geophysical Research Letters* 44.16, pp. 8473–8480. DOI: 10.1002/2017GL074688.

Came, R. E., D. W. Oppo, W. B. Curry, and J. Lynch-Stieglitz (2008). "Deglacial Variability in the Surface Return Flow of the Atlantic Meridional Overturning Circulation". In: *Paleoceanography* 23.1, PA1217. DOI: 10.1029/2007PA001450.

Camenisch, C. et al. (2016). "The Early Spörer Minimum - a Period of Extraordinary Climate and Socio-Economic Changes in Western and Central Europe". In: 2016, pp. 1–33. DOI: 10.5194/cp-2016-7.

Castagna, J. P. and S. Sun (2006). "Comparison of Spectral Decomposition Methods". In: *First break* 24.3.

Chang, P., L. Ji, and H. Li (1997). "A Decadal Climate Variation in the Tropical Atlantic Ocean from Thermodynamic Air-Sea Interactions". In: *Nature* 385.6616, pp. 516–518. DOI: 10.1038/385516a0.

Cheng, H., P. Z. Zhang, C. Spötl, R. L. Edwards, Y. J. Cai, D. Z. Zhang, W. C. Sang, M. Tan, and Z. S. An (2012). "The Climatic Cyclicity in Semiarid-Arid Central Asia over the Past 500,000 Years". In: *Geophysical Research Letters* 39.1, n/a–n/a. DOI: 10.1029/2011GL050202.

Christiansen, B. and F. C. Ljungqvist (2012). "The Extra-Tropical Northern Hemisphere Temperature in the Last Two Millennia: Reconstructions of Low-Frequency Variability". In: *Climate of the Past* 8.2, pp. 765–786. DOI: 10.5194/cp-8-765-2012.

Christiansen, B. (2014). "Straight Line Fitting and Predictions: On a Marginal Likelihood Approach to Linear Regression and Errors-in-Variables Models". In: *Journal of Climate* 27.5, pp. 2014–2031.

Christiansen, B. and F. C. Ljungqvist (2017). "Challenges and Perspectives for Large-Scale Temperature Reconstructions of the Past Two Millennia". In: *Reviews of Geophysics* 55.1, pp. 40–96. DOI: 10.1002/2016RG000521.

Cook, B. I., K. J. Anchukaitis, R. Touchan, D. M. Meko, and E. R. Cook (2016). "Spatiotemporal Drought Variability in the Mediterranean over the Last 900 Years". In: *Journal of Geophysical Research: Atmospheres* 121.5, 2015JD023929. DOI: 10.1002/2015JD023929.

Cook, E. R., R. D. D'Arrigo, and K. R. Briffa (1998). "A Reconstruction of the North Atlantic Oscillation Using Tree-Ring Chronologies from North America and Europe". In: *The Holocene* 8.1, pp. 9–17. DOI: 10.1191/095968398677793725.

Cook, E. R. et al. (2015). "Old World Megadroughts and Pluvials during the Common Era". In: *Science Advances* 1.10, e1500561. DOI: 10.1126/sciadv.1500561.

Coombes, P. and K. Barber (2005). "Environmental Determinism in Holocene Research: Causality or Coincidence?" In: *Area* 37.3, pp. 303–311. DOI: 10.1111/j.1475-4762.2005.00634.x.

Cronin, T. M. (2010). *Paleoclimates: Understanding Climate Change Past and Present.* New York: Columbia University Press. 441 pp.

Crowley, T. J. (2000). "Causes of Climate Change Over the Past 1000 Years". In: *Science* 289.5477, pp. 270–277. DOI: 10.1126/science.289.5477.270.

Curry, J. A., J. L. Schramm, and E. E. Ebert (1995). "Sea Ice-Albedo Climate Feedback Mechanism". In: *Journal of Climate* 8.2, pp. 240–247. DOI: 10.1175/1520-0442(1995)008<0240:SIACFM>2.0.CO;2.

Curry, W. B. and D. W. Oppo (1997). "Synchronous, High-Frequency Oscillations in Tropical Sea Surface Temperatures and North Atlantic Deep Water Production

during the Last Glacial Cycle". In: *Paleoceanography* 12.1, pp. 1–14. DOI: 10.1029/96PA02413.

Curry, W. B. and D. W. Oppo (2005). "Glacial Water Mass Geometry and the Distribution of δ^{13}C of ΣCO$_2$ in the Western Atlantic Ocean". In: *Paleoceanography* 20.1, PA1017. DOI: 10.1029/2004PA001021.

D'Arrigo, R., R. J. S. Wilson, and G. Jacoby (2006). "On the Long-Term Context for Late Twentieth Century Warming". In: *Journal of Geophysical Research* 111.D3. DOI: 10.1029/2005JD006352.

Deininger, M., F. McDermott, M. Mudelsee, M. Werner, N. Frank, and A. Mangini (2016). "Coherency of Late Holocene European Speleothem δ18O Records Linked to North Atlantic Ocean Circulation". In: *Climate Dynamics*, pp. 1–24. DOI: 10.1007/s00382-016-3360-8.

Delworth, T. L. and F. Zeng (2016). "The Impact of the North Atlantic Oscillation on Climate through Its Influence on the Atlantic Meridional Overturning Circulation". In: *Journal of Climate* 29.3, pp. 941–962. DOI: 10.1175/JCLI-D-15-0396.1.

Delworth, T. L., F. Zeng, G. A. Vecchi, X. Yang, L. Zhang, and R. Zhang (2016). "The North Atlantic Oscillation as a Driver of Rapid Climate Change in the Northern Hemisphere". In: *Nature Geoscience* 9.7, pp. 509–512. DOI: 10.1038/ngeo2738.

deMenocal, P. B. (2001). "Cultural Responses to Climate Change During the Late Holocene". In: *Science* 292.5517, pp. 667–673. DOI: 10.1126/science.1059287.

Denton, G. H., R. F. Anderson, J. R. Toggweiler, R. L. Edwards, J. M. Schaefer, and A. E. Putnam (2010). "The Last Glacial Termination". In: *Science* 328.5986, pp. 1652–1656. DOI: 10.1126/science.1184119.

Desprat, S., M. F. Sánchez Goñi, and M.-F. Loutre (2003). "Revealing Climatic Variability of the Last Three Millennia in Northwestern Iberia Using Pollen Influx Data". In: *Earth and Planetary Science Letters* 213.1–2, pp. 63–78. DOI: 10.1016/S0012-821X(03)00292-9.

Diamond, J. M. (1997). *Guns, Germs, and Steel: The Fates of Human Societies.* 1st ed. New York: W.W. Norton & Co. 480 pp.

— (2005). *Collapse: How Societies Choose to Fail or Succeed.* New York: Penguin.

Diaz, H. and V. Trouet (2014). "Some Perspectives on Societal Impacts of Past Climatic Changes". In: *History Compass* 12.2, pp. 160–177. DOI: 10.1111/hic3.12140.

Dickson, A. J., C. J. Beer, C. Dempsey, M. A. Maslin, J. A. Bendle, E. L. McClymont, and R. D. Pancost (2009). "Oceanic Forcing of the Marine Isotope Stage 11 Interglacial". In: *Nature Geoscience* 2.6, pp. 428–433. DOI: 10.1038/ngeo527.

Divine, D., E. Isaksson, T. Martma, H. A. Meijer, J. Moore, V. Pohjola, R. S. W. van de Wal, and F. Godtliebsen (2011). "Thousand Years of Winter Surface Air Temperature Variations in Svalbard and Northern Norway Reconstructed from Ice-Core Data". In: *Polar Research* 30.1, p. 7379. DOI: 10.3402/polar.v30i0.7379.

Dobrovolný, P. et al. (2010). "Monthly, Seasonal and Annual Temperature Reconstructions for Central Europe Derived from Documentary Evidence and Instrumental Records since AD 1500". In: *Climatic Change* 101.1-2, pp. 69–107. DOI: 10.1007/s10584-009-9724-x.

Domínguez-Castro, F., J. C. de Miguel, J. M. Vaquero, M. C. Gallego, and R. García-Herrera (2014). "Climatic Potential of Islamic Chronicles in Iberia: Extreme Droughts (Ad 711–1010)". In: *The Holocene* 24.3, pp. 370–374. DOI: 10.1177/0959683613518591.

Donges, J. F., R. V. Donner, and J. Kurths (2013). "Testing Time Series Irreversibility Using Complex Network Methods". In: *EPL (Europhysics Letters)* 102.1, p. 10004. DOI: 10.1209/0295-5075/102/10004.

Donges, J. F., R. V. Donner, N. Marwan, S. F. Breitenbach, K. Rehfeld, and J. Kurths (2015a). "Non-Linear Regime Shifts in Holocene Asian Monsoon Variability: Potential Impacts on Cultural Change and Migratory Patterns". In: *Climate of the Past* 11.5, pp. 709–741. DOI: 10.5194/cp-11-709-2015.

Donges, J. F., R. V. Donner, M. H. Trauth, N. Marwan, H.-J. Schellnhuber, and J. Kurths (2011a). "Nonlinear Detection of Paleoclimate-Variability Transitions Possibly Related to Human Evolution". In: *Proceedings of the National Academy of Sciences* 108.51, pp. 20422–20427.

Donges, J. F., I. Petrova, A. Loew, N. Marwan, and J. Kurths (2015b). "How Complex Climate Networks Complement Eigen Techniques for the Statistical Analysis of Climatological Data". In: *Climate Dynamics* 45.9-10, pp. 2407–2424. DOI: 10.1007/s00382-015-2479-3.

Donges, J. F., H. C. H. Schultz, N. Marwan, Y. Zou, and J. Kurths (2011b). "Investigating the Topology of Interacting Networks". In: *The European Physical Journal B* 84.4, pp. 635–651. DOI: 10.1140/epjb/e2011-10795-8.

Donner, R. V. and J. F. Donges (2012). "Visibility Graph Analysis of Geophysical Time Series: Potentials and Possible Pitfalls". In: *Acta Geophysica* 60.3, pp. 589–623. DOI: 10.2478/s11600-012-0032-x.

Donner, R. V., M. Wiedermann, and J. F. Donges (2017). "Complex Network Techniques for Climatological Data Analysis". In: *Nonlinear and Stochastic Climate Dynamics*. Ed. by C. L. E. Franzke and T. J. O'Kane. Cambridge: Cambridge University Press, pp. 159–183.

Donner, R. V., Y. Zou, J. F. Donges, N. Marwan, and J. Kurths (2010a). "Ambiguities in Recurrence-Based Complex Network Representations of Time Series". In: *Physical Review E* 81.1. DOI: 10.1103/PhysRevE.81.015101.

— (2010b). "Recurrence Networks—A Novel Paradigm for Nonlinear Time Series Analysis". In: *New Journal of Physics* 12.3, p. 033025. DOI: 10.1088/1367-2630/12/3/033025.

Dorado Liñán, I., U. Büntgen, F. González-Rouco, E. Zorita, J. P. Montávez, J. J. Gómez-Navarro, M. Brunet, I. Heinrich, G. Helle, and E. Gutiérrez (2012). "Estimating 750 Years of Temperature Variations and Uncertainties in the Pyrenees by Tree-Ring Reconstructions and Climate Simulations". In: *Climate of the Past* 8.3, pp. 919–933. DOI: 10.5194/cp-8-919-2012.

Drake, B. L. (2017). "Changes in North Atlantic Oscillation Drove Population Migrations and the Collapse of the Western Roman Empire". In: *Scientific Reports* 7.1. DOI: 10.1038/s41598-017-01289-z.

Elsner, J. B., T. H. Jagger, and E. A. Fogarty (2009). "Visibility Network of United States Hurricanes". In: *Geophysical Research Letters* 36.16, p. L16702. DOI: 10.1029/2009GL039129.

Engler, S. (2012). "Developing a Historically Based "Famine Vulnerability Analysis Model" (FVAM) – An Interdisciplinary Approach". In: *Erdkunde*, pp. 157–172. DOI: 10.3112/erdkunde.2012.02.05.

Engler, S. and J. P. Werner (2015). "Processes Prior and during the Early 18th Century Irish Famines—Weather Extremes and Migration". In: *Climate* 3.4, pp. 1035–1056. DOI: 10.3390/cli3041035.

Esper, J. et al. (2012). "Orbital Forcing of Tree-Ring Data". In: *Nature Climate Change* 2.12, pp. 862–866. DOI: 10.1038/nclimate1589.

Esteves, M. A. and M. D. Manso Orgaz (2001). "The Influence of Climatic Variability on the Quality of Wine". In: *International Journal of Biometeorology* 45.1, pp. 13–21. DOI: 10.1007/s004840000075.

Fagan, B. M. (2000). *The Little Ice Age: How Climate Made History, 1300-1850*. Basic Books, New York. DOI: 10.5772/1965.

Faust, J. C., K. Fabian, G. Milzer, J. Giraudeau, and J. Knies (2016). "Norwegian Fjord Sediments Reveal NAO Related Winter Temperature and Precipitation Changes of the Past 2800 Years". In: *Earth and Planetary Science Letters* 435, pp. 84–93. DOI: 10.1016/j.epsl.2015.12.003.

Fischer, H., M. Werner, D. Wagenbach, M. Schwager, T. Thorsteinnson, F. Wilhelms, J. Kipfstuhl, and S. Sommer (1998). "Little Ice Age Clearly Recorded in Northern Greenland Ice Cores". In: *Geophysical Research Letters* 25.10, pp. 1749–1752. DOI: 10.1029/98GL01177.

Fisher, R. A. (1915). "Frequency Distribution of the Values of the Correlation Coefficient in Samples from an Indefinitely Large Population". In: *Biometrika* 10.4, p. 507. DOI: 10.2307/2331838.

Folland, C. K., J. Knight, H. W. Linderholm, D. Fereday, S. Ineson, and J. W. Hurrell (2009). "The Summer North Atlantic Oscillation: Past, Present, and Future". In: *Journal of Climate* 22.5, pp. 1082–1103. DOI: 10.1175/2008JCLI2459.1.

Frank, D., J. Esper, E. Zorita, and R. J. S. Wilson (2010). "A Noodle, Hockey Stick, and Spaghetti Plate: A Perspective on High-Resolution Paleoclimatology: A Noodle, Hockey Stick, and Spaghetti Plate". In: *Wiley Interdisciplinary Reviews: Climate Change* 1.4, pp. 507–516. DOI: 10.1002/wcc.53.

Franke, J. G. and R. V. Donner (2017). "Dynamical anomalies in terrestrial proxies of North Atlantic climate variability during the last 2 ka". In: *Climatic Change* 143.1, pp. 87–100. DOI: 10.1007/s10584-017-1979-z.

— (2019a). "Correlating Paleoclimate Time Series: Sources of Uncertainty and Potential Pitfalls". Submitted to: *Quaternary Science Reviews*.

— (2019b). "Relative timing and spatial co-variability of stable isotopes in benthic foraminifera in the Atlantic ocean during the last glacial termination". In preparation for: *Paleoceanography and Paleoclimatology*.

Franke, J. G., F. Särdquist, and R. V. Donner (2019). "Spatial variability of the TraCE-21ka simulation: a network perspective". In preparation for: *Nature Scientific Reports*.

Franke, J. G., J. P. Werner, and R. V. Donner (2017). "Reconstructing Late Holocene North Atlantic atmospheric circulation changes using functional paleoclimate networks". In: *Climate of the Past* 13.11, pp. 1593–1608. DOI: 10.5194/cp-13-1593-2017.

Fyke, J., O. Sergienko, M. Löfverström, S. Price, and J. T. M. Lenaerts (2018). "An Overview of Interactions and Feedbacks Between Ice Sheets and the Earth System". In: *Reviews of Geophysics* 56.2, pp. 361–408. DOI: 10.1029/2018RG000600.

García, M. J. G., M. B. R. Zapata, J. I. Santisteban, R. Mediavilla, E. López-Pamo, and C. J. Dabrio (2007). "Late Holocene Environments in Las Tablas de Daimiel (South Central Iberian Peninsula, Spain)". In: *Vegetation History and Archaeobotany* 16.4, pp. 241–250. DOI: 10.1007/s00334-006-0047-9.

Gelman, A. (2014). *Bayesian Data Analysis*. 3rd. Boca Raton: CRC Press. 661 pp.

Gherardi, J.-M., L. Labeyrie, S. Nave, R. Francois, J. F. McManus, and E. Cortijo (2009). "Glacial-Interglacial Circulation Changes Inferred from ^{231}Pa/ ^{230}Th Sedimentary Record in the North Atlantic Region". In: *Paleoceanography* 24.2, PA2204. DOI: 10.1029/2008PA001696.

Gilks, W. R., S. Richardson, and D. Spiegelhalter (1995). *Markov Chain Monte Carlo in Practice.* London: CRC press.

Gillett, N. P., H. F. Graf, and T. J. Osborn (2003). "Climate Change and the North Atlantic Oscillation". In: *Geophysical Monograph Series.* Ed. by J. W. Hurrell, Y. Kushnir, G. Ottersen, and M. Visbeck. Vol. 134. Washington, D. C.: American Geophysical Union, pp. 193–209. DOI: 10.1029/134GM09.

Gomez, N., L. J. Gregoire, J. X. Mitrovica, and A. J. Payne (2015). "Laurentide-Cordilleran Ice Sheet Saddle Collapse as a Contribution to Meltwater Pulse 1A". In: *Geophysical Research Letters* 42.10, pp. 3954–3962. DOI: 10.1002/2015GL063960.

Goswami, B., J. Heitzig, K. Rehfeld, N. Marwan, A. Anoop, S. Prasad, and J. Kurths (2014). "Estimation of Sedimentary Proxy Records Together with Associated Uncertainty". In: *Nonlinear Processes in Geophysics* 21.6, pp. 1093–1111. DOI: 10.5194/npg-21-1093-2014.

Gouirand, I., H. W. Linderholm, A. Moberg, and B. Wohlfarth (2008). "On the Spatiotemporal Characteristics of Fennoscandian Tree-Ring Based Summer Temperature Reconstructions". In: *Theoretical and Applied Climatology* 91.1-4, pp. 1–25. DOI: 10.1007/s00704-007-0311-7.

Gregoire, L. J., A. J. Payne, and P. J. Valdes (2012). "Deglacial Rapid Sea Level Rises Caused by Ice-Sheet Saddle Collapses". In: *Nature* 487.7406, pp. 219–222. DOI: 10.1038/nature11257.

Grifoni, D., M. Mancini, G. Maracchi, S. Orlandini, and G. Zipoli (2006). "Analysis of Italian Wine Quality Using Freely Available Meteorological Information". In: *American Journal of Enology and Viticulture* 57.3, pp. 339–346.

Grootes, P. M. and M. Stuiver (1997). "Oxygen 18/16 Variability in Greenland Snow and Ice with 10^{-3} - to 10^{5}-Year Time Resolution". In: *Journal of Geophysical Research: Oceans* 102.C12, pp. 26455–26470. DOI: 10.1029/97JC00880.

Guez, O. C., A. Gozolchiani, and S. Havlin (2014). "Influence of Autocorrelation on the Topology of the Climate Network". In: *Physical Review E* 90.6, p. 062814. DOI: 10.1103/PhysRevE.90.062814.

Gunnarson, B. E., H. W. Linderholm, and A. Moberg (2011). "Improving a Tree-Ring Reconstruction from West-Central Scandinavia: 900 Years of Warm-Season Temperatures". In: 36.1, pp. 97–108. DOI: 10.1007/s00382-010-0783-5.

Haigh, J. D. (1996). "The Impact of Solar Variability on Climate". In: *Science* 272.5264, pp. 981–984. DOI: 10.1126/science.272.5264.981.

Halsall, G. (2007). *Barbarian Migrations and the Roman West, 376–568.* Cambridge: Cambridge University Press.

Haltia-Hovi, E., T. Saarinen, and M. Kukkonen (2007). "A 2000-Year Record of Solar Forcing on Varved Lake Sediment in Eastern Finland". In: *Quaternary Science Reviews* 26.5–6, pp. 678–689. DOI: 10.1016/j.quascirev.2006.11.005.

Haslett, J. and A. Parnell (2008). "A Simple Monotone Process with Application to Radiocarbon-Dated Depth Chronologies". In: *Journal of the Royal Statistical Society: Series C (Applied Statistics)* 57.4, pp. 399–418. DOI: 10.1111/j.1467-9876.2008.00623.x.

He, F. (2011). *Simulating Transient Climate Evolution of the Last Deglaciation with CCSM~3*. Dissertation.

He, F., J. D. Shakun, P. U. Clark, A. E. Carlson, Z. Liu, B. L. Otto-Bliesner, and J. E. Kutzbach (2013). "Northern Hemisphere Forcing of Southern Hemisphere Climate during the Last Deglaciation". In: *Nature* 494.7435, pp. 81–85. DOI: 10.1038/nature11822.

Hegerl, G. C., T. J. Crowley, M. Allen, W. T. Hyde, H. N. Pollack, J. Smerdon, and E. Zorita (2007). "Detection of Human Influence on a New, Validated 1500-Year Temperature Reconstruction". In: *Journal of Climate* 20.4, pp. 650–666. DOI: 10.1175/JCLI4011.1.

Heitzig, J., J. F. Donges, Y. Zou, N. Marwan, and J. Kurths (2012). "Node-Weighted Measures for Complex Networks with Spatially Embedded, Sampled, or Differently Sized Nodes". In: *The European Physical Journal B* 85.1. DOI: 10.1140/epjb/e2011-20678-7.

Heitzig, J. (2013). "Moving Taylor Bayesian Regression for Nonparametric Multidimensional Function Estimation with Possibly Correlated Errors". In: *SIAM Journal on Scientific Computing* 35.4, A1928–A1950. DOI: 10.1137/12087846X.

Helama, S., M. Timonen, J. Holopainen, M. G. Ogurtsov, K. Mielikäinen, M. Eronen, M. Lindholm, and J. Meriläinen (2009). "Summer Temperature Variations in Lapland during the Medieval Warm Period and the Little Ice Age Relative to Natural Instability of Thermohaline Circulation on Multi-Decadal and Multi-Centennial Scales". In: *Journal of Quaternary Science* 24.5, pp. 450–456. DOI: 10.1002/jqs.1291.

Hoffman, J. L. and D. C. Lund (2012). "Refining the Stable Isotope Budget for Antarctic Bottom Water: New Foraminiferal Data from the Abyssal Southwest Atlantic". In: *Paleoceanography* 27.1, PA1213. DOI: 10.1029/2011PA002216.

Hoffman, M. D. and A. Gelman (2014). "The No-U-Turn Sampler: Adaptively Setting Path Lengths in Hamiltonian Monte Carlo." In: *Journal of Machine Learning Research* 15.1, pp. 1593–1623.

Hollander, M., D. A. Wolfe, and E. Chicken (2014). *Nonparametric Statistical Methods*. 3. ed. Wiley Series in Probability and Statistics. Hoboken, NJ: Wiley. 819 pp.

Huang, N. E., Z. Shen, S. R. Long, M. C. Wu, H. H. Shih, Q. Zheng, N.-C. Yen, C. C. Tung, and H. H. Liu (1998). "The Empirical Mode Decomposition and the Hilbert Spectrum for Nonlinear and Non-Stationary Time Series Analysis". In: *Proceedings of the Royal Society A: Mathematical, Physical and Engineering Sciences* 454.1971, pp. 903–995. DOI: 10.1098/rspa.1998.0193.

Huang, N. E. and Z. Wu (2008). "A Review on Hilbert-Huang Transform: Method and Its Applications to Geophysical Studies". In: *Reviews of Geophysics* 46.2. DOI: 10.1029/2007RG000228.

Hughes, M. K. and H. F. Diaz (1994). "Was There a 'Medieval Warm Period', and If so, Where and When?" In: *Climatic Change* 26.2, pp. 109–142. DOI: 10.1007/BF01092410.

Hurrell, J. W., Y. Kushnir, G. Ottersen, and M. Visbeck (2003). "An Overview of the North Atlantic Oscillation". In: *The North Atlantic Oscillation: Climatic Significance and Environmental Impact*. Ed. by J. W. Hurrell, Y. Kushnir, G. Ottersen, and r. Visbeck. Washington, D. C.: American Geophysical Union, pp. 1–35. DOI: 10.1029/134GM01.

Iles, C. and G. Hegerl (2017). "Role of the North Atlantic Oscillation in Decadal Temperature Trends". In: *Environmental Research Letters* 12.11, p. 114010. DOI: 10.1088/1748-9326/aa9152.

IPCC (2013). *Climate Change 2013 - The Physical Science Basis: Working Group I Contribution to the Fifth Assessment Report of the Intergovernmental Panel on Climate Change.* Cambridge University Press, Cambridge. DOI: 10.1017/CBO9781107415324.004.

Isaksson, E., D. Divine, J. Kohler, T. Martma, V. Pohjola, H. Motoyama, and O. Watanabe (2005). "Climate Oscillations as Recorded in Svalbard Ice Core Ω18o Records between Ad 1200 and 1997". In: *Geografiska Annaler: Series A, Physical Geography* 87.1, pp. 203–214. DOI: 10.1111/j.0435-3676.2005.00253.x.

Ivanovic, R. F., L. J. Gregoire, A. D. Wickert, P. J. Valdes, and A. Burke (2017). "Collapse of the North American Ice Saddle 14,500 Years Ago Caused Widespread Cooling and Reduced Ocean Overturning Circulation: Ice Collapse Caused Cooling ~14.5 Ka". In: *Geophysical Research Letters* 44.1, pp. 383–392. DOI: 10.1002/2016GL071849.

Kadushin, C. (2012). *Understanding Social Networks: Theories, Concepts, and Findings.* New York: Oxford University Press. 252 pp.

Kaufman, L. and P. J. Rousseeuw (1990). *Finding Groups in Data: An Introduction to Cluster Analysis.* Wiley Series in Probability and Mathematical Statistics. New York: Wiley. 342 pp.

Kendall, M. G. (1970). *Rank Correlation Methods.* 4th ed. London: Griffin. 202 pp.

Kettlewell, P., R. Sothern, and W. Koukkari (1999). "U.K. Wheat Quality and Economic Value Are Dependent on the North Atlantic Oscillation". In: *Journal of Cereal Science* 29.3, pp. 205–209. DOI: 10.1006/jcrs.1999.0258.

Kirchhefer, A. J. (2001). "Reconstruction of Summer Temperatures from Tree-Rings of Scots Pine (Pinus Sylvestris L.) in Coastal Northern Norway". In: *The Holocene* 11.1, pp. 41–52. DOI: 10.1191/095968301670181592.

Klein, S. A., B. J. Soden, and N.-C. Lau (1999). "Remote Sea Surface Temperature Variations during ENSO: Evidence for a Tropical Atmospheric Bridge". In: *Journal of Climate* 12.4, pp. 917–932. DOI: 10.1175/1520-0442(1999)012<0917:RSSTVD>2.0.CO;2.

Knight, J. R., C. K. Folland, and A. A. Scaife (2006). "Climate Impacts of the Atlantic Multidecadal Oscillation". In: *Geophysical Research Letters* 33.17, p. L17706. DOI: 10.1029/2006GL026242.

Labeyrie, L., C. Waelbroeck, E. Cortijo, E. Michel, and J.-C. Duplessy (2005). "Changes in Deep Water Hydrology during the Last Deglaciation". In: *Comptes Rendus Geoscience* 337.10-11, pp. 919–927. DOI: 10.1016/j.crte.2005.05.010.

Lacasa, L., B. Luque, F. Ballesteros, J. Luque, and J. C. Nuno (2008). "From Time Series to Complex Networks: The Visibility Graph". In: *Proceedings of the National Academy of Sciences* 105.13, pp. 4972–4975. DOI: 10.1073/pnas.0709247105.

Lacasa, L., B. Luque, J. Luque, and J. C. Nuño (2009). "The Visibility Graph: A New Method for Estimating the Hurst Exponent of Fractional Brownian Motion". In: *EPL (Europhysics Letters)* 86.3, p. 30001. DOI: 10.1209/0295-5075/86/30001.

Lacasa, L., A. Nuñez, É. Roldán, J. M. R. Parrondo, and B. Luque (2012). "Time Series Irreversibility: A Visibility Graph Approach". In: *The European Physical Journal B* 85.6. DOI: 10.1140/epjb/e2012-20809-8.

Lacasa, L. and R. Flanagan (2015). "Time Reversibility from Visibility Graphs of Nonstationary Processes". In: *Physical Review E* 92.2, p. 022817. DOI: 10.1103/PhysRevE.92.022817.

Larsen, D. J., G. H. Miller, Á. Geirsdóttir, and T. Thordarson (2011). "A 3000-Year Varved Record of Glacier Activity and Climate Change from the Proglacial Lake Hvítárvatn, Iceland". In: 30.19, pp. 2715–2731.

Laskar, J., P. Robutel, F. Joutel, M. Gastineau, A. C. M. Correia, and B. Levrard (2004). "A Long-Term Numerical Solution for the Insolation Quantities of the Earth". In: *Astronomy & Astrophysics* 428.1, pp. 261–285. DOI: 10.1051/0004-6361:20041335.

Lawrance, A. J. (1991). "Directionality and Reversibility in Time Series". In: *International Statistical Review / Revue Internationale de Statistique* 59.1, p. 67. DOI: 10.2307/1403575.

Lehmann, E. L. and G. Casella (1998). *Theory of Point Estimation.* 2nd. New York: Springer. 589 pp.

Lehner, F., C. C. Raible, and T. F. Stocker (2012). "Testing the Robustness of a Precipitation Proxy-Based North Atlantic Oscillation Reconstruction". In: *Quaternary Science Reviews* 45, pp. 85–94. DOI: 10.1016/j.quascirev.2012.04.025.

Leijonhufvud, L., R. J. S. Wilson, A. Moberg, J. Söderberg, D. Retsö, and U. Söderlind (2010). "Five Centuries of Stockholm Winter/Spring Temperatures Reconstructed from Documentary Evidence and Instrumental Observations". In: *Climatic Change* 101.1-2, pp. 109–141. DOI: 10.1007/s10584-009-9650-y.

Lenoir, G. and M. Crucifix (2018a). "A General Theory on Frequency and Time–Frequency Analysis of Irregularly Sampled Time Series Based on Projection Methods – Part 1: Frequency Analysis". In: *Nonlinear Processes in Geophysics* 25.1, pp. 145–173. DOI: 10.5194/npg-25-145-2018.

— (2018b). "A General Theory on Frequency and Time–Frequency Analysis of Irregularly Sampled Time Series Based on Projection Methods – Part 2: Extension to Time–Frequency Analysis". In: *Nonlinear Processes in Geophysics* 25.1, pp. 175–200. DOI: 10.5194/npg-25-175-2018.

Lewandowski, D., D. Kurowicka, and H. Joe (2009). "Generating Random Correlation Matrices Based on Vines and Extended Onion Method". In: *Journal of Multivariate Analysis* 100.9, pp. 1989–2001. DOI: 10.1016/j.jmva.2009.04.008.

Li, J., C. Sun, and F.-F. Jin (2013). "NAO Implicated as a Predictor of Northern Hemisphere Mean Temperature Multidecadal Variability". In: *Geophysical Research Letters* 40.20, pp. 5497–5502. DOI: 10.1002/2013GL057877.

Linderholm, H. W. and D. Chen (2005). "Central Scandinavian Winter Precipitation Variability during the Past Five Centuries Reconstructed from Pinus Sylvestris Tree Rings". In: *Boreas* 34.1, pp. 43–52. DOI: 10.1111/j.1502-3885.2005.tb01003.x.

Lindholm, M., Ó. Eggertsson, N. Lovelius, O. Raspopov, O. Shumilov, and A. Laanelaid (2001). "Growth Indices of North European Scots Pine Record the Seasonal North Atlantic Oscillation". In: *Boreal Environment Research* 6.4, pp. 275–284.

Lisiecki, L. E. and M. E. Raymo (2005). "A Pliocene-Pleistocene Stack of 57 Globally Distributed Benthic δ^{18}O Records". In: *Paleoceanography* 20.1, PA1003. DOI: 10.1029/2004PA001071.

Lisiecki, L. E. and J. V. Stern (2016). "Regional and Global Benthic δ^{18}O Stacks for the Last Glacial Cycle: Last Glacial Cycle Benthic δ^{18}O". In: *Paleoceanography* 31.10, pp. 1368–1394. DOI: 10.1002/2016PA003002.

Little, M., R. Schneider, D. Kroon, B. Price, T. Bickert, and G. Wefer (1997). "Rapid Palaeoceanographic Changes in the Benguela Upwelling System for the Last 160,000 Years as Indicated by Abundances of Planktonic Foraminifera". In: *Palaeogeography, Palaeoclimatology, Palaeoecology* 130.1-4, pp. 135–161. DOI: 10.1016/S0031-0182(96)00136-8.

Liu, C., W.-X. Zhou, and W.-K. Yuan (2010). "Statistical Properties of Visibility Graph of Energy Dissipation Rates in Three-Dimensional Fully Developed Turbulence". In: *Physica A: Statistical Mechanics and its Applications* 389.13, pp. 2675–2681. DOI: 10.1016/j.physa.2010.02.043.

Liu, Z. et al. (2009). "Transient Simulation of Last Deglaciation with a New Mechanism for Bolling-Allerod Warming". In: *Science* 325.5938, pp. 310–314. DOI: 10.1126/science.1171041.

Liu, Z. et al. (2012). "Younger Dryas Cooling and the Greenland Climate Response to CO2". In: *Proceedings of the National Academy of Sciences* 109.28, pp. 11101–11104. DOI: 10.1073/pnas.1202183109.

Liu, Z., A. C. G. Henderson, and Y. Huang (2006). "Alkenone-Based Reconstruction of Late-Holocene Surface Temperature and Salinity Changes in Lake Qinghai, China". In: *Geophysical Research Letters* 33.9. DOI: 10.1029/2006GL026151.

Ljungqvist, F. C., P. J. Krusic, G. Brattström, and H. S. Sundqvist (2012). "Northern Hemisphere Temperature Patterns in the Last 12 Centuries". In: *Climate of the Past* 8.1, pp. 227–249. DOI: 10.5194/cp-8-227-2012.

Ljungqvist, F. C. (2010). "A New Reconstruction of Temperature Variability in the Extra-Tropical Northern Hemisphere During the Last Two Millennia". In: *Geografiska Annaler: Series A, Physical Geography* 92.3, pp. 339–351. DOI: 10.1111/j.1468-0459.2010.00399.x.

Löfverström, M. and J. M. Lora (2017). "Abrupt Regime Shifts in the North Atlantic Atmospheric Circulation over the Last Deglaciation". In: *Geophysical Research Letters* 44.15, pp. 8047–8055. DOI: 10.1002/2017GL074274.

López-Moreno, J. I. and S. M. Vicente-Serrano (2008). "Positive and Negative Phases of the Wintertime North Atlantic Oscillation and Drought Occurrence over Europe: A Multitemporal-Scale Approach". In: *Journal of Climate* 21.6, pp. 1220–1243. DOI: 10.1175/2007JCLI1739.1.

Lund, D. C., A. C. Tessin, J. L. Hoffman, and A. Schmittner (2015). "Southwest Atlantic Water Mass Evolution during the Last Deglaciation". In: *Paleoceanography* 30.5, pp. 477–494. DOI: 10.1002/2014PA002657.

Luque, B., L. Lacasa, F. Ballesteros, and J. Luque (2009). "Horizontal Visibility Graphs: Exact Results for Random Time Series". In: *Physical Review E* 80.4. DOI: 10.1103/PhysRevE.80.046103.

Luterbacher, J. and C. Pfister (2015). "The Year without a Summer". In: *Nature Geoscience* 8.4, pp. 246–248. DOI: 10.1038/ngeo2404.

Luterbacher, J. et al. (2016). "European Summer Temperatures since Roman Times". In: *Environmental Research Letters* 11.2, p. 024001. DOI: 10.1088/1748-9326/11/2/024001.

Lynch-Stieglitz, J., W. B. Curry, and D. C. Lund (2009). "Florida Straits Density Structure and Transport over the Last 8000 Years". In: *Paleoceanography* 24.3, PA3209. DOI: 10.1029/2008PA001717.

Malik, N., B. Bookhagen, N. Marwan, and J. Kurths (2012). "Analysis of Spatial and Temporal Extreme Monsoonal Rainfall over South Asia Using Complex Networks". In: *Climate Dynamics* 39.3-4, pp. 971–987. DOI: 10.1007/s00382-011-1156-4.

Maluck, J. and R. V. Donner (2015). "A Network of Networks Perspective on Global Trade". In: *PLOS ONE* 10.7, e0133310. DOI: 10.1371/journal.pone.0133310.

Mann, M. E., R. S. Bradley, and M. K. Hughes (1998). "Global-Scale Temperature Patterns and Climate Forcing over the Past Six Centuries". In: *Nature* 392, p. 779.

Mann, M. E., Z. Zhang, S. Rutherford, R. S. Bradley, M. K. Hughes, D. Shindell, C. Ammann, G. Faluvegi, and F. Ni (2009). "Global Signatures and Dynamical Origins of the Little Ice Age and Medieval Climate Anomaly". In: *Science* 326.5957, pp. 1256–1260. DOI: 10.1126/science.1177303.

Mann, M. E., Z. Zhang, M. K. Hughes, R. S. Bradley, S. K. Miller, S. Rutherford, and F. Ni (2008). "Proxy-Based Reconstructions of Hemispheric and Global Surface Temperature Variations over the Past Two Millennia". In: *Proceedings of the National Academy of Sciences* 105.36, pp. 13252–13257. DOI: 10.1073/pnas.0805721105.

Marcott, S. A. and J. D. Shakun (2015). "Holocene Climate Change and Its Context for the Future". In: *PAGES Magazine Workshop Report*. Vol. 23, p. 28.

Martín-Chivelet, J., M. B. Muñoz-García, R. L. Edwards, M. J. Turrero, and A. I. Ortega (2011). "Land Surface Temperature Changes in Northern Iberia since 4000yrBP, Based on δ13C of Speleothems". In: *Global and Planetary Change* 77.1-2, pp. 1–12. DOI: 10.1016/j.gloplacha.2011.02.002.

Maslin, M. A. and G. E. Swann (2006). "Isotopes in Marine Sediments". In: *Isotopes in Palaeoenvironmental Research*. Ed. by M. J. Leng. Vol. 10. Dordrecht: Kluwer Academic Publishers, pp. 227–290.

Matzke, D., A. Ly, R. Selker, W. D. Weeda, B. Scheibehenne, M. D. Lee, and E.-J. Wagenmakers (2017). "Bayesian Inference for Correlations in the Presence of Measurement Error and Estimation Uncertainty". In: *Collabra: Psychology* 3.1, p. 25. DOI: 10.1525/collabra.78.

McCarroll, D. et al. (2013). "A 1200-Year Multiproxy Record of Tree Growth and Summer Temperature at the Northern Pine Forest Limit of Europe". In: *The Holocene* 23.4, pp. 471–484. DOI: 10.1177/0959683612467483.

McCormick, M., K. Harper, A. M. More, and K. Gibson (2012a). "Geodatabase of Historical Evidence on Roman and Post-Roman Climate". In: *DARMC Scholarly Data Series, DataContributionSeries* 1.

McCormick, M. et al. (2012b). "Climate Change during and after the Roman Empire: Reconstructing the Past from Scientific and Historical Evidence". In: *Journal of Interdisciplinary History* 43.2, pp. 169–220. DOI: 10.1162/JINH_a_00379.

McGee, D., E. Moreno-Chamarro, B. Green, J. Marshall, E. Galbraith, and L. Bradtmiller (2018). "Hemispherically Asymmetric Trade Wind Changes as Signatures of Past ITCZ Shifts". In: *Quaternary Science Reviews* 180, pp. 214–228. DOI: 10.1016/j.quascirev.2017.11.020.

McGregor, G. R. (2005). "Winter North Atlantic Oscillation, Temperature and Ischaemic Heart Disease Mortality in Three English Counties". In: *International Journal of Biometeorology* 49.3, pp. 197–204. DOI: 10.1007/s00484-004-0221-7.

McKay, N. P. and D. S. Kaufman (2014). "An Extended Arctic Proxy Temperature Database for the Past 2,000 Years". In: *Scientific Data* 1. DOI: 10.1038/sdata.2014.26.

McRobie, F., T. Stemler, and K.-H. Wyrwoll (2015). "Transient Coupling Relationships of the Holocene Australian Monsoon". In: *Quaternary Science Reviews* 121, pp. 120–131. DOI: 10.1016/j.quascirev.2015.05.011.

Melvin, T. M., H. Grudd, and K. R. Briffa (2013). "Potential Bias in Updating Tree-Ring Chronologies Using Regional Curve Standardisation: Re-Processing 1500 Years of Torneträsk Density and Ring-Width Data". In: *The Holocene* 23.3, pp. 364–373. DOI: 10.1177/0959683612460791.

Milanković, M. (1930). *Mathematische Klimalehre Und Astronomische Theorie Der Klimaschwankungen.* Handbuch Der Klimatologie. Berlin: Gebrüder Borntraeger.

Miller, G. H. et al. (2012). "Abrupt Onset of the Little Ice Age Triggered by Volcanism and Sustained by Sea-Ice/Ocean Feedbacks". In: *Geophysical Research Letters* 39.2, p. L02708. DOI: 10.1029/2011GL050168.

Moberg, A., D. M. Sonechkin, K. Holmgren, N. M. Datsenko, and W. Karlén (2005). "Highly Variable Northern Hemisphere Temperatures Reconstructed from Low- and High-Resolution Proxy Data". In: *Nature* 433.7026, pp. 613–617. DOI: 10.1038/nature03265.

Monahan, A. H., J. C. Fyfe, M. H. P. Ambaum, D. B. Stephenson, and G. R. North (2009). "Empirical Orthogonal Functions: The Medium Is the Message". In: *Journal of Climate* 22.24, pp. 6501–6514. DOI: 10.1175/2009JCLI3062.1.

Mudelsee, M. (2010). *Climate Time Series Analysis.* Red. by L. A. Mysak and K. Hamilton. Vol. 42. Atmospheric and Oceanographic Sciences Library. Dordrecht: Springer Netherlands. DOI: 10.1007/978-90-481-9482-7.

Mulitza, S., M. Prange, J.-B. Stuut, M. Zabel, T. von Dobeneck, A. C. Itambi, J. Nizou, M. Schulz, and G. Wefer (2008). "Sahel Megadroughts Triggered by Glacial Slowdowns of Atlantic Meridional Overturning". In: *Paleoceanography* 23.4, PA4206. DOI: 10.1029/2008PA001637.

Newman, M. E. J. (2004). "Analysis of Weighted Networks". In: *Physical Review E* 70.5. DOI: 10.1103/PhysRevE.70.056131.

— (2006). "Modularity and Community Structure in Networks". In: *Proceedings of the National Academy of Sciences* 103.23, pp. 8577–8582. DOI: 10.1073/pnas.0601602103.

— (2018). *Networks.* Second edition. Oxford, United Kingdom ; New York, NY, United States of America: Oxford University Press. 780 pp.

NGRIP members et al. (2004). "High-Resolution Record of Northern Hemisphere Climate Extending into the Last Interglacial Period". In: *Nature* 431.7005, pp. 147–151. DOI: 10.1038/nature02805.

Nocke, T., S. Buschmann, J. F. Donges, N. Marwan, H.-J. Schulz, and C. Tominski (2015). "Review: Visual Analytics of Climate Networks". In: *Nonlinear Processes in Geophysics* 22.5, pp. 545–570. DOI: 10.5194/npg-22-545-2015.

North, G. R., J. Wang, and M. G. Genton (2011). "Correlation Models for Temperature Fields". In: *Journal of Climate* 24.22, pp. 5850–5862. DOI: 10.1175/2011JCLI4199.1.

Nuñez, A. M., L. Lacasa, J. P. Gomez, and B. Luque (2012). "Visibility Algorithms: A Short Review". In: *New Frontiers in Graph Theory.* Ed. by Y. Zhang. London: InTech.

Ojala, A. E. and T. Alenius (2005). "10000 Years of Interannual Sedimentation Recorded in the Lake Nautajärvi (Finland) Clastic–Organic Varves". In: 219.3, pp. 285–302.

Olsen, J., N. J. Anderson, and M. F. Knudsen (2012). "Variability of the North Atlantic Oscillation over the Past 5,200 Years". In: *Nature Geoscience* 5.11, pp. 808–812. DOI: 10.1038/ngeo1589.

Oppo, D. W., W. B. Curry, and J. F. McManus (2015). "What Do Benthic δ ^{13} C and δ ^{18} O Data Tell Us about Atlantic Circulation during Heinrich Stadial 1?" In: *Paleoceanography* 30.4, pp. 353–368. DOI: 10.1002/2014PA002667.

Ortega, P., F. Lehner, D. Swingedouw, V. Masson-Delmotte, C. C. Raible, M. Casado, and P. Yiou (2015). "A Model-Tested North Atlantic Oscillation Reconstruction for the Past Millennium". In: *Nature* 523.7558, pp. 71–74. DOI: 10.1038/nature14518.

Oster, J. L. and N. P. Kelley (2016). "Tracking Regional and Global Teleconnections Recorded by Western North American Speleothem Records". In: *Quaternary Science Reviews* 149, pp. 18–33. DOI: 10.1016/j.quascirev.2016.07.009.

PAGES 2k Consortium (2013). "Continental-Scale Temperature Variability during the Past Two Millennia". In: *Nature Geoscience* 6.5, pp. 339–346. DOI: 10.1038/ngeo1797.

Paillard, D. (2015). "Quaternary Glaciations: From Observations to Theories". In: *Quaternary Science Reviews* 107, pp. 11–24. DOI: 10.1016/j.quascirev.2014.10.002.

Paninski, L. (2003). "Estimation of Entropy and Mutual Information". In: *Neural Computation* 15.6, pp. 1191–1253. DOI: 10.1162/089976603321780272.

Papana, A. and D. Kugiumtzis (2009). "Evaluation of Mutual Information Estimators for Time Series". In: *International Journal of Bifurcation and Chaos* 19.12, pp. 4197–4215. DOI: 10.1142/S0218127409025298.

Parish, T. R. and D. H. Bromwich (1987). "The Surface Windfield over the Antarctic Ice Sheets". In: *Nature* 328.6125, pp. 51–54. DOI: 10.1038/328051a0.

Parrenin, F., V. Masson-Delmotte, P. Kohler, D. Raynaud, D. Paillard, J. Schwander, C. Barbante, A. Landais, A. Wegner, and J. Jouzel (2013). "Synchronous Change of Atmospheric CO2 and Antarctic Temperature During the Last Deglacial Warming". In: *Science* 339.6123, pp. 1060–1063. DOI: 10.1126/science.1226368.

Patterson, W. P., K. A. Dietrich, C. Holmden, and J. T. Andrews (2010). "Two Millennia of North Atlantic Seasonality and Implications for Norse Colonies". In: *Proceedings of the National Academy of Sciences* 107.12, pp. 5306–5310. DOI: 10.1073/pnas.0902522107.

Pedro, J. B., M. Jochum, C. Buizert, F. He, S. Barker, and S. O. Rasmussen (2018). "Beyond the Bipolar Seesaw: Toward a Process Understanding of Interhemispheric Coupling". In: *Quaternary Science Reviews* 192, pp. 27–46. DOI: 10.1016/j.quascirev.2018.05.005.

Peltier, W. and R. Fairbanks (2006). "Global Glacial Ice Volume and Last Glacial Maximum Duration from an Extended Barbados Sea Level Record". In: *Quaternary Science Reviews* 25.23-24, pp. 3322–3337. DOI: 10.1016/j.quascirev.2006.04.010.

Pimm, S. L. (1982). *Food Webs*. Dordrecht: Springer Netherlands.

Piper, D. and M. Kunz (2017). "Spatiotemporal Variability of Lightning Activity in Europe and the Relation to the North Atlantic Oscillation Teleconnection Pattern". In: *Natural Hazards and Earth System Sciences* 17.8, pp. 1319–1336. DOI: 10.5194/nhess-17-1319-2017.

Pocock, J. G. A. (1962). "The Origins of Study of the Past: A Comparative Approach". In: *Comparative Studies in Society and History* 4.02, p. 209. DOI: 10.1017/S0010417500001341.

Poli, P. et al. (2016). "ERA-20C: An Atmospheric Reanalysis of the Twentieth Century". In: *Journal of Climate* 29.11, pp. 4083–4097. DOI: 10.1175/JCLI-D-15-0556.1.

Polson, N. G. and J. G. Scott (2012). "On the Half-Cauchy Prior for a Global Scale Parameter". In: *Bayesian Analysis* 7.4, pp. 887–902. DOI: 10.1214/12-BA730.

Popa, I. and Z. Kern (2009). "Long-Term Summer Temperature Reconstruction Inferred from Tree-Ring Records from the Eastern Carpathians". In: *Climate Dynamics* 32.7-8, pp. 1107–1117. DOI: 10.1007/s00382-008-0439-x.

Post, E. and M. C. Forchhammer (2002). "Synchronization of Animal Population Dynamics by Large-Scale Climate". In: *Nature* 420.6912, pp. 168–171. DOI: 10.1038/nature01064.

Praetorius, S. K., J. F. McManus, D. W. Oppo, and W. B. Curry (2008). "Episodic Reductions in Bottom-Water Currents since the Last Ice Age". In: *Nature Geoscience* 1.7, pp. 449–452. DOI: 10.1038/ngeo227.

Quian Quiroga, R., T. Kreuz, and P. Grassberger (2002). "Event Synchronization: A Simple and Fast Method to Measure Synchronicity and Time Delay Patterns". In: *Physical Review E* 66.4. DOI: 10.1103/PhysRevE.66.041904.

Radebach, A., R. V. Donner, J. Runge, J. F. Donges, and J. Kurths (2013). "Disentangling Different Types of El Niño Episodes by Evolving Climate Network Analysis". In: *Physical Review E* 88.5. DOI: 10.1103/PhysRevE.88.052807.

Rahmstorf, S. (2002). "Ocean Circulation and Climate during the Past 120,000 Years". In: *Nature* 419.6903, pp. 207–214. DOI: 10.1038/nature01090.

Rasmussen, T., T. van Weering, and L. Labeyrie (1996). "High Resolution Stratigraphy of the Faeroe-Shetland Channel and Its Relation to North Atlantic Paleoceanography: The Last 87 Kyr". In: *Marine Geology* 131.1-2, pp. 75–88. DOI: 10.1016/0025-3227(95)00145-X.

Rasmussen, T. L., E. Thomsen, and T. C. E. Van Weering (1998). "Cyclic Sedimentation on the Faeroe Drift 53-10 Ka BP Related to Climatic Variations". In: *Geological Society, London, Special Publications* 129.1, pp. 255–267. DOI: 10.1144/GSL.SP.1998.129.01.16.

Ravetti, M. G., L. C. Carpi, B. A. Gonçalves, A. C. Frery, and O. A. Rosso (2014). "Distinguishing Noise from Chaos: Objective versus Subjective Criteria Using Horizontal Visibility Graph". In: *PLoS ONE* 9.9, e108004. DOI: 10.1371/journal.pone.0108004.

Rehfeld, K. (2013). "Embracing Nature's Inhomogeneity". Humboldt-Universität zu Berlin, Mathematisch-Naturwissenschaftliche Fakultät I. DOI: http://dx.doi.org/10.18452/16821.

Rehfeld, K. and J. Kurths (2014). "Similarity Estimators for Irregular and Age-Uncertain Time Series". In: *Climate of the Past* 10.1, pp. 107–122. DOI: 10.5194/cp-10-107-2014.

Rehfeld, K., N. Marwan, J. Heitzig, and J. Kurths (2011). "Comparison of Correlation Analysis Techniques for Irregularly Sampled Time Series". In: *Nonlin. Processes Geophys.* 18.3, pp. 389–404. DOI: 10.5194/npg-18-389-2011.

Rehfeld, K., N. Marwan, S. F. M. Breitenbach, and J. Kurths (2013). "Late Holocene Asian Summer Monsoon Dynamics from Small but Complex Networks of Paleoclimate Data". In: *Climate Dynamics* 41.1, pp. 3–19. DOI: 10.1007/s00382-012-1448-3.

Rehfeld, K., T. Münch, S. L. Ho, and T. Laepple (2018). "Global Patterns of Declining Temperature Variability from the Last Glacial Maximum to the Holocene". In: *Nature* 554.7692, pp. 356–359. DOI: 10.1038/nature25454.

Reimer, P. J. et al. (2013). "IntCal13 and Marine13 Radiocarbon Age Calibration Curves 0–50,000 Years Cal BP". In: *Radiocarbon* 55.04, pp. 1869–1887. DOI: 10.2458/azu_js_rc.55.16947.

Robock, A. (2000). "Volcanic Eruptions and Climate". In: *Reviews of Geophysics* 38.2, pp. 191–219. DOI: 10.1029/1998RG000054.

Rodwell, M. J., D. P. Rowell, and C. K. Folland (1999). "Oceanic Forcing of the Wintertime North Atlantic Oscillation and European Climate". In: *Nature* 398.6725, pp. 320–323. DOI: 10.1038/18648.

Rogers, J. C. (1997). "North Atlantic Storm Track Variability and Its Association to the North Atlantic Oscillation and Climate Variability of Northern Europe". In: *Journal of Climate* 10.7, pp. 1635–1647. DOI: 10.1175/1520-0442(1997)010<1635:NASTVA>2.0.CO;2.

Ruggieri, E. (2013). "A Bayesian Approach to Detecting Change Points in Climatic Records". In: *International Journal of Climatology* 33.2, pp. 520–528. DOI: 10.1002/joc.3447.

Rühlemann, C., S. Mulitza, P. J. Müller, G. Wefer, and R. Zahn (1999). "Warming of the Tropical Atlantic Ocean and Slowdown of Thermohaline Circulation during the Last Deglaciation". In: *Nature* 402.6761, pp. 511–514. DOI: 10.1038/990069.

Runge, J., V. Petoukhov, and J. Kurths (2014). "Quantifying the Strength and Delay of Climatic Interactions: The Ambiguities of Cross Correlation and a Novel Measure Based on Graphical Models". In: *Journal of Climate* 27.2, pp. 720–739. DOI: 10.1175/JCLI-D-13-00159.1.

Saarni, S., T. Saarinen, and P. Dulski (2016). "Between the North Atlantic Oscillation and the Siberian High: A 4000-Year Snow Accumulation History Inferred from Varved Lake Sediments in Finland". In: *The Holocene* 26.3, pp. 423–431. DOI: 10.1177/0959683615609747.

Saarni, S., T. Saarinen, and A. Lensu (2015). "Organic Lacustrine Sediment Varves as Indicators of Past Precipitation Changes: A 3,000-Year Climate Record from Central Finland". In: *Journal of Paleolimnology* 53.4, pp. 401–413. DOI: 10.1007/s10933-015-9832-8.

Sarnthein, M. (2004). "Age Determination of Sediment Core GIK13289-2". In: DOI: 10.1594/PANGAEA.134609.

Sarnthein, M., K. Winn, S. J. A. Jung, J.-C. Duplessy, L. Labeyrie, H. Erlenkeuser, and G. Ganssen (1994). "Changes in East Atlantic Deepwater Circulation over the Last 30,000 Years: Eight Time Slice Reconstructions". In: *Paleoceanography* 9.2, pp. 209–267. DOI: 10.1029/93PA03301.

Schleussner, C.-F., D. V. Divine, J. F. Donges, A. Miettinen, and R. V. Donner (2015). "Indications for a North Atlantic Ocean Circulation Regime Shift at the Onset of the Little Ice Age". In: *Climate Dynamics* 45.11, pp. 3623–3633. DOI: 10.1007/s00382-015-2561-x.

Schmutz, C., J. Luterbacher, D. Gyalistras, E. Xoplaki, and H. Wanner (2000). "Can We Trust Proxy-Based NAO Index Reconstructions?" In: *Geophysical Research Letters* 27.8, pp. 1135–1138. DOI: 10.1029/1999GL011045.

Schreiber, T. and A. Schmitz (2000). "Surrogate Time Series". In: *Physica D: Nonlinear Phenomena* 142.3–4, pp. 346–382. DOI: 10.1016/S0167-2789(00)00043-9.

Schurer, A. P., S. F. Tett, and G. C. Hegerl (2014). "Small Influence of Solar Variability on Climate over the Past Millennium". In: *Nature Geoscience* 7.2, pp. 104–108. DOI: 10.1038/ngeo2040.

Seim, A., U. Büntgen, P. Fonti, H. Haska, F. Herzig, W. Tegel, V. Trouet, and K. Treydte (2012). "Climate Sensitivity of a Millennium-Long Pine Chronology from Albania". In: *Climate Research* 51.3, pp. 217–228. DOI: 10.3354/cr01076.

Serreze, M. C., F. Carse, R. G. Barry, and J. C. Rogers (1997). "Icelandic Low Cyclone Activity: Climatological Features, Linkages with the NAO, and Relationships with Recent Changes in the Northern Hemisphere Circulation". In: *Journal of Climate* 10.3, pp. 453–464. DOI: 10.1175/1520-0442(1997)010<0453:ILCACF>2.0.CO;2.

Shi, F., B. Yang, A. Mairesse, L. von Gunten, J. Li, A. Br‰uning, F. Yang, and X. Xiao (2013). "Northern Hemisphere Temperature Reconstruction during the Last Millennium Using Multiple Annual Proxies". In: *Climate Research* 56.3, pp. 231–244. DOI: 10.3354/cr01156.

Sigl, M. et al. (2015). "Timing and Climate Forcing of Volcanic Eruptions for the Past 2,500 Years". In: *Nature* 523.7562, pp. 543–549. DOI: 10.1038/nature14565.

Skinner, L. C., S. Fallon, C. Waelbroeck, E. Michel, and S. Barker (2010). "Ventilation of the Deep Southern Ocean and Deglacial CO2 Rise". In: *Science* 328.5982, pp. 1147–1151. DOI: 10.1126/science.1183627.

Sortor, R. N. and D. C. Lund (2011). "No Evidence for a Deglacial Intermediate Water Δ14C Anomaly in the SW Atlantic". In: *Earth and Planetary Science Letters* 310.1-2, pp. 65–72. DOI: 10.1016/j.epsl.2011.07.017.

Steinhilber, F., J. Beer, and C. Fröhlich (2009). "Total Solar Irradiance during the Holocene". In: *Geophysical Research Letters* 36.19, p. L19704. DOI: 10.1029/2009GL040142.

Stolbova, V., E. Surovyatkina, B. Bookhagen, and J. Kurths (2016). "Tipping Elements of the Indian Monsoon: Prediction of Onset and Withdrawal". In: *Geophysical Research Letters* 43.8, pp. 3982–3990. DOI: 10.1002/2016GL068392.

Storch, H. von and F. W. Zwiers (2003). *Statistical Analysis in Climate Research*. 1. paperback ed., reprinted. OCLC: 249539667. Cambridge: Cambridge Univ. Press. 484 pp.

Stothers, R. B. (1984). "Mystery Cloud of AD 536". In: *Nature* 307.5949, pp. 344–345. DOI: 10.1038/307344a0.

Strogatz, S. H. (2014). *Nonlinear Dynamics And Chaos: With Applications To Physics, Biology, Chemistry, And Engineering*. Westview Press, Boulder.

Tarbuck, E. J. and F. K. Lutgens (2014). *Earth: An Introduction to Physical Geology*. 11th ed. Boston: Pearson. 876 pp.

Telesca, L. and M. Lovallo (2012). "Analysis of Seismic Sequences by Using the Method of Visibility Graph". In: *EPL (Europhysics Letters)* 97.5, p. 50002. DOI: 10.1209/0295-5075/97/50002.

Tessin, A. C. and D. C. Lund (2013). "Isotopically Depleted Carbon in the Mid-Depth South Atlantic during the Last Deglaciation". In: *Paleoceanography* 28.2, pp. 296–306. DOI: 10.1002/palo.20026.

Thornalley, D. J. R., H. Elderfield, and I. N. McCave (2010). "Intermediate and Deep Water Paleoceanography of the Northern North Atlantic over the Past 21,000 Years". In: *Paleoceanography* 25.1, PA1211. DOI: 10.1029/2009PA001833.

Tiljander, M., M. Saarnisto, A. E. K. Ojala, and T. Saarinen (2003). "A 3000-Year Palaeoenvironmental Record from Annually Laminated Sediment of Lake Korttajarvi, Central Finland". In: *Boreas* 32.4, pp. 566–577. DOI: 10.1111/j.1502-3885.2003.tb01236.x.

Toggweiler, J. R. (2009). "Shifting Westerlies". In: *Science* 323.5920, pp. 1434–1435. DOI: 10.1126/science.1169823.

Torres, M. E., M. A. Colominas, G. Schlotthauer, and P. Flandrin (2011). "A Complete Ensemble Empirical Mode Decomposition with Adaptive Noise". In: IEEE, pp. 4144–4147. DOI: 10.1109/ICASSP.2011.5947265.

Trachsel, M. and R. J. Telford (2017). "All Age–Depth Models Are Wrong, but Are Getting Better". In: *The Holocene* 27.6, pp. 860–869. DOI: 10.1177/0959683616675939.

Trouet, V., J. Esper, N. E. Graham, A. Baker, J. D. Scourse, and D. C. Frank (2009). "Persistent Positive North Atlantic Oscillation Mode Dominated the Medieval Climate Anomaly". In: *Science* 324.5923, pp. 78–80. DOI: 10.1126/science.1166349.

Tsonis, A. and P. Roebber (2004). "The Architecture of the Climate Network". In: *Physica A: Statistical Mechanics and its Applications* 333, pp. 497–504. DOI: 10.1016/j.physa.2003.10.045.

Tsonis, A. A. and K. L. Swanson (2008). "Topology and Predictability of El Niño and La Niña Networks". In: *Physical Review Letters* 100.22. DOI: 10.1103/PhysRevLett.100.228502.

Tsonis, A. A., K. L. Swanson, and P. J. Roebber (2006). "What Do Networks Have to Do with Climate?" In: *Bulletin of the American Meteorological Society* 87.5, pp. 585–596. DOI: 10.1175/BAMS-87-5-585.

Tsonis, A. A., G. Wang, K. L. Swanson, F. A. Rodrigues, and L. d. F. Costa (2011). "Community Structure and Dynamics in Climate Networks". In: *Climate Dynamics* 37.5-6, pp. 933–940. DOI: 10.1007/s00382-010-0874-3.

Vaganov, E. A., M. K. Hughes, A. V. Kirdyanov, F. H. Schweingruber, and P. P. Silkin (1999). "Influence of Snowfall and Melt Timing on Tree Growth in Subarctic Eurasia". In: *Nature* 400.6740, pp. 149–151. DOI: 10.1038/22087.

Vanschoren, J., B. Pfahringer, and G. Holmes (2008). "Learning from the Past with Experiment Databases". In: *PRICAI 2008: Trends in Artificial Intelligence.* Ed. by T.-B. Ho and Z.-H. Zhou. Vol. 5351. Berlin, Heidelberg: Springer Berlin Heidelberg, pp. 485–496. DOI: 10.1007/978-3-540-89197-0_45.

Vidal, L., L. Labeyrie, E. Cortijo, M. Arnold, J. Duplessy, E. Michel, S. Becqué, and T. van Weering (1997). "Evidence for Changes in the North Atlantic Deep Water Linked to Meltwater Surges during the Heinrich Events". In: *Earth and Planetary Science Letters* 146.1-2, pp. 13–27. DOI: 10.1016/S0012-821X(96)00192-6.

Vidal, L., R. Schneider, O. Marchal, T. Bickert, T. Stocker, and G. Wefer (1999). "Link between the North and South Atlantic during the Heinrich Events of the Last Glacial Period". In: *Climate Dynamics* 15.12, pp. 909–919. DOI: 10.1007/s003820050321.

Vinther, B. M., K. K. Andersen, A. W. Hansen, T. Schmith, and P. D. Jones (2003). "Improving the Gibraltar/Reykjavik NAO Index". In: *Geophysical Research Letters* 30.23, p. 2222. DOI: 10.1029/2003GL018220.

Vinther, B. M., H. B. Clausen, D. A. Fisher, R. M. Koerner, S. J. Johnsen, K. K. Andersen, D. Dahl-Jensen, S. O. Rasmussen, J. P. Steffensen, and A. M. Svensson (2008). "Synchronizing Ice Cores from the Renland and Agassiz Ice Caps to the Greenland Ice Core Chronology". In: *Journal of Geophysical Research: Atmospheres* 113.D8, p. D08115. DOI: 10.1029/2007JD009143.

Vinther, B. M., P. D. Jones, K. R. Briffa, H. B. Clausen, K. K. Andersen, D. Dahl-Jensen, and S. J. Johnsen (2010). "Climatic Signals in Multiple Highly Resolved Stable Isotope Records from Greenland". In: *Quaternary Science Reviews* 29.3–4, pp. 522–538. DOI: 10.1016/j.quascirev.2009.11.002.

Vinther, B. M. et al. (2006). "A Synchronized Dating of Three Greenland Ice Cores throughout the Holocene". In: *Journal of Geophysical Research: Atmospheres* 111.D13, p. D13102. DOI: 10.1029/2005JD006921.

Voelker, A., S. Lebreiro, J. Schonfeld, I. Cacho, H. Erlenkeuser, and F. Abrantes (2006). "Mediterranean Outflow Strengthening during Northern Hemisphere Coolings: A Salt Source for the Glacial Atlantic?" In: *Earth and Planetary Science Letters* 245.1-2, pp. 39–55. DOI: 10.1016/j.epsl.2006.03.014.

Von Toussaint, U. (2011). "Bayesian Inference in Physics". In: *Reviews of Modern Physics* 83.3, pp. 943–999. DOI: 10.1103/RevModPhys.83.943.

Waelbroeck, C., C. Levi, J. Duplessy, L. Labeyrie, E. Michel, E. Cortijo, F. Bassinot, and F. Guichard (2006). "Distant Origin of Circulation Changes in the Indian Ocean during

the Last Deglaciation". In: *Earth and Planetary Science Letters* 243.1-2, pp. 244–251. DOI: 10.1016/j.epsl.2005.12.031.

Waelbroeck, C., L. C. Skinner, L. Labeyrie, J.-C. Duplessy, E. Michel, N. Vazquez Riveiros, J.-M. Gherardi, and F. Dewilde (2011). "The Timing of Deglacial Circulation Changes in the Atlantic". In: *Paleoceanography* 26.3, PA3213. DOI: 10.1029/2010PA002007.

Wallace, J. M., Q. Fu, B. V. Smoliak, P. Lin, and C. M. Johanson (2012). "Simulated versus Observed Patterns of Warming over the Extratropical Northern Hemisphere Continents during the Cold Season". In: *Proceedings of the National Academy of Sciences* 109.36, pp. 14337–14342. DOI: 10.1073/pnas.1204875109.

Wang, G., A. J. Dolman, and A. Alessandri (2011). "A Summer Climate Regime over Europe Modulated by the North Atlantic Oscillation". In: *Hydrology and Earth System Sciences* 15.1, pp. 57–64. DOI: 10.5194/hess-15-57-2011.

Wang, Q. (2008). "On the Cultural Constitution of Collective Memory". In: *Memory* 16.3, pp. 305–317. DOI: 10.1080/09658210701801467.

Wang, T., D. Surge, and K. J. Walker (2013). "Seasonal Climate Change across the Roman Warm Period/Vandal Minimum Transition Using Isotope Sclerochronology in Archaeological Shells and Otoliths, Southwest Florida, USA". In: *Quaternary International* 308-309, pp. 230–241. DOI: 10.1016/j.quaint.2012.11.013.

Wanner, H. et al. (2008). "Mid- to Late Holocene Climate Change: An Overview". In: *Quaternary Science Reviews* 27.19, pp. 1791–1828. DOI: 10.1016/j.quascirev.2008.06.013.

Watts, D. J. and S. H. Strogatz (1998). "Collective Dynamics of 'Small-World' Networks". In: *Nature* 393.6684, pp. 440–442. DOI: 10.1038/30918.

Weiss, G. (1975). "Time-Reversibility of Linear Stochastic Processes". In: *Journal of Applied Probability* 12.04, pp. 831–836. DOI: 10.2307/3212735.

Weiss, H. and R. S. Bradley (2001). "What Drives Societal Collapse?" In: *Science* 291.5504, pp. 609–610. DOI: 10.1126/science.1058775.

Weldeab, S., T. Friedrich, A. Timmermann, and R. R. Schneider (2016). "Strong Mid-depth Warming and Weak Radiocarbon Imprints in the Equatorial Atlantic during Heinrich 1 and Younger Dryas: Deglacial Warming of EEA Middepth Water". In: *Paleoceanography* 31.8, pp. 1070–1082. DOI: 10.1002/2016PA002957.

Werner, J. P., D. V. Divine, F. Charpentier Ljungqvist, T. Nilsen, and P. Francus (2018). "Spatio-Temporal Variability of Arctic Summer Temperatures over the Past 2 Millennia". In: *Climate of the Past* 14.4, pp. 527–557. DOI: 10.5194/cp-14-527-2018.

Wetter, O. and C. Pfister (2011). "Spring-Summer Temperatures Reconstructed for Northern Switzerland and Southwestern Germany from Winter Rye Harvest Dates, 1454–1970". In: *Climate of the Past* 7.4, pp. 1307–1326. DOI: 10.5194/cp-7-1307-2011.

Wiedermann, M., J. F. Donges, D. Handorf, J. Kurths, and R. V. Donner (2016a). "Hierarchical Structures in Northern Hemispheric Extratropical Winter Ocean–Atmosphere Interactions". In: *International Journal of Climatology*, pp. 3821–3836. DOI: 10.1002/joc.4956.

Wiedermann, M., A. Radebach, J. F. Donges, J. Kurths, and R. V. Donner (2016b). "A Climate Network-Based Index to Discriminate Different Types of El Niño and La Niña". In: *Geophysical Research Letters* 43.13, pp. 7176–7185. DOI: 10.1002/2016GL069119.

Wilson, R. J. S. et al. (2016). "Last Millennium Northern Hemisphere Summer Temperatures from Tree Rings: Part I: The Long Term Context". In: *Quaternary Science Reviews* 134, pp. 1–18. DOI: 10.1016/j.quascirev.2015.12.005.

Wolf, F., C. Kirsch, and R. V. Donner (2018). "Edge Directionality Properties in Complex Spherical Networks". In: arXiv: 1811.05317.

Woollings, T., C. Franzke, D. L. R. Hodson, B. Dong, E. A. Barnes, C. C. Raible, and J. G. Pinto (2015). "Contrasting Interannual and Multidecadal NAO Variability". In: *Climate Dynamics* 45.1-2, pp. 539–556. DOI: 10.1007/s00382-014-2237-y.

Wu, Z. and N. E. Huang (2009). "Ensemble Empirical Mode Decomposition: A Noise Assisted Data Analysis Method". In: *Advances in Adaptive Data Analysis* 01.01, pp. 1–41. DOI: 10.1142/S1793536909000047.

Yamasaki, K., A. Gozolchiani, and S. Havlin (2008). "Climate Networks around the Globe Are Significantly Affected by El Niño". In: *Physical Review Letters* 100.22. DOI: 10.1103/PhysRevLett.100.228501.

Yang, Y., J. Wang, H. Yang, and J. Mang (2009). "Visibility Graph Approach to Exchange Rate Series". In: *Physica A: Statistical Mechanics and its Applications* 388.20, pp. 4431–4437. DOI: 10.1016/j.physa.2009.07.016.

Yeats, R. S. and C. S. Prentice (1996). "Introduction to Special Section: Paleoseismology". In: *Journal of Geophysical Research: Solid Earth* 101.B3, pp. 5847–5853. DOI: 10.1029/95JB03134.

Yom-Tov, E., Y. Yom-Tov, S. Yom-Tov, M. Andersen, D. Rosenfeld, A. Devasthale, and E. Geffen (2017). "The Complex Effects of Geography, Ambient Temperature, and North Atlantic Oscillation on the Body Size of Arctic Hares in Greenland". In: *Biological Journal of the Linnean Society* 120.4, pp. 909–918. DOI: 10.1093/biolinnean/blw018.

Zarriess, M. and A. Mackensen (2011). "Testing the Impact of Seasonal Phytodetritus Deposition on δ^{13}C of Epibenthic Foraminifer *Cibicidoides Wuellerstorfi* : A 31,000 Year High-Resolution Record from the Northwest African Continental Slope". In: *Paleoceanography* 26.2, PA2202. DOI: 10.1029/2010PA001944.

Zhang, J., Z. Liu, E. C. Brady, D. W. Oppo, P. U. Clark, A. Jahn, S. A. Marcott, and K. Lindsay (2017a). "Asynchronous Warming and δ^{18}O Evolution of Deep Atlantic Water Masses during the Last Deglaciation". In: *Proceedings of the National Academy of Sciences* 114.42, pp. 11075–11080. DOI: 10.1073/pnas.1704512114.

Zhang, P., H. W. Linderholm, B. E. Gunnarson, J. A. Björklund, and D. Chen (2016). "1200 Years of Warm-Season Temperature Variability in Central Scandinavia Inferred from Tree-Ring Density". In: *Climate of the Past* 12.6, pp. 1297–1312. DOI: 10.5194/cp-12-1297-2016.

Zhang, P. et al. (2008). "A Test of Climate, Sun, and Culture Relationships from an 1810-Year Chinese Cave Record". In: *Science* 322.5903, pp. 940–942. DOI: 10.1126/science.1163965.

Zhang, R., Y. Zou, J. Zhou, Z.-K. Gao, and S. Guan (2017b). "Visibility Graph Analysis for Re-Sampled Time Series from Auto-Regressive Stochastic Processes". In: *Communications in Nonlinear Science and Numerical Simulation* 42, pp. 396–403. DOI: 10.1016/j.cnsns.2016.04.031.

Zori, D. M. (2016). *The Norse in Iceland*. Vol. 1. Oxford University Press. DOI: 10.1093/oxfordhb/9780199935413.013.7.

Zorita, E. and F. González-Rouco (2002). "Are Temperature-Sensitive Proxies Adequate for North Atlantic Oscillation Reconstructions?" In: *Geophysical Research Letters* 29.14, pp. 48–1. DOI: 10.1029/2002GL015404.

Zou, Y., R. V. Donner, N. Marwan, J. F. Donges, and J. Kurths (2018). "Complex Network Approaches to Nonlinear Time Series Analysis". In: *Physics Reports*. DOI: 10.1016/j. physrep.2018.10.005.

Declaration

I hereby assure that I wrote this present thesis independently and no different sources were used besides the indicated ones.

Berlin, December 6, 2018